Investigating Mars surface icecaps using the NOMAD spectrometer on board Trace Gas Orbiter

Luca Ruiz Lozano
Secteur des Sciences et Technologies
Earth and Life Institute

Thesis presented to obtain the degree of Doctor of Science
October 2023

À abuelo,

Comité

Promotrice	
Prof. Véronique Dehant	Université catholique de Louvain & Observatoire Royal de Belgique
Présidente	
Prof. Qiuzhen Yin	Université catholique de Louvain
Secrétaire	
Prof. Michel Crucifix	Université catholique de Louvain
Autres membres du jury	
Dr. Özgür Karatekin	Observatoire Royal de Belgique
Dr. Ir. Ann Carine Vandaele	Institut royal d'Aéronomie Spatiale de Belgique
Dr. Séverine Robert	Institut royal d'Aéronomie Spatiale de Belgique

Remerciements

Premièrement, je tiens à remercier Véronique Dehant de m'avoir encouragé et permis d'entreprendre un doctorat en sciences au sein de son équipe. Je remercie également Özgür Karatekin pour son aide, ses conseils et son dévouement tout au long de la thèse. Özgür m'a toujours soutenu et défendu dans les moments compliqués. Je tiens également à remercier Giancarlo Bellucci et Fabrizio Oliva pour leur encadrement, leur enseignement, leur soutien et leur patience durant toutes ces années.

Je souhaite remercier les membres de mon jury, Quizhen Yin, Véronique Dehant, Özgür Karatekin, Michel Crucifix, Ann Carine Vandaele et Séverine Robert, d'avoir accepté ce rôle. Leurs remarques et conseils m'ont grandement aidé à améliorer le manuscrit. Je remercie l'Université catholique de Louvain pour les moyens fournis nécessaire à la réalisation de cette thèse, ainsi que mes collègues de l'Observatoire Royal de Belgique pour ces années partagées, ces temps de midi et toutes ces réunions qui m'ont énormément apporté. Je remercie aussi mes collègues de l'Institut royal d'Aéronomie Spatiale de Belgique, Ian Thomas et Yannick Willame, pour leur aide et encadrement dans ce travail. Je n'oublierai jamais toutes ces conférences à l'étranger qui m'ont permis de voyager et de rencontrer des personnes formidables. Je pense notamment à Geronimo Villanueva et Giuliano Liuzzi. Plus qu'un travail, ces années passées ont été une aventure passionante me permettant de réaliser un rêve d'enfant.

Je remercie infiniment ma soeur, Livia, et mes parents qui ont su trouver les solutions pour que je puisse réaliser tout ce dont je rêvais. Je tiens également à remercier Elise qui m'a toujours soutenu. Lors des périodes de doute et de questionnement, elle a su trouver les mots pour me remotiver et me remobiliser. Je lui en serai toujours reconnaissant. Enfin, je souhaite remercier mes amis pour leur soutien inconditionnel et leur compréhension durant ces années. Ils ont toujours été présents pour moi, et ce, jusqu'à la relecture de cette page (merci Ségolène!).

Abstract

The sublimation and condensation processes of the seasonal Martian caps are linked to the CO_2 cycle, the main cycle on Mars. Observing the seasonal growth and recession rates of the caps provides insight into the local and global environment. These seasonal processes strongly influence the global energy budget of Mars. While they are repeatable over the Martian Years (MY), interannual variability exists due to global dust storms.

Since April 2018, the Nadir and Occultation for Mars Discovery (NOMAD) instrument on board ExoMars-Trace Gas Orbiter has been monitoring the Martian atmosphere. Although NOMAD is not primarily dedicated to surface analysis, this PhD thesis develops high spectral resolution methods to analyse the information content of NOMAD's nadir infrared channel (2.3-3.8 μm) for surface information. By identifying ice absorption bands in this spectral range, spectral indices are defined to distinguish CO_2 ice from H_2O ice. The research compares seasonal processes in the Martian caps during MY34-36 (April 2018 to December 2022), and analyses the potential impact of the MY34 global dust storm on the Southern polar cap. In addition, the present thesis demonstrates that NOMAD is also able to detect atmospheric ice signatures, such as the Polar Hood clouds (H_2O ice clouds) at high latitudes and mesospheric CO_2 ice clouds at mid-equatorial latitudes. Finally, the high spectral resolution of NOMAD offers the possibility to retrieve some microphysical ice properties.

Contents

List of Abbreviations

Acronyms

ACB	Aphelion Cloud Belt
AII	Adapted Ice Index
AOTF	Acoustic-optical tunable filter
au	Astronomical units
BD2292	Band depth at 2.29 μm
BIRA-IASB	Royal Belgian Institute for Space Aeronomy
CaSSIS	Colour and Stereo Surface Imaging System
CRISM	Compact Reconnaissance Imaging Spectrometer
ESA	European Space Agency
FCI	Frost and Clouds Index
GCM	General Circulation Model
HRSC	High Resolution Stereo Camera
ICIR	Reversed Ice Cloud Index
II	Ice Index
InSight	Interior Exploration using Seismic Investigations, Geodesy and Heat Transport
IR	Infrared
JUICE	JUpiter ICy moon Explorer
LMD	Laboratoire de Météorologie Dynamique

LNO	Limb Nadir and Occultation
LST	Local Solar Time
MAJIS	Moons And Jupiter Imaging Spectrometer
MARCI	Mars Color Imager
MARSIS	Mars Advanced Radar for Subsurface and Ionosphere Sounding
MCD	Mars Climate Database
MCS	Mars Climate Sounder
MEX	Mars Express
MGS	Mars Global Surveyor
MIRS	MMX InfraRed Spectrometer
MITRA	Multiple scattering Inverse radiative TRansfer Atmospheric
MMX	Martian Moons eXploration
MOC	Mars Orbiter Camera
MOLA	Mars Orbiter Laser Altimeter
MRO	Mars Reconnaissance Orbiter
MY	Martian Year
NASA	National Aeronautics and Space Administration
NII	New Ice Index
NIR	Near infrared
NOMAD	Nadir and Occultation for MArs Discovery
NPH	Northern Polar Hood
NPLD	Northen polar deposits
OMEGA	Observatoire pour la Minéralogie, l'Eau, les Glaces et l'Activité
PCT	Perihelion cloud trails

PFS	Planetary Fourier Spectrometer
PH	Polar Hoods
PLD	Polar deposits
PSG	Planetary Spectrum Generator
RISE	Rotation and Interior Structure Experiment
ROB-ORB	Royal Observatory of Belgium
SAM	Spectral Angle Mapper χ index
SHARAD	SHAllow RADar
SNR	Signal-to-noise ratio
SO	Solar Occultation
SOIR	Solar Occultation in the Infrared
SPH	Southern Polar Hood
SPICAM	SPectroscopy for the Investigation of the Characteristics of the Atmosphere of Mars
SPLD	Southern polar deposits
SZA	Solar zenith angle
TES	Thermal Emission Spectrometer
TGO	Trace Gas Orbiter
THEMIS	Thermal Emission Imaging System
TIRI	Thermal Infrared Imager
UVIS	Ultraviolet-visible
WIC	Water ice column

Physics parameters

μ	Mean value of a Gaussian distribution
ϕ_λ	Solar flux
σ	Standard deviation of a Gaussian distribution

τ_λ	Optical depth at wavelength λ
d_{Mars}	Sun-Mars distance
L_λ	Spectral radiance
L_S	Solar longitude
R	Reflectance factor
r_{eff}	Effective grain size radius
T	Surface temperature
v_{eff}	Effective variance

List of Figures

List of Tables

Chapter 1

General Introduction

The planet Mars, the fourth planet in our Solar System, has always captivated the human imagination. Prior to the era of space exploration, Mars was shrouded in mystery. In the 19^{th} century, Giovanni Schiaparelli was a pioneer in astronomical observation. In 1877, he published his detailed observations of the Martian surface, in which he described the presence of dark linear features on the planet (detailed in Abetti and Abetti (1910)). Called *canali*[1], his observations led to popular speculation about the possibility of Martian civilisations constructing canals (Evans and Maunder, 1903). Astronomer Percival Lowell continued Schiaparelli's research and developed a theory that the Martian canals were artificial constructions, used by an advanced civilisation to irrigate the desert planet (Basalla, 2006).

In 1965, the NASA Mariner 4 spacecraft provided the first close-up images of Mars, revealing a dry landscape devoid of clearly defined canals (Leighton et al., 1965). These observations confirmed that the Martian canals were optical illusions, natural formations, or artifacts resulting from the observational limitations of previous ground-based telescopes. Since then, numerous other Mars exploration missions, such as the rovers Spirit (Arvidson et al., 2010), Opportunity (Arvidson et al., 2011), Curiosity (Vasavada, 2022), and Perseverance (Farley et al., 2020), as well as the orbiters Mars Odyssey (Saunders et al., 2004), Mars Reconnaissance Orbiter (Zurek and Smrekar, 2007), Mars Express (Chicarro et al., 2004) and ExoMars Trace Gas Orbiter (Vago et al., 2015) have extensively mapped the surface of Mars, providing additional evidence that the canals are not of artificial origin. Although the idea of Martian canals has been denied, Mars remains fascinating thanks to the different

[1] Martian surface channels.

space missions that have revealed the presence of ancient lakes, rivers and deltas, suggesting the presence of liquid water, thought to have occurred around 3.5 billion years ago (Carr, 1996). In the coming years, through the Mars Sample Return program (Cataldo et al., 2022), NASA and ESA will attempt to bring back the first samples of Martian surface to Earth for detailed analysis. This program includes several missions, each involving a significant step. Since 2021, the Perseverance rover collects samples of the Martian surface, which will be retrieved by helicopters and a lander, then sent into the Martian atmosphere in early 2030s. After that, the Earth Return Orbiter will capture and bring them back to Earth after 2033. The in-depth analysis of these Martian samples on Earth will contribute to better characterise the surface of Mars, providing precise insights into the timing of water flow on the planet's surface and the potential existence of life.

1.1 General features of Mars

Mars is a dry and rocky planet with a cold climate, in which surface temperature ranges from −160°C to 20°C (Gómez-Elvira et al., 2014; Jiang et al., 2023; Munguira et al., 2023). The red planet has a radius of 3396 kilometres, making it about half the size of the Earth. Its average distance from the Sun is 228 million kilometres, or 1.5 astronomical units (au)[2]. At this distance, it takes about 13 minutes for sunlight to travel from the Sun to Mars (Government Publishing Office, 2019).

Rotating on its axis, the planet completes one revolution every 24.6 hours. Martian days are known as sols, from "solar day". A Martian year consists of 668.6 sols, or 687 Earth days. Like the Earth, Mars has seasons, causing by the 25° tilt of its axis of rotation with respect to the plane of its orbit around the Sun. On the other hand, the eccentricity of the Martian orbit has an impact on the seasons. Indeed, they vary in length making spring in the Northern hemisphere (autumn in the South) the longest season (194 sols) and autumn in the Northern hemisphere (spring in the South) the shortest (142 sols). Therefore, the Martian months also have a different number of days, ranging from 46 to 67 sols (Seidelmann et al., 2007). A commonly used method for defining Martian seasons and days is through solar longitude, which measures the Mars-Sun angle relative to the spring equinox in the Northern hemi-

[2] An astronomical unit is the standard distance from the Sun to the Earth = 149 597 871 km (International Astronomical Union, 2013).

sphere, where L_S=0°. By this definition, L_S=90° represents the Northern summer solstice, L_S=180° indicates the Northern autumn equinox, and L_S=270° signifies the Northern winter solstice (see Figure 1.1). Accordingly, Martian months are defined as spanning 30 degrees of solar longitude, and a Martian Year (MY) ranges from L_S=0° to 360° (Forget et al., 1999; Clancy et al., 2000).

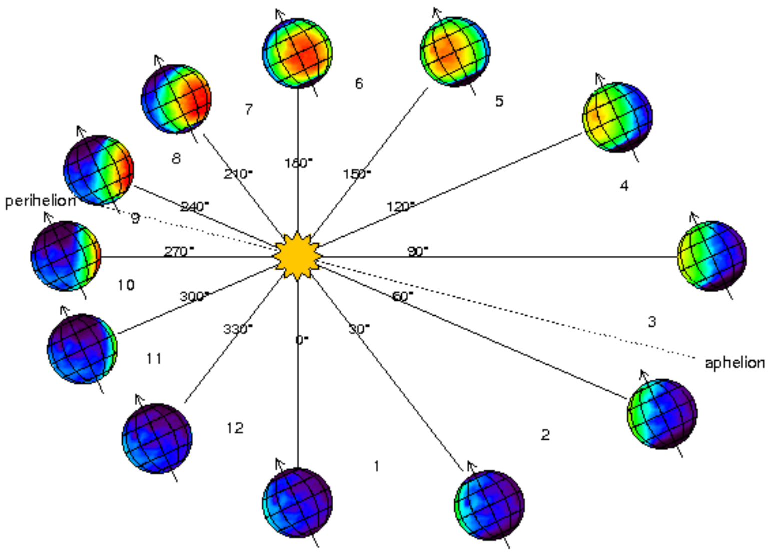

Figure 1.1: Martian solar longitude (L_S) definition: L_S=0° is the spring equinox in the Northern hemisphere, L_S=90° the Northern summer solstice, L_S=180° the Northern autumn equinox, and L_S=270° the Northern winter solstice (Forget et al., 1999; Clancy et al., 2000).

Despite being a dry and cold world, Mars has several fascinating features. The Red Planet presents a hemispheric dichotomy, representing a significant difference in elevation between the low Northern hemisphere and the high Southern hemisphere. The low Northern hemisphere is characterised by young terrains and lightly cratered plains, resulting from possible volcanic activities or periods of tectonic plate recycling in the early history of Mars. The correlation between low elevation and high topographic smoothness suggests the possible location of an ancient Martian ocean. On the other hand, the Southern hemisphere appears old and heavily cratered. It hosts one of the deepest known impact craters, the Hellas Basin, and a vast canyon system called Valles Marineris stretching for kilometers on the Martian surface (see Figure

1.2). The global dichotomy boundary is interrupted by the Tharsis province, which is a vaste region of ancient volcanoes with the tallest volcano in the entire Solar System, i.e. the Olympus Mons (Smith et al., 1999; Bills and Nerem, 2001). Moreover, polar caps are present at both poles. Mainly composed of CO_2 ice with a H_2O ice subsurface, they play an important role in the Martian climate (see Section 1.2) (Becerra et al., 2021). The atmosphere of Mars is mainly composed of carbone dioxyde CO_2 (95.3%), nitrogen N_2 (2.7%) and argon Ar (1.6%) (Owen et al., 1977; Oyama and Berdahl, 1977; Owen, 1992). It also contains small amounts of oxygen O_2, water vapour H_2O, and trace quantities of noble gases such as neon Ne, krypton Kr, and xenon Xe. Additionally, there are molecular species like carbon monoxide CO, ozone O_3, nitrogen oxide NO, and hydrogen peroxide H_2O_2, which are formed through photochemical processes[3] involving the primary volatiles (Haberle et al., 2017). All these gases contribute to an average annual surface pressure of 6 mbar on Mars (Haberle, 1997, 2015; Withers, 2012; Banfield et al., 2020).

On the other hand, the presence of methane CH_4 in the Martian atmosphere is the subject of much debate in the scientific community (Formisano et al., 2004; Geminale et al., 2008; Lefèvre and Forget, 2009; Mumma et al., 2009). Recently, no detection of CH_4 was reported by the ExoMars Trace Gas Orbiter-NOMAD spectrometer (Korablev et al., 2019; Liuzzi et al., 2019). The instrument has been scanning the Martian atmosphere accurately up to 6 km altitude since 2018. These results are not in line with the measurements in the Gale Crater of the NASA Curiosity rover (Webster and Mahaffy, 2011; Webster et al., 2018; Moores et al., 2019) or the total atmospheric column measurements of ESA Mars-Express spacecraft (Formisano et al., 2004; Geminale et al., 2008; Giuranna et al., 2019), indicating small amounts of methane. This demonstrates the complexity of the subject and that there may exist an unknown rapid destruction mechanism in order to reconcile the different results (Knutsen et al., 2021).

[3]Chemical reactions occurring when molecules absorb energy in the form of light. They hence enter transient excited states that possess distinct chemical and physical properties compared to their original states. These excited states can undergo various transformations such as decomposition, structural changes, combination with other molecules, or transfer of electrons, hydrogen atoms, protons, or electronic excitation energy to other molecules (Fleming et al., 2018).

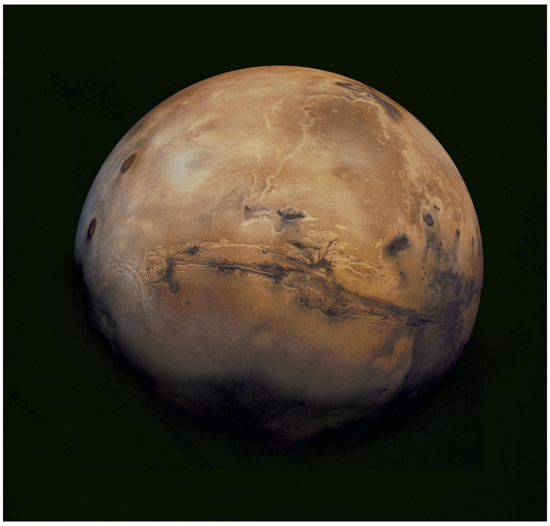

Figure 1.2: Compilation of images captured by the Viking Orbiter 1. The center of the scene shows the entire Valles Marineris canyon system, over 3000 km long and up to 8 km deep (U.S. Geological Survey and NASA).

The planet is surrounded by two small moons: Phobos and Deimos (see Figure 1.3). Their compositions are poorly understood and their origins are still an open issue (Fraeman et al., 2014; Ramsley and Head, 2021). Globally, two scenarios of formation are considered. Either Phobos and Deimos are asteroids captured by Mars (Rosenblatt et al., 2016) or they formed in-situ in a disk following a giant impact on Mars (Le Maistre et al., 2019). The capture scenario relies on surface analysis that demonstrates a different composition compared to the Martian surface (Chapman, 2004; Rosenblatt, 2011; Pieters et al., 2014). Nevertheless, the low density of Phobos and Deimos suggests a high porosity and/or an important content of water ice, which can be the result of re-accretion of debris in Mars' orbit and be favorable to the in-situ formation scenario (Glotch et al., 2018; Le Maistre et al., 2019).

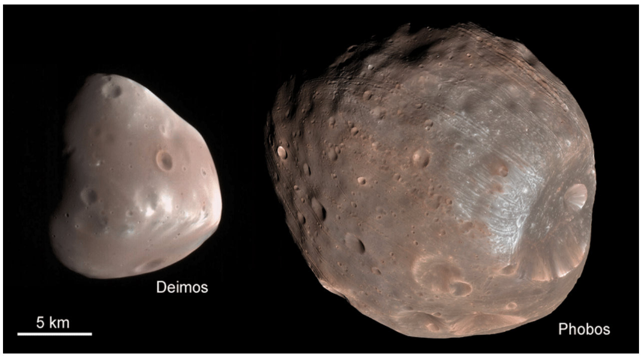

Figure 1.3: MRO HiRISE camera images (McEwen et al., 2007) of Deimos (averaged diameter of 12 kilometers) and Phobos (averaged diameter of 22 kilometers) in accentuated colours. Phobos has a heavily cratered surface, with the largest crater being Stickney crater, as can be seen on its right side in the picture (Thomas et al., 2011; Ramsley and Head, 2021).

1.2 Martian climate

The present climate of Mars is mainly influenced by the CO_2 cycle, but also the water and dust cycles. These cycles involve the exchange of materials between the surface and atmosphere of Mars, driven by daily and seasonal variations in the amount of sunlight received by the planet (Dehant et al., 2020).

As mentioned in Section 1.1, the polar caps play an important role in the Martian climate. During winter hemisphere, CO_2 condenses and forms CO_2 ice deposits on the poles, as the CO_2 frost point temperature is reached (T $\sim$148K at 6 mbar, Piqueux et al. (2016)). When spring arrives, the amount of ligth and hence surface temperature increase, leading to the sublimation of the caps. CO_2 is released back into the Martian atmosphere. These condensation and sublimation processes are responsible for the growth and retreat of the polar ice caps (Piqueux et al., 2003; Langevin et al., 2007; Brown et al., 2010; Appéré et al., 2011; Piqueux et al., 2015), in which approximately 25% of the Martian atmosphere is involved (Hess et al., 1979, 1980).

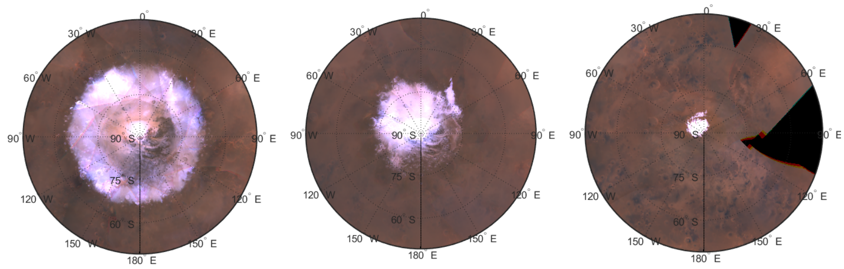

(a) (b) (c)

Figure 1.4: Retreat of the Southern polar cap observed by MARCI in MY29: (a) $L_S = 225°$, (b) $L_S = 250°$, (c) $L_S = 340°$. Mars MRO MARCI Daily Global Weather Maps PDS4 Archive: `https://astrogeology.usgs.gov/search/map/Mars/MarsReconnaissanceOrbiter/MARCI/MARS-MRO-MARCI-Mars-Daily-Global-Maps`.

During the Southern winter (L_S 90°-180°), spectrometers such as the Observatoire pour la Minéralogie, l'Eau, les Glaces et l'Activité (OMEGA) (Bibring et al., 2004b) onboard Mars Express and the Compact Reconnaissance Imaging Spectrometer (CRISM) (Murchie et al., 2007) onboard Mars Reconnaissance Orbiter (see Section 1.3) observed strong CO_2 ice signatures over the Southern seasonal cap with a weak albedo contrast between ice-covered and ice-free regions (Langevin et al., 2007; Schmidt et al., 2010; Brown et al., 2014). After the equinox (L_S 180°), the seasonal cap becomes much brighter than the surrounding regions, suggesting a decrease in the CO_2 ice thickness. During Southern spring (L_S <200°), a low albedo region appears within the retreating seasonal ice cap. This so-called cryptic region (latitudes <70°S and longitudes from 60°E to 210°E) has been observed to be associated with the ejection of dust material from beneath the seasonal ice, which darkens the upper surface of the seasonal ice cap and even obscures the CO_2 ice signature of the seasonal ice cap (Kieffer et al., 2000; Langevin et al., 2006, 2007; Pommerol and et al., 2011). Both the OMEGA and CRISM instruments have noted the presence of H_2O ice (L_S ∼225°), persisting over the cap even after the end of the recession, possibly mixed with dust (Langevin et al., 2007; Brown et al., 2014). The polar cap does not completely disappear during summer, revealing a bright residual cap as shown in Figure 1.4. As observed by the Thermal Emission Spectrometer (TES) (Christensen et al., 2001) onboard Mars Global Surveyor (MGS) (see Section 1.3), the growth and retreat of the Southern polar cap follows an assymetric pattern influenced by local topography, particularly the Hellas Basin (see Section 1.1) (Piqueux et al., 2015).

On the other hand, it is extremely rare to observe pure CO_2 ice on the Northern polar cap, even during winter observations. Indeed, the Northern polar cap is dominated by H_2O ice. As reported by CRISM and OMEGA, during the Northern winter, the seasonal cap is characterised by a uniform distribution of CO_2 ice surrounded by a H_2O ice annulus. In spring (L_S <90°), the distribution of CO_2 exhibits an inhomogeneous pattern, becoming more and more patchy and leading to the apparent enlargement of the H_2O ice annulus. In summer (L_S >180°), the CO_2 ice signatures disappear completely, leaving a residual cap of pure H_2O ice (Appéré et al., 2011; Brown et al., 2012). The growth and retreat of the Northern polar cap appears monotonic and slow, following a symmetric pattern through the seasons (Kieffer and Titus, 2001).

Directly linked to the CO_2 cyle, these seasonal processes in the polar ice caps have a strong influence on the global energy budget of the Red Planet, showing repeated growth and retreat of the ice caps throughout the Martian years (Piqueux et al., 2015). Subsurface sounding radar allows to investigate the internal structure of the Martian polar deposits (PLD), as ice is transparent to the radar wavelengths. The Mars Advanced Radar for Subsurface and Ionosphere Sounding (MARSIS) on Mars Express (Jordan et al., 2009) and the SHAllow RADar (SHARAD) on Mars Reconnaissance Orbiter (Seu et al., 2007) revealed that the PLD are composed by ice layers and different dust content in the layers between the Northern and the Southern polar deposits (NPLD/SPLD). SHARAD observed massive deposits of burried CO_2 ice within the SPLD, which can double the Martian pressure if it sublimates. The radar instrument also revealed depths of 1000 m in the SPLD. It consists of alternating thick layers of CO_2 ice and thin layers of H_2O ice (Bierson et al., 2016).

CO_2 ice is also present in the Martian atmosphere. NASA's Mars Pathfinder spacecraft first suggested the presence of CO_2 ice clouds in the mesosphere of Mars (Clancy and Sandor, 1998), i.e. at altitudes where the temperature is cold enough for CO_2 to condense. Since then, they have been observed directly by a number of instruments. While OMEGA provided the first spectral signature of CO_2 ice cloud, with the TES, CRISM and Thermal Emission Imaging System (THEMIS) (Christensen et al., 2004) spectrometers, they contributed to the understanding of their spatial distribution (McConnochie et al., 2010; Vincendon et al., 2011; Clancy et al., 2019). CO_2 ice clouds exhibit distinct patterns in their distribution, depending on the region, altitude, and seasonal variations. At equatorial latitudes, they are present at altitudes of about 50 to 100 km, ranging from L_S 0° to 140° (Clancy et al., 2007; Montmessin et al., 2007; Määttänen et al., 2010). They are also present at high latitudes during the polar night in altitudes lower than 20 km (Glandorf et al., 2002; Colaprete and Toon, 2003). The SPectroscopy for the Investigation of the Characteristics of the Atmosphere of Mars (SPICAM) onboard Mars Express reported nighttime clouds observations, which are expected to be CO_2 ice clouds (Montmessin et al., 2006).

Water ice also sublimates into the atmosphere. Water vapour is then transported to middle and low latitudes, before re-condensing onto the polar caps in autumn and winter seasons, which defines the Martian water cycle. High water vapour abundances are found at high Northern latitudes during summer, indicating that the Northern summer ice cap is an important source of atmospheric water vapour. In contrast, the polar regions experience minimum water vapour abundances in winter (Fedorova et al., 2006, 2018; Smith et al., 2009; Clancy et al., 2017b; Aoki et al., 2018, 2022; Daerden et al., 2019, 2022; Neary et al., 2020). Water vapour in the Martian atmosphere is regulated by saturation, leading to the formation of water ice clouds. They are most pronounced during the Northern summer in the tropics. Called the Aphelion Cloud Belt (ACB), they are generally diffuse, except over the volcanoes in the Tharsis region, where optically thick orographic clouds can be observed (see Figure 1.5). On the other hand, in the polar regions, they occur during winter. Known as the Polar Hoods (PH), they are optically thick and spread across all longitudes (see left picture in Figure 1.6).

CO_2 ice and water ice clouds have an impact on the radiative balance in the atmosphere of Mars, playing an important role in the radiative heat transfer in the infrared wavelength. Their presence influences the atmospheric distribution of heat, affecting indirectly the surface heat balance (Forget and Pierrehumbert, 1997; Colaprete and Toon, 2003; Madeleine et al., 2012b; Forget et al., 2013; Steele et al., 2014; Wilson and Guzewich, 2014).

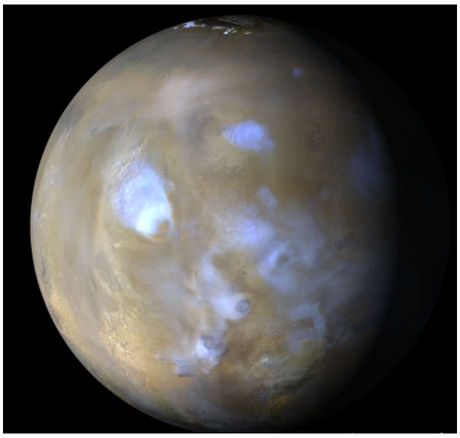

Figure 1.5: Ice clouds above the volcanoes in the Tharsis region as observed by the Mars Color Imager (MARCI) on the Mars Reconnaissance Orbiter (MRO) (Malin et al., 2001; Bell et al., 2009). MARCI weather report, December 2021 (Malin and Cantor, 2021).

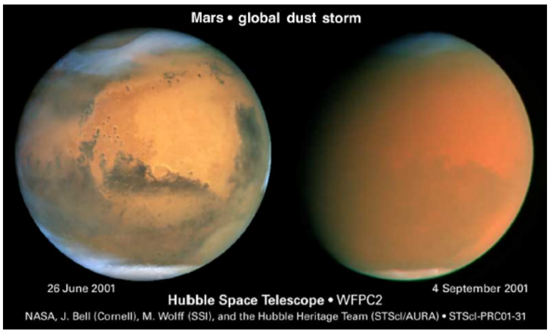

Figure 1.6: Before and during the 2001 Martian global dust storm observed by the Hubble Space Telescope (Bell et al., 2001).

Figure 1.6 shows the NASA Hubble Space Telescope observations of Mars before and during the 2001 global dust storm. Dust is an important aerosol in the Martian atmosphere (Kahre et al., 2015). Seasonal changes promote the formation of strong winds that lifts regolith dust into the atmosphere, creating dust clouds. These storms can be local and occurring every day, or cover large regions and even the entire planet in large global storms, which generally begin in the Southern hemisphere during Southern spring and summer. The Martian dust cycle shows a large amount of interannual variability (Benson and James, 2005). These extreme events seriously impact the radiative heat transfer of Mars, affecting the CO_2 and water cycles, and hence the climate, and even the surface temperature (Wolkenberg et al., 2018). Indeed, atmospheric dust reduces the flux of direct solar energy towards the ground, but increases the temperature of the atmosphere and its thermal infrared flux towards the surface. Intuitively, the seasonal growth and retreat rates of the caps should exhibit some degree of interannual variability (Benson and James, 2005; Piqueux et al., 2015).

Previous studies using satellite data have attempted to characterise the effects of global dust storms on the condensation and sublimation processes of the polar ice caps (Benson and James, 2005; Calvin et al., 2015; Piqueux et al., 2015; Calvin et al., 2017). Based on the available observations, different results have been reported.

- Effects of global dust storms on the dynamics of the Northern polar cap:

  The formation of such storms generally occurs during the Southern spring. For this reason, few observations of the North polar ice cap are available during this period due to low solar radiation.

  During this time, CO_2 begins to condense on the surface of the Northern polar cap. The presence of atmospheric dust could affect the rate at which the CO_2 condenses, and any dust deposited on the surface during this condensation phase could potentially alter the rate of coming recession (Benson and James, 2005).

  Benson and James (2005) used images from Mars Global Surveyor's Mars Orbiter Camera (MOC) wide-angle cameras to compare the rate of recession of the Northern Polar cap during the MY25 global dust storm with MY24 and MY26. They reported similar recession rate between these 3 Martian years. Nevertheless, depending on the longitudes (330°W to 60°W), the recession rate was about 1° to 2° latitude slower in MY26 than in MY24. It is still unclear whether the MY25 global dust storm affected the recession rate in MY26 or whether it is related to the topography, which influences the local climate. Using TES and Mars Climate Sounder (MCS) data, Piqueux et al. (2015) compared the growth and retreat of the North seasonal cap between MY24 to MY31. During MY25, they observed no apparent change on the dynamics of the cap compared with other years.

On the other hand, Piqueux et al. (2015) observed an accelerated retreat of the cap in MY29, following the MY28 global dust storm occurring in the Southern summer. Calvin et al. (2015) also noticed this acceleration in MY29 using daily maps from the Mars Reconnaissance Orbiter's Mars Colour Imager (MARCI) camera (see Section 1.3).

- Effects of global dust storms on the dynamics of the Southern polar cap:

  Benson and James (2005) noticed small variations in the Southern polar cap recession between MY24 and MY26. The MY25 global dust storm had negligible effects on the average cap recession that year. Nevertheless, they observed faster regression at the end of the sublimation phase (i.e. $L_S \sim 262°$) by about 5° of L_S compared to MY24 and MY26. This result is consistent with those reported by Bonev et al. (2002) and Piqueux et al. (2015), stating that the MY25 global dust storm appeared in late Southern spring.

  Considering the MY28 global dust storm, it occurred when the Southern polar cap was almost completely sublimed. Piqueux et al. (2015) observed no apparent change compared to other years (MY24-31). Calvin et al. (2017) confirmed the trend. They analysed the Southern seasonal cap retreat in MY28-31 using daily maps from MARCI.

The effects of global dust storm on the seasonal polar ice caps vary considerably, ranging from negligible effects on a global scale to significant effects. The acceleration of the recession rate of the Southern polar cap in MY25 and the Northern polar cap in MY29 have distinct characteristics that may be related to the atmospheric conditions during these dusty events (Piqueux et al., 2015). Nevertheless, the current sample of polar cap observations during global dust storms is limited. A more comprehensive catalogue of seasonal cap behaviours observed during different global dust storms could provide valuable insights. It will help to refine our understanding of the various feedback mechanisms that operate between the atmosphere and the surface of Mars.

1.3 Mars spectrometers for surface ices

Nadir observations, i.e. observations directed towards the centre of the planet, are important to provide a detailed and direct view of the surface, which is invaluable for applications such as mapping, topographic analysis, chemical composition studies and environmental monitoring. This technique of observation has been used extensively by various instruments orbiting Mars to study surface ice for example (see Sections 1.2 and 2.4). The main spectrometers orbiting the Red Planet are listed below:

- OMEGA onboard Mars Express (Bibring et al., 2004b) is an imaging spectrometer with two spectral channels: a visible-near infrared channel, VNIR, in the 0.38-1.05 μm range, and a shortwave infrared channel, SWIR, in the 0.93-5.1 μm range. The SWIR channel consists of two subchannels, C (0.93-2.73 μm) and L (2.55-5.1 μm). In August 2010, the cooling of the SWIR-C channel failed, but OMEGA operated on the other channels from February 2003 until June 2022. It provided global cartography of Mars, at high spatial resolution for specific regions (Riu et al., 2019a,b). OMEGA identified various mineral in Martian soils, frosts and ices (such as silicates, hydrated minerals, oxides, and carbonates) (e.g. Langevin et al. (2007)). The instrument also studied the distribution of atmospheric gases such as CO_2, CO, H_2O and aerosols in the Martian atmosphere (e.g. Vincendon et al. (2010a, 2011); Vincendon (2015); Szantai et al. (2021)).

- Complementary to OMEGA, CRISM onboard Mars Reconnaissance Orbiter (Murchie et al., 2007) acquired hyperspectral images through two channels (VNIR: 0.36-1.05 μm, and infrared: 1-3.93 μm) of the Martian surface and atmosphere from September 2006 to May 2022 (Seelos et al., 2023). The imager spectrometer provided geologic context, measurements of surface targets at high spatial and spectral resolutions (e.g. Viviano et al. (2014)) and information on spatial and seasonal variations in various cycle, i.e. CO_2 through polar caps observations, H_2O, dust and ice aerosols (e.g. Brown et al. (2010, 2012, 2014); Clancy et al. (2019)).

- TES onboard Mars Global Surveyor (Christensen et al., 2001) operated between April 1999 and October 2006. TES used an infrared spectrometer with broadband thermal (6-50 μm) and VNIR radiometer (0.3-2.9 μm). It studied the composition of Martian surface minerals, rocks, and ices (e.g. Bandfield et al. (2000); Christensen et al. (2001); Rogers and Christensen (2003)) and determined their thermophysical properties (e.g. Cushing and Titus (2008); Piqueux et al. (2015)). TES provided surface albedo map of Mars that is widely used in the scientific community (Christensen et al., 2001; Rogers et al., 2007). By studying the polar regions, the instrument discovered that they exhibited diverse forms of condensed CO_2 (e.g. Kieffer et al. (2000); Kieffer and Titus (2001)). In addition, it analysed the temperature and dynamics of the atmosphere (e.g. Clancy et al. (2000); Smith (2004)), and investigated atmospheric aerosols and clouds (e.g. Clancy et al. (2003); Smith (2004)).

- THEMIS onboard Mars Odyssey (Christensen et al., 2004) is an imaging spectrometer using 5 visual bands (0.42 μm, 0.54 μm, 0.65 μm, 0.75 μm, 0.86 μm) and 10 infrared bands (6.78 μm, 7.93 μm, 8.56 μm, 9.35 μm, 10.21 μm, 11.04 μm, 11.79 μm, 12.57 μm, 14.88 μm). Since February 2002, the instrument has been studying the distribution of minerals on the Martian surface and their correlation with landforms (Christensen et al., 2003). In the polar regions, THEMIS revealed that mysterious dark markings on Mars' South polar cap are caused by powerful jets of CO_2 gas erupting through the ice layers in spring, carrying fine and dark dust. This phenomenon results in the formation of dark spots (Kieffer et al., 2006). In addition, THEMIS discovered the presence of water ice beneath the South polar cap, challenging the long-standing theory of a perennial CO_2 ice cap in the region (Byrne and Ingersoll, 2003; Titus et al., 2003).

Since March 2018, the Nadir and Occultation for MArs Discovery (NOMAD) instrument onboard ExoMars-Trace Gas Orbiter operates around Mars. Although the instrument is mainly dedicated to atmospheric studies, it has a nadir infrared channel allowing to gather detailed information about the surface and atmosphere from the spectral signatures of ice in the infrared spectral range (Vandaele et al., 2015b, 2018). At the time of writing, NOMAD is the only high-resolution nadir spectrometer in operation around Mars (see Chapter 2).

1.4 Motivation and outline of the thesis

Mars Polar Science is key to understand the Martian climate. As mentioned in Section 1.2, the polar caps play a fundamental role in the atmospheric dynamics of the planet, through the sublimation and condensation processes in the polar regions which involves large amounts of gas (mainly CO_2, H_2O, etc.). Observing the seasonal growth and recession rates of the caps provides direct information about the associated regional and global environment. Although the growth and retreat of the caps are repeatable throughout the Martian years, interannual variability can occur in the presence of global dust storms and needs to be understood (Piqueux et al., 2015). These storms also affect the water cycle and atmospheric escape.

The global atmospheric circulation and the Martian atmospheric conditions (low temperature and pressure) allow the formation of ice clouds in the Martian atmosphere (see Section 1.2). While water ice clouds present a seasonal behaviour at equatorial and high latitudes, the processes and properties of CO_2 ice clouds in the mesosphere are less understood (Clancy et al., 2017a).

Given the above discussion, continuous observations play a critical role in quantifying seasonal and interannual variability of the physical mechanisms that govern Mars' current climate. Moreover, the global dust storm occurring in MY34 (Guzewich and Smith, 2019; Kass et al., 2019; Smith and Guzewich, 2019; Viúdez-Moreiras et al., 2019) provides a new opportunity to study its effects on the seasonal processes of the polar caps (see Section 1.2).

From our current knowledge of the seasonal processes in the polar regions, some general questions can be raised:

1. In dust-free years, is there any variability in the caps?
2. What are the effects of the MY34 global dust storm on the dynamics of the Northern and Southern seasonal caps?
3. Do ice clouds exhibit recurring seasonal behaviour, even in dusty years?

To achieve this goal, we will use nadir observations from the only high-resolution spectrometer still in operation around Mars, the ExoMars Trace Gas Orbiter-NOMAD (see Section 1.3 and Chapter 2).

The primarily purpose of this research is to observe the seasonal and spatial variations of the polar caps, allowing to refine our current knowledge of the CO_2 cycle. We also aim at better quantifying the interannual variability of the sublimation of CO_2 ice on Mars during the MY34 global dust storm. In addition to the CO_2 cycle, another important cycle on Mars is the water vapour cycle, in which water ice clouds play a role (see Section 1.2). Therefore, we also analyse the seasonal distribution and variations of the water ice clouds in this thesis.

Specifically, the outline of this thesis is as follows:

- **Chapter 2** presents the Nadir and Occultation for MArs Discovery (NOMAD) instrument onboard ExoMars-Trace Gas Orbiter, based on a literature review. This is essential for understanding the use and interpretation of the spectral observations in this thesis.

- **Chapter 3** explores the potential of NOMAD for surface ice detection in the infrared wavelengths. Based on spectral absorptions, we define two different approaches in order to identify the CO_2 ice deposits in the polar regions for the Martian Years (MY) 34 and 35. Moreover, we look at the impact of the MY34 global dust storm on the detection of polar ice caps. We also investigate the spatial distribution of CO_2 ice clouds. This work has been published in the Journal of Geophyscal Reasearch Planets (JGR Planets), in which I am a co-author.

- **Chapter 4** focuses the analysis on the seasonal and interranual variations of the Southern polar cap during and after the MY34 global dust storm over a 3 Martian Years period (MY34-36). This work has been published in the Icarus Journal, in which I am the first author.

- **Chapter 5** presents the first results of a morning frost campaign of joint observations by NOMAD and the Colour and Stereo Surface Imaging System (CaSSIS), another instrument onboard ExoMars-Trace Gas Orbiter. This work has been submitted and is under consideration for publication. I am a co-author of this study.

- **Chapter 6** deals with atmospheric ice detection, presenting a method allowing to detect water ice clouds with the NOMAD spectrometer. More technical than the other chapters, this work mainly study the distribution of the Polar Hood clouds. It was published in the Remote Sensing Journal, in which I am the first author.

Chapter 2

The Nadir and Occultation for MArs Discovery instrument

This chapter provides an overview of Neefs et al. (2015), Vandaele et al. (2015b, 2018), Thomas et al. (2016, 2022a), Liuzzi et al. (2019) and Cruz Mermy et al. (2022). The purpose of this chapter is to introduce the Nadir and Occultation for MArs Discovery (NOMAD) instrument, whose observations we have used throughout the thesis. We review the principles on which the instrument is based, and discuss its instrumental features and limitations (see Section 2.2). The calibration process is introduced in Section 2.3 (see Annexe A for more information). We conclude this chapter with a discussion on the advantages and drawbacks of NOMAD compared with similar instruments (see Section 2.4), to give the reader a better understanding of the selection of observations that will be used in subsequent chapters.

The NOMAD instrument was selected as one of the four instruments for the European Space Agency's ExoMars Trace Gas Orbiter (TGO) mission (Vago et al., 2015), launched on March 14^{th} 2016. After a seven month journey, the Trace Gas Orbiter successfully entered an elliptical orbit around Mars. During the following months, the orbiter executed several critical maneuvers to place itself in a circular orbit with an inclination of 74° at an altitude of approximately 400 kilometers above the Martian surface. The nominal science mission started in April 2018.

The objectives of NOMAD can be categorised into three areas: chemical composition, climatology and seasonal cycles, and sources and sinks of trace gases in the Martian atmosphere. The mission aims in particular to analyse a wide range of trace gases and isotopes to gain insight into the origin and destruction processes of methane, which could have different origins (i.e. geophysical, exogenous or biological). In addition, NOMAD contributes to the understanding of atmospheric escape mechanisms and their implications for past and future atmospheric evolution. Regarding climatology and seasonal cycles, the instrument characterises the spatial and temporal variations of trace gases, dust, clouds, and surface ice. It refines existing climatology, such as the water, carbon and ozone cycles. It also provides insights into atmospheric dynamics at fine scales. The final objective attempts to characterise the sources and sinks of trace gases, including their production and loss mechanisms, and their relationship to surface mineralogy and ices. Overall, the ExoMars Trace Gas Orbiter mission is a critical step in unravelling the mysteries of the Martian atmosphere and its potential to support life (Neefs et al., 2015; Vandaele et al., 2015b,c, 2018; Thomas et al., 2016).

2.1 Spectrometer suite

Led by the Royal Belgian Institute for Space Aeronomy (BIRA-IASB), NOMAD is a high resolution spectrometer suite based on the legacy of the Venus Express mission (Svedhem et al., 2009), which achieved great success in studying the composition of Venus' atmosphere with the Solar Occultation in the Infrared (SOIR) channel (Mahieux et al., 2012; Wilquet et al., 2012; Vandaele et al., 2015a). By definition, a spectrometer is a scientific device that measures the properties of light over a spectral range, by splitting the incoming light through the different wavelengths and measuring its intensity. Spectrometers are essential for studying the composition and structure of materials, identifying chemical compounds, and determining the physical properties of light sources such as planets, stars and galaxies (Elachi and van Zyl, 2021).

NOMAD consists of three independent channels operating in the ultraviolet-visible (UV-VIS), and infrared (IR) spectral ranges (Neefs et al., 2015). A first spectrometer is devoted to solar occultation observations (SO channel), which has identical optical designs as SOIR. Both spectrometers are composed by an infrared acoustic-optical tunable (AOTF) filter combine with a high resolution echelle grating with a resolving power of about $\lambda/\Delta\lambda = 20000$ in the spectal range 2.3 to 4.3 μm. A second spectrometer is capable of performing nadir, limb, and solar occultation observations (LNO channel, see Section 2.2). Similar to the SO channel, the LNO channel was optimised for observing weak IR light sources when observing Mars at nadir or limb. Indeed, during the Venus Express mission, it was found that the signal-to-noise ratio (SNR) of SOIR was too low when observing at the limb or nadir due to the contribution of the thermal background. The LNO channel has a reduced spectral range of 2.3 to 3.8 μm and a resolving power of approximately $\lambda/\Delta\lambda = 10000$. Finally, a third spectrometer (UVIS channel) can work in the three observation modes covering the UV-VIS spectral range from 200 nm in the ultraviolet to 650 nm in the visible, with a spectral resolution of approximately 1.5 nm (Neefs et al., 2015; Thomas et al., 2016). Table 2.1 summarises the main characteristics of the three channels, while Figure 2.1 illustrates the NOMAD instrument and its different modes of observations.

	SO channel	**LNO channel**	**UVIS channel**
Detector size	320 × 256 pixels	320 × 256 pixels	1024 × 256 pixels
Spectral range	2.3-4.3 μm	2.3-3.8 μm	200-650 nm
Resolving power	20000	10000	
Resolution	0.15-0.22 cm^{-1}	0.3 cm^{-1}	1-2 nm
FOV (spectral × spatial)	2 arcmin × 30 arcmin	4 arcmin × 150 arcmin	2 arcmin × 2 arcmin (solar occ.); 43 arcmin (nadir);
Instantaneous footprint		0.5 km × 17 km	5 km × 5 km

Table 2.1: Main NOMAD characteristics and performances (Vandaele et al., 2015c).

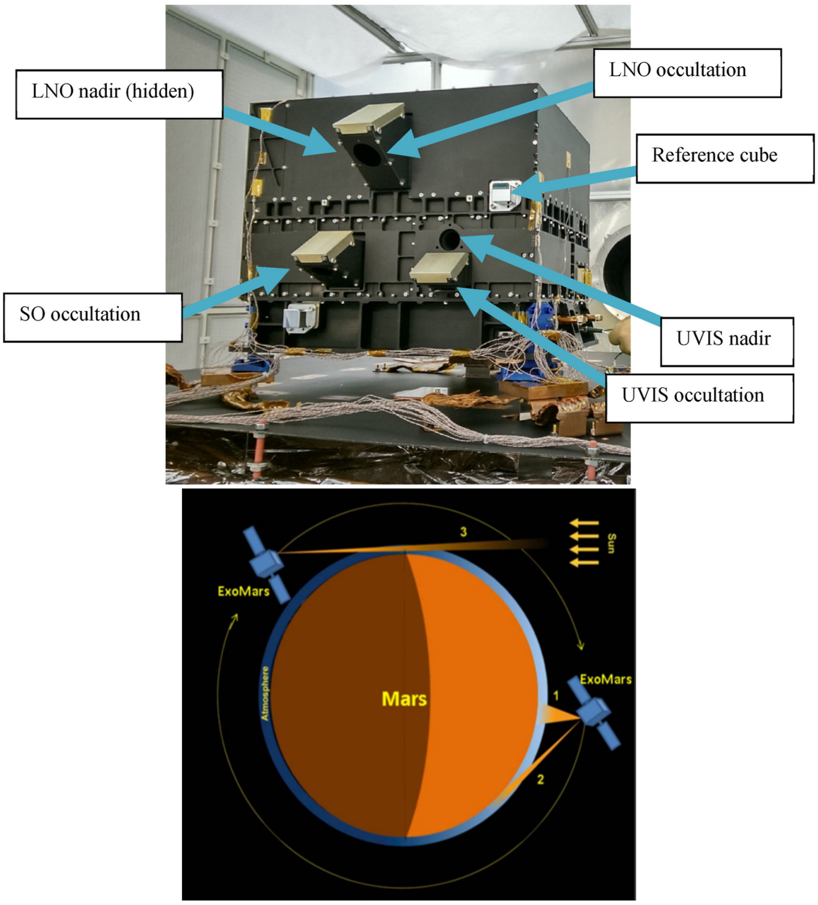

Figure 2.1: The upper panel shows a picture of the NOMAD instrument during the ground calibration. The three channels are labelled on the picture (Thomas et al., 2016). The bottom panel gives the different modes of observation of NOMAD around Mars: (1) nadir, (2) limb, and (3) solar occultation.

2.2 The Limb Nadir and Occultation channel

As stated in Section 1.4, the present research focuses on detecting surface ice on Mars. For this purpose, we use nadir observations of the LNO channel. It is hence essential to provide a more comprehensive overview of this infrared spectrometer. In this section, we concentrate on its design. We also discuss the different concepts that characterise it, as well as its possible limitations in terms of observations.

2.2.1 LNO design

The LNO channel is a compact echelle grating spectrometer combined with an acoustic-optical tunable (AOTF) crystal filter for the selection of the diffraction orders to be observed (Neefs et al., 2015; Vandaele et al., 2015c; Thomas et al., 2016). An AOTF is a type of optical filter that uses an acoustic wave to select a specific wavelength or a small spectral portion of a broadband source (Bei et al., 2004). For the LNO channel, the filter works by passing light through a TeO_2 crystal in which an acoustic wave is applied, creating a periodic modulation of the refractive index that diffracts the light and separates it into different diffraction orders (small spectral windows) (Neefs et al., 2015). By changing the frequency of the acoustic wave, the wavelengths of the selected light can be tuned. The second optical device is the echelle grating, which is capable of diffracting light into multiple beams (Hutley, 1982). More information about the AOTF and the echelle grating can be found in Annexe A.1 and A.2.

Figure 2.2 presents the optical principal of the channel. The nadir entrance consists of a single flat flip mirror (number 2) allowing to observe in nadir or the Sun. The incoming light arrives at the AOTF entrance optics (number 3), which acts as the front-end optics for the LNO channel. The intermediate image plane of the entrance optics is a diaphragm (number 4) limiting the field of view of the system in order to minimise scatter and ghost images. Then, after going through an additional folding mirror (number 5), light arrives at the AOTF entrance optics and at the AOTF itself (number 6). All the other orders are blocked by the AOTF output optics (number 7). In the spectrometer section, a parabolic mirror (number 10) provides a parallel beam to the echelle grating (number 11). After being dispersed by the grating, the light passes again through the parabolic mirror (number 10), which acts as an imaging lens with the detector optics (number 13). Finally, a folding mirror (number 12) projects the beam onto the detector (number 14).

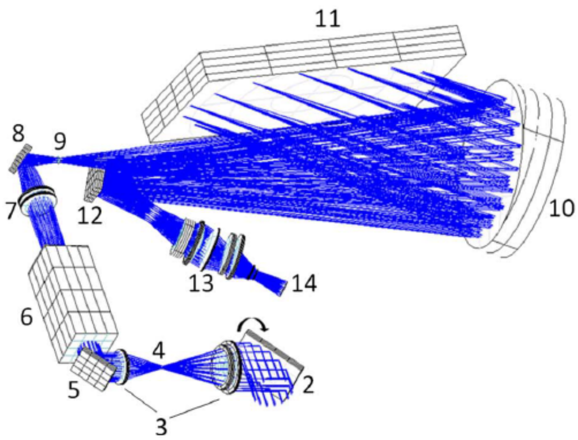

Figure 2.2: Optical design of the LNO channel in 3D (Neefs et al., 2015).

2.2.2 Sequence mode

As shown in Table 2.1, the detector in the LNO channel presents a focal plane array of 320 columns by 256 rows. Nevertheless, during nadir observations, some of the pixels located at the upper and lower parts of the detector remain unused. In fact, only 144 of the 256 spatial pixels are illuminated. On the other hand, the number of detector lines that can be processed and sent to Earth during one sampling time is limited due to the data rate limitations of the TGO spacecraft. The 144 read lines will always be reduced to 24 equivalent lines through binning by six. Therefore, if only one order is used in a measurement, all 24 lines will be transmitted to Earth. On the contrary, if several orders are used, then a corresponding line binning will be applied. The sampling time, known as the rhythm, is a 15 seconds period which is divided by the number of orders. For example, if 5 orders are selected, they will be used for 3 seconds each. In order to increase the signal-to-noise ratio (see Section 2.2.3), all the measured bins of the detector are summed together for each order. This technique is called accumulation (Neefs et al., 2015; Thomas et al., 2022a). Finally, the LNO channel is able to map the quasi-complete[1] Martian surface every 30 sols.

[1]The inclination of TGO's orbit means that NOMAD can only observe between latitudes 74°N and 75°S.

2.2.3 Signal and noise

The sensitivity of an instrument is estimated by the signal-to-noise ratio (SNR), which is defined during each observation as

$$(SNR)_i = \frac{S_i}{Ni} \tag{2.1}$$

where S_i is the signal and N_i is the noise on pixel i of the detector. During nadir observations, the incoming signal is much weaker than solar occultation measurements, hence affecting the signal intensity of the LNO channel. Moreover, the bandwidth and diffraction efficiency of the AOTF and the grating also impact the signal. It can vary over orders and also pixels, making the signal weaker at the edge of the detector with respect to the central pixel. Therefore, it is important to minimise the system noise.

By definition, the total noise N_{tot} in the LNO channel can be expressed as

$$N_{tot} = N_{dark} + N_{ro} + N_{quant} + N_{shot} + N_{tb} \tag{2.2}$$

The N_{dark}, dark current noise, and N_{ro}, pixel electronic readout noise, are fixed and known as noises of the detector. The error in the digitalisation of the signal is given by N_{quant}, while N_{shot} is the shot noise representing the error on the signal impact on the detector. Finally, N_{tb} is the noise coming from the thermal background. It represents the thermal radiation produced by an element in the LNO channel, which increases with the instrument temperature. Thermal background has been identified as the main contribution of noise (Neefs et al., 2015; Thomas et al., 2016). Taking into account all these quantities, the SNR can be improved in two ways. First of all, it is important to reduce the main source of noise, i.e. thermal background, by cooling the elements in the LNO channel. Then, an appropriate integration time is required in order to avoid the detector saturation. Saturation occurs when the detector receives more radiation than it can handle. In this case, a conservative integration time of 200 ms has been estimated to avoid detector saturation, taking into account the instrument temperature (Neefs et al., 2015; Thomas et al., 2016, 2022a).

2.3 LNO data calibration

As mentioned in Section 2.2.3 (see also Annexe A.1), LNO observations can be affected by various factors such as temperature and instrumental features, which might cause errors in the measurements. Calibration helps to improve the precision of the measurements and reduce measurement errors. For this reason, it is a crucial step in ensuring the quality and accuracy of the nadir observations. In this section, we outline the different steps that lead to the spectral and radiometric calibration of LNO observations, allowing the transformation of raw data into reflectance factor (see Section 2.3.2). This section reviews the work of Liuzzi et al. (2019), Thomas et al. (2022a) and Cruz Mermy et al. (2022).

2.3.1 Spectral calibration

The first step is the spectral calibration, whose goal is to obtain an analytical relationship between the detector pixel number, the diffraction order, and the corresponding wavelength (Liuzzi et al., 2019). This process considers the characteristics of the AOTF and the grating. It hence involves defining their respective functions.

The calibration measurements consist of solar observations, i.e. when the LNO channel directly points to the Sun. During a solar measurement, the AOTF selection varies over the whole LNO spectral range, one order at a time. This kind of measurement is called a full scan. At the time of writing, 108 LNO full scans have been performed and are all used in this calibration process. It is hence an ongoing work that needs to be constantly renewed. Full scan solar spectra are used to identify the position of well-known solar lines, which can then be used to relate its frequency to its position in pixel number. The brightest solar lines are analysed to identify their corresponding pixel number, keeping in mind that a shift in pixel number may occur due to variations in instrument temperature. A pixel shift gradient of each solar line can be measured and an average is estimated for each order. Then, it is possible to study the solar line intensity as a function of AOTF frequency (see Section 2.2.1 and Annexe A.1) across the different orders (Mahieux et al., 2008, 2009). All solar lines intensity are analised depending on the AOTF frequency in order to determine the maximum sensibility of the LNO channel at the wavelength where the solar lines are located. This can also be correlated to the AOTF transfer function (see Annexe A.1), which can be represented by a suitable model. It has been defined as a sum of a sinc-squared function and a Gaussian function (Liuzzi et al., 2019; Cruz Mermy et al., 2022). This corresponds to a combination of a main lobe with several side-lobes (small wings). These small wings at the shorter and longer wavelengths allow the radiation incoming from adjacent orders to fall on the grating. As a result, an unexpected signal can be summed with the expected spectral information (Neefs et al., 2015; Liuzzi et al., 2019; Cruz Mermy et al., 2022; Thomas et al., 2022a). Finally, the observed continuum shape is a combination of the incoming continuum, from the Martian surface in nadir mode, modified by the instrumental effects: i.e. the AOTF transfer function and the grating efficiency. Called the Blaze function, the grating efficiency is defined as a sinc-squared function (Liuzzi et al., 2019). More information can be found in Annexe A.3.

2.3.2 Radiometric calibration

The second step consists in converting the raw signal reaching the LNO detector into a reflectance factor, after having been transmitted by the different instrumental elements (see section 2.3.1). This section is based on Thomas et al. (2022a) and Cruz Mermy et al. (2022).

Reflectance factor is defined as the LNO signal divided by the measured solar signal at Mars and by the cosine of the solar zenith angle (SZA), which is the angle between the Sun direction and the zenith of the surface point being observed. To do this, it is essential that the solar spectra are measured under the same conditions as the nadir observations, as temperature variations shift the location of the spectral lines absorption (see Section 2.3.1). As mentioned in Section 2.3.1, there are currently 108 solar spectra available. Nevertheless, this does not cover all the possible instrument temperatures of the nadir observations. By interpolation, a synthetic solar spectrum is created for each temperature of the instrument. Then, spectral calibration (see Section 2.3.1) is applied to the solar and nadir observations, using the best available solar lines present in the spectra. For the nadir observations, molecular lines are also used for the orders containing such absorption, improving the spectral calibration. On the other hand, illumination angles impact the quality of the nadir data. If the absorption line fit is poor due to noise, the spectral calibration might fail for the selected order. To prevent this, the best nadir spectra of the observation are averaged together, selecting only those spectra with sufficient raw signal. Solar and/or molecular absorptions are then identified in the averaged nadir spectrum, where the deeper absorptions are selected for the spectral calibration. As the radiometric calibration uses LNO solar observations to calibrate the LNO nadir observations, it minimises any instrumental effects. The procedure of the LNO radiometric calibration is illustrated in Figure 2.3.

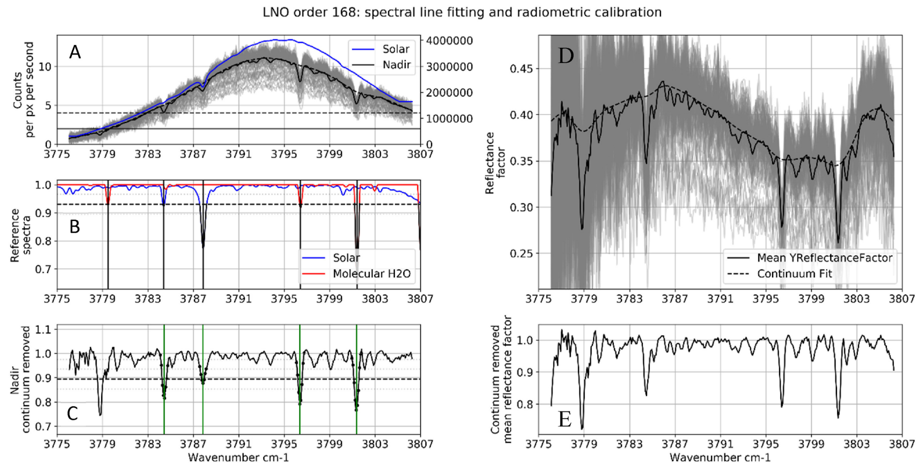

Figure 2.3: Example of the radiometric calibration steps for order 168 (2.627-2.648 μm) (Thomas et al., 2022a). (A): Averaging of the nadir raw spectra having the best SNR together (black) and creation of a synthetic solar spectrum for the same instrument temperature (blue). (B): Analyse of the simulated reference molecular (red) and solar spectra (blue) to find the wavenumbers of possible absorption lines (black vertical lines). (C): Identification of absorption lines outside the noise level in the mean nadir spectrum normalised by the continuum fit (green vertical lines). (D): Ratio of the shift-corrected nadir spectra by the solar spectra and convertion to reflectance factor (grey lines). (E): Example of the mean reflectance factor spectrum after removal of the continuum.

2.4 LNO channel advantages and drawbacks

In this section we discuss the advantages and drawbacks of NOMAD-LNO compared to other infrared spectrometers such as OMEGA (Bibring et al., 2004b), CRISM (Murchie et al., 2007) and TES (Christensen et al., 2001) (see Section 1.3)[2]. This section aims in particular to show the reader the difficulties of using LNO data due to instrumental characteristics. We also present the orders chosen for ice detection, which will be discussed and used in the following chapters.

The LNO channel provides nadir observations of the Martian surface in the infrared (see Section 2.1). This is essential for this work, as ice presents different absorption bands at these wavelengths, allowing its identification (discussed in Chapter 3 and 4). Nadir observations are acquired at high spectral resolution through different diffraction orders (see Section 2.2), giving access to ice absorption bands invisible to CRISM, OMEGA and TES. Nevertheless, as NOMAD is primarily designed for atmospheric studies, its design is not really conducive to surface studies. The acquisition of data by diffraction orders affects the SNR, which is 10 times lower than that of CRISM and OMEGA. As the entire infrared spectrum is not observed simultaneously, spectral behaviours of ice clouds and dust in the Martian atmosphere challenge surface ice detection (discussed in Chapter 3 and 6). In addition, the orders are not used uniformly, which affects their spatial[3] and temporal coverage. In spite of this, the circular orbit of TGO and a suitable selection of the orders allow the LNO channel to observe a wide range of local times, which is important for transient phenomena (e.g. morning frost, discussed in Chapter 5). Table 2.2 compares the NOMAD-LNO's characteristics with those of other infrared spectrometers.

[2]While THEMIS also studies the Martian surface through nadir observations, it acquires images at specific wavelengths, rather than over a spectral range. For this reason, we do not compare its instrumental characteristics with those of NOMAD-LNO as the operating modes are not similar.

[3]Spatial coverage is also affected by the inclination of TGO's orbit.

	NOMAD-LNO	**OMEGA**	**CRISM**	**TES**
Spectral range	2.3-3.8 μm	0.93-2.73 μm and 2.55-5.1 μm	0.36-3.92 μm	0.3-2.9 μm
Acquisition through diffraction orders	Yes	No	No	No
Spectral resolution	0.3 cm^{-1}	14 nm and 21 nm	6.55 nm	10 cm^{-1}
SNR	10-15	100	100	
Instantaneous foot-print	0.5 km $\times$ 17 km	1.5 km $\times$ 4.8 km	38 m spot	3 km $\times$ 8 km
Latitude coverage	74°N-74°S	87°N-87°S	all	all
Local time coverage	all	all	around 15:00	around 14:00

Table 2.2: Comparison of the LNO channel characteristics to OMEGA (Bibring et al., 2004b), CRISM (Murchie et al., 2007) and TES (Christensen et al., 2001) spectrometers. NOMAD-LNO advantages are in red.

As shown in red in Table 2.2, NOMAD-LNO offers few advantages for surface studies compared to other spectrometers, making its observations difficult to use. With this in mind, we reviewed the existing orders with the aim of selecting the most favourable for studying surface ice (more details in Chapter 3 and 4). During the first year of the thesis, several unsuccessful approaches were tested, illustrating the difficulty in selecting and using orders. Finally, six of them were selected, allowing the identification of CO_2 ice and H_2O ice using different spectral combinations. Table 2.3 lists the selected orders for this work and the chapters that define the corresponding method.

Orders	**Wavelengths (μm)**	**Main interest**	**Information**
167	2.64-2.66	CO_2 ice and H_2O ice	Chapter 4 and 6
168	2.62-2.64	CO_2 ice and H_2O ice	Chapter 4, 5 and 6
169	2.61-2.63	CO_2 ice and H_2O ice	Chapter 3, 4 and 6
189	2.33-2.35	CO_2 ice	Chapter 3
190	2.32-2.34	Spectral continuum	Chapter 3, 4 and 5
193	2.28-2.30	CO_2 ice	Chapter 4

Table 2.3: Selection of 6 orders for surface ice analysis, taking into account their ice sensitivity and availability. More details in the chapters mentioned in the third column.

Chapter 3

Martian CO_2 Ice Observation at High Spectral Resolution With ExoMars/TGO NOMAD

This chapter is the first study of LNO data for surface ice detection. This work was published in the Special Issue "ExoMars Trace Gas Orbiter: One Martian Year of Science" of the Journal of Geophyscal Reasearch Planets (JGR Planets) (Oliva et al., 2022)[1]. It is presented from Section 3.1. As a co-author, I participated in the investigation (see Section 3.2.3) and validation of the results (see Sections 3.4.1, 3.4.2 and 3.5) as well as in the review and editing of the article.

Although NOMAD is primarily designed to study the Martian atmosphere (see Chapter 2, Sections 3.1 and 3.2.2), the aim of this chapter is to highlight its ability to study surface ice. We explore the NOMAD data set information content in orders 169, 189 and 190 for MY34-35 (see Section 3.2.3) and define the Ice Index (see Section 3.4.1) and the Spectral Angle Mapper (SAM) χ index (see Section 3.4.2). These orders (169, 189 and 190) have the best spatial and temporal coverage from L_S 150° in MY34 to L_S 150° in MY35 (April 2018 to February 2020). Table 3.1 lists the definition of each index and the sections in which we describe the method.

[1] Oliva, F., D'Aversa, E., Bellucci, G., Carrozzo, F. G., **Ruiz Lozano, L.**, Altieri, F., et al. (2022). Martian CO_2 ice observation at high spectral resolution with ExoMars/TGO NOMAD. *Journal of Geophysical Research: Planets*, 127, e2021JE007083.

Spectral method	Orders	Wavelength	Interest	Information
Ice Index	169 and 190	2.7 μm	CO_2 ice and H_2O ice	Section 3.4.1
SAM χ index	189	2.35 μm	CO_2 ice	Section 3.4.2

Table 3.1: Overview of the spectral indices defined in this chapter: selected orders, ice absorption band, main interest and corresponding section for more details.

Previous studies based on laboratory and solar measurements (before the start of the scientific phase, April 2018) predicted a SNR of 100 for NOMAD-LNO (see Table 3.2 in Section 3.2.1). Nevertheless, we have found that such values are never achieved, especially in polar regions where unfavourable lighting conditions reduce signal intensity. Topographic shadowing is also amplified, implying increased average mixing of illuminated and unilluminated areas (see Section 3.5). The NOMAD-LNO SNR is significantly reduced, taking average values of $\sim$15 at high latitudes. Moreover, the instrumental characteristics (AOTF and grating) affect the signal from one pixel to another, making the signal at the edge of the detector weaker compared to the central pixel (see Section 3.3.2).

For these reasons, we adopt a semi-qualitative approach based on the statistical behaviour of the spectral data set. This allows to define confidence intervals to assess the sensitivity of the data set to the presence of surface CO_2 ice and its discrimination from surface water ice. We perform a seasonal study of ice cover in the polar regions (see Section 3.4). We obtain good overall agreement between our seasonal surface CO_2 ice maps and the Mars Express-OMEGA observations and the Mars Climate Database (MCD) predictions (see Section 3.5). Detections of CO_2 ice have also been found at mid-equatorial latitudes. Following a qualitative grain size analysis of the 2.35 μm absorption band, the cloud hypothesis seems the most likely scenario. It represents the first detection of CO_2 ice clouds through this band (see Section 3.5.1). This hence shows that NOMAD-LNO has great potential for analysing the microphysical properties of CO_2 ice.

Regarding the perspectives (see Section 3.6), a qualitative study for surface CO_2 ice microphysical properties is detailed in Chapter 4, while an in-depth radiative transfer analysis of the 2.35 μm feature in CO_2 ice clouds spectra is still planned. On the other hand, a study focusing on the detection of ice clouds is discussed in Chapter 6.

JGR Planets

RESEARCH ARTICLE
10.1029/2021JE007083

Special Section:
ExoMars Trace Gas Orbiter - One Martian Year of Science

Martian CO_2 Ice Observation at High Spectral Resolution With ExoMars/TGO NOMAD

F. Oliva[1], E. D'Aversa[1], G. Bellucci[1], F. G. Carrozzo[1], L. Ruiz Lozano[2,3], F. Altieri[1], I. R. Thomas[4], O. Karatekin[3], G. Cruz Mermy[5], F. Schmidt[5,6], S. Robert[2,4], A. C. Vandaele[4], F. Daerden[4], B. Ristic[4], M. R. Patel[7], J.-J. López-Moreno[8], and G. Sindoni[9]

[1]Istituto di Astrofisica e Planetologia Spaziali (IAPS/INAF), Rome, Italy, [2]Université Catholique de Louvain-la-Neuve (UCLouvain), Louvain-la-Neuve, Belgium, [3]Royal Observatory of Belgium, Brussels, Belgium, [4]Royal Belgian Institute for Space Aeronomy (IASB-BIRA), Brussels, Belgium, [5]CNRS, GEOPS, Université Paris-Saclay, Orsay, France, [6]Institut Universitaire de France (IUF), Paris, France, [7]School of Physical Sciences, The Open University, Milton Keynes, UK, [8]Instituto de Astrofisica de Andalucia (IAA), Consejo Superior de Investigaciones Científicas (CSIC), Granada, Spain, [9]Agenzia Spaziale Italiana (ASI), Rome, Italy

3.1 Introduction

CO_2 is the main component of the Martian atmosphere, in which temperatures can be low enough to induce local condensation of the molecule as ice/snow on the surface or as clouds at high altitude (Schofield et al., 1997; Clancy and Sandor, 1998; Clancy et al., 2007, 2019; Langevin et al., 2007; Montmessin et al., 2007; Schmidt et al., 2009, 2010; McConnochie et al., 2010; Vincendon et al., 2011; Aoki et al., 2018). The presence of CO_2 ice on the surface has been widely investigated remotely in different spectral ranges by instruments aboard several missions, such as Mariner 9/IRIS (Hanel et al., 1972), Viking/IRTM (Kieffer et al., 1972), Mars Global Surveyor/TES (Christensen et al., 2001), Mars Express OMEGA (Bibring et al., 2004b) and PFS (Formisano et al., 2005) spectrometers, and the Mars Reconnaissance Orbiter-CRISM instrument (Murchie et al., 2007). CO_2 ice is mainly found at high latitude in form of seasonal cap (Herr and Pimental, 1969; Larson and Fink, 1972; Kieffer and Titus, 2001; Langevin et al., 2007; Schmidt et al., 2009, 2010; Brown et al., 2010, 2012; Andrieu et al., 2018) and its physical and spatial characteristics strongly affect (and are affected by) the climatology of its gaseous counterpart (Leighton and Murray, 1966; Forget et al., 1995, 1998). Models and surface pressure measurements indicate that more than one quarter of atmospheric CO_2 deposits seasonally on each hemisphere (Tillman et al., 1993; Forget et al., 1998; Kieffer and Titus, 2001). On the other hand, the freezing of atmospheric CO_2 over the polar caps has an impact on the total atmospheric pressure of the planet (e.g., Leighton and Murray (1966)). In general, the sublimation/condensation processes of CO_2 on Mars have a fundamental role in sculpting the planet's energy budget (e.g., Kieffer (1979)).

Spectrally wide CO_2 ice absorption bands can be investigated in the infrared spectral range between 1 and 5 μm (Larson and Fink, 1972;

Schmitt et al., 1998). This interval is commonly covered by multispectral imaging spectrometers, such as Mars Express/OMEGA and Mars Reconnaissance Orbiter/CRISM, operating at a moderate spectral resolution (resolving power $\sim 10^2$). Studies of surface ice at higher spectral resolution (resolving power $\sim 10^3$) have been performed from ground-based telescopes allowing differentiation of the polar caps' CO_2 frost spectral features from those related to gaseous CO_2 (Larson and Fink, 1972). The same resolution has been reached by the Mars Express/PFS instrument studying the Northern seasonal cap (Giuranna et al., 2007). On the other hand, an analysis with even higher spectral resolution (resolving power $\sim 10^4$) from space, has not yet been performed.

ExoMars Trace Gas Orbiter (TGO)/Nadir and Occultation for MArs Discovery (NOMAD) is a suite of three spectrometers conceived to study the Martian atmosphere at high spectral resolution (Section 3.2). The first analyses of its data were devoted to methane, other trace gases, and suspended aerosols abundances and climatology (López-Valverde et al. (2018); Aoki et al. (2019); Korablev et al. (2019); Liuzzi et al. (2019, 2020); Vandaele et al. (2019); Gérard et al. (2020), to cite a few). In this work we start exploring the NOMAD data set information content in order to assess the feasibility of surface ices studies.

Since the instrumental characteristics are not optimal for surface spectroscopy, we adopt a semi-qualitative approach aimed to assess the sensitivity of the data set to the presence of CO_2 ice exposed on the surface and its discrimination from surface water ice and clouds. Moreover, we discuss the potential of the CO_2 ice 2.35 μm absorption band for the retrieval of the ice grains size and optical depth. This kind of investigation represents a useful framework for more quantitative and extended retrievals of CO_2 ice properties, which will be discussed in follow-up papers (Section 3.6). We include data spanning the second half of Martian Year (MY) 34 and the first half of MY35. In particular, MY34 data cover the 2018 global dust storm (Guzewich and Smith, 2019; Kass et al., 2019; Smith and Guzewich, 2019; Viúdez-Moreiras et al., 2019), allowing considerations on how suspended dust can affect the ice identification.

The tools and the methodology of the analysis are described in Section 3.3 and 3.4 respectively and the results are debated in Section 3.5. Finally, our conclusions are given in Section 3.6 along with the discussion about possible future work on this topic.

3.2 Instrument and Data Processing

3.2.1 The NOMAD Spectrometer

The NOMAD instrument is a spectrometer suite aboard the ESA ExoMars TGO spacecraft. NOMAD is capable of studying both the atmosphere and the surface of Mars, with primary focus on the investigation of trace gases. It observes with different pointing geometries taking advantage of three channels: UVIS, operating in the ultraviolet/visible range 0.2-0.65 μm, working both in nadir and solar occultation geometries; Limb, Nadir, and Occultation (LNO), covering the infrared range 2.2-3.8 μm, working in nadir, limb and solar occultation geometries; SO, working in the range 2.3-4.3 μm and performing dedicated solar occultation measurements (Neefs et al., 2015). While UVIS design is inherited from the ultraviolet/visible spectrometer developed for the ExoMars lander mission as part of the Humboldt payload (Vandaele et al., 2015c; Patel et al., 2017), both LNO and SO channels share the same design of the echelle grating Solar Occultation in the InfraRed (SOIR) spectrometer, part of the SPICAV instrument on board the Venus Express (VEx) spacecraft (Nevejans et al., 2006). They do not acquire the data in the whole spectral range at once, but only in small portions, in spectral regions of approximately 22 cm^{-1}, determined by the bandpass (hereafter called "order") selected on a tunable entrance filter (Acousto-Optical-Tunable-Filter, AOTF, Section 3.2.2). Both LNO and UVIS perform nadir observations and, hence, can be used to study the surface of Mars. In this work we focus on the investigation of LNO information content alone, while UVIS investigation will be covered in a follow-up paper in preparation. For a complete explanation of the LNO instrumental structure and operation the reader is referred to Neefs et al. (2015) and Thomas et al. (2016). In the next section we report the main issues of the LNO operations that strongly affect the processes of calibration and modeling of the measurements within the framework of our investigation. The main instrumental characteristics of LNO for the nadir geometry are reported in Table 3.2.

LNO Channel Instrumental Characteristics (NADIR)	
Wavelength range λ	2.3-3.8 (μm)
Wavenumber range k	2630-4250 (cm^{-1})
Resolving power $\frac{\lambda}{\Delta\lambda}$	10^4
Field of view	4 × 150 (arcmin^2)
Instantaneous footprint (400 km orbit)	0.5 × 17.5 (km^2)
Average integration time	15 (s)
Signal-to-noise ratio	100

Table 3.2: Limb, Nadir, and Occultation (LNO) Channel Instrumental Characteristics for Nadir Geometry (Neefs et al., 2015; Vandaele et al., 2018; Liuzzi et al., 2019).

3.2.2 Data Calibration and Uncertainties

The shape of the raw NOMAD-LNO spectra is strongly modulated by the AOTF spectral transmission curve and by the spectral response of the grating (the so-called Blaze function). Both curves are characterized by strong peaks, whose exact position on the detector is determined differently and changes from one order to the other. The AOTF peak position is tunable through an internal radio frequency generator, whereas the peak width, which defines the nominal spectral range assigned to a given order, is nearly constant (∼22 cm^{-1}). On the other hand, while the Blaze function is well approximated by a Gaussian curve, the AOTF transmission curve includes several secondary peaks (side-lobes, i.e., relative maxima at both sides of the main lobe) and is better modeled as a combination of a sinus-cardinal with a Gaussian (Liuzzi et al., 2019). It is worth noting that the presence of the side-lobes in the AOTF curve allows photons from a spectral range much wider than the nominal to fall on the grating. The signal produced by these unwanted photons sums up with the nominal one, in different locations on the detector, yielding a partial mixing of spectral information, more and more significant in moving from the center to the edges of any order. As a result, LNO spectra can show misplaced spectral signatures, that is, features pertaining to a given wavelength placed or replicated in a wrong position. We have to point out that the conversion from raw to radiance spectra implies the full correction of the lobed shape typical of raw spectra. However, even if the instrumental parameters of relevance were known with high accuracy (and this is not always the case), the partial spectral mixing due to the side-lobes cannot be removed by the radiometric calibration procedure.

The complete method for converting raw data to reflectance factor is given in Thomas et al. (2022a) while an alternative equivalent method is given in Cruz Mermy et al. (2022). In short, occasional calibration measurements are made where the LNO channel directly observes the Sun-albeit with a much shorter integration time-which are then used as a known reference source to calibrate the Mars nadir spectra. Corrections are applied to account for differences in instrument temperature between the solar spectra and the Mars spectra, and the spectral calibration is corrected by fitting to strong solar and/or atmospheric absorption lines.

Once the solar and nadir spectra have been normalized to counts per pixel per second, the reflectance factor conversion is then:

$$R = \frac{C_{nadir} d^2_{Mars}}{C_{solar} r^2_{Sun} \mu_0} \tag{3.1}$$

where C_{nadir} and C_{solar} are the LNO measured nadir and solar counts, d_{Mars} is the Sun-Mars distance, r_{Sun} is the solar radius and μ_0=cos(SZA), SZA being the Solar Zenith Angle.

The spectral mixing issue due to the AOTF side-lobes also propagates to the reflectance calibration. In this case, this effect also introduces low-frequency oscillations in the spectral continuum, making the direct comparison in absolute values between measurements and radiative transfer models complex. For the above reasons, we only deal with the NOMAD intensities close to the center of each spectral order, being less affected by the aforementioned issues, or with relative quantities obtained through normalization and continuum-removal processing.

The main source of noise in LNO observations comes from the thermal background of the instrument itself (Thomas et al., 2016). The channel operates at around -10 to $+10$°C, and so emission at infrared wavelengths reaches the detector, contributing to the majority of the signal recorded by the detector. On board background subtraction is employed to remove this contribution from the spectra, by taking consecutive Mars and dark frames (where the AOTF is switched off) and subtracting the dark frames from the Mars frames to leave the Mars signal which is then transmitted to Earth. As the thermal background is the principal source of radiation, the integration time is limited by the temperature of the instrument - and as saturation of the detector must always be avoided, a conservative value of around 200 ms is used. However, a shorter integration time means that more frames can be co-added on board, up to a maximum period defined by the channel's measurement cycle (Thomas et al., 2016). For standard nadir observations, this period is calculated by dividing 15 s by the number of diffraction orders measured (LNO typically measures 2, 3, or 4 diffraction orders per observation).

3.2.3 Data Selection

Several CO_2 ice spectral features fall within the LNO spectral range and are covered by different diffraction orders (Figure 3.1; Table 3.3). Orders 193 through 199, conceived for dust and surface nadir observations, cover the range 2.22-2.31 μm. In particular, orders 193 and 194, combined together, cover the 2.28 μm CO_2 ice absorption band. Orders 186 through 192, nominally devoted to the study of atmospheric CO, cover the spectral range 2.30-2.39 μm. This interval contains the 2.35 μm CO_2 ice absorption band that is well covered by order 189. Orders 149 through 171, dedicated to the study of gaseous CO_2 and H_2O, cover the strong 2.7 μm CO_2 and H_2O ices absorption bands and several weaker CO_2 ice bands within the 2.58-2.98 μm range. Finally, orders 119 through 136, dedicated to atmospheric HDO, CO_2, H_2O, and CH_4, cover different moderate to weak CO_2 ice absorption bands within the range 3.25-3.74 μm.

Order	**Wavelength range (μm)**	**Wavenumber range (cm^{-1})**	**Main focus**
119-136	3.245-3.738	2674.90-3081.44	HDO, CO_2, CH_4, H_2O (gas)
149-171	2.581-2.986	3349.24-3874.46	H_2O, CO_2 (gas)
186-192	2.299-2.392	4180.93-4440.90	CO (gas)
193-199	2.218-2.305	4338.28-4508.88	Nadir dust, surface
169	**2.612-2.632**	**3798.80-3829.15**	**H_2O (gas)**
189	**2.335-2.354**	**4248.36-4282.30**	**CO (gas)**
190	**2.323-2.341**	**4270.84-4304.96**	**CO (gas)**

Table 3.3: Diffraction Orders Covering CO_2 Ice Spectral Features Within Limb, Nadir, and Occultation Spectral Range. Orders in bold are the ones selected for the analysis described in Section 3.4.

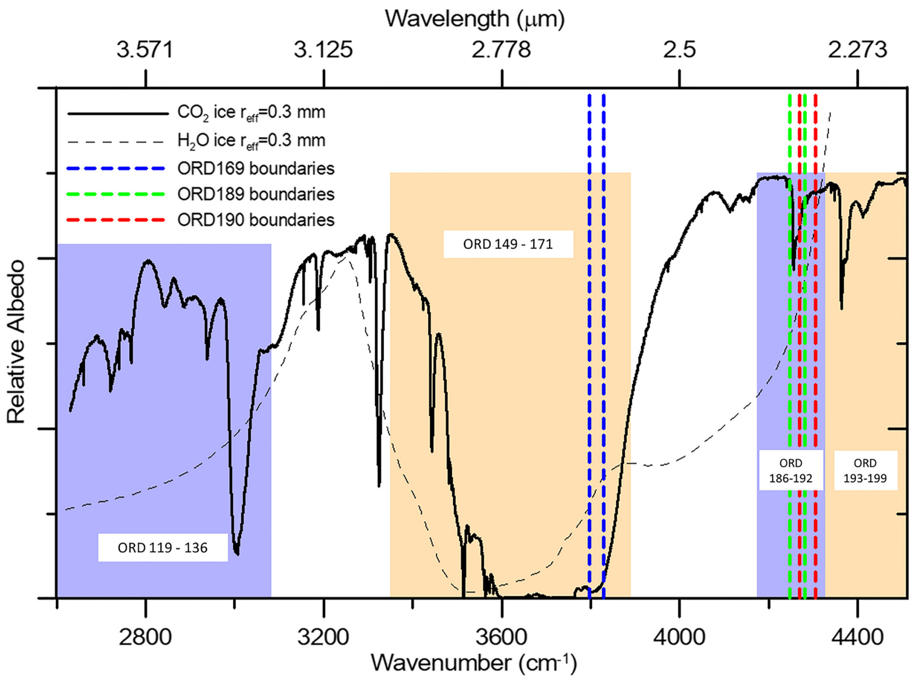

Figure 3.1: CO_2 ice (thick solid black line) and H_2O ice (thin dashed black line) albedo spectra (see Section 3.3.1 for surface ice albedo modeling details). The ranges covered by Limb, Nadir, and Occultation orders described in Section 3.2.3 (Table 3.3) are highlighted in colored shaded rectangles. Orders 169, 189, and 190 ranges are highlighted by the blue, green and red vertical dashed lines respectively.

These orders are not all equally effective for our purpose, that is to establish the CO_2 ice detection capability of NOMAD data, from the point of view of both spectral and spatial coverage. Among all the aforementioned CO_2 ice features, the 2.7 μm absorption band is the strongest in the LNO range, hence the most sensitive to small ice abundances, but it has the side effect of easily becoming saturated, especially on Martian ice-abundant deposits where large slabs (>20 cm) are expected (Langevin et al., 2007; Andrieu et al., 2018). Moreover, it is worth stressing that also water ice is absorbing at these wavelengths (Figure 3.1). Nevertheless, we can define a reflectance ratio to estimate the relative depth of the 2.7 μm absorption band (Section 3.4.1) for use as a general measure of the presence of ice (both H_2O and CO_2). This is achieved by taking advantage of orders 169 and 190 (blue and red dashed lines in Figure 3.1), being the ones with the best spatial coverage in the data set so far available. Order 190 falls between CO_2

ice absorption bands at 2.28 and 2.35 μm. It also encompasses some gaseous CO absorption lines, but they are narrow enough to not affect the measurement of the continuum.

Toward the thermal range of the LNO spectrum (wavelengths larger than 3.2 μm covered by orders 119-136, see Table 3.3), the instrumental signal-to-noise ratio (SNR) of LNO becomes worse due to a reduced instrumental sensitivity (maximum SNR $\sim$20, compared to 70 at shorter wavelengths, see below) and, moreover, a limited number of observations are available. This makes the CO_2 ice absorption bands longward of 3 μm difficult to use at the global scale we are interested in.

As stated above, the combination of orders 193 and 194 covers the 2.28 μm absorption band. However, since a relatively low number of observations are available for these orders, the spatial coverage they provide is somewhat limited. Moreover, the AOTF-induced spectral mixing (Section 3.2.2) makes the reconstruction of the full, non-modulated 2.28 μm band quite challenging.

On the other hand, the absorption band at 2.35 μm (4255 cm^{-1}) is a more promising feature, since it never saturates and is well covered by LNO order 189. This band is already known to be diagnostic of the presence of CO_2 ice on the surface of Mars (Schmitt et al., 1998) and, as demonstrated through laboratory measurements (Kieffer, 1970) and observations (Larson and Fink, 1972), it is related to a forbidden transition in solid CO_2 (Calvin and Martin, 1994). It lies in the solar reflected part of the spectrum where the detector sensitivity is higher, thus allowing a higher SNR (70 at max) with respect to longer wavelengths. Moreover, since this band is relatively weak, it is affected to a lesser degree by atmospheric particulate scattering (Section 3.4.3). However, the moderate SNR of the LNO nadir data set makes its measurement rather noisy and, therefore, we take advantage of a spectral classification method for describing the overall behavior of this band in the data set (see Section 3.4.2).

For the above reasons, we focus this investigation of the LNO information content about CO_2 ice on the analysis of the data of orders 169, 189, and 190 (Table 3.3), to which we apply the Minimum Noise Fraction algorithm (Green et al., 1988; Lee et al., 1990; Boardman and Kruse, 1994) in order to mitigate the noise. Regarding spatial coverage, we point out that the selected NOMAD orders are acquired on consecutive spacecraft orbits, hence they are neither spatially nor temporally coincident. This yields non-uniform coverage at global scale for each order. In order to work on a common spatial base and reduce possible biases, we reduce all data to the coverage of order 189, which is the most sparse among the others. A more complete spatial coverage can be achieved by accumulating data in a wider range of solar longitudes (Section 3.4), but with a consequent reduction of the temporal resolution of seasonal trends. A similar issue affects the seasonal coverage too, since the data averaged in bins of latitudes and solar longitudes are acquired at varying longitudes. Taking into account MY34 and MY35 data, the selected orders provide a near-global coverage of the planetary surface between latitudes ±75° (Figure 3.2), with Southern and Northern latitudes mostly covered by MY34 and MY35 data respectively. Local times values vary between early morning and late afternoon, while SZA are moderate at mid-latitudes (0°-50° on average) and reach night-time values (SZA >90°) in the winter pole. However, in order to avoid observations with very low SNR, we select only data with SZA <80°. The temporal coverage of the data considered here encompasses a full Martian year, from Northern summer of MY34 to Northern summer of MY35 (solar longitudes 150°-360° in MY34, and 0°-150° in MY35).

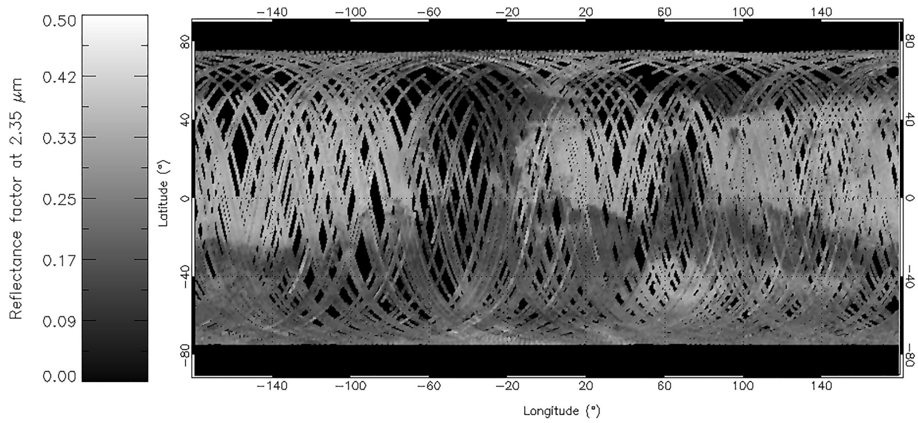

Figure 3.2: Map of all MY34 (150° < L_S < 360°) and MY35 (0° < L_S < 150°) 2.35 μm reflectance factor data of order 189, averaged in bins of longitude and latitude.

It is important to note that the high spectral resolution of LNO data (Table 3.2) is counterbalanced by a moderate spatial resolution, as the instantaneous footprint on the surface is quite large (0.5 km × 17 km, Table 3.2). This can impact the identification of the ice features, in particular in regions of transition between non-icy and icy terrains or if observing small ice deposits. In these cases in which the pixel ice filling factor (i.e., the ratio between the instantaneous apparent section of icy terrain and the angular size subtended by the instrument pixel) is less than unity, the ice diagnostic features may be diluted or mixed to different extents with non-icy spectral features. This fact, in addition to the spectral contamination by AOTF side lobes (Section 3.2.2), may result in complex deformation in the observed ice spectrum when mixed with other spectral components, making the ice identification less reliable. For the above reasons, we focus our analysis and discussion only in regions where the ice signature can be unequivocally identified (see Section 3.4.1).

3.3 Spectral Modeling

As stressed in Sections 3.1 and 3.2.1, in this work we focus on relative analyses of LNO spectra, whereas more comprehensive radiative transfer studies are postponed to future work (Section 3.6). This approach makes our results mostly independent from radiative transfer models and calibration issues. Nevertheless, we use simplified radiative transfer models for giving a context to our results and assessing their behavior (Section 3.5.1). In this section we briefly describe such models, used to perform the simulations of surface ice and dust/ice clouds spectra discussed in Sections 3.2.3, 3.4.2, 3.4.3 and 3.5.1. For both surface and cloud models, we perform the simulations with SZA = 70° (unless specified otherwise), consistent with NOMAD observing geometry at Southern polar latitudes. Moreover, scattering parameters are computed using Mie theory (through the MIEV0 routine, Wiscombe (1980)). The wavelength range we consider is that covered by orders 169, 189 and 190 (Table 3.3). Given the qualitative purpose of the modeling, we do not apply the Blaze and AOTF functions to the simulations, since they would require a specific characterization depending on the considered order and observation that is not yet fully established (see Section 3.2.2). For this reason, the models we compare to LNO data in Section 3.5.1 (Figure 3.8A) should not be considered as best fits in a retrieval framework, but they still provide valuable information about the physical quantities that, in principle, can be retrieved by means of a more in-depth radiative transfer analysis of this data set (Section 3.6).

3.3.1 Surface Ice Albedo Spectra

The albedo spectra of surface ice have been simulated using the SNow Ice and Aerosol Radiation (SNICAR) tool by Flanner et al. (2007), formerly developed for H_2O snow Earth-based studies (Singh and Flanner, 2016) and here extended to compute CO_2 ice albedo using the optical constants from Hansen (2005). The model takes advantage of the multiple scattering, multilayer two-stream radiative approximation (Toon et al., 1989), with the delta-hemispheric mean approximation. We adopt a CO_2 ice mass density of 1000 kg m^{-3} that is indicative of Mars' South pole (Titus et al., 2008; Brown et al., 2010) and, for models whose only purpose is to showcase the peculiar spectral signatures of surface ice (Section 3.2.3, Figure 3.1 and Section 3.4.2, Figure 3.5), we adopt the assumption that the thickness of the ice slabs is equal to the grain size (Langevin et al., 2007). However, such an assumption is not realistic in general since in the considered spectral range we are only sensitive to the upper layers of surface ice deposits. For this reason, in order to compare the models to LNO observations in a semi-qualitative way (Section 3.5.1) we vary the slabs' optical depth by changing both their thickness and size.

3.3.2 Airborne Dust and CO_2 Ice Clouds Reflectance Factor Spectra

The reflectance factor of Martian dust layers and CO_2 ice clouds is obtained through the MITRA radiative transfer tool (Adriani et al., 2015; Oliva et al., 2016, 2018; Sindoni et al., 2017; D'Aversa et al., 2022), already applied to the atmospheres of Saturn, Jupiter and Mars. Dust layers are simulated using the optical constants from Wolff et al. (2009, 2010) while for CO_2 ice clouds we adopt the refractive index defined by Hansen (2005), as in the case of surface ice modeling. Dust layers and ice clouds are described adopting lognormal particle size distributions with 0.5 effective variances (parameters taken from Mars Climate Database, MCD, Millour et al. (2018)). Regarding dust opacity, at the wavelengths considered in this work we are more sensitive to abundance than grain size variations and, hence, the latter parameter is assumed constant (1 μm effective radius) in all the simulations. Given the considered spectral range, gaseous absorption has no impact for our purpose and, for this reason, it is not considered in the computations. In Section 3.5.1, where we compare our models to LNO data, we adopt their specific illumination and observing conditions, and use the method from McGuire et al. (2009) on OMEGA data to estimate the spectral surface albedo required to perform the simulations.

3.4 Data Analysis

Two different approaches were used to identify and map the CO_2 ice on the surface: (a) the analysis of the short-wavelength shoulder of the 2.7 μm band, through orders 169 and 190 investigation (Section 3.4.1) and (b) the application of a spectral matching method to the shape of the 2.35 μm band (Section 3.4.2).

3.4.1 Ice Detection Through the 2.7 μm Band

As already explained (Section 3.2.3) the 2.7 μm band is usually saturated at the expected conditions for surface CO_2 ice on Mars. Moreover, given the band strength, it is also quite sensitive to atmospheric particulate scattering (Vincendon et al. (2008); see Section 3.4.3). For the above reasons, albeit this band is not reliable to quantify the amount of ice on the surface without a proper radiative transfer analysis, or for its detection in no-ice to ice transition regions (Section 3.5), it can be exploited to identify spatially homogeneous and relatively abundant deposits. Therefore, the simplest indications of ice detection can rely on coupling a high absolute reflectivity level of the spectrum at continuum wavelengths with a stronger absorption inside the 2.7 μm band. We define the Ice Index as the ratio between the reflectances measured in orders 190 and 169 (Section 3.2.3):

$$IceIndex = \frac{R_{190}}{R_{169}} \tag{3.2}$$

This ratio is of course applicable also to other datasets, for example, for OMEGA, that we use here as a benchmark to test its effectiveness in detecting ice. As we can clearly see in Figure 3.3, the Ice Index calculated for OMEGA spectra (for OMEGA, Equation 3.2 reduces to the simple ratio of reflectance factors at 2.62 and 2.33 μm) correlates with CO_2 ice abundance, measured through the depth of the 2.35 μm band (panel C in the figure). This test also confirms the Ice Index to be sensitive to H_2O ice, measured through the depth of the 1.5 μm band (panel B in the same figure). As expected, the Ice Index has a value of about 1 on non-icy terrains while it becomes larger for stronger band depths. Since the Ice Index is evaluated on the 2.7 μm band shoulder, different growth regimes versus the band depth are visible, depending on the width and shape of the considered H_2O and CO_2 ice absorption bands. Its slow growth rate with smaller band depths makes its uncertainty larger in smaller or more dusty ice deposits. Nevertheless, it is evident how, aside from its uncertainty in transition regions, the Ice Index can be reliably used to identify deposits where the ice abundance (and hence the band depth) is large. In the OMEGA case, the possibility to directly measure the band depths, although at moderate spectral resolution, enables each pixel to be flagged as icy or not and consequently to potentially derive threshold values for ice detection based on the actual uncertainty associated with the OMEGA data. However, this approach cannot be extrapolated to the NOMAD data set, since the differences in data acquisition and processing affect the threshold values.

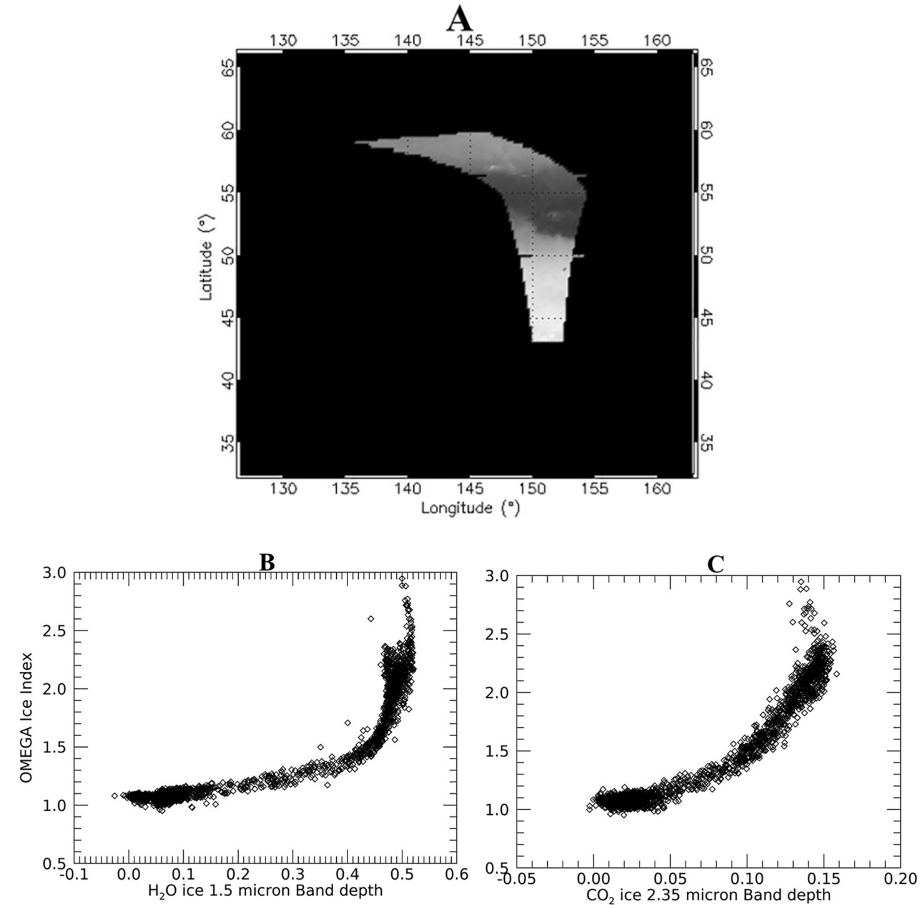

Figure 3.3: Cylindrical projection of a cut of OMEGA orbit 0228_3, covering mid to polar Northern latitudes during MY27, displayed at 2.33 μm (panel A). Panels (B and C) show the trend of the OMEGA Ice Index computed on OMEGA orbit 0228_3 (panel A) with the 1.5 μm H_2O ice band depth (B) and the 2.35 μm CO_2 ice band depth (C).

With NOMAD data we are interested in longitudinally averaging the Ice Index, in order to perform a seasonal study of the ice coverage. To achieve this, we group the reflectance factors taken at the central wavelengths of the selected orders (R_{169} and R_{190}, taken at 2.62 and 2.33 μm respectively) in bins of latitude and L_S, by averaging the data at all available longitudes. As a result, we obtain a latitudinal-seasonal map for each order. As mentioned in Section 3.2.3, a different longitudinal coverage pertains to orders 169 and 190, making their direct ratio biased by spatial albedo inhomogeneities. In order to mitigate this issue we resort to MGS/TES data on Mars bolometric albedo (Christensen et al., 2001). By keeping track of the longitudes falling in each bin of the two orders' seasonal maps, we average TES data the same way as NOMAD ones, obtaining a corresponding map for each order. We can then use these maps as weighting factors to correct for the different spatial coverage of the two orders. We define the zonally averaged index <Ice Index> that is sensitive to the presence of ices.

$$< IceIndex >= \frac{R_{<190>}}{R_{<169>}} \frac{TES_{<169>}}{TES_{<190>}} \tag{3.3}$$

where $R_{<X>}$ and $TES_{<X>}$ are the zonally averaged NOMAD and TES seasonal maps respectively, and $< X >$ denotes the average along the longitudes inside the same latitude/L_S bin of order X. The ratio of the reflectance in the two orders, weighted by TES albedo data, correlates with the amount of ice in the footprint.

It is evident how the approach in the computation of the Ice Index with OMEGA and NOMAD datasets is quite different. Significant differences between the two datasets come from the relatively high LNO noise level, its spectral resolution, the related penetration depth in the ice layers, and the TES data uncertainty. Regarding this last issue, we remind the reader here that TES albedo is bolometric, and therefore carries information related to a wider spectral range with respect to the single wavelengths we are considering with NOMAD data. Moreover, despite the TES map being filtered to minimize the effect of atmospheric dust and clouds, it still contains surface ice (Christensen et al., 2001), increasing the uncertainty in transitional regions. Another difference between OMEGA and NOMAD datasets is that OMEGA spectral resolution is lower (resolving powers of 10^2 and 10^4 for OMEGA and NOMAD respectively). This implies that the OMEGA steep short wavelength shoulder of the 2.7 μm band is probably probing different depths of penetration in the ice with respect to NOMAD, due to the wider wavelength range convolved in a single spectral point. All these sources of uncertainty are particularly significant in ice/no-ice transition regions, and, overall, prevent the definition of an absolute threshold value for ice detection. For this reason, we focus on the global distribution of the Ice Index and its qualitative correlation with regions of interest on the planet. As in the case of OMEGA, in the NOMAD data set Ice index values as low as 1 are found in regions where no large concentrations of ices are expected, for example, at the equator and mid-latitudes. On the other hand, an Ice Index larger than 2 is found on the polar caps where both H_2O and CO_2 ices are known to be abundant (Figure 3.4A). Values between 1 (ice free terrains) and 2 (polar caps) possibly still indicate the presence of ices in transition regions with smaller ice filling factors, making it difficult to obtain an unambiguous detection. The same effect could be produced by dust areal mixing on the ice slabs, as observed by Langevin et al. (2006) on the "cryptic" region (latitudes $<-70°$) of the South polar cap. However, due to the averaging procedure described above and to LNO spatial resolution (Table 3.2), the resulting seasonal data set we analyze here is poorly sensitive to such region. Instead, in regions where the Ice Index is larger than 2 the pixels are more likely to contain mostly ice and, hence, its information is more consistent. It is worth stressing again that this value should not be considered as a threshold between non-icy and icy terrains, but rather an indication for abundant deposits in which the ice spectral signature is stronger. The terrains identified with Ice Index >2 mostly fall within Mars polar caps but a few regions are also located at mid-latitudes (Section 3.5.1).

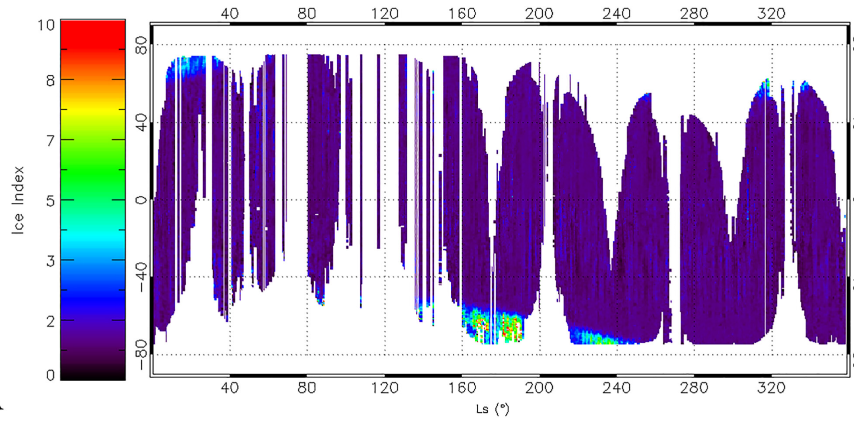

A

Continued on the next page.

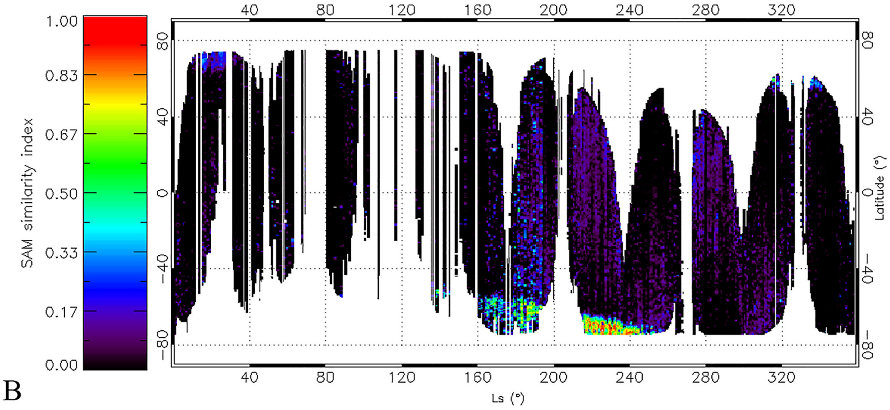

B

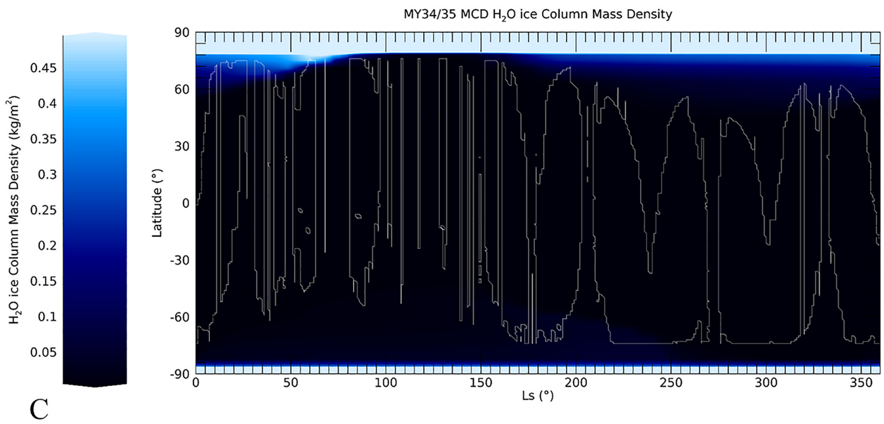

C

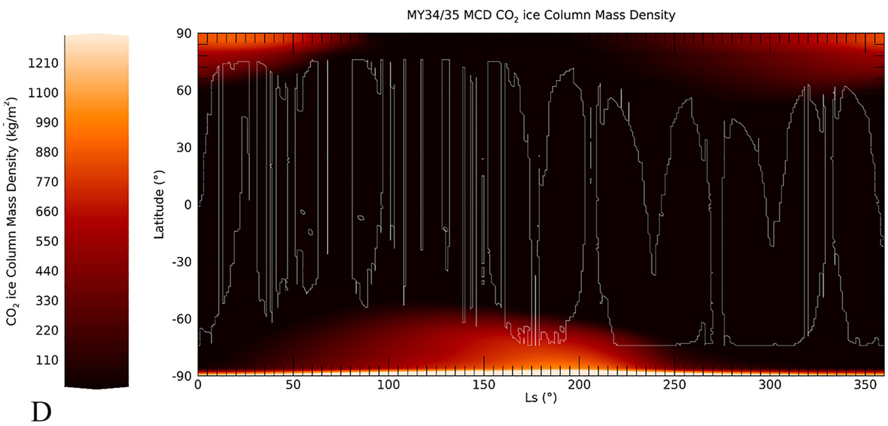

D

Continued on the next page.

Figure 3.4: In all maps, L_S between 0° and 150° refer to MY35, while L_S between 150° and 360° are related to MY34. The image shows latitudinal-seasonal maps of Ice Index (A), Spectral Angle Mapper (SAM) similarity index $\chi = 1-\alpha/\alpha_{mid}$ (panel B, α_{mid} is the average SAM angle α estimated at mid-latitudes, see Section 3.4.2) and (C) MCD predictions of H_2O and (D) CO_2 ices columnar mass density in kg/m^2. The boundaries of the Nadir and Occultation for MArs Discovery data set as shown in panels (A and B) are superimposed on panels (C and D) for a qualitative comparison.

3.4.2 CO_2 Ice Detection Through the 2.35 μm Band

As described in the previous section, the Ice Index is sensitive to both CO_2 and H_2O ices. An independent method is therefore desirable in order to distinguish them. The 2.35 μm band of CO_2 ice is covered by the LNO order 189. The icy spectra in this order show a stronger absorption band centered at about 2.35 μm (4255 cm^{-1}) embedded in a wider absorption between 2.339 μm (4275 cm^{-1}) and 2.351 μm (4253 cm^{-1}; an example is given in Figure 3.5). The spectral shape measured by LNO is affected by the AOTF side-lobes contamination (Section 3.2.2), which results in a ghost absorption band appearing at 2.337 μm (4278 cm^{-1}). Since the width of the 2.35 μm absorption band is of the same order of the AOTF bandwidth, the measurement of the full band depth is not possible, as the continuum level of the reflectance is hardly determined. Moreover, the SNR at the edges of the order, at wavelengths shorter than 2.337 μm and longer than 2.351 μm drops significantly. The definition of a pseudo-continuum between 2.339 μm (4275 cm^{-1}) and 2.351 μm (4253 cm^{-1}) will allow the measurement of a partial band depth which cannot quantify the amount of CO_2 ice (since its continuum is still affected by CO_2 ice absorption) but it is qualitatively correlated to its abundance. However, the uncertainties associated with such parameters are still large, since they always deal with the LNO signal measured in few spectral channels.

Spectral Angle Mapper Analysis

In order to obtain a more robust parameter, able to statistically map the CO_2 ice detection with LNO, we use the Spectral Angle Mapper (SAM) method (Boardman, 1992; Kruse et al., 1993). The SAM algorithm determines the spectral similarity between a sample spectrum and reference ones by treating them as vectors in a space with dimensionality equal to the number of considered bands and by calculating the correlation, expressed by the angle α (in radians) between them. Hence, the smaller the angle, the better the agreement with the considered reference spectrum. This technique, when used on calibrated reflectance data, is relatively insensitive to illumination and albedo effects (Kruse et al., 1993), and is also effective in mitigating the propagation of uncertainties since it involves the whole central part of the spectral range.

We apply the SAM algorithm to the LNO spectra of order 189 between 2.337 μm (4278 cm^{-1}) and 2.351 μm (4253 cm^{-1}). As a reference endmember, we adopt a bulk Southern polar cap spectrum in which the 2.35 μm CO_2 ice absorption band is clearly recognizable and whose spectral shape is in agreement with that expected from radiative transfer models (Figure 3.5). Before the application of the algorithm, we apply the same spatial averaging procedure described for the Ice Index (Section 3.4.1), in order to obtain a spectral array in bins of latitudes and solar longitudes. Then, we define a SAM index of spectral similarity as $\chi = 1 - \alpha/\alpha_{mid}$ (where α_{mid} is the average angle estimated at mid-latitudes where surface ice is unlikely to be present). The resulting map of the SAM similarity index χ is shown in Figure 3.4B. We tested different endmembers, finding no significant difference in the SAM results as long as the endmembers are taken in the bulk of the polar caps, where the mixing with non-icy terrains is likely negligible. On the other hand, endmembers taken at the borders of the cap result in noisy SAM maps, where the polar caps are not even detectable.

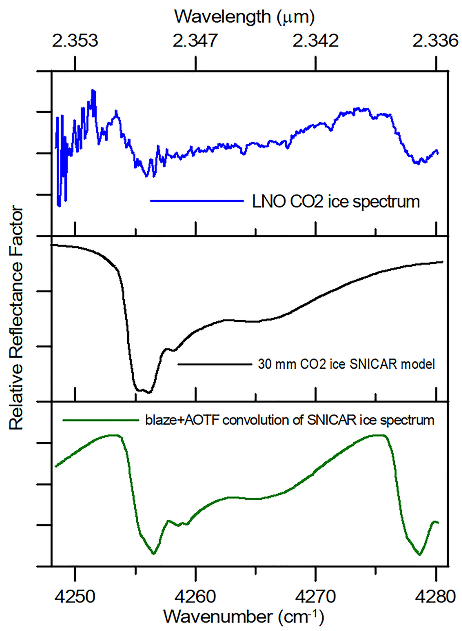

Figure 3.5: Blue: Nadir and Occultation for MArs Discovery (NOMAD) reflectance spectrum of the South polar region. The CO_2 ice absorption is visible at 2.35 μm (4255 cm^{-1}). Black: model spectrum of a 30 mm thick CO_2 ice slab obtained with the SNICAR tool (Section 3.3.1). Green: the black spectrum convolved with the NOMAD instrumental functions (the Blaze and AOTF response).

Ice Index and SAM Seasonal Maps Qualitative Comparison

It is evident how the SAM map in Figure 3.4B is noisier with respect to the Ice Index one in Figure 3.4A, due to the fact that order 189 has a more limited spatial coverage with respect to orders 169 and 190, used for the Ice Index computation, hence yielding a poorer SNR in the zonal averages. This is particularly evident in the pre-storm period ($180° < L_S < 200°$) at mid-latitudes, where the relative errors of the Ice Index and SAM similarity index are maximum and reach 30% and 50% respectively. Nevertheless, we note that the polar caps regions correlate with χ values larger than 0.2 (Figure 3.4B). As in the case of the Ice Index (Section 3.4.1), we stress that this value should not be considered as a threshold for the CO_2 ice detection, but rather an indication of deposits where the ice abundance is large and the 2.35 μm band signature strong. Such χ values also identify several non-polar latitude regions that are discussed in Section 3.5.1.

We can now qualitatively compare the seasonal Ice Index (Figure 3.4A) and SAM χ index (Figure 3.4B) maps with the simulations of seasonal H_2O and CO_2 ices abundance, expressed as columnar mass density in kg/m^2 (Figures 3.4C and 3.4D respectively) obtained from the MCD (version 6, Millour et al. (2018)). In these simulations, airborne dust climatology is treated with the method described in Montabone et al. (2020). Both the Ice Index and the SAM maps are effective in reproducing the condensation and sublimation patterns taking place in the Martian polar caps. In particular, during the Northern spring ($L_S \sim 0°$) the sublimation of the Northern polar cap is observed in both maps, in agreement with MCD simulations. Although fewer observations are available for Southern winter ($L_S \sim 90°$), we observe some clear detections of the Southern polar cap in the Ice Index map. These are in agreement with the presence of both H_2O and CO_2 ices and, since no coincident detections are available in SAM map, we cannot determine which ice is being probed by the Ice Index. During the Southern late winter/spring we observe the sublimation of the Southern polar cap both in the Ice Index and SAM maps ($140° < L_S < 260°$). This solar longitude range is also affected by the 2018 global dust storm ($L_S \sim 180°$-$250°$, Smith and Guzewich (2019); Viúdez-Moreiras et al. (2019)) allowing investigations of the impact of dust on the ice detection (Section 3.5). The SAM map is noisier than the Ice Index map before the peak of the storm ($160° < L_S < 200°$), due to the scarce data coverage and poor SNR of order 189 data near the poles in the illumination conditions typical of late winter. During the decay phase of the storm ($L_S \sim 200°$-$250°$) both maps correctly reproduce the sublimation pattern of the ice caps predicted by the MCD.

Finally, a few detections appear during Northern autumn and winter ($L_S > 255°$), indicating the condensation and the peak winter phase of the Northern polar cap. In this period, ice is identified in both the SAM and Ice Index maps only for $L_S > 280°$. On the other hand, at $L_S \sim 255°$ only Ice Index detections are found, suggesting that the parameter is probably probing H_2O ice at those solar longitudes. The dichotomy between the SAM and the Ice Index map makes it possible to distinguish the presence of H_2O and CO_2 ices and is discussed further in Section 3.5.

3.4.3 Airborne Dust Effect

The CO_2 ice detection approach described in Sections 3.4.1 and 3.4.2 is based on the assumption that suspended dust has a negligible impact on the detection of CO_2 ice spectral features. We verify this assumption by performing radiative transfer simulations with different dust optical depths in the wavelength range covered by orders 169, 189, and 190 (Table 3.3). We compute the CO_2 ice surface spectral albedo using the SNICAR model (Section 3.3.1) and the MITRA radiative transfer tool to simulate the Martian reflectance factor with different dust loadings (Section 3.3.2). The results are shown in Figure 3.6. The presence of dust decreases the relative depth of the CO_2 ice absorptions at 2.60 and 2.35 μm, while changes in spectral shape happen only for very high abundances, as it is evident in the blue simulations in which $\tau_2 = 10$ (where τ_2 is the dust optical depth at 2 μm). As a consequence, dust lowers the Ice Index value (Section 3.4.1) affecting its effectiveness in the identification of ice. Ordinary dust abundances (τ_2 <1) can impact the detection of small/thin ice deposits through the Ice Index, but conditions of high dust optical depth can even mask extended icy surfaces. Indeed, with respect to the clear sky case, we estimate a decrease of the Ice Index down to 85% with $\tau_2 = 2$. This analysis confirms that, even if it is beyond the scope of this paper (Section 3.5), the CO_2 ice 2.7 μm absorption band can be used to estimate the atmospheric dust content, as already done with OMEGA data by Vincendon et al. (2008). It is worth stressing that the vertical distribution of dust is not constrained in these simulations, so the same effect holds either for dust suspended in the whole atmospheric column, concentrated in an atmospheric layer or directly deposited over the surface ice.

On the other hand, dust has a lesser impact on the CO_2 ice identification through the SAM similarity index χ (Section 3.4.2). This is expected from a theoretical point of view because the 2.35 μm band is relatively weak and its depth is less affected by scattering. Moreover, the SAM algorithm is more sensitive to the band shape than to its depth. Therefore, the ice identification is still possible as long as the 2.35 μm absorption band is above the noise level. The relatively low SNR of order 189 is the most limiting factor in the effectiveness of the SAM algorithm application. The percent decreases of both the Ice Index and SAM similarity index due to the dust presence with respect to the clear sky case (ΔII and ΔSAM respectively) are given in Figure 3.6.

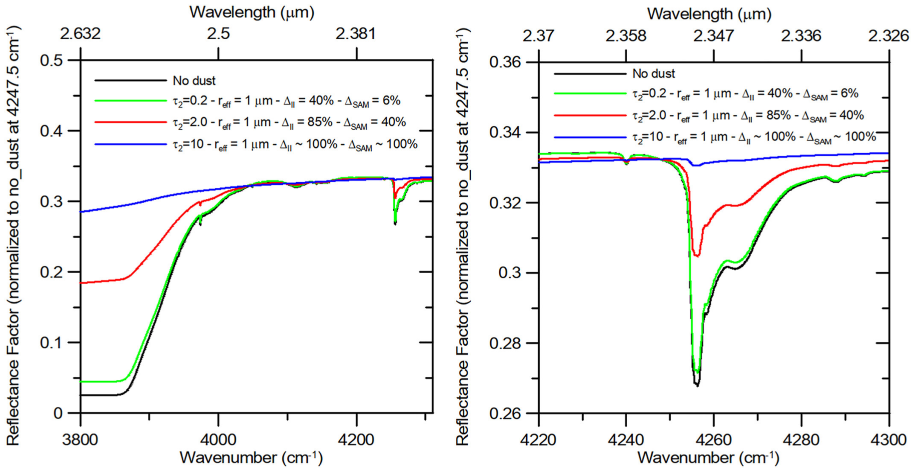

Figure 3.6: Radiative transfer simulations performed with the MITRA tool (Section 3.3.2) adopting different optical depths (τ_2 is the optical depth at 2 μm). ΔII and ΔSAM indicate the percent decrease of the Ice Index and Spectral Angle Mapper similarity index with respect to the no dust simulation (black lines). All simulations have been normalized to the no dust one at 4247.5 cm^{-1}. The CO_2 ice albedo underneath the dust is computed with the SNICAR tool (Section 3.3.1), assuming a 30 mm slab. Left panel shows a wide spectral range including both the 2.35 μm and the broader 2.60 μm CO_2 absorptions, while the right panel shows the zoom on the 2.35 μm band.

3.5 Results and Discussion

As described in Section 3.4, if we focus on regions where ice is abundant, that is, the polar cap regions, the Ice Index and SAM seasonal maps of surface ice coverage are in good agreement with general climate models (Figure 3.4). It should be noted that polar caps observations are unavoidably acquired at high solar zenith angles (between 50° and 80°). Such geometry yields unfavorable illumination conditions in which both the incident and reflected radiation are reduced in intensity and topographic shadowing is amplified, implying increased average mixing of illuminated and unilluminated areas and reduced SNR. This issue affects both the Ice Index and the SAM maps, possibly enlarging those regions that we identify as transition between icy and non-icy terrains.

The noise level in the SAM χ index map is higher with respect to the Ice Index map (Section 3.4.2, Figure 3.4). As a result, some structures identified in the latter are not recognizable in the former. This is evident in Figures 3.7A and 3.7B, where the red and green points indicate pixels with Ice Index >2 (Section 3.4.1) and SAM χ index >0.2 (Section 3.4.2) respectively, highlighting regions in which the two parameters mostly correlate with the polar caps. In particular, the SAM map misses some points at the North pole in regions A and G. This is in agreement with the fact that CO_2 ice requires colder temperatures to condense and, hence, suggests that it is probably located at latitudes higher than those covered in the analyzed data set. The mid latitude detections in the SAM map are discussed in Section 3.5.1.

From the Ice Index and SAM maps we can estimate the extension of the polar caps by studying the latitudinal trend of the two parameters for every bin of L_s. We define the edge of a cap at a given L_s as the latitude of the most equatorward group of at least three adjacent pixels in which the parameters exceed by three sigma their average value on mid-latitudes non-icy terrains. Such a condition has been chosen to ensure ruling out the aforementioned ice transitional regions, where filling factor issues can make ice parameters values unreliable (Sections 3.2.3 and 3.4.1). The results we obtain are compared in Figure 3.7C to the MCD CO_2 ice abundance simulations and to OMEGA data estimated boundaries for MY27-28. In the image, red and green stars indicate the Ice Index and the SAM estimated boundaries respectively, while the dots represent the minimum latitudes in the polar caps at which OMEGA 1.43 μm CO_2 ice absorption band is non-zero, extrapolated from Figures 12-19 from Langevin et al. (2007) and from Figures 4-9 from Appéré et al. (2011). The colored regions of interest labeled with letters identify the polar caps (green regions) and mid latitude ice detections (magenta regions). For comparison, these are also shown in Figures 3.7A and 3.7B. It must be noted that there is not always coincidence between these regions and the colored points in Figures 3.7A and 3.7B (see e.g., region H), being their identification based on conceptually different conditions.

Since our boundary estimates are not sensitive to transition regions, the comparison we make with MCD is merely qualitative and no attempt to perform a quantitative retrieval of the ice abundance is being made. The MCD CO_2 ice column density isolines shown in Figure 3.7C are those coincident with our cap boundaries estimates and highlight some gradients in abundance across the edges that are worth discussing. OMEGA boundaries are consistent with our estimates and with the lower density MCD simulations, confirming the seasonal patterns of the polar caps in different MY. As in the case of the Ice Index and SAM points in Figures 3.7A and 3.7B, there is not always correspondence between the red and the green stars clusters in Figure 3.7C. This is particularly evident in regions C and G, in which the SAM boundaries only appear in coincidence with the highest L_S Ice Index clusters. As explained above, this behavior is related to the fact that, in these regions, CO_2 ice is probably condensing at lower temperatures pertaining to latitudes higher than those covered in our analysis. Indeed, in region A the SAM boundary appears farther north with respect to the Ice Index boundary. The MCD predicts average surface temperatures of about 160 K for the red stars cluster in region A, above the CO_2 frost temperature, suggesting that the Ice Index points are actually probing the H_2O ice polar cap there. On the other hand, temperatures of the order of $\sim$150K are predicted for the green stars cluster, within Mars CO_2 frost temperature range (Piqueux et al., 2016) and in agreement with the presence of the CO_2 ice points. In all regions where green clusters overlap on the red ones (regions E, F, and at $L_S \sim 140°$ in region C and $L_S \sim 340°$ in region G), the Ice Index is probing both H_2O and CO_2 ices. On the other hand, in the lower L_S clusters in regions C ($85° < L_S < 105°$) and G ($255° < L_S < 320°$) only Ice Index derived boundaries appear, suggesting that the parameter is only probing H_2O ice there. The estimated cap boundaries show a drift to larger MCD CO_2 ice column densities from the peak phase to the sublimation phase of both the North (regions G to A) and the South (regions C, E and F) polar caps. Such a trend may be related to non-uniform sublimation processes (enlarging ice-free areas embedded in icy terrains at several spatial scales), possibly yielding an increase of the areal mixing of terrains within the NOMAD footprint, leading to the concept of inner/outer crocus line (Schmidt et al., 2009). This is consistent with the spatially inhomogeneous sublimation known to take place in Mars seasonal caps (Piqueux et al., 2003; Schmidt et al., 2009; Cull et al., 2010; Hansen et al., 2013) and is also observed in OMEGA data during the sublimation phase of the North polar cap (region A, Figure 3.7C).

As a consequence, our boundary detection condition is close to the inner crocus line, that is, where the ice abundance is still large and its spatial distribution more homogenous. On the other hand, OMEGA boundaries (black and blue dots in Figure 3.7C) are consistently located at latitudes lower than those pertaining to the Ice Index and SAM estimated ones and, hence, closer to the outer crocus line.

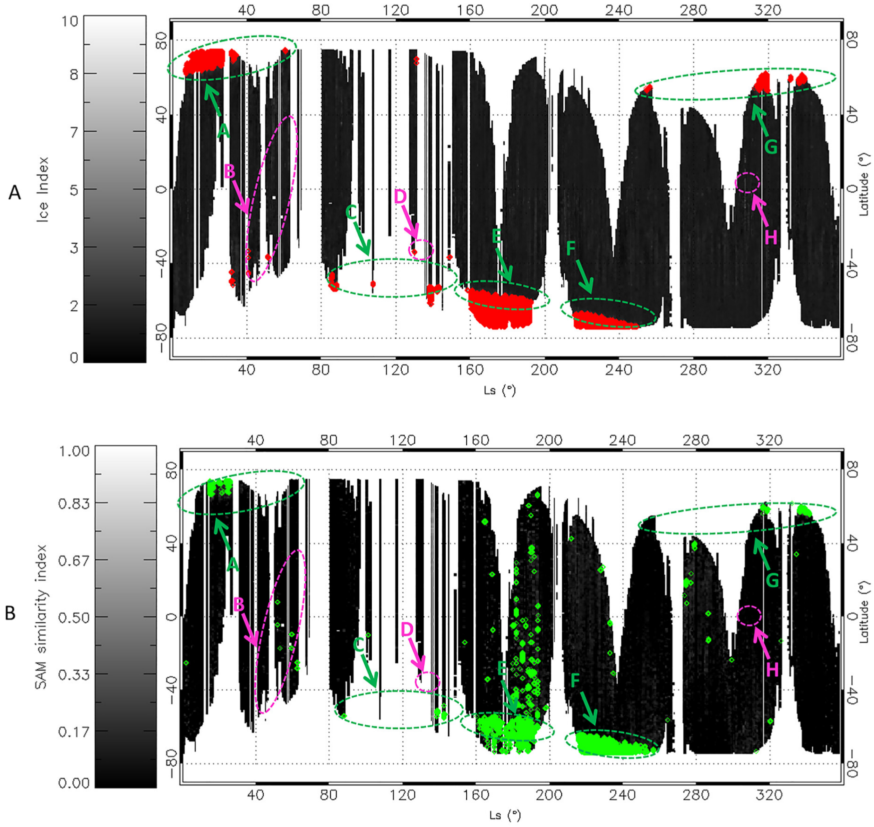

Continued on the next page.

C

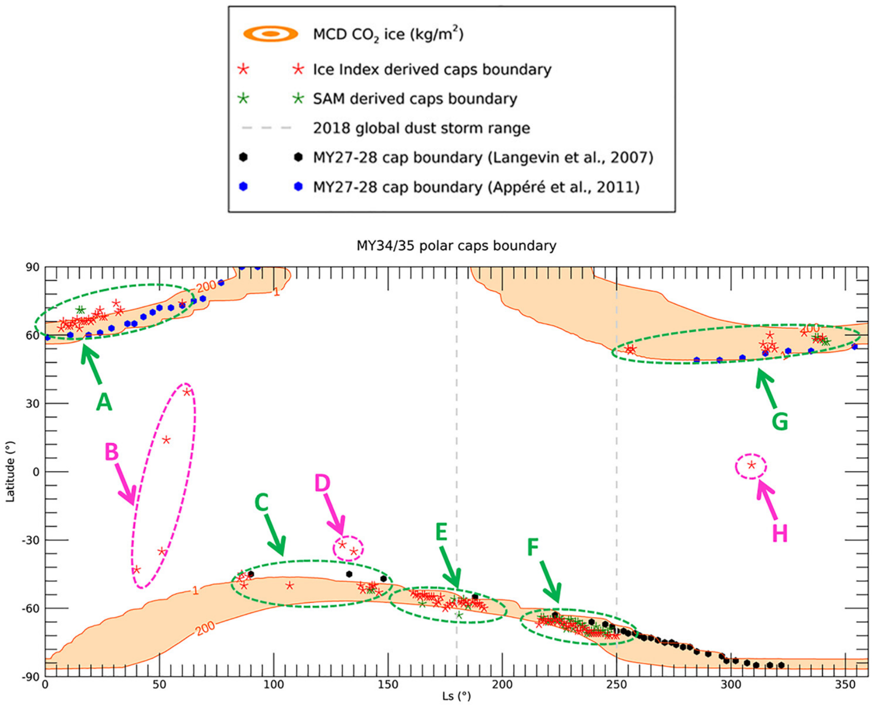

Continued on the next page.

D

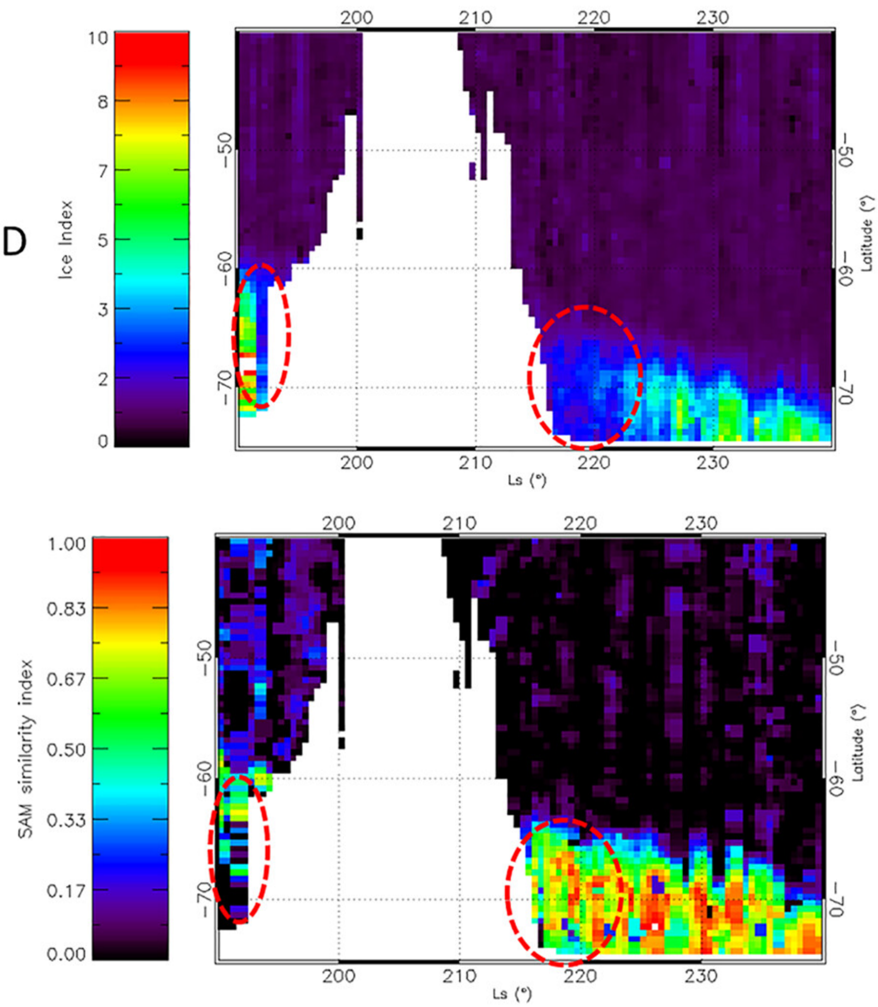

Continued on the next page.

Figure 3.7: In all panels, L_S between 0° and 150° refer to MY35, while L_S between 150° and 360° are related to MY34. Panels (A and B) Ice Index (A) and Spectral Angle Mapper (SAM) χ (B) maps where red and green points indicate regions with Ice Index >2 and SAM index χ >0.2 respectively (see Section 3.4.1 and Section 3.4.2). Colored labeled arrows indicate structures of interest identified in panel (C), on the polar caps (green) and at mid-latitudes (magenta, Section 3.5.1). Panel (C) red and green stars indicate the polar caps boundaries estimated through Ice Index and SAM similarity index χ respectively (Section 3.5). These are compared to the MCD simulated abundances of CO_2 ice corresponding to the observed cap boundaries positions (orange regions, representing surface column mass densities in kg/m^2) and to OMEGA observations (black and blue dots for the South and North poles respectively) from MY27-28 (Langevin et al., 2007; Appéré et al., 2011). The dashed gray lines indicate the 2018 global dust storm L_S range. Panel (D) comparison of the South polar cap in the Ice Index and SAM χ index maps within the storm L_S range. The red dashed circles indicate regions in which the dust storm strongly impacts the Ice Index value.

The data we are considering also partially cover the evolution of the 2018 global dust storm (vertical dashed gray lines in Figure 3.7C), from its maturation (L_S ~180°-190°) to its decay phase (L_S ~203°-250°, Smith and Guzewich (2019); Viúdez-Moreiras et al. (2019)). Figure 3.7D compares the Ice Index (left) and SAM (right) maps from Figures 3.4A and 3.4B zooming them within the storm L_S range, and shows how the two parameters behave across the storm at the Southern pole. While there is a gap of observations during the peak phase, the impact of the storm on the Ice Index map around L_S ~220° can be seen (dashed red circle). In this region, its value decreases significantly, while the same does not happen in the SAM similarity index map. A similar behavior is observed at L_S ~190°, during the storm peak phase, where the Ice Index experiences a sudden drop just before the observation gap. This is as expected, as demonstrated in Section 3.4.3, since the strength of the 2.7 μm band makes it strongly sensitive to the presence of dust, unlike the 2.35 μm absorption band which is weaker (Figure 3.6). Despite this drop in the Ice Index, the parameter successfully identifies the ice in the polar cap at those solar longitudes (Figures 3.7A and 3.7C). Unfortunately, the gap in observations prevents us from verifying if the Ice Index fails in spotting the ice when a very high dust optical depth is reached during the storm peak phase. Under the same assumptions made in Section 3.4.3 for the modeling of dust, a decrease of the Ice

Index as that observed in the highlighted regions in Figure 3.7D (about 50% with respect to the surrounding regions in the Southern polar cap) would indicate a dust optical depth τ_2 ~0.5. Such an approach indicates that an estimation of the dust abundance through the Ice Index is in principle possible (see Section 3.4.3). However, in order to be quantitatively feasible, this would require a dedicated radiative transfer analysis of both surface ice and airborne dust distribution and microphysical properties that is beyond the scope of this paper.

Some isolated ice detections from the Ice Index map appear in non-polar regions and are identified in magenta in Figure 3.7C. These detections cover latitudes between 40°S and 40°N in regions B and D and even approach the equator in region H. A faint 2.35 μm absorption band is recognizable in all these observations (Figure 3.8), confirming the presence of CO_2 ice. The discussion of these cases is presented in the following Section 3.5.1.

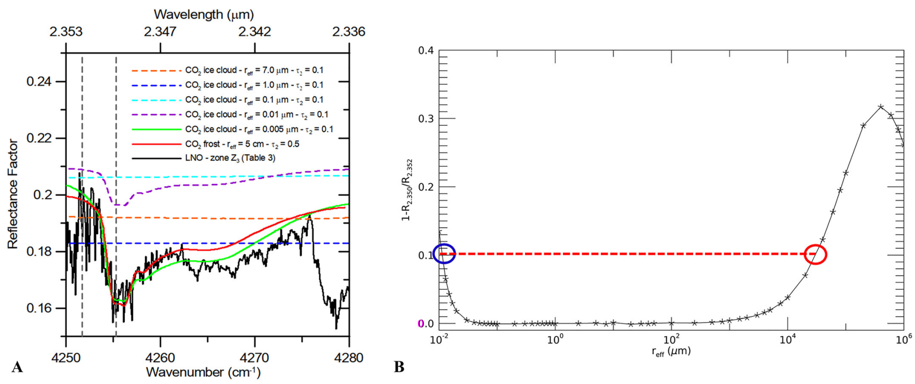

Figure 3.8: (A) Example of CO_2 ice spectrum from region Z_3 in Table 3.4, showing the 2.35 μm CO_2 ice band (solid black line) compared with CO_2 ice clouds simulations (Section 3.3.2) with different grain sizes (orange, blue, cyan, purple dashed lines, and solid green line and for r_{eff} = 7, 1, 0.1, 0.01, and 0.005 μm respectively, τ_2 is the optical depth at 2 μm). A 5 cm surface CO_2 ice simulation is also shown (solid red line). Vertical dashed gray lines indicate the wavelengths adopted to quantify the left shoulder slope of the 2.35 μm band as 1-$R_{2.35}/R_{2.352}$ (R is the reflectance factor and the subscripts indicate the wavelength in μm). (B) Trend of 1-$R_{2.35}/R_{2.352}$ with the CO_2 ice effective radius, for a fixed optical depth τ_2 = 0.4. The red dashed line indicates the order of magnitude of the slope values measured in the observed spectra (about 10%), in agreement with the synthetic ones in the 1-10 nm and 1-10 cm size regimes (blue and red circles respectively).

3.5.1 Non-Polar Ice Detections

Non-polar CO_2 ice zone	Observation date (yy/mm/dd)	Lon (°)	Lat (°)	L_S (°)	LST (h)	T (K)
B_1	2019/06/19	-42.3	-46.2	41.5	10.5	190
B_2	2019/07/11	-157.1	-37.8	51.3	15.8	206
B_3	2019/07/14	-164.8	15.9	52.7	16.3	243
B_4	2019/08/02	164.8	33.8	60.8	12.8	277
D_1	2020/01/05	134.3	-27.6	131.1	15.2	239
D_2	2020/01/17	12.09	-31.6	136.7	12.8	249
H	2018/12/21	-95.1	4.3	310.1	14.2	281
Z_1	2018/04/21	90.9	54.8	163.1	9.5	230
Z_2	2018/05/25	103.6	-31.8	181.9	14.7	274
Z_3	2018/06/14	82.9	-26.8	193.1	10.4	261

Table 3.4: Dates, Longitudes (Lon), Latitudes (Lat), Solar Longitudes (L_S), Local Solar Times (LST), and MCD estimated surface temperatures (T) of the non-polar CO_2 ice detections identified from regions B, D, and H in Figure 3.7C and from the SAM map (Figure 3.7B) green bins analysis (Zones Z, Section 3.5.1).

As shown in Figures 3.7A and 3.7B, some high values of Ice index and SAM χ index are found not only at the polar caps but also in bins at lower latitudes. Most of these detections (some of which are false positives due to poor SNR in the longitudinal averages, in particular in the SAM map in the range $180° < L_S < 200°$, see Section 3.4.2) are filtered out by the condition we adopted for the identification of the cap boundaries, described in Section 3.5. However, some of those related to the Ice Index still appear in Figure 3.7C (magenta regions). The presence of ice in longitudinal averages at these latitudes cannot easily be explained, but the analysis of the distribution of the individual spectra averaged within those bins reveals that these detections are driven by single pixel occurrences of icy spectra. These individual spectra of LNO order 189 all show the 2.35 μm absorption band confirming the identification of CO_2 ice in these regions (zones B-H in Table 3.4). Given this finding, we similarly scan the single pixel observations falling in the bins highlighted in green in Figure 3.7B and find other observations at mid-low latitudes in which the CO_2 ice signature can be clearly identified (Figure 3.8A, zones Z in Table 3.4). Of course, with such an approach we could actually be missing other observations in which the ice signature is present, since the method described in this paper is mostly effective for spatially extended and abundant ice deposits where the ice signature is strong (Sections 3.2.3, 3.4.1 and 3.4.2). Since the ice filling factor in these pixels is not known it is not possible to estimate the spatial extension of these ice deposits within the LNO footprint (Table 3.2).

Although water ice surface deposits are known to exist at mid-latitudes (Carrozzo et al., 2009), in principle the surface temperatures pertaining to these observations are too high to trigger CO_2 ice condensation (Table 3.4). Nevertheless, small CO_2 ice patches are known to exist at mid-low latitudes, in particular in steep craters' rims with pole-facing slopes where shadows could preserve colder temperatures even during daytime (Vincendon et al., 2010b; Vincendon, 2015). Another possible explanation for our detections is that residual night-time frost (Piqueux et al., 2016; Khuller et al., 2021) is being observed for some time after sunrise. However, the local times of our detections concentrate within about 3-4 hr around noon, and the predicted surface temperatures are always higher than 190 K, way beyond the CO_2 frost point. For the above reasons, we also investigate the possibility that our detections are related to atmospheric ice condensing at high altitude. LNO pixels' footprint is quite large (0.5×17.5 km^2, Table 3.2) and, hence, makes it difficult to verify if these observations are related to small ice patches in mixed terrains (see also Sections 3.2.3 and 3.4.1) or to clouds. CO_2 ice clouds are known to form in low temperature pockets at mesospheric altitudes, composed of populations of coarse grains as large as 7 μm (Clancy et al., 2019), as well as micron (about 1 μm) and sub-micron (about 0.1 μm) particles (Montmessin et al., 2006; Montmessin et al., 2007; Aoki et al., 2018). The optical depth reported in literature is typically rather low (less than 0.5). On the other hand, frost grains expected size range varies from a few μm to some mm (Kieffer et al., 2000; Titus et al., 2001; Vincendon, 2015). Since the depth and shape of the 2.35 μm band are driven by the ice microphysics, a grain size analysis can be a useful way to test the interpretation of NOMAD mid-latitude ice detections as either frost on the surface or CO_2 ice clouds. For the sizes pertaining to the clouds regime, we perform radiative transfer simulations with the MITRA tool (Section 3.3.2), varying the optical thickness of the CO_2 ice clouds in order to obtain a radiometric signal and a 2.35 μm absorption band that are comparable to those of the observed spectra. As we can see in Figure 3.8A, where the synthetic spectra are compared to the observation from zone Z_3 in Table 3.4, all grain sizes in the range 0.1-7 μm do not yield any significant absorption at 2.35 μm (dashed orange, blue and cyan lines). The band depth increases for smaller grains, such as nanometer-sized particles (order of magnitude 1-10 nm, dashed purple and solid green lines).

In this small-size range, a good match with the observation in Figure 3.8A is obtained with a cloud with r_{eff} = 5 nm. However, a similar spectral shape can also be obtained with larger sizes pertaining to the surface ice regime (5 cm ice size, solid red line, obtained through the SNICAR tool, see Section 3.3.1). As reference, we verify that sizes this large (>1 cm) are needed in order to match the signal and the band shape of spectra related to the bulk of the South polar cap.

This dichotomy is verified in Figure 3.8B, showing the trend of the 2.35 μm band depth (that for simplicity we compute as 1-$R_{2.35}/R_{2.352}$, where R is the reflectance factor and the subscripts indicate the wavelength in microns) with very large variations of the CO_2 ice effective radius. In this computation, we span from sizes comparable or smaller to those expected for CO_2 ice clouds to sizes pertaining to the surface ice regime, up to slabs as large as 100 cm, always keeping constant the optical depth at $\tau_2 = 0.4$. From the figure it is evident how for sizes between approximately 100 nm and 1 mm the 2.35 μm band is practically absent. Instead, for both r_{eff} <100 nm and r_{eff} >1 mm the band depth increases. While the band depth increase for large sizes is ascribable to the increasing interaction of the light with the particle volume, the behavior for nanometric sizes is typical of the Rayleigh regime (i.e., when the size parameter $2\pi r/\lambda << 1$, where r is the particle size and λ is the wavelength), where the absorption tends to progressively dominate the scattering with the decreasing sizes (Van De Hulst, 1981). Consistently with Figure 3.8A, two dimension regimes yield a band depth that is comparable to that of the observed spectra (order of magnitude 10% in all detections, red dashed line in Figure 3.8B), namely 1-10 nm and 1-10 cm.

As said above, the latter regime is consistent with extended and abundant surface ice deposits (Langevin et al., 2007; Andrieu et al., 2018) and, hence, pertains to particles larger than those expected for diurnal CO_2 frost (about 1-103 μm, Kieffer et al. (2000); Titus et al. (2001); Vincendon (2015)). For this reason, and taking into account the considered local times and surface temperatures (Table 3.4), we discuss if the size range 1-10 nm is preferable to describe the mid-latitude observations. This regime is compatible with diurnal high altitude (about 100 km) CO_2 ice clouds with grains smaller than 100 nm (Montmessin et al., 2006), higher in the atmosphere with respect to the expected larger ones (0.1-7 μm, Montmessin et al. (2007); Aoki et al. (2018); Clancy et al.

(2019)), and to which the 2.35 μm absorption band appears to be particularly sensitive, as demonstrated through our grains size investigation (Figure 3.8).

Under the clouds hypothesis, all detections B and D (Table 3.4) are seasonally compatible with CRISM (MY 29-33) and OMEGA (MY 28-30) CO_2 ice clouds detections (Figure 14 in Clancy et al. (2019); Figure 8 in Vincendon et al. (2011)) in the L_S ranges 40°-62° and 130°-135° respectively. In particular, detections D are also latitudinally consistent with MY27 detections from Montmessin et al. (2006) observed at L_S $\sim$135° and latitudes $\sim -35°$ by the SPICAM instrument aboard Mars Express. Under the frost hypothesis, on the other hand, no matches of our detections have been found with the seasonal and spatial estimates from other authors (e.g., Vincendon (2015); and Figure 3 in Vincendon et al. (2010b)).

By performing the analysis described above to all detections in Table 3.4, we obtain the order of magnitude of the grains size and optical depth of the ice under the hypotheses that it is either pure frost on the surface or condensed in high altitude clouds. Taking into account the ice clouds hypothesis, we find grain sizes between 5 and 10 nm with optical depths in the range 0.1-0.3. Instead, under the hypothesis that those detections are related to surface CO_2 frost, we find sizes in the range 1-10 cm with optical depths between 0.1 and 1.0.

Of course, the analysis described above cannot be considered as a quantitative retrieval of physical quantities but, as already stressed, provides an estimate of their order of magnitude. A more quantitative approach should rely on a number of assumptions that are still not well assessed, like the detailed instrumental response (e.g., AOTF and blaze functions, see Sections 3.2.2 and 3.3), the effect of non-icy contaminants in the footprint, as well as uncertainties related to the spectral surface albedo or dust content. All these can easily affect the overall signal. For this reason, as a first stage we favored a qualitative approach, based on the statistical behavior of the spectral data set so far available, and trying to highlight that its information content about ice can be significant, although quite far from the main purposes which the instrument was devoted to.

Given the above discussion, we suggest that mid-latitudes ice detections are more likely to be ascribed to clouds than to surface frost for context reasons and band depth estimates, resulting in the first detection of clouds through the study of the CO_2 ice 2.35 μm absorption band. Nevertheless, a more conclusive discrimination between the two hypothesis is only achievable through a more comprehensive radiative transfer analysis of the 2.35 μm band as well as other spectral features, whose study is clearly beyond the scope of this paper and will be the subject of a future work (Section 3.6). Nevertheless, this analysis demonstrates that the 2.35 μm band, sampled by LNO order 189, has large potential to be exploited for the estimation of the grain size and optical depth of CO_2 ice.

3.6 Conclusions and Future Work

In this work we explored NOMAD-LNO information content of orders 169, 189, and 190 (Table 3.3) demonstrating that, although its main focus is on atmospheric gases, this data set can be exploited for the investigation of surface ice. Taking advantage of orders 169 and 190, partially covering the 2.7 μm band, we defined an index for the identification of abundant CO_2 and H_2O ices deposits (Ice Index, Section 3.4.1). We produced seasonal maps of the ice coverage that are in general in good agreement with MCD global climate model and with OMEGA data (Section 3.5), during both the peak and the sublimation phases of the polar caps. A seasonal map of the exposed CO_2 ice was obtained using the 2.35 μm absorption band, which is well covered by LNO order 189 (Section 3.4.2). While the observed spectral features can only probe the first centimeters of ice deposits and hence cannot fully correlate with the total ice column predicted by global climate models, a meaningful comparison between observations and models has been achieved through an analysis of the average latitudinal extension of the polar caps and their seasonal variations. We verified that, while such an approach can be reliably used for the identification of abundant and spatially extended ice deposits, related to the inner crocus line (Section 3.5), it is not fully reliable in those transitional regions where icy to non-icy terrains are strongly spatially mixed (taking also into account the relatively large NOMAD footprint).

We also investigated the impact of the 2018 global dust storm on the ice detection in the Southern polar cap during the spring season. In this case, the high concentration of dust in the atmosphere reduces the number of solar photons reaching the surface and thus back to the NOMAD detector, affecting the capability to spot the surface ice through the Ice Index investigation. On the other hand, we verified that the SAM algorithm is less affected by the presence of dust, making it a robust tool for the detection of spatially homogeneous and abundant CO_2 ice deposits (Sections 3.4.3 and 3.5).

Through our analysis, CO_2 ice detections were also found at mid-equatorial latitudes, away from the polar regions. CO_2 ice has already been detected at these latitudes both as surface ice/frost and high altitude clouds, and the discrimination of these conditions is not easy in nadir-looking spectra.

While CO_2 surface ice is known to exist at these latitudes in pole facing slopes remaining in shadow during daytime (Vincendon et al., 2010b; Vincendon, 2015) or as residual night-time frost in the early morning (Piqueux et al., 2016; Khuller et al., 2021), given the high temperatures and local times pertaining to these observations we also investigated the possibility that they are instead related to CO_2 ice clouds. Through a grain size analysis (Section 3.5.1) we verified that two size regimes can reproduce the observations, namely 1-10 nm and 1-10 cm (see Section 3.5.1). The latter regime is too large for both the frost and the CO_2 ice clouds hypotheses, while the 1-10 nm regime is compatible with fine grains in CO_2 ice clouds condensing higher in the atmosphere (Montmessin et al., 2006) with respect to the larger dimension regimes of micron (1-7 μm) and sub-micron (0.1 μm) particles. Given the above considerations, the clouds hypothesis results to be preferable and would imply the first detection of CO_2 ice clouds through the 2.35 μm absorption band analysis. This investigation demonstrates how LNO order 189 has large potential to be exploited to retrieve CO_2 ice microphysical properties. Moreover, this sets the basis for an in-depth investigation of the band also in other datasets, like OMEGA and CRISM ones, even if characterized by a lower spectral resolution.

The analysis presented in this paper sheds some light on the possibility of conducting surface and aerosol science using a data set that is nominally conceived for the study of Martian trace gases, such that of NOMAD-LNO, and opens the way for several follow up studies. An analysis of NOMAD UVIS channel information content, focused again on surface studies, is currently being performed as a continuation for the study presented in this paper. A dedicated quantitative radiative transfer analysis for the retrieval of surface ice microphysical and geometrical properties such as grains size, mass density and layers thickness, is already in progress and is the subject for a future paper. Moreover, an investigation focused on ice clouds detection is also being performed. Finally, an in depth radiative transfer analysis of the 2.35 μm feature in CO_2 ice clouds spectra is planned.

Chapter 4

Observation of the Southern Polar cap during MY34-36 with ExoMars-TGO NOMAD-LNO

This chapter was published in the Icarus Journal in the frame of the Special Issue "Ices in the Solar System; origin, evolution and distribution"(Ruiz Lozano et al., 2023)[1], and can be found from Section 4.1. I led the research conceptualisation, model development and validation, formal analysis, visualisation of results, and the writing and revisions of the manuscript.

In Chapter 3, we show that NOMAD is suitable for studying surface ice using orders 169, 190 (Ice Index, see Section 3.4.1) and surface CO_2 ice with order 189 (SAM χ index, see Section 3.4.2). We analyse the global ice cover in the polar regions through latitudinal-seasonal ice maps for the Martian Years 34 and 35. In addition, we investigate how suspended dust affects the Ice Index and SAM χ index during the MY34 global dust storm. Nevertheless, the effects of the MY34 global dust storm on the seasonal processes of the polar ice caps are not studied

[1] **Ruiz Lozano, L.**, Oliva, F., Karatekin, Ö., Bellucci, G., Dehant, V., D'Aversa, E., Carrozzo, F. G., Schmidt, F., Cruz Mermy, G., Thomas, I. R., Vandaele, A. C., Daerden, F., Ristic, B., Patel, M. R. and López Moreno, J. J. (2023). Observation of the Southern Polar cap during MY34-36 with ExoMars-TGO NOMAD-LNO. *Icarus*, `https://doi.org/10.1016/j.icarus.2023.115698`.

due to the limited temporal coverage of the data set at the time of this study (only one full Martian year).

We hence address the issue in this chapter by comparing the sublimation process of the Southern polar cap[2] for MY34-36 in order to observe potential interannual changes (see Section 4.5). To do this, we update the Ice Index (orders 169 and 190) by adding orders 167 and 168 in order to improve the temporal coverage. We here define the New Ice Index (orders 167, 168, 169 and 190) (see Section 4.4.1). Acquisitions through the orders are based on a pre-selection process. Their frequency of observation can change. The use of orders 167 and 168 increased in MY35-36, showing interesting spatial and temporal coverage for this study. In Chapter 3, order 189 (2.35 μm) is presented as the only candidate for CO_2 ice identification. Nevertheless, over the MY35-36 period, order 193 (2.29 μm) is widely used. Unlike order 189 (see Figure 3.5 in Chapter 3), order 193 presents a central CO_2 ice absorption band, which is less affected by instrumental effects (see Section 2.2.3). We hence opt for order 193 and define a new spectral index for CO_2 ice detection (see Section 4.4.2). Table 4.1 lists the selected orders and indices defined in this chapter with their relevant sections.

Spectral method	**Orders**	**Wavelength**	**Interest**	**Information**
New Ice Index	167, 168, 169 and 190	2.7 μm	CO_2 ice and H_2O ice	Section 4.4.1
BD2292	193	2.29 μm	CO_2 ice	Section 4.4.2

Table 4.1: Overview of the spectral indices defined in this chapter: selected orders, ice absorption band, main interest and corresponding section for more details.

The second objective of this chapter is the study of the microphysical properties of surface CO_2 ice through order 193. We adopt a semi-qualitative approach to reproduce the 2.29 μm CO_2 absorption band by using the Planetary Spectrum Generator (PSG) model (Villanueva et al., 2018) associated with an online interface (see Section 4.5.3). We attempt to estimate the equivalent grain size, which is defined as the free mean path of photons within the CO_2 ice, i.e. the mean distance

[2]The Southern polar cap has better spatial and temporal coverage in the NOMAD-LNO dataset than the Northern polar cap.

between interfaces (Langevin et al., 2007). This is defined as the thickness of the upper layers of ice slabs in the PSG model (see Section 4.5.3).

We obtain an equivalent grain size in the centimetre range for selected spectra (5) over the Southern polar cap (with a strong CO_2 signature and low illumination angles, see Table 4.2). These results are in good agreement with the order of magnitude of previous studies, i.e. Calvin and Martin (1994); Kieffer et al. (2000); Langevin et al. (2007); Brown et al. (2010); Andrieu et al. (2018). All of these studies, except Calvin and Martin (1994), define the seasonal Southern polar cap as a CO_2 ice slab and estimate the equivalent grain size of the upper layer. Calvin and Martin (1994) interpret CO_2 ice as granular, estimating the diameter of spherical grain. Nevertheless, they obtain grain size values in the centimetre range, suggesting that the slab model is the most appropriate. Regarding Kieffer et al. (2000), Langevin et al. (2007) and Brown et al. (2010), they use a spectral classification based on albedo value and relative band strength of the CO_2 ice feature observed on mosaic maps. They estimate a minimum (Kieffer et al., 2000; Brown et al., 2010) and a mean (Langevin et al., 2007) equivalent grain size value for different periods of time. On the other hand, Andrieu et al. (2018) estimate equivalent grain sizes in the same location (latitude 72°S) for the full sublimation phase. The difference in the classification method and the selected location between our study (see Section 4.5.3) and these previous works may explain the different values in Table 4.2.

In Chapter 3, we compute the CO_2 ice surface spectral albedo using the SNICAR model (see Section 3.3.1) and the MITRA radiative transfer tool for the atmospheric constraints (see Section 3.3.2). These models are based on libraries and several modules to be installed locally. In this chapter, we choose the PSG model for convenience. It is easily accessible via a web interface, combining a radiative transfer model with the option of choosing a surface model. We did not use it in Chapters 3 and 6 because it was not fully available online at the time of these works.

As mentioned in Chapter 3, an in-depth radiative transfer analysis of CO_2 ice signature is still planned (using both orders 189 and 193). This will complement the results in Table 4.2. In addition, it will provide additional information on the microphysical properties of CO_2 ice clouds discussed in Section 3.5.1 of Chapter 3.

Contents lists available at ScienceDirect

Icarus

journal homepage: www.elsevier.com/locate/icarus

ELSEVIER

ICARUS

Observation of the Southern Polar cap during MY34-36 with ExoMars-TGO NOMAD LNO

L. Ruiz Lozano [a,b,*], F. Oliva [c], Ö. Karatekin [a], G. Bellucci [c], V. Dehant [a,b], E. D'Aversa [c], F.G. Carrozzo [c], F. Schmidt [d,e], G. Cruz Mermy [d], I.R. Thomas [f], A.C. Vandaele [f], F. Daerden [f], B. Ristic [f], M.R. Patel [g], J.-J. López-Moreno [h]

[a] *Royal Observatory of Belgium (ROB-ORB), B-1180 Brussels, Belgium*
[b] *Earth and Life Institute, Secteur des Sciences et Technologies, Université Catholique de Louvain (UCLouvain), 3, Place Louis Pasteur/L4.03.08, B-1348 Louvain-la-Neuve, Belgium*
[c] *Istituto di Astrofisica e Planetologia Spaziali (IAPS-INAF), 00133 Rome, Italy*
[d] *Université Paris-Saclay, CNRS, GEOPS, Orsay, France*
[e] *Institut Universitaire de, France*
[f] *Royal Belgian Institute for Space Aeronomy (BIRA-IASB), B-1180 Brussels, Belgium*
[g] *School of Physical Sciences, The Open University (OU), Milton Keynes MK7 6AA, UK*
[h] *Instituto de Astrofísica de Andalucía (IAA), Consejo Superior de Investigaciones Científicas (CSIC), 18008 Granada, Spain*

4.1 Introduction

Historically, the Martian polar caps have been observed from Earth for more than a century (ground based observations and documentations reported in Fischbacher et al. (1969); Dollfus (1973); Iwasaki et al. (1986); James et al. (1987, 1990); Benson and James (2005)) and, in 1969, NASA Mariner 6 and 7 spacecrafts directly observed the recession of the Southern polar cap. For the first time, the twin satellites identified CO_2 ice as its major component (Herr and Pimental, 1969). In the late 1970s, the Viking landers made the first efforts in measuring the pressure variations on the surface of Mars during a whole Martian Year (MY). These variations, estimated to be over 25%, were found to be directly linked to the atmospheric CO_2 cycle (Hess et al., 1979, 1980). Indeed, the Martian atmosphere is strongly controlled by the seasonal changes in the polar cap deposits, resulting from the sublimation and condensation processes of CO_2 (Kieffer, 1979). These CO_2 exchanges between the atmospheric layers and the solid planet alter the atmospheric angular momentum (Karatekin et al., 2011) and impacts even the rotation of the solid planet at seasonal time scales (up to 0.4 milliseconds in Length-of-Day, Cazenave and Balmino (1981); Defraigne et al. (2000); Van den Acker et al. (2002); Karatekin et al. (2006); Konopliv et al. (2011)). Therefore, observing the seasonal and interannual variabilities of CO_2 ices on the Martian surface is important for understanding the CO_2 cycle, which drives the current atmospheric dynamics in close connection with water and dust cycles (Karatekin et al., 2005, 2011; Dehant et al., 2020). The variability of Martian atmospheric dynamics provides insight into the planet's global atmosphere and its long-term evolution (Lange et al., 2022).

Several orbiter missions have deeply analysed the Martian CO_2 ice in different spectral ranges: Mars Global Surveyor TES (Christensen et al., 2001), Mars Odyssey THEMIS (Christensen et al., 2004), Mars Express OMEGA (Bibring et al., 2004b) and PFS (Formisano et al., 2005) spectrometers and the Mars Reconnaissance Orbiter CRISM (Murchie et al., 2007) and MARCI instruments (Bell et al., 2009). Spectrally active in the infrared spectral range, CO_2 ice has been observed at the poles (Kieffer et al., 2000; Titus and Kieffer, 2002; Langevin et al., 2007; Pelkey et al., 2007; Appéré et al., 2011; Brown et al., 2010, 2014; Schmidt et al., 2009, 2010), and also as ice clouds in the mesosphere (at altitudes above 50 km) at equatorial latitudes (Formisano et al., 2006; Montmessin et al., 2006; Montmessin et al., 2007; Clancy et al., 2007; Määttänen et al., 2010; Vincendon et al., 2011; Liuzzi et al., 2021). Moreover, using this spectral range allowed to distinguish CO_2 and H_2O ices as they present different IR spectral signatures (Bibring et al., 2005). On the other hand, forward models (Singh and Flanner, 2016) and radiative transfer models of IR reflectance spectra (Hapke, 1981; Andrieu et al., 2018) provided information on the CO_2 ice microphysical properties, such as the grain size, the layer thickness and the icy mixture composition (Langevin et al., 2007; Brown et al., 2010, 2014; Appéré et al., 2011).

Since March 2018, ExoMars-Trace Gas Orbiter NOMAD, mainly designed for the study of trace gases, atmospheric aerosol abundances and Martian climatology (Neefs et al., 2015; Vandaele et al., 2015c, 2018; Thomas et al., 2016), has been providing IR observations of Mars at high spectral resolution. Oliva et al. (2022) demonstrated that the NOMAD nadir IR channel can also be exploited to study surface CO_2 ice. Using a semi-qualitative approach, they studied the respectively narrow and strong CO_2 ice absorption bands at 2.35 μm and 2.7 μm over MY34-35. They obtained CO_2 ice seasonal-latitudinal maps in good agreement with the Mars Climate Database v6.1 (MCD) predictions (Forget et al., 1999; Millour et al., 2018) and with the OMEGA spectrometer observations (Schmidt et al., 2009, 2010; Appéré et al., 2011). They hence opened a new possibility of surface science with NOMAD.

In direct continuation of Oliva et al. (2022), in this work, we further explore the NOMAD nadir data set information content by focusing the analysis on the Southern polar cap. Following a qualitative approach, we present an updated method based on the characterisation of the 2.7

μm ice absorption band in order to detect the presence of surface ice. We also analyse the seasonal and interannual changes of the Southern polar cap during 3 Martian Years. Nevertheless, this band is not suitable for the identification of CO_2 ice due to the overlapping signal of water ice. Therefore, we use the 2.29 μm absorption band for CO_2 ice detection and discuss the potential of this band for grain size retrieval.

We present in Section 4.2 and 4.3 a brief description of the NOMAD instrument and the nadir observations used in this study. Then, we describe the methodology and perform the analysis of NOMAD nadir data for MY34-36 in Section 4.4. Finally, the results are discussed and compared to previous studies in Section 4.5.

4.2 NOMAD instrument

The Nadir and Occultation for MArs Discovery (NOMAD) instrument is a suite of three high resolution spectrometers that was selected as part of the payload of the 2016 ExoMars Trace Gas Orbiter (TGO) mission. Led by the Royal Belgian Institute for Space Aeronomy (BIRA-IASB), NOMAD has been observing the Martian atmosphere since March 2018 ($L_S = 150°$ in MY34) through three channels, one operating in the ultraviolet-visible spectral range (UV-VIS) and the two others in the infrared (IR). A first spectrometer is devoted to solar occultation observations (SO channel). A second spectrometer is capable of performing nadir, limb, and solar occultation observations (LNO channel). Both spectrometers cover the near IR spectral range. On the other hand, a third spectrometer (UVIS channel) can work in the three observation modes covering the UV-VIS spectral range. A complete description of the instrument can be found in the following papers: (Neefs et al., 2015; Vandaele et al., 2015b,c; Thomas et al., 2016; Patel et al., 2017).

To study surface ice, we select the LNO channel providing nadir observations with a typical integration time of around 200 ms. This channel covers the 2.3-3.8 μm IR spectral range with a spectral resolution of 0.3 cm^{-1} (Liuzzi et al., 2019). From the TGO orbit, the LNO ground track footprint is defined as an elongated rectangle of 0.5 km by 17.5 km, allowing to map most of the surface of the planet every 30 sols (Thomas et al., 2016). The NOMAD-LNO spectrometer has the particularity of not observing the entire spectral range at once. The data are acquired in 22 cm^{-1} wide spectral windows. These small portions, (hereafter referred as spectral orders) represent specific diffraction orders of the diffraction grating. Each LNO observation can select a maximum number of 6 diffraction orders every 15 seconds, in order to ensure the best possible signal-to-noise ratio (SNR).

The selection of different orders is obtained by appropriately adjusting the frequency of the entrance Acousto-Optical Tunable Filter (AOTF) (Liuzzi et al., 2019) through an internal radio-frequency generator. As a result, the general shape of the LNO raw spectra is strongly affected by the AOTF transmission and by the spectral response of the grating, i.e., the Blaze function (defined by a sinc-squared function, Liuzzi et al. (2019)). On the other hand, the AOTF is characterised by a strong peak with several side-lobes, and can be represented by a combination of a sinc-squared function with a Gaussian curve (Liuzzi et al., 2019). Considering the secondary peaks in the AOTF curve, it is worth noting that photons incoming from outside the selected spectral range can fall on the grating. An unexpected signal is hence summed with the expected spectral information and can become significant on the edges of each order (see Section 4.5.3).

For this work, we use spectrally and radiometrically calibrated LNO data converted into a reflectance factor. The reflectance factor R_λ is defined as the LNO radiance divided by the measured Solar irradiance at Mars and by the cosine of the solar zenith angle (SZA). Therefore, the LNO reflectance factor defined at wavelength λ can be written as

$$R_\lambda = \frac{1}{\cos SZA} \frac{\pi L_\lambda}{\phi_\lambda d_{Mars}^2} \tag{4.1}$$

where L_λ is the LNO measured spectral radiance (W m^{-2} sr^{-1} μm^{-1}), ϕ_λ is the Solar flux at 1 astronomical unit (au), d_{Mars} is the Sun-Mars distance in au, and finally SZA is the solar zenith angle. All details about the spectral and radiometric LNO calibration can be found in (Liuzzi et al., 2019; Cruz Mermy et al., 2022; Thomas et al., 2022a). It is important to note that the AOTF and Blaze modulations also propagate to the reflectance factor conversion in the form of low-frequency oscillations in the spectral continuum. For this reason, we exclude the reflectance factors at the outer parts of each spectral order in order to mitigate these oscillations (see Section 4.4 and 4.5.3).

Thomas et al. (2016) identified the instrumental thermal background as the main source of noise, limiting the integration times in order to avoid the saturation of the detector. As already mentioned, the 15 seconds period of observations is divided by the number of orders (maximum of 6). The SNR hence increases with fewer orders. Typically with LNO, two or three orders are measured in the same sequence of observations. The SNR generally takes values around 8-10. For the best scenario, i.e. when the SZA is around zero (when the Sun is directly overhead), the SNR is expected to be around 15-20. As a comparison, spectrometers dedicated for surface study, such as OMEGA and CRISM, present a SNR higher than 100 (Bibring et al., 2004b; Murchie et al., 2007).

4.3 Dataset

During an acquisition, NOMAD alternates observations according to orders planned several weeks in advance. The choice of orders depends on several factors, such as their main focus (i.e. different gas, dust, surface) and the limitations of the instrument (see Section 4.2 and Chapter 2). Moreover, the LNO channel has reduced instrument sensitivity at the wavelengths above 2.8 μm. This results in a low SNR. Therefore, not all orders are used with the same frequency of observation, making the available wavelength ranges highly dependent on such strategy. This affects the spatial and temporal coverage of the orders, i.e. the availability of the observations for this study.

As already described in Oliva et al. (2022), CO_2 ice exhibits several features in the LNO spectral range, which are covered by different orders (see Figure 4.1). Top panel shows a simulated CO_2 ice albedo spectrum (in blue) using the Planetary Spectrum Generator (PSG) tool (see Section 4.5.3, Villanueva et al. (2018)), while the bottom panel gives its imaginary refractive index, describing the absorption coefficient in the LNO spectral range (Hansen, 2005). For comparison, both panels show H_2O ice spectra in the LNO spectral range (in black). Due to the low SNR, the CO_2 ice absorption bands above 2.8 μm in Figure 4.1 are poorly covered by NOMAD in MY34-36. Few observations are made, leading to limited surface coverage over the Southern polar cap. For these reasons, these wavelengths are not included in this work.

Regarding the 2.7 μm absorption band, the strongest in the LNO range, it is important to mention that water ice also presents spectral features at this wavelength (see bottom panel in Figure 4.1). Moreover, this band can easily be saturated, especially in the presence of a thick ice layer. As shown in top panel of Figure 4.1, orders 169 (2.612-2.632

μm), 168 (2.627-2.648 μm) and 167 (2.643-2.664 μm) cover the short-wavelength shoulder of the strong 2.7 μm ice absorption band. Order 169 has been already used in a spectral ratio with order 190 (2.323-2.341 μm) for surface ice detection (Ice Index; Oliva et al. (2022)). Indeed, as order 190 falls into the continuum range, these two orders allow an estimation of the intensity of the 2.7 μm band. Regarding orders 168 and 167, Ruiz Lozano et al. (2022) discussed their potential to be used for surface ice detection, but also for more transient phenomena such as ice clouds thanks to a particular combination of these orders.

On the other hand, Oliva et al. (2022) have already proven that the 2.35 μm absorption band, widely used for the LNO observations (order 189: 2.335-2.354 μm, see top panel in Figure 4.1), is never saturated and offers an interesting opportunity for the detection of CO_2 ice and the retrieval of its microphysical properties. In addition to the analysis of surface ice in the polar regions, they have discovered CO_2 ice signatures at low latitudes. After several considerations, the CO_2 ice clouds hypothesis is the most likely scenario.

Compared to (Oliva et al., 2022), the narrow band at 2.29 μm covered by order 193 (2.286-2.305 μm, see top panel in Figure 4.1) has been considerably used in MY35 and 36. This order turns it into a new candidate for the CO_2 ice study, given the high number of observations made and good instrument sensitivity.

Considering the different points listed above, we investigate, in this work, the information content of the LNO observations through orders 169, 168, 167 (the 2.7 μm ice absorption band) combined with order 190 (continuum part) and order 193 (the 2.29 μm CO_2 ice absorption band). The time coverage is over MY34-36, starting at $L_S = 150°$ in MY34 (start of the science phase, March 2018) to $L_S = 360°$ in MY36 (December 2022), for orders 169, 168, 167 and 190. On the other hand, order 193 covers only MY35-36 (March 2019 to December 2022), as there is no LNO observation with this order in MY34. We exclude LNO observations with a SZA larger than 75°, as the signal intensity reaching NOMAD is strongly affected by large illumination angles. Therefore, we remove SNRs below $\sim$8.

As we focus the analysis on the Southern polar cap, it is worth noting that the results should not be affected by the presence of the Polar Hood clouds. As they are composed of water ice (Benson et al., 2010; Wolff et al., 2019), only the 2.7 μm band would be suitable for their detection.

Nevertheless, their microphysical properties do not strongly influence the spectral absorption bands compared to the extensive, abundant and thick surface ice deposits that characterise the cap. Due to the low SNR of the instrument, the Ice Index is unable to detect them[3].

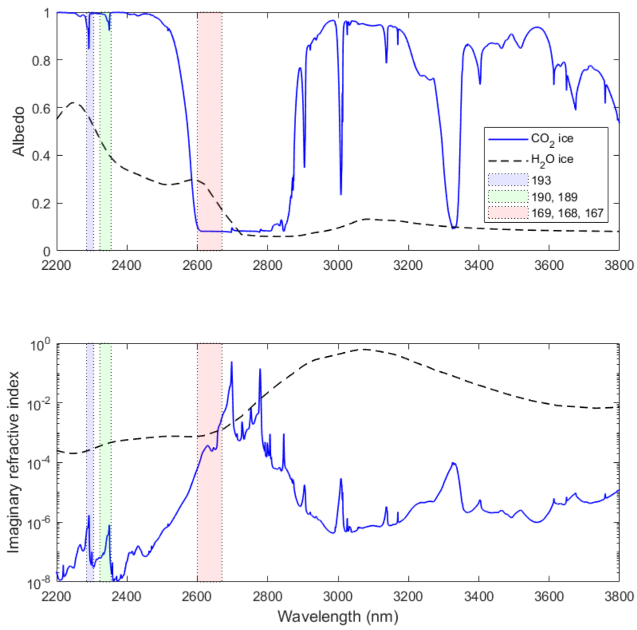

Figure 4.1: Top panel: simulated CO_2 ice (solid blue line; equivalent grain size of 10 mm, see Section 4.5.3) and H_2O ice (dashed black line, equivalent grain size of 0.3 mm) albedo spectra using the Planetary Spectrum Generator (PSG) tool (see Section 4.5.3, Villanueva et al. (2018)) over the LNO spectral range. The different orders mentioned in the text (orders 167, 168, 169, 189, 190 and 193) are highlighted in blue, green and red (see figure legend). Bottom panel: imaginary refractive index for CO_2 ice (Hansen, 2005) and H_2O ice (Warren and Brandt, 2008) describing the absorption coefficient over the LNO spectral range. Same legend as top panel.

[3] More details can be found in Chapter 6.

4.4 Methodology

4.4.1 Ice detection through the 2.7 μm absorption band

In this section, we focus the analysis on the short-wavelength shoulder of the 2.7 μm band. As already mentioned in Section 4.3, this band cannot be used to distinguish CO_2 ice from H_2O ice. Nevertheless, it can easily detect abundant surface ice deposits, as it has been proved with the Ice Index in Oliva et al. (2022) using a spectral ratio between orders 190 and 169. The number of nadir acquisitions using order 169 decreased significantly during MY35 and MY36. This hence affects the observation of the Southern polar cap. In order to take into account the best spatial and temporal coverage to build a seasonal map, we adapt the Ice Index by considering also the ratios between orders 167 and 168 and order 190. It is worth noting that, in nadir mode, the main source of variability in the reflectance factors comes from the surface albedo variations resulting from different Martian surface mineralogy absorptions (Christensen et al., 2001; Viviano et al., 2014; Riu et al., 2019b). Therefore, normalising the LNO reflectance factor to a Martian albedo allows to remove spatial albedo variations over the whole Martian surface. For each order, we define the LNO_{Norm} ratio (Ruiz Lozano et al., 2022) as R/TES, where R is the LNO reflectance factor value taken at the centre of the selected order (see Section 4.2), and TES is the MGS-TES bolometric Martian albedo (0.3 to 2.9 μm) (Christensen et al., 2001). Both R and TES are zonally averaged in each considered L_S-latitude bin of the selected order. Then, we compute the New Ice Index (NII) as

$$NII = \frac{1}{3}\left(\frac{LNO_{Norm}190}{LNO_{Norm}169} + \frac{LNO_{Norm}190}{LNO_{Norm}168} + \frac{LNO_{Norm}190}{LNO_{Norm}167}\right) \quad (4.2)$$

We apply the NII to the LNO data and construct a latitudinal-seasonal map in order to analyse the seasonal ice coverage (see Figure 4.2). LNO data are organised in terms of latitude (from 90°N to 90°S) and time (solar longitude, L_S) binned 1° by 1°. As we can see in Figure 4.2, high NII values are present at the highest probed latitudes. They represent the sublimation and condensation phases of the Northern polar cap (L_S ∼0°-25° in the middle and bottom panels, and L_S ∼310°-360° in the top panel respectively) (Cull et al., 2010; Brown et al., 2012; Hansen et al., 2013) and the sublimation phase of the Southern polar cap (L_S ∼150°-250° in the three panels) (Piqueux et al., 2003; Langevin et al., 2007; Schmidt et al., 2009, 2010; Brown et al., 2010, 2014; Oliva et al., 2022), better covered with respect to the North. For that reason, we focus the analysis on the South only (see Section 4.5). It is interesting to notice that MY34 covers the 2018 global dust storm from $L_S \sim 180°$ to 250° (Viúdez-Moreiras et al., 2019; Gillespie et al., 2020). As discussed in Oliva et al. (2022), high dust abundances occurring during a global dust storm reduce the 2.7 μm ice absorption band, impacting its effectiveness in the identification of the ice. Nevertheless, the NII is still able to detect the polar cap at the South pole during this period, as shown in Figure 4.2 (top panel, see also Section 4.5.1).

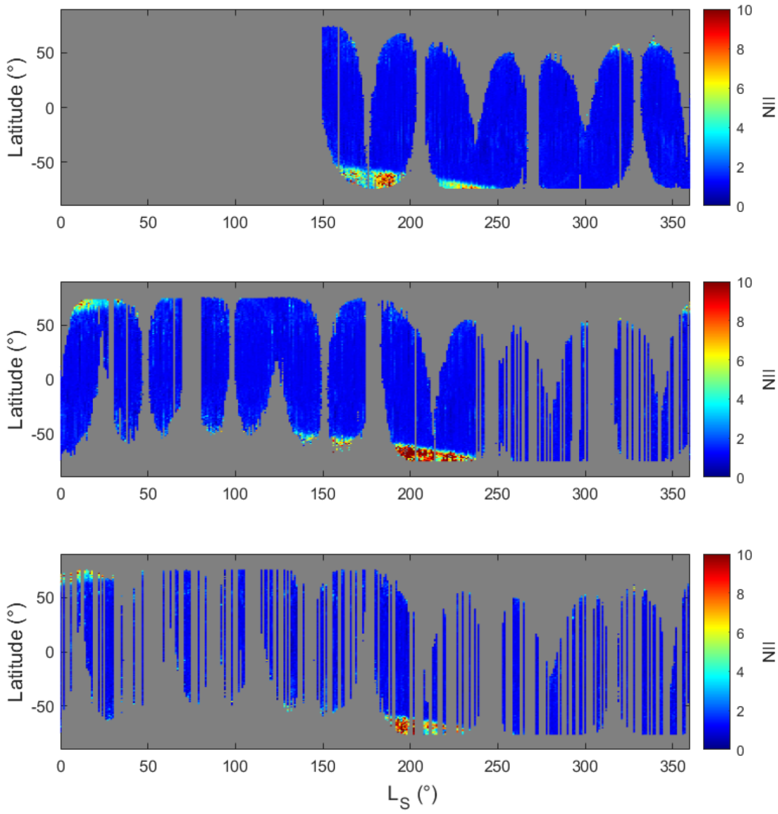

Figure 4.2: Latitudinal-seasonal map of NII binned 1° by 1°. Latitudes range from -90° to 90°. By definition, the highest NII values indicate the presence of surface ice. Top panel: LNO observations cover MY34, from L_S = 150° to 360°, with a SZA <75°. Middle panel: same for all MY35. Bottom panel: same for all MY36.

4.4.2 CO_2 ice detection through the 2.29 μm absorption band

In order to identify CO_2 ice, this section concerns the analysis of the 2.29 μm CO_2 ice absorption band, covered by order 193 (see Figure 4.3). Being the band centred in this order, it has the advantage of being less affected by instrumental response modulations, with respect to the 2.35 μm absorption band used in Oliva et al. (2022) (see Figure 4.1).

In order to study the 2.29 μm absorption band, we rely on a band depth analysis. The same approach already succeeded to identify the diversity of the Martian surface mineralogy (Bell et al., 2000; Murchie et al., 2000; Bibring et al., 2004a; Gendrin et al., 2005; Langevin et al., 2005a,b; Pelkey et al., 2007). Pelkey et al. (2007) already defined a band depth by selecting wavelength at 2.25 μm and 2.35 μm, and centred on the 2.29 μm CO_2 ice absorption band, but since NOMAD-LNO works with small spectral ranges, we here adapt the band depth computation. By keeping the same formulation as Pelkey et al. (2007), we select other wavelengths. Therefore, the 2.29 μm band depth (BD2292) is defined, in this work, as

$$BD2292 = 1 - \frac{R2292}{R2292^*} = \frac{R2292}{a \times R2288 + b \times R2296} \tag{4.3}$$

where $R2292$ is the LNO reflectance factor value at the centre of the band (2.292 μm) and $R2292^*$ is derived from the continuum fit across the band. $R2292^*$ is defined as $a \times R2288 + b \times R2296$, where $R2288$ and $R2296$ are the LNO reflectance factor values at the wavelengths 2.288 μm (left side of the band) and 2.296 μm (right side of the band) respectively, and finally $a = 1 - b$ and $b = (\lambda_{2292} - \lambda_{2288})/(\lambda_{2296} - \lambda_{2288})$ (see Figure 4.3).

It is worthwhile to mention that the adapted BD2292 is defined as a pseudo-band depth, since $R2288$ is not totally outside the absorption band. It can be seen as a proxy for CO_2 ice, which qualitatively estimates the CO_2 ice presence and abundance. In general, as shown in Figure 4.3 (bottom panel), band depth varies with the abundance of the absorbing component and its particle size (Clark and Roush, 1984; Langevin et al., 2007; Pelkey et al., 2007; Brown et al., 2010, 2014; Appéré et al., 2011).

On the other hand, dust and water ice impurities can also affect CO_2 ice spectra and hence, the BD2292 estimation (Pelkey et al., 2007;

Bernard-Michel et al., 2009; Andrieu et al., 2018). For that reason, we investigate the impurities effect in Figure 4.4 by using the PSG model (see Section 4.5.3). Globally, the increase in the H_2O ice amount tends to produce a decrease in the spectral albedo values, as H_2O ice presents a broadband absorption at these wavelengths (see Figure 4.1). It becomes significant at 2.296 μm by adding 20% of H_2O ice. Nevertheless, this variation is not as pronounced at 2.292 μm (see top panel in Figure 4.4). On the other hand, dust appears brighter in the IR spectral range. Increasing its percentage hence raises the spectral albedo values in order 193. This time, we observe most of the changes at 2.292 μm, reducing the band depth (see middle panel in Figure 4.4). Although the two aerosols have opposite effects on the CO_2 ice spectrum, by definition they affect the BD2292 estimation in the same way (see Equation 4.3). In conclusion, both significant amounts of H_2O ice or dust impurities will underestimate the BD2292 estimation (see bottom panel in Figure 4.4). In other words, they will conceal the CO_2 ice signature.

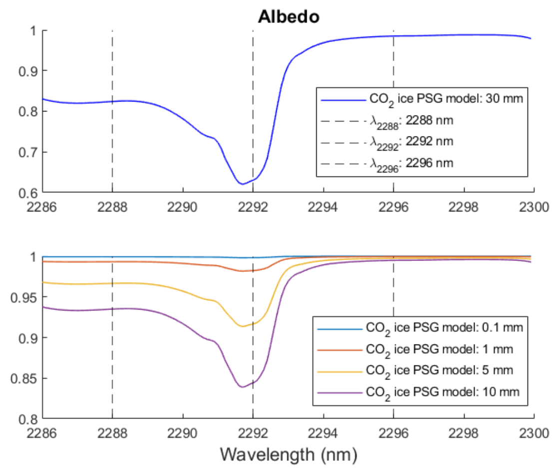

Figure 4.3: CO_2 ice albedo spectra simulated with PSG model for order 193. CO_2 ice absorption band is visible at 2292 nm. Vertical dashed lines indicate the selected wavelengths for BD2292. Top panel: CO_2 ice equivalent grain size of 30 mm. Bottom panel: Effect of the CO_2 ice equivalent grain size on the band depth assuming a value of 0.1 mm, 1 mm, 5 mm and 10 mm.

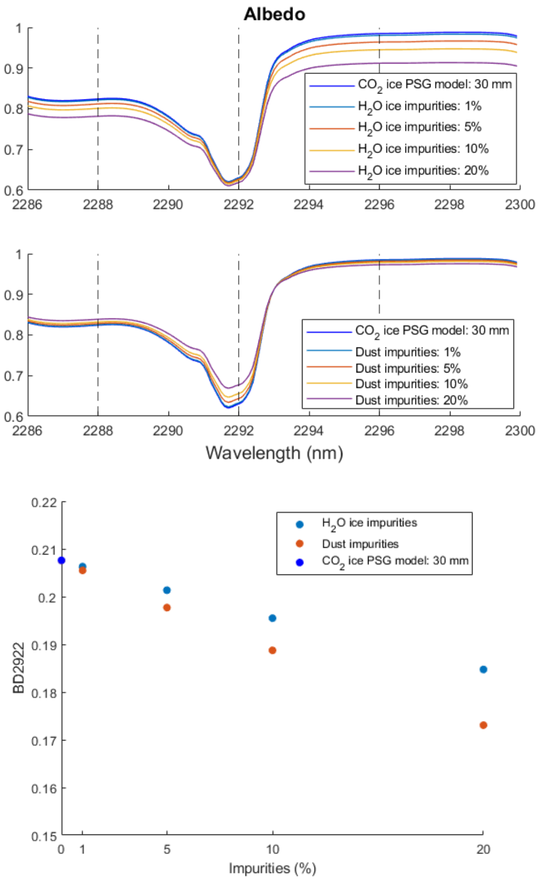

Figure 4.4: CO_2 ice albedo spectra simulated with PSG model for order 193. CO_2 ice absorption band is visible at 2292 nm. Vertical dashed lines indicate the selected wavelengths for BD2292. Top panel: effect of the H_2O ice contamination on the band depth assuming impurities of 1%, 5%, 10% and 20%. Middle panel: same with dust impurities. Bottom panel: effect of dust and H_2O ice impurities on the BD2292 estimation.

Similarly to Figure 4.2, we apply the BD2292 to the LNO data set and construct a CO_2 ice latitudinal-seasonal map in Figure 4.5 covering all MY35 and 36 (no LNO data in MY34, see Section 4.3). Although the spatial coverage is more limited than with NII (see Figure 4.2), BD2292 is able to detect the sublimation (L_S ∼30° to 30° in the North and L_S ∼150° to 250° in the South) and condensation (L_S ∼300° to 360° in the North) phases of the CO_2 ice polar deposits (Oliva et al., 2022). It is interesting to note the different range of BD2292 values between the Northern (starting at L_S 0°) and Southern (starting at L_S ∼150°) sublimation phases. Regarding the North Pole, it is extremely rare to find pure CO_2 ice during the recession. In fact, H_2O ice mainly composes the surface of the Northern polar cap, which obscures the seasonal CO_2 ice layer. While CO_2 ice distribution is inhomogeneous during early spring (L_S ~0°-30°), a H_2O ice annulus is present at latitude 50°N (Brown et al., 2012). This hence has an impact on the BD2292 estimation, as seen in Figure 4.4 (bottom panel). On the other hand, the Southern polar cap is known to be composed of clean thick CO_2 ice slabs in winter and fine-grained CO_2 ice during the spring at its edges (Langevin et al., 2007). Therefore, strong CO_2 ice signatures are represented by the highest BD2292 values. Nevertheless, we observe smaller BD2292 values around L_S 200°. During this period, H_2O frost contamination has been observed over the seasonal cap, occulting the CO_2 ice signatures at latitudes above 75°S (Langevin et al., 2007; Appéré et al., 2011), and hence impacting the BD2292 estimation (see bottom panel in Figure 4.4).

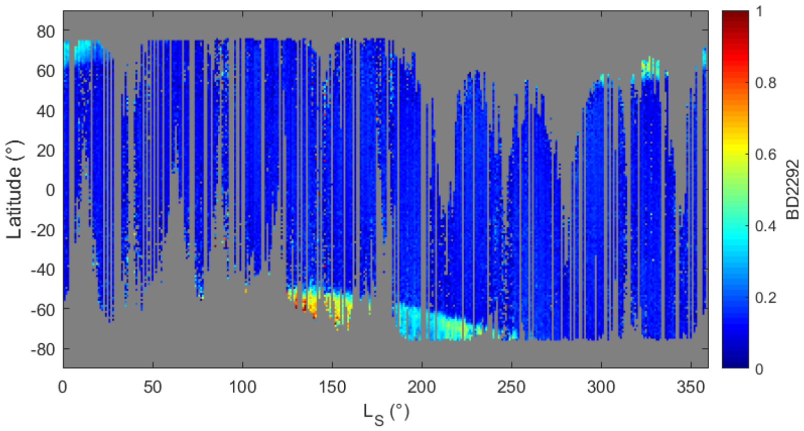

Figure 4.5: Latitudinal-seasonal map of BD2292 binned 1° by 1°. LNO observations cover all MY35 and 36 for a SZA <75°.

4.5 Results and discussion

4.5.1 South Polar cap edges

In this section, we qualitatively discuss the possible interannual changes of the Southern polar cap for MY34-36. To do that, we estimate the extension of the polar cap deposits through the latitudinal-seasonal trend by using the NII for the best temporal coverage (see Figure 4.2).

As in Oliva et al. (2022), we define the edge of a cap at a given L_S as the latitude where the NII values suddenly increase with respect to the mean value obtained for the equatorial regions (see Figure 4.6).

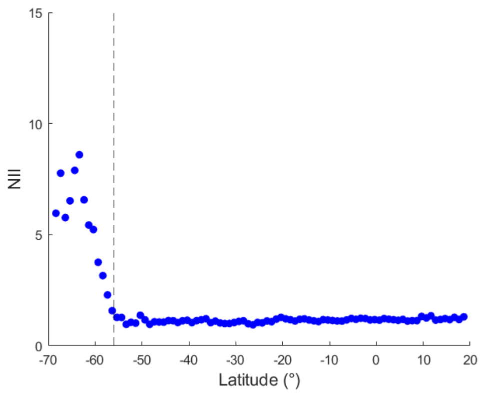

Figure 4.6: Latitudinal trend of the NII for $L_S = 180°$ (MY34). The vertical dashed black line indicates the latitude in which the NII values suddenly increase due to the presence of the seasonal cap.

We apply this criterion on the map shown in Figure 4.2 for the South Pole and compare its recession for MY34-36. The results are presented in Figure 4.7 (top panel). The comparison with the MCD v6.1 CO_2 ice column density is purely qualitative. Indeed, our polar cap boundaries should be considered as an indication of abundant ice, and not as an ice transitional region. We hence do not attempt to perform a quantitative retrieval of the ice abundance. As we can see in the top panel of Figure 4.7, MY36 is the year with the lowest spatial coverage, which may challenge the comparison with the two other years. Nevertheless, before $L_S = 170°$, the few blue points seem to follow the trend of MY34 and 35. Seasonal variations in the three Martian Years globally show a correlation for that period.

As already mentioned in Section 4.4.1, MY34 covers the 2018 global dust storm from L_S ~180° to 250° (Viúdez-Moreiras et al., 2019; Gillespie et al., 2020), impacting the ice detection (see top panel in Figure 4.2). For that reason, we compare our boundaries definition for MY34 with the CO_2 ice column density of the Laboratoire de Météorologie Dynamique Global Climate Model (LMD GCM) using the MY34 dust activity (see bottom panel in Figure 4.7) (Forget et al., 1999; Madeleine et al., 2011; Millour et al., 2018; Montabone et al., 2020). We still notice a good correlation between our cap edges and the simulations. A gap in the detections is present between L_S ~190° and ~215°, resulting from the interruption of nadir acquisitions using the orders 190, 169, 168 and 167 during this period. As shown in Figure 4.7 (top panel), only MY35 and MY36 cover this period, presenting a correlation in the cap boundaries results.

It is known that the global dust storm has an effect on the sublimation phase of the south polar cap (Piqueux et al., 2015; Calvin et al., 2017). Similarities have been observed between the two global dust storms occurring in MY25 and MY34 (Wolkenberg et al., 2020). They encircle the entire planet at a similar season (L_S ~190°), although the MY34 storm is characterised by a shorter decay phase compared to the one in MY25. During this season, the Southern latitudes are more exposed to the Sun than Northern latitudes. Due to high dust opacity, the heating rate of the atmosphere is enhanced (Guzewich and Smith, 2019; Kass et al., 2020; López-Valverde et al., 2023). Wolkenberg et al. (2020) observed a clear trend of atmospheric temperatures with dust. On the other hand, atmospheric dust inhibits the solar radiation from reaching the lower atmospheric layers, and hence the surface (Wolkenberg et al., 2018). Therefore, surface temperature tends to decrease during the day. The more dust in the atmosphere, the more the surface is cooling during the day (Streeter et al., 2020). An opposite effect occurs during the night. Indeed, a surface and near-surface warming effect is observed due to increased long-wave emission and backscattering from the increased aerosol and resulting higher atmospheric temperatures (Martínez et al., 2017; Guzewich and Smith, 2019). Higher dust opacity and higher surface temperatures at night have been observed in MY34 compared to MY25 (Wolkenberg et al., 2020). Moreover, nightside warming in MY34 was more important and persistent over time than diurnal cooling, allowing to counterbalance the dayside cooling. It resulted an effect of surface warming in diurnally averaged surface temperature (Streeter et al., 2020). In the Southern polar region, Mars Climate Sounder observed a large amount of dust over the polar cap (Kleinböhl et al., 2020). The atmosphere and its near surface layers progressively warmed, reaching a temperature of 200K from L_S ~190° to ~235°, with a peak of ~230K at L_S 215°-220° (~130K-150K before the global dust storm).

Based on the above discussion, an acceleration of the recession of the cap should be observed in MY34 compared to MY35 and 36. Nevertheless, the limited temporal coverage during the global dust storm in MY34 (yellow points in Figure 4.7) complicates the comparison between the three Martian Years. Moreover, such a comparison must be carried out on a homogeneous spatial coverage between years. To do this, NOMAD has to provide more data in order to reach a significant number of observations of the cap. For these reasons, the current data set does not allow us to investigate the possible effects of dust storms on the Southern polar cap.

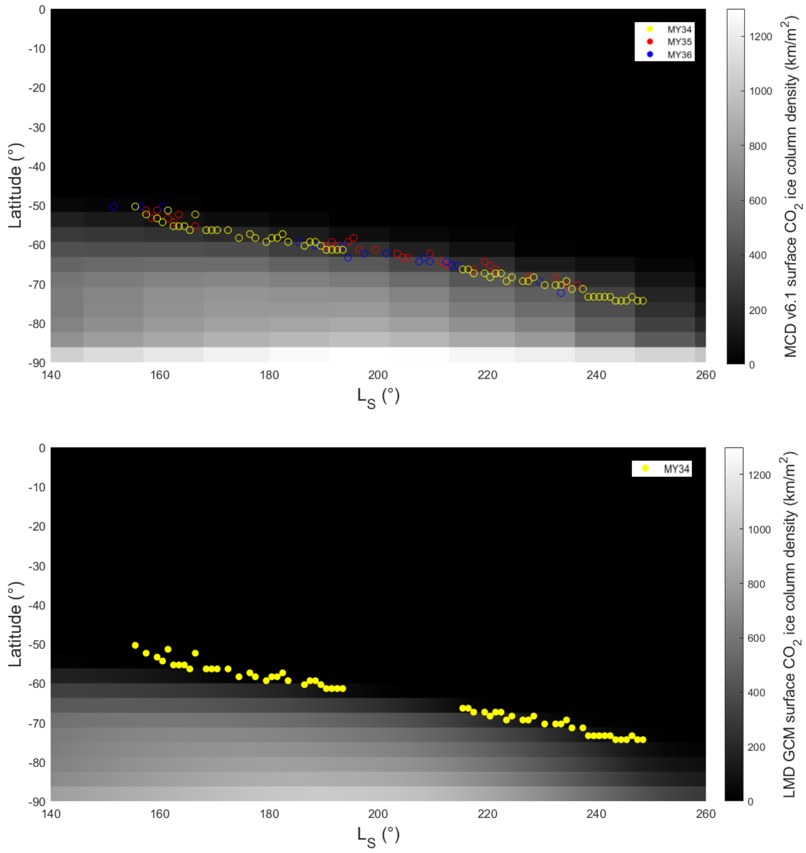

Figure 4.7: Polar cap edges estimated from the latitudinal trend of the NII. Top panel: comparison between our cap boundaries estimation for MY34-36 and the MCD v6.1 CO_2 ice column density predictions. Bottom panel: comparison between our cap boundaries definition for MY34 and LMD GCM simulations using MY34 dust activity.

4.5.2 Polar projection

In this section, we discuss the Southern sublimation phase during early and mid-spring for MY34-36 (data are binned 1° by 1° of longitude and latitude) by studying the polar projections of NII and BD2292 in 4 periods of time, L_S = 180°-190°, L_S = 200°-210°, L_S = 220°-230° and L_S = 240°-250°. Due to the specific TGO orbit, LNO observations are acquired up to latitudes 75°S. Therefore, the retreat of the cap can be observed until L_S ∼250°. After that period, the polar cap no longer extends to these latitudes (Langevin et al., 2007; Brown et al., 2010). The results are presented in Figure 4.8 and Figure 4.9. In Figure 4.8, left panels show the NII (see Section 4.4.1), while right panels give the BD2292 (see Section 4.4.2). Figure 4.9 presents the latitudinal trend of the BD2292. As already mentioned (see Section 4.2), the main objective of NOMAD is the analysis of trace gases and, hence, the spatial coverage is not optimised for surface analysis. Nevertheless, thanks to the NII and BD2292, it is possible to partially distinguish the seasonal variations along the LNO ground tracks during the presublimation and the cryptic phases (Brown et al., 2010).

Figure 4.8 (see line 1) shows the presublimation phase. During this period, the seasonal cap clearly extends equatorward of 60°S (see left panel). Similarly to Figure 4.6, we study the latitudinal trend of the BD2292, in which the values suddenly increase at latitude 56°S (see Figure 4.9). This indicates the presence of the seasonal cap, which is symmetrical and characterised by low and homogenous albedo presenting strong CO_2 ice signatures (see right panel in Figure 4.8) (Langevin et al., 2007).

The cryptic phase is observed in lines 2 and 3 in Figure 4.8. The low albedo cryptic region is localised between longitudes 60°E and 150°W (i.e. 60°E and 210°E) and below latitude 70°S. It has been identified as a region in which the CO_2 ice slab is contaminated by dust (Kieffer et al., 2000; Langevin et al., 2007). As we can see in the right panels in Figure 4.8 (lines 2 and 3), the probed parts of the cryptic region (between longitudes 150°E and 150°W, i.e. 150°E to 210°E, and around latitude 75°S)[4] present lower BD2292 values, with respect to the other parts of the cap, due to the possible dust contamination (see bottom panel in Figure 4.4). Regarding the NII (see left panel in line 2), we also notice lower values in the cryptic region, which should confirm the presence of high dust abundance (Oliva et al., 2022). On the other hand, the change

[4] See black arrows.

in the NII values for this region is not so evident in line 3. This can be explained by the presence of water ice inside the cryptic region during this period (Brown et al., 2010), which can counterbalance the effects of dust on the NII. Regarding the retreat of the cap (see Figure 4.9), the seasonal cap extends below latitudes 60°S, where a very high albedo characterises its outer regions (Kieffer et al., 2000; Langevin et al., 2007; Schmidt et al., 2009).

The last period partially covered by NOMAD is the asymmetrical retreat of the seasonal cap. During this period, the seasonal cap completely disappears in latitudes above 75°S between longitudes 60°E and 150°W (i.e. 60°E to 210°E) (Langevin et al., 2007). Both NII and BD2292 present a scarce surface coverage in Figure 4.8 (line 4). Nevertheless, we can see that the seasonal cap is present in latitudes above 75°S between longitudes 90°W and 60°E (see black arrows in right panel). This is consistent with OMEGA and CRISM observations, which have identified these bright albedo regions defined by strong CO_2 ice signatures (Langevin et al., 2007; Schmidt et al., 2009; Brown et al., 2010).

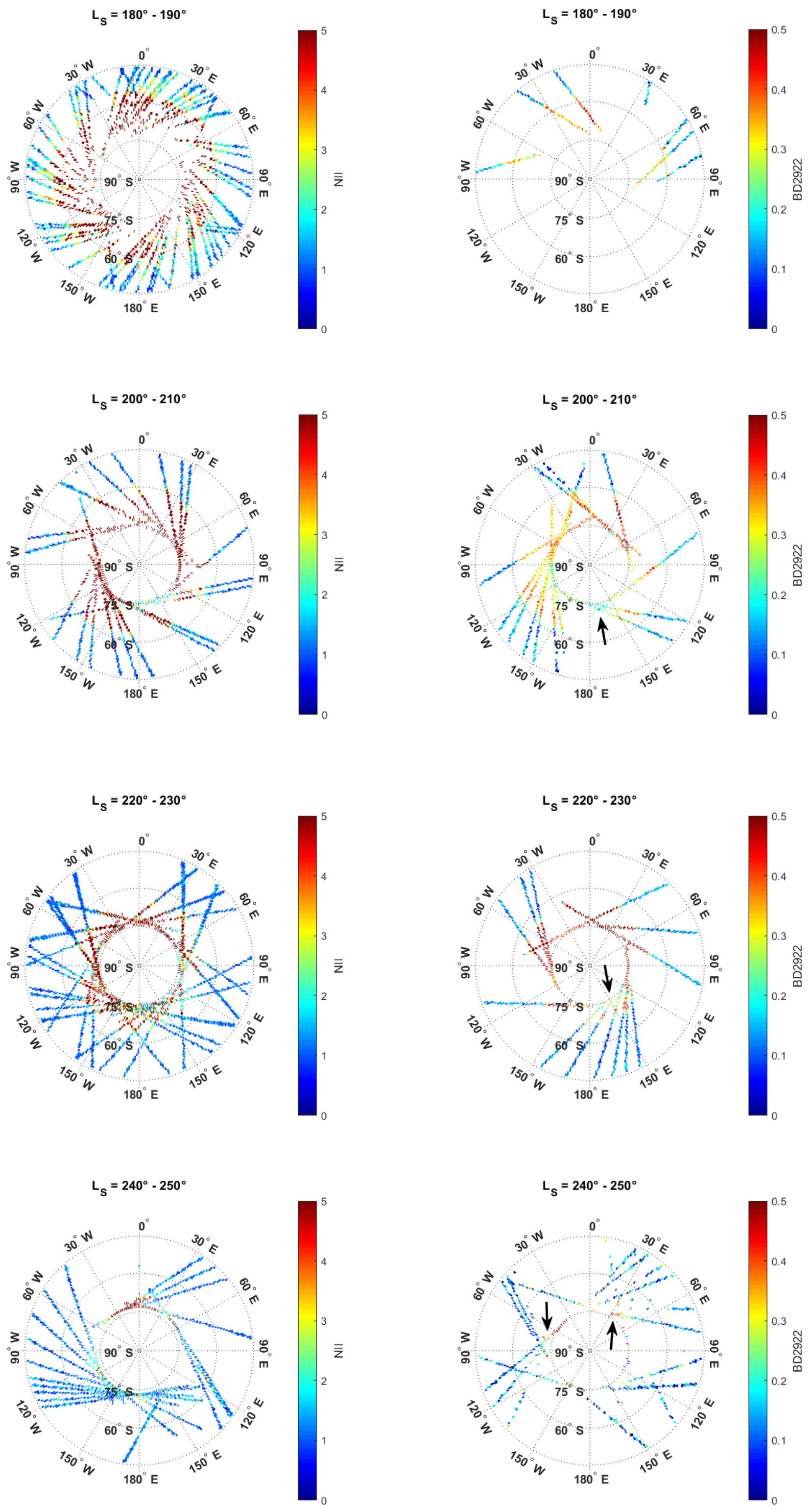

Continued on the next page.

Figure 4.8: First row: South polar projections of NII (left) and BD2292 (right) for the period of L_S = 180°-190° in MY34-36 binned 1° by 1°. The colour bars have been saturated in order to emphasise the colour dynamic. The lower values (blue tint) correspond to ice-free regions. Second row: same for the period of L_S = 200°-210°. Third row: same for the period of L_S = 220°-230°. Fourth row: same for the period of L_S = 240°-250°.

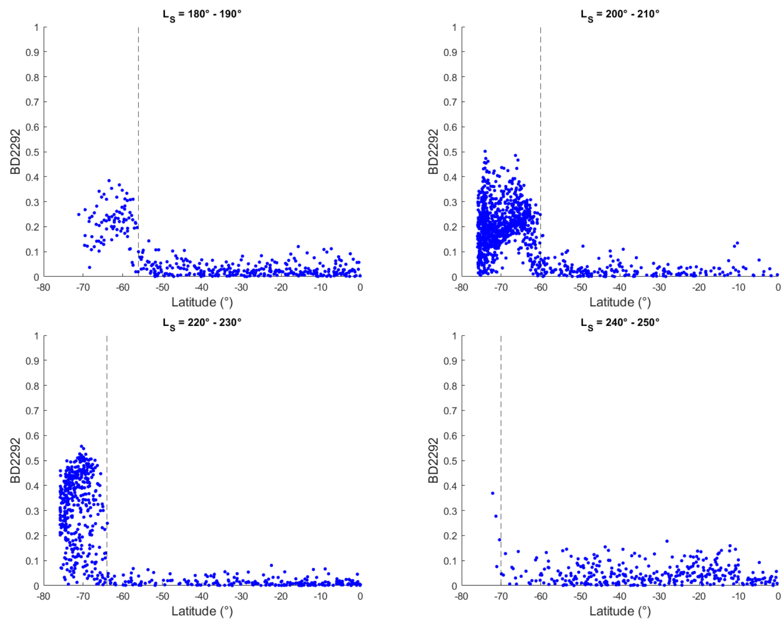

Figure 4.9: The BD2292 profiles over the probed latitudes helps in the visualisation of the retreat of the cap (right). The vertical dashed black line indicates the latitude in which the BD2292 values increase suddenly due to the presence of CO_2 ice. Same period as Figure 4.8.

4.5.3 CO_2 ice thickness

The high spectral resolution of NOMAD offers the possibility to retrieve some CO_2 ice properties. Nevertheless, the main difficulty remains in the acquisition of LNO observations through the different orders, hence impacting the spectral and spatial coverages. Moreover, the instrumental characteristics are not fully ideal for surface spectroscopy (see Section 4.2). Therefore, in this section, we adopt a semi-qualitative approach to discuss the possibility to reproduce the 2.29 μm CO_2 ice absorption band (order 193) using the Planetary Spectrum Generator (PSG) model (Villanueva et al., 2018). We attempt to estimate the "equivalent grain size" (henceforth called grain size), which is defined as the mean distance between two scattering interfaces within the CO_2 ice (Langevin et al., 2007). This is defined as the "CO_2 ice thickness" in the PSG model.

PSG model

The PSG model is an online tool dedicated to the synthesis and retrieval of planetary spectra (atmospheres and surfaces) for a broad range of wavelengths (0.5 μm to 100 mm) from any observatory (ground based telescope, orbiter or lander). PSG also permits to synthesise/retrieve mass-spectrometry data of orbiters, landers and laboratory instrumentation. It combines several state-of-the-art radiative transfer models, spectroscopic databases and planetary databases (i.e. climatological and orbital). This tool is hence suitable for the analysis of the NOMAD observations (Liuzzi et al., 2020). For the first time, PSG is used in a frame of a surface ice analysis with the LNO data in order to estimate the CO_2 ice equivalent grain size, i.e. the CO_2 ice thickness. In this work, we consider the Lambert (isotropic scattering) model for simulating the absorbed light at a surface, taking into account the LNO observing geometry. Regarding the surface composition, the model includes more than 20000 species. We use the CO_2 ice optical constant from the NASA Goddard Space Flight Center (GSFC) (Gerakines and Hudson, 2020). The retrievals are performed on LNO observations acquired over regions where clean CO_2 ice slabs are expected. For that reason, we do not include H_2O ice optical constant in the surface composition. Nevertheless, for any dust impurities on the CO_2 ice, we rely on the optical constant from the Air Force Cambridge Research Labs (AFCRL) (Harris and Rowan-Robinson, 1977). PSG is also able to perform multiple scattering from atmospheric aerosols by using the discrete ordinate method (Stamnes et al., 2017). Therefore, for suspended dust, we use the refractive indices derived with CRISM observations (Wolff et al., 2009). The model assumes a thermal structure of the Martian atmosphere coming from the MCD climatology predictions (Millour et al., 2018). During the retrievals, it employs the Optimal Estimation Method (Rodgers, 2000), which analyses each spectrum individually through a Gauss-Newton iterative approach. More details about the PSG model and the retrievals method can be found in Villanueva et al. (2018) and Liuzzi et al. (2020).

Errors estimation

In order to perform the retrievals with PSG, the AOTF and Blaze functions convolution are applied to the synthetic spectra. Indeed, as already mentioned in Section 4.2 (and detailed in Chapter 2), the general shape of the LNO spectra is affected by the AOTF transmission (defined as the sum of a sinc-squared and a Gaussian function) and by the Blaze function (defined as a sinc-squared function). It is important to mention that the sinc-squared AOTF function allows some photons from adjacent diffraction orders to reach the detector (Liuzzi et al., 2019). This complexity hence challenges the AOTF definition for the LNO channel, impacting the uncertainty on the LNO spectra. In addition to these instrumental errors, the SNR also depends on the radiation entering the spectrometer, and so observational parameters such as SZA, surface albedo, etc. can affect it (see Section 4.2 and 4.3).

In this section, we adopt an independent manner in order to estimate the total uncertainties, i.e. the instrumental and observational errors, associated with the spectra and to analyse the source of variability. To do so, we select all the spectra falling in a dayside equatorial region of 10° latitude by 10° longitude for MY35-36 (>100), for which we assume that no surface CO_2 ice is present. As the SZA strongly impacts the SNR, the sample spectra are divided in 10° SZA intervals, ranging from SZA = 20° to 75°. Moreover, we normalise each spectrum with the signal intensity at the middle of the order. This is done in order to mitigate eventual surface albedo and aerosols variations that would mostly affect the radiometric signal of the considered observations. Then, we compute, for each SZA interval, an averaged intensity value for each wavelength and estimate the standard deviation. As an example, Figure 4.10 (upper panel) shows the averaged spectrum (in blue) for SZA = 40°-50° in MY35-36. We can see that the spectrum is modulated, especially at the edges, whereas normally we should obtain a normalised continuum spectrum around 1 (as we assume the absence of surface CO_2 ice in a dayside equatorial region). In fact, the modulation in the spectrum is the result of the AOTF function. We estimate an averaged standard deviation of 20% for all wavelengths. As we can see in Figure 4.10 (bottom panel), it increases from the middle of the order to its edges. The standard deviation ranges from 4% to 9% between 2288 nm and 2298 nm, while it is larger than 100% at 2305 nm due to a reduced Blaze efficiency at this edge of the detector. This difference in uncertainty value in the order suggests that the dominant source of variability results from the instrumental effects (instrumental noise, the AOTF and Blaze functions). From this analysis, we can hence provide an estimation of the error associated with the spectra (instrumental and observations uncertainties) to the PSG model.

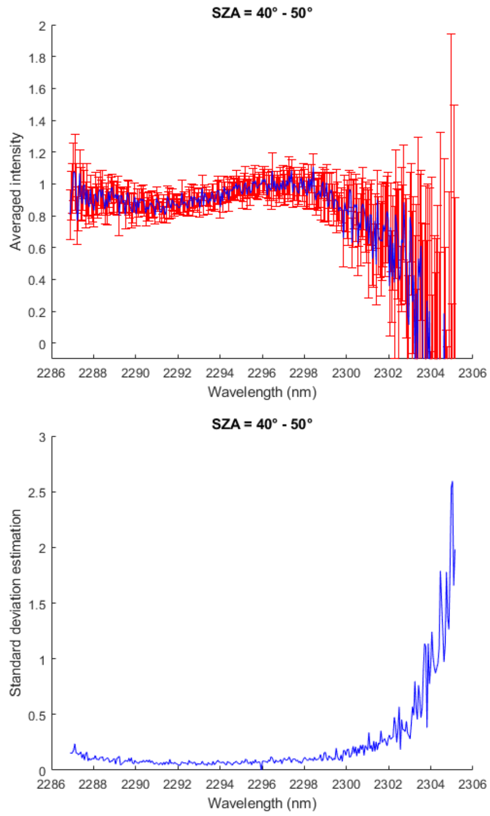

Figure 4.10: Upper panel: averaged spectrum (in blue) of an equatorial region for SZA = 40°-50° in MY35-36. For each wavelength, the standard deviation is computed given the error bars estimation in red. Bottom panel: variation of the standard deviation values, ranging from 4% in the middle of the order to more than 100% at 2305 nm.

Equivalent grain size estimation

For this exercise, we select some spectra of the South polar regions with the lowest SZA and where a strong CO_2 ice signature is expected during the presublimation (see first row in Figure 4.8) and the cryptic phases (see second and third rows in Figure 4.8).

Table 4.2 shows spatial and physical parameters related to some examples of observations registered during these two different periods (2 in the presublimation phase and 3 in the cryptic phase). As already mentioned in Section 4.5.2, low and homogenous albedo characterises the CO_2 ice seasonal cap during the presublimation phase. We observe surface albedo around 0.1-0.15 with a BD2292 estimation around 0.4-0.5. Such spectra acquired over the seasonal cap can be interpreted as a clean CO_2 ice slab with a grain size of tens of centimetres (20 cm-50 cm). They are observed over a large range of longitudes, except at the edges of the cap (Langevin et al., 2007). The PSG tool is able to model the selected spectrum by estimating a grain size of ~27 cm (see line 1 in Table 4.2). At the cap edge, i.e. close to the sublimating frost, we obtain grain sizes of ~12 cm (see line 2 in Table 4.2). This suggests that the grain size decreases with time as the ice sublimes, which has been also observed by TES and CRISM (Kieffer et al., 2000; Brown et al., 2010; Andrieu et al., 2018).

Regarding the cryptic phase, spectra are characterised by relatively high albedo. We observe values of 0.4-0.5, while Lange et al. (2022) reported albedo values of 0.7 using OMEGA observations. They found grain sizes of 5-10 cm at the outer regions. Figure 4.11 presents the PSG fit obtained for a LNO spectrum over the outer regions of the cap. The model reproduces the data by estimating a grain size of ~8 cm (see line 3 in Table 4.2), hence consistent with OMEGA observations (Langevin et al., 2007). The two last observations listed in Table 4.2 are acquired close to the so-called Mountains of Michel area (around latitudes 70°S ± 3° and longitudes 35°W ± 5°), defined as a bright albedo region (James et al., 1979; Smith et al., 1999; Kieffer et al., 2000; Langevin et al., 2007; Brown et al., 2010). The retrievals return grain sizes of ~15 cm and ~12 cm. This range of values is quite consistent with the order of magnitude found by Langevin et al. (2007) (grain size at outer bright region ~5-10 cm) and Andrieu et al. (2018), but not with TES observations. Indeed, Kieffer et al. (2000) suggested fine grains of a 100 μm radius. On the other hand, under low atmospheric dust abundance (dust mass mixing ratio <10^{-4} kg/kg), they have observed grain sizes much larger than 1 cm. Therefore, we use the MCD v6.1 predictions in order to estimate the suspended dust content for the last observation in Table 4.2, which is the closest to the Mountains of Michel. The model returns a dust mass mixing ratio of 4.1×10^{-6} kg/kg, which means that the order of magnitude of grain size (in centimetre) is in agreement with TES observations.

Andrieu et al. (2018) estimated the full sublimation phase in the Richardson crater (at longitude 180°W and latitude 72°S) outside a dark spot. They found a global decrease in the CO_2 ice slab thickness from 40 cm at L_S=197° to 1 cm at L_S=250°, taking inclusions and aerosols into account. Even though the global trend is in agreement with our study, the value can be different by a factor of 3 (see lines 1 to 3 in Table 4.2). This may be due to the radiative transfer assumptions and/or the difference in spatial scale and localisation between our study and that of Andrieu et al. (2018).

The errors of the retrieved parameters in Table 4.2 have been estimated by a statistical approach, i.e. a bootstrapping procedure (Efron and Tibshirani, 1994). We use the measurement errors to create randomised spectra within the error bars of the nominal one. Each iteration provides a randomised spectrum that follows the same statistical characteristics as the real observations. Then, we perform the retrieval for a statistically significant number of times. Therefore, the distribution of the retrieved parameter values can be analysed to estimate the associated errors. It is important to mention that we do not attempt to analyse in-depth the 2.29 μm feature. A more robust quantitative modelling would require to take into account several physical parameters and a complete estimation of the retrieved parameters errors. This is beyond the scope of this work. As already mentioned, we analyse the possibility to reproduce the 2.29 μm absorption band by adopting a semi-qualitative approach in order to provide the order of magnitude of the grain size. As shown in Table 4.2, the PSG model is able to reproduce correctly the LNO spectra. The obtained results are in good agreement with the order of magnitude of the grain size estimation of previous studies (Calvin and Martin, 1994; Kieffer et al., 2000; Langevin et al., 2007; Brown et al., 2010; Andrieu et al., 2018). To conclude, this section shows that the PSG model is suitable for a surface CO_2 ice analysis through the order 193.

Phase	Orbit	L_S (°)	Latitude (°)	Longitude (°)	SZA (°)	Grain size (cm)	Reduced χ^2	Literature
Presubl.	20220310_070842	187.8	58.2 S	9.9 W	65.5	27 ± 3.8	0.13	20-50 cm$^{(a)}$ 80 cm$^{(b)}$
Presubl.	20200504_083128	194.8	61.9 S	57.6 W	66.2	12 ± 1	0.6	12-15 cm$^{(c)}$ ~10 cm$^{(d)}$ 6-8 cm$^{(e)}$ 40 cm$^{(b)}$
Cryptic	20200527_090659	208.6	66.2 S	95.1 E	56.8	8 ± 0.8	0.15	5-10 cm$^{(a)}$ 2-3 cm$^{(e)}$ 30 cm$^{(b)}$
Cryptic	20220508_203944	223.7	68.1 S	53.8 W	52.4	15 ± 0.8	0.40	>1 cm$^{(d)}$ 5-10 cm$^{(a)}$ 20 cm$^{(b)}$
Cryptic	20220524_021241	233.2	67.4 S	34.2 W	62.2	12 ± 1.5	0.66	>1 cm$^{(d)}$ 5-10 cm$^{(a)}$ 10 cm$^{(b)}$

Table 4.2: Orbits, L_S, latitudes, longitudes, SZA, equivalent grain size estimations with PSG, goodness of the fit and comparison with previous studies are listed for some selected LNO spectra during the presublimation and cryptic phases. (a) Langevin et al. (2007); (b) Andrieu et al. (2018); (c) Calvin and Martin (1994); (d) Kieffer et al. (2000); (e) Brown et al. (2010)

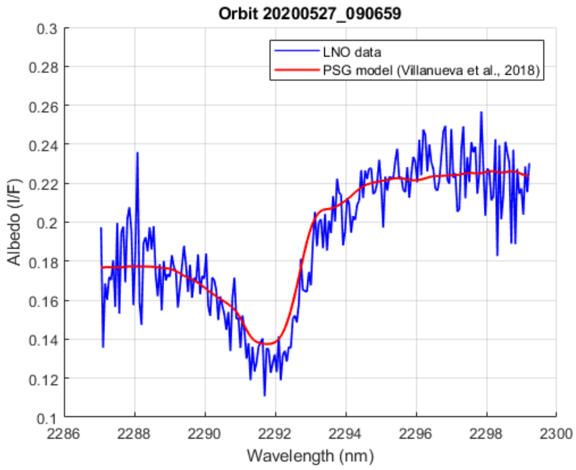

Figure 4.11: PSG fit on the 2.29 μm CO_2 ice absorption band well present in the LNO spectrum (orbit 20200527_090659). A reduced χ^2 of 0.15 is obtained. See line 3 in Table 4.2 for more details.

4.6 Conclusion

Even if devoted to trace gases in the Martian atmosphere, NOMAD has also proven to be a suitable spectrometer to study surface CO_2 ice of Mars at high resolution using the LNO nadir IR channel (Oliva et al., 2022), despite the instrumental features (see Section 4.2). In this work, we have further explored the LNO dataset information content. We have defined an updated method using the three diffraction orders (orders 167, 168, 169) located on the short wavelength shoulder of the 2.7 μm ice absorption band in order to map surface ice by considering the best spatial coverage. The method is based on spectral ratio capable of detecting surface albedo variations related to ice (New Ice Index, see Section 4.4.1). Moreover, we have also investigated CO_2 ice by defining a pseudo-band depth for NOMAD (BD2292, see Section 4.4.2) through the 2.29 μm absorption band (order 193). We applied both spectral parameters on the LNO dataset from MY34 (L_S = 150°) to MY36 (L_S = 360°) and constructed latitudinal-seasonal maps for surface ice detection. It represents the highest spatial coverage to date of these observations. We focused specifically on the Southern polar cap to analyse the seasonal and potential interannual changes over MY34-36 (see Section 4.5.1 and 4.5.2). To do that, we have estimated the polar cap edges based on the latitudinal trend of the spectral parameters. Our polar cap edges definition is consistent with the MCD v6.1 (Forget et al., 1999; Millour et al., 2018) and LMD GCM CO_2 ice column predictions (Forget et al., 1999; Madeleine et al., 2011; Millour et al., 2018; Montabone et al., 2020). Globally, seasonal changes seem repeatable for MY34-36 (see Section 4.5.1). Finally, we discussed the potential for using the 2.29 μm absorption band to retrieve information about CO_2 ice grain size by adopting a semi-qualitative approach. We used the Planetary Spectrum Generator tool (Villanueva et al., 2018) on observations where a clean and thick CO_2 ice slab is expected (see Section 4.5.3). The results obtained for the presublimation and cryptic phases are in the order of centimetres, which is consistent with previous studies (Calvin and Martin, 1994; Kieffer et al., 2000; Langevin et al., 2007; Brown et al., 2010; Andrieu et al., 2018) (see Section 4.5.3).

Continuous observations enhance our understanding of the Martian surface ice. The results presented in this work (see Section 4.5) appear to be consistent with previous studies (e.g. using OMEGA, CRISM, TES data). They confirm and help in refining our current knowledge of the Southern polar cap, through observation of the sublimation process. Additionally, order 193 appears to be a good candidate for the CO_2 ice identification, opening further perspectives for the analysis of Martian ice deposits. Indeed, the use of the PSG model reveals its highly sensitivity to the microphysical properties of the ice. This indicates the large potential for more detailed exploitation of this order, e.g. for the analysis of small ice crystals. A dedicated radiative transfer model will allow to analyse in depth CO_2 ice at a higher resolution. This will provide significant insights of the microphysical properties of the ice, complementing the results of previous studies (see Table 4.2 in Section 4.5.3). As it was done with order 189 in Oliva et al. (2022), another possible perspective with order 193 is the CO_2 ice cloud detection, which can provide additional information on their distribution, seasonality and microphysical properties.

Finally, this paper represents one of several studies dedicated to the exploitation of the LNO nadir dataset and opens the way for different follow-up papers. As a direct continuation to this work, an in-depth radiative transfer analysis of the 2.29 μm feature in CO_2 ice is already planned. Regarding the cloud analysis (Oliva et al., 2022; Ruiz Lozano et al., 2022), further comparison with the NOMAD-UVIS channel about cloud detection is currently being performed[5].

[5] This analysis, outside the scope of the thesis, is in progress at the time of writing, and hence not shown in this thesis.

Chapter 5

Water Frost on Martian volcanoes

Led by the Colour and Stereo Surface Imaging System (CaSSIS) team (Thomas et al., 2017), this chapter presents a morning frost campaign on Martian volcanoes joint observations by CaSSIS and NOMAD, two instruments onboard ExoMars-TGO (*submitted*)[1]. This work is presented from Section 5.1. I led the investigation and validation of the NOMAD-LNO results (see Section 5.4.2) and participated in the review of the article.

A part from the polar regions, surface frost/ice has been detected at mid and low latitudes on Mars (between 32°N to 13°S), where local illumination conditions favor exceptional low surface temperatures (Schorghofer and Edgett, 2006; Carrozzo et al., 2009; Vincendon et al., 2010b) (see Section 5.2.1). In the tropics of Mars, the Tharsis region is an interesting province favourable to atmospheric phenomena (i.e. water ice clouds: Benson et al. (2006); Hernández-Bernal et al. (2021) and water vapour enrichment: Maltagliati et al. (2008)) and low surface temperature (predicted by models: Spiga et al. (2011), Lange et al. (2022), and retrieved: Stcherbinine et al. (2023)) due to its topography (see Section 5.2.1). Therefore, the high humidity and low surface temperature may allow the formation of frost in this high altitude region.

[1]Valantinas, A., Thomas, N., Pommerol, A., Hauber, E., **Ruiz Lozano, L.**, Bickel, V., Karatekin, Ö., Senel, C. B., Temel, O., Tirsch, D., Munaretto, G., Pajola, M., Oliva, F., Schmidt, F., Thomas, I., McEwen, A. S., Almeida, M., Read, M., Rangarajan, V. G., El-Maarry, M. R., Re, C., Carrozzo, F. G., D'Aversa, E., Vandaele, A. C. and Cremonese, G. Water Frost on Martian volcanoes. *Under consideration.*

Since November 2022, a collaboration between the CaSSIS and NOMAD-LNO teams has started in the framework of a morning frost campaign of joint observations. The two instruments acquire a few joint observations per month, ranging from 1 to 6 (at the time of writing). In collaboration with the CaSSIS team, we have defined regions of interest, starting from Olympus Mons (November 2022) to most of the volcanoes in the Tharsis region (July 2023), as well as places in the far East such as Elyssium Mons (February 2023) and Apollinaris Mons (July 2023). This list is not exhaustive. Other regions and observations will be added in the near future. Figure 5.1 shows the regions of interest at the start of this campaign.

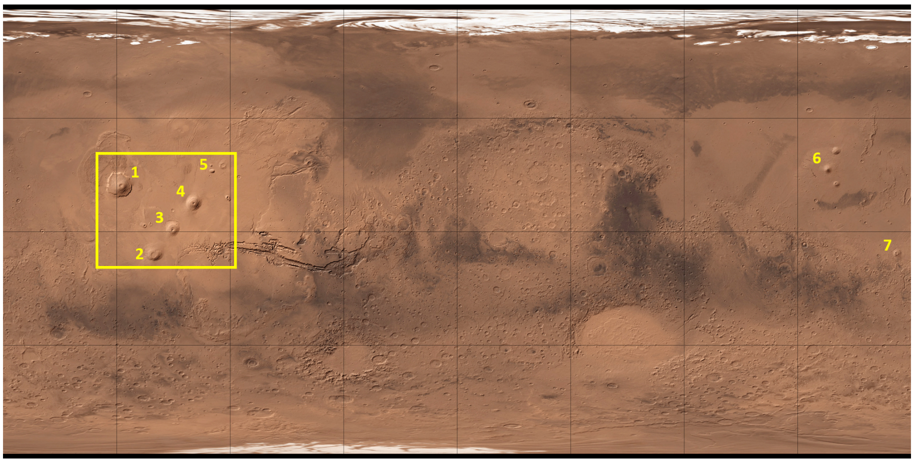

Figure 5.1: Regions of interest for the frost morning campaign. In the Tharsis region (yellow rectangle); 1: Olympus Mons, 2: Arsia Mons, 3: Pavonis Mons, 4: Ascraes Mons and 5: Ceraunius Tholus. In the far East; 6: Elysium Mons and 7: Apollinaris Mons. (Bills and Nerem, 2001)

The analyse of the CaSSIS observations through different filters reveals a blue halo at the top of different volcanoes (i.e. Olympus Mons, Arsia Mons, Ascraeus Mons but also on the smaller Ceraunius Tholus volcano, see Figure 5.1) in the early morning, ranging from a Local Solar Time of 7:00 to 8:30. The blue tint is found mainly on the floor of the caldera, but not on the well-illuminated and warm slopes of the volcanoes. At the time of writing, 14 cases have been observed within the CaSSIS dataset.

Regarding the Olympus Mons, CaSSIS acquired images in the late Northern winter in MY36 at LST = 7:11 (25^{th} November 2022, L_S = 344°), showing an extended blue halo on the top of the volcano covering the entire caldera. In the frame of joint observations with CaSSIS, NOMAD-LNO acquired observations of the Olympus Mons (25^{th} November 2022, LNO orbit 0221125_082524, L_S = 344°, LST = 7:12) using orders 190, 189 and 168 (for order 189, more details in Section 3.2.3 in Chapter 3 and for orders 190 and 168, more details in Section 4.3 in Chapter 4). Unlike other spectrometers (e.g. OMEGA, CRISM and TES)[2], NOMAD is able to observe the Tharsis region in the first hours after sunrise (LST <08:30), thanks to TGO's orbit. Nevertheless, this implies high illumination angles. Generally, the SZA ranges from ∼70° to ∼90°, affecting the SNR seriously. In order to remove low SNRs, we remove observations with a SZA above 80°.

In this chapter we adjust the Ice Index (see Section 3.4.1 in Chapter 3) and define the adapted Ice Index (AII) by considering the available orders of the joint CaSSIS-NOMAD observations, i.e. orders 190 and 168 (see Section 5.4.2). In addition, we remove spatial albedo variations by normalising the LNO data to the OMEGA albedo map, which is more suitable than the TES albedo for the Tharsis region (see discussion for equatorial regions and low albedo regions in Section 6.3.2 in Chapter 6). By using the AII, we prove that the blue halo observed by CaSSIS is extensive frost covering the bottom of the caldera (see Section 5.4.2). Spectral analyses have also been performed on order 189 covering the 2.35 μm CO_2 ice absorption band (not discussed in Section 5.4.2). Nevertheless, no CO_2 ice lines have been observed. This can be explained by the fact that either the observed frost is H_2O ice or that the microphysical properties of CO_2 frost (i.e. grain size) result in a weak absorption band within the noise level of the instrument. As a result, the 2.35 μm CO_2 ice line would be not visible in these LNO spectra. Therefore, Mars Global Climate Model (GCM) simulations have been performed using the Mars Weather Research and Forecasting (WRF) model (Richardson et al., 2007) in order to estimate surface temperature in the Olympus Mons caldera[3]. For this observation, the MarsWRF predictions suggest that the presence of CO_2 frost is unlikely, as the CO_2 frost point is not reached in the caldera (∼138K, see Figure 5.2). This hence supports the

[2]OMEGA is able to observe the Tharsis region after LST 8:00 (Madeleine et al., 2012a), while CRISM and TES observe Mars at LST 15:00 and 14:00 respectively (see Table 2.2).

[3]C.B. Senel and O. Temel, from the Royal Observatory of Belgium (ROB-ORB) and co-authors of the study, led and performed the Mars GCM simulations.

presence of H_2O frost (see Section 5.4.3).

Concerning other CaSSIS blue halo detections (i.e. Arsia Mons, Ascraeus Mons, etc.), no frost confirmation could be reported by NOMAD, either by the AII or spectral analysis on orders containing a CO_2 ice absorption (e.g. order 189, see Section 3.4.2, and 193, see Section 4.4.2), due to a low SNR of the LNO data (high illumination angles, SZA $\sim$80°-90°). Any weak signal coming from potential diffuse frost can easily fall within the LNO level noise, making its detection impossible. Nevertheless, these CaSSIS detections are interpreted as surface frost based on a photometric comparison of images taken at different times of the day. Although the CaSSIS images reveal a bright blue halo at the top of Arsia Mons (see Figure 5.4), it seems difficult to validate all the detections without a spectral analysis and surface temperature predictions (see Figure 5.8 and 5.10)[4].

This work involves NOMAD observing in conditions that are not optimal for nadir data acquisition. On the other hand, it proved that the spectrometer is capable of detecting morning frost, which is more diffuse than surface ice and therefore more difficult to observe. This opens up new possibilities for the near future. As the campaign is still ongoing, new observations are planned in the coming months. The spectral analysis will be adapted for this work, allowing the FOV of the instrument to be reduced in order to detect less extensive frost. Observations with a SZA <80° must be respected in order to obtain a signal just above the instrumental noise level. The next objective of NOMAD will be to search for CO_2 frost using order 189 and 193, when surface temperatures are most favourable for its formation (at L_S $\sim$90°-100°, see Figure 5.2).

[4]The CaSSIS team reveals the presence of artefacts in images acquired at SZA >85° (see Section 5.4.1).

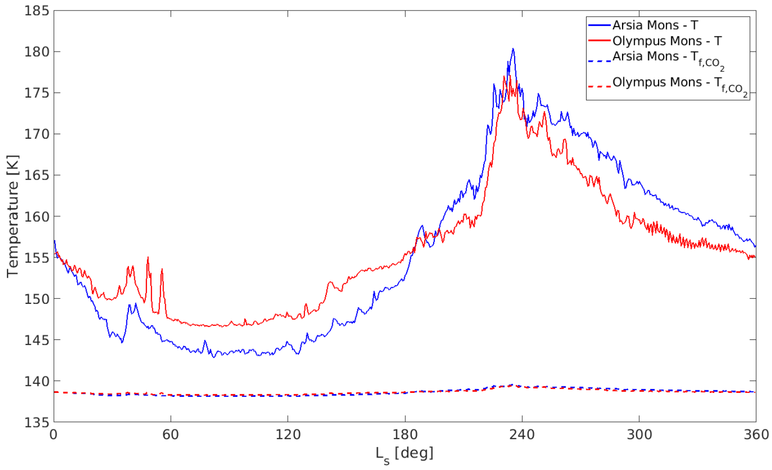

Figure 5.2: MarsWRF morning surface temperature predictions for LST = 7:00 in the Olympus (red line) and Arsia Mons (blue line) over a full Martian Year. Dashed lines indicate the CO_2 frost point temperature for the two volcanoes (same colour definition). While predicted surface temperature at L_S 355° is not suitable for CO_2 frost formation, MarsWRF model shows surface temperatures approaching the CO_2 frost in the Arsia Mons caldera from L_S 60° to 120°.

Chapter 6

Evaluation of the Capability of ExoMars-TGO NOMAD Infrared Nadir Channel for Water Ice Clouds Detection on Mars

This chapter was published in the frame of the Special Issue "Techniques for the Exploitation of Remotely Sensed Data of Planetary Atmospheres", belonging to the section "Satellite Missions for Earth and Planetary Exploration"of the Remote Sensing journal (Ruiz Lozano et al., 2022)[1]. It can be found from Section 6.1. I led the research conceptualisation, model development and validation, formal analysis, visualisation of results, and the writing and revisions of the manuscript.

[1] **Ruiz Lozano, L.**, Karatekin, Ö., Dehant, V., Bellucci, G., Oliva, F., D'Aversa, E., Carrozzo, F. G., Altieri, F., Thomas, I. R., Willame, Y., Robert, S., Vandaele, A. C., Daerden, F., Ristic, B., Patel, M. R. and López Moreno, J. J. Evaluation of the Capability of ExoMars-TGO NOMAD Infrared Nadir Channel for Water Ice Clouds Detection on Mars. *Remote Sensing.* 2022; 14(17):4143.

In the previous chapters, we presented various spectral indices for:

- Observing the polar ice caps and studying their seasonal processes through the 2.7 μm ice absorption band (Ice Index, see Chapter 3; New Ice Index, see Chapter 4)
- Identifying surface CO_2 ice using the 2.35 μm (SAM χ Index, see Chapter 3) and the 2.29 μm CO_2 ice bands (BD2292, see Chapter 4)
- Detecting frost on the summit of Olympus Mons using the 2.7 μm ice absorption band (Adapted Ice Index, see Chapter 5).

In addition, we discovered mesospheric CO_2 ice clouds using the SAM χ index (see Chapter 3). Nevertheless, none of the indices listed above was able to detect water ice clouds. We hence address this issue in this chapter.

As discussed in the previous chapters (e.g. see Section 3.2.3 in Chapter 3), water ice has a spectral absorption at 2.7 μm, covered by orders 167, 168, 169 (see Section 4.3 in Chapter 4). The difficulty in this study still lies in the method of acquiring NOMAD-LNO data through the orders. The microphysical properties of ice clouds give a spectral signal that can be mimicked by suspended dust, making them difficult to differentiate through orders (see Section 6.3.1). Therefore, in this chapter, we describe a technique using a peculiar combination of orders 167, 168 and 169 to enhance the signature of water ice. We define the Frost and Cloud Index (FCI) (see Section 6.3.2). While the previous spectral indices using the 2.7 μm ice band (i.e. Ice Index, New Ice Index and Adapted Ice Index) are sensitive to abundant ice (i.e. surface ice), the FCI is also sensitive to spectral anomalies in the presence of water ice from transient phenomena such as ice clouds (see Section 6.4.2).

In this chapter we remove spatial albedo variations coming from different surface mineralogy absorptions by normalising the LNO data to the TES bolometric albedo. This allows to spotlight anomalous detections resulting from water ice cloud's spectral signature (see Section 6.3.2). In contrast to Chapter 5 (local study over Olympus Mons), we perform a latitudinal-seasonal study where the TES albedo is more appropriate than OMEGA albedo. Indeed, TES takes into account the effects of low-albedo equatorial terrain on the LNO data. Nevertheless, artefacts in the results can still remain over low-albedo terrain in the Northern hemisphere. This point is discussed in Section 6.4.3.

In nadir mode, it is difficult to distinguish the spectral signal from surface ice and clouds. An independent manner to do this is to consider the Local Solar Time and the surface temperature. We use the Mars Climate Database v5.3 (MCD) to predict surface temperature at the local time of the observation. If the MCD predicted surface temperatures are higher than the H_2O frost point (T $\sim$193K at 610 Pa, Carrozzo et al. (2009)), we can exclude the presence of surface ice and confirm the presence of water ice clouds (see Section 6.4.1 and 6.4.2). Nevertheless, this assumption is based on a prediction of average surface temperatures. This point could be refined using the retrieved surface temperature from MRO-MCS observations.

remote sensing MDPI

Article

Evaluation of the Capability of ExoMars-TGO NOMAD Infrared Nadir Channel for Water Ice Clouds Detection on Mars

Luca Ruiz Lozano [1,2,*], Özgür Karatekin [2], Véronique Dehant [1,2], Giancarlo Bellucci [3], Fabrizio Oliva [3], Emiliano D'Aversa [3], Filippo Giacomo Carrozzo [3], Francesca Altieri [3], Ian R. Thomas [4], Yannick Willame [4], Séverine Robert [4], Ann Carinne Vandaele [4], Frank Daerden [4], Bojan Ristic [4], Manish R. Patel [5] and José Juan López Moreno [6]

[1] Earth and Life Institute, Secteur des Sciences et Technologies, Université Catholique de Louvain (UCLouvain), 3, Place Louis Pasteur/L4.03.08, B-1348 Louvain-la-Neuve, Belgium
[2] Royal Observatory of Belgium (ROB-ORB), B-1180 Brussels, Belgium
[3] Istituto di Astrofisica e Planetologia Spaziali (IAPS-INAF), 00133 Rome, Italy
[4] Royal Belgian Institute for Space Aeronomy (BIRA-IASB), B-1180 Brussels, Belgium
[5] School of Physical Sciences, The Open University (OU), Milton Keynes MK7 6AA, UK
[6] Instituto de Astrofísica de Andalucía (IAA), Consejo Superior de Investigaciones Científicas (CSIC), 18008 Granada, Spain
* Correspondence: luca.ruizlozano@oma.be or luca.ruizlozano@uclouvain.be

6.1 Introduction

Understanding the exchanges between the atmosphere and the surface remains pivotal in planetary climate research. On Mars, seasonal variations in the main atmospheric gaseous components are strongly affected by their condensation and sublimation within the polar caps (Langevin et al., 2007). In this framework, the formation of ice clouds plays a fundamental role in sculpting the Martian climate. By observing their spatial and seasonal distributions, we can improve our knowledge on atmospheric transport, as well as on water vapour and CO_2 cycles. Moreover, studying the formation and composition of ice clouds can help to better understand smaller scale phenomena such as convective regimes and thermal effects of radiative forcing (Montmessin et al., 2007).

Over the two past decades, water ice clouds have been deeply analysed in their composition, microphysical properties and vertical distribution (Clancy et al., 2003, 2019; Wolff and Clancy, 2003; Smith, 2004; Smith et al., 2013; Liuzzi et al., 2020; Wolff et al., 2019; Olsen et al., 2021), also identifying two main seasonal cloud structures emerging at a planetary scale: the Aphelion Cloud Belt (ACB) and Polar Hood (PH) clouds (Clancy et al., 1996; Smith, 2008, 2009; Benson et al., 2010, 2011; Madeleine et al., 2012a; Willame et al., 2017; Szantai et al., 2021; Wu et al., 2022). Important variations in the Martian topography can also promote the formation of water ice clouds. This is the case, for instance, of the highest volcanoes in the Tharsis region, where extremely elongated orographic clouds have been observed (Benson et al., 2003, 2006; Hernández-Bernal et al., 2021). The interpretation of such observations can rely on theoretical circulation models needed for a comprehensive understanding of the Martian climate in its complexity (Forget and Pierrehumbert, 1997; Forget et al., 1998, 1999; Richardson et al., 2002; Montmessin et al., 2004; Navarro et al., 2014; Daerden et al., 2010, 2019). These General Climate Models (GCMs) are in turn trained by continuously comparing their outputs with new observations. Further observations are hence always necessary.

In this work, we investigate the information content of the ExoMars-TGO NOMAD infrared channel nadir dataset. NOMAD is a suite of high spectral resolution instruments mainly dedicated to studying the Martian atmosphere trace gases and climatological processes (Aoki et al., 2019; Liuzzi et al., 2019; Vandaele et al., 2019; Korablev et al., 2021; Smith et al., 2021). Given the peculiar mode of operations of the instrument for nadir observations, it is difficult to discern clouds from suspended dust and surface ice deposits. For that reason, we define here a method aimed to identify H_2O ice clouds in NOMAD infrared nadir data, based on the characterisation of the 2.7 μm ice absorption band. A brief description of the NOMAD instrument and of the nadir observations that we used in this study is presented in Section 6.2. Then, we describe the methodology of the study and derive the Frost and Clouds Index in Section 6.3. The analysis of NOMAD nadir data for MY34 and MY35 is performed in Section 6.4, where the results obtained over 1.5 MY of NOMAD acquisition are discussed and compared to previous studies and model predictions.

6.2 NOMAD instrument

The Nadir and Occultation for MArs Discovery (NOMAD) instrument is a suite of three high resolution spectrometers that was selected as part of the payload of the 2016 ExoMars-Trace Gas Orbiter (TGO) mission. Led by the Royal Belgian Institute for Space Aeronomy (BIRA-IASB), NOMAD has been observing the Martian atmosphere since March 2018 ($L_S = 150°$ in MY34) through three channels operating in the ultraviolet-visible (UV-VIS), and infrared (IR) spectral ranges. A first spectrometer is devoted to solar occultation observations (SO channel), operating in the 2.3-4.3 μm IR spectral range. A second spectrometer, capable of performing nadir, limb, and solar occultation observations (LNO channel) covers the 2.3-3.8 μm IR spectral range. A third spectrometer (UVIS channel) can work in the three observation modes covering the 200-650 nm UV-VIS spectral range. A complete description of the instrument can be found in the following papers[2]: Neefs et al. (2015), Vandaele et al. (2015c), Thomas et al. (2016), and Patel et al. (2017).

In the present work, we select the LNO channel for the nadir observations covering the 2.3-3.8 μm IR spectral range with a spectral resolution of 0.3 cm^{-1} (Liuzzi et al., 2019). This channel provides observations of the Martian surface and atmosphere with a typical integration time of around 200 ms. The ground track footprint is approximately 0.5 km $\times$ 17.5 km from the TGO orbit, 400 km above Mars. Therefore, NOMAD-LNO is able to map the majority of the surface of the planet every 30 sols (Thomas et al., 2016). The spectrometer does not observe the whole LNO spectral range simultaneously. Instead, acquisitions are performed nearly simultaneously in 22 cm^{-1} wide spectral windows (called here orders from now on), representing specific diffraction orders of the diffraction grating. Considering the signal-to-noise ratio (SNR), a maximum number of 6 diffraction orders can be selected for each observation every 15 s, by suitably tuning the frequency of the entrance Acousto-Optical Tunable Filter (AOTF) (Liuzzi et al., 2019) through an internal radio-frequency generator. We use level 1A LNO data, which provides data converted into a reflectance factor, i.e., the LNO radiance divided by the measured Solar flux at Mars and by the cosine of the solar zenith angle. The LNO reflectance factor defined at wavelength λ can be written as

$$R_\lambda = \frac{1}{\cos(SZA)} \frac{\pi L_\lambda}{\Phi_{Sun_\lambda} d_{Mars}^2} \tag{6.1}$$

where L_λ is the LNO measured spectral radiance (W m^{-2} sr^{-1} μ m^{-1}), Φ_{Sun_λ} is the Solar flux at 1 astronomical unit (au), d_{Mars} is the Sun-Mars distance in au, and SZA is the solar zenith angle. More details about the LNO calibration we adopt are presented in Thomas et al. (2022a). A slightly different calibration approach, in agreement with the former, within 3%, is given by Cruz Mermy et al. (2022).

[2]See also Chapter 2.

It is important to note that the general shape of the NOMAD raw spectra is strongly affected by the AOTF transmission and by the spectral response of the grating, i.e., the Blaze function (Thomas et al., 2016). While the Blaze function is defined by a sinc-squared function, the AOTF transmission presents a strong peak with several side-lobes. A combination of a sinc-squared function with a Gaussian is used to represent the AOTF curve (Liuzzi et al., 2019). Nevertheless, these secondary peaks allow photons from a larger spectral range to fall on the grating. As a result, an unexpected signal is summed with the expected spectral information. This becomes significant on the edges of each order. After the spectral and radiometric calibrations (Liuzzi et al., 2019; Thomas et al., 2022a; Cruz Mermy et al., 2022), the AOTF and Blaze modulations also propagate to the reflectance factor conversion in the form of low-frequency oscillations in the spectral continuum. For this reason, we only work with reflectance factors at the central value of each spectral order in order to mitigate these oscillations.

Regarding the SNR of the data, Thomas et al. (2016) made an analysis taking into account different sources of uncertainty. The main source of noise is represented by the instrument thermal background, which limits the integration times in order to avoid the saturation of the detector. The 15 s period of observations is divided by the number of orders (maximum of 6). Therefore, measuring fewer orders achieves a better SNR. In the same sequence of observations, two or three orders are typically measured, given an average SNR value of 10. For the best scenario, strongly affected by SZA, the measured SNR is expected to be around 15-20 (Thomas et al., 2022a).

6.3 Methodology

6.3.1 Data selection

The first step of this work is to identify the water ice spectral features covered by NOMAD diffraction orders. A brief description of the spectral content and main scientific focus of each available LNO diffraction order is presented in Oliva et al. (2022), who discussed the capability of the NOMAD infrared nadir channel to detect surface ice by using a spectral ratio with orders 190 (2322.9-2341.5 nm) and 169 (2611.8-2632.7 nm)[3]. These two orders allowed estimation of the relative depth of the 2.7 μm absorption band, which is the strongest CO_2

[3]See Section 3.4.1 in Chapter 3.

and H_2O ice absorption band in the LNO spectral range. However, this approach is less effective for the detection of transient phenomena such as ice clouds. It hence requires a more stringent temporal and spatial coincidence between the two orders. Nevertheless, as detailed in Section 6.2, NOMAD is not capable of observing its entire spectral range simultaneously due to its mode of operation and high resolution. Therefore, NOMAD alternates observations according to diffraction orders[4]. As a result, the observation period of order 190 does not fully coincide with the other. We are therefore very limited in the temporal coverage. For this reason, we investigate an alternative approach focused on orders 169 (2611.8-2632.7 nm), 168 (2627.2-2648.2 nm) and 167 (2642.8-2663.9 nm), all falling on the short-wavelength shoulder of the strong 2.7 μm ice absorption band (see Figure 6.1).

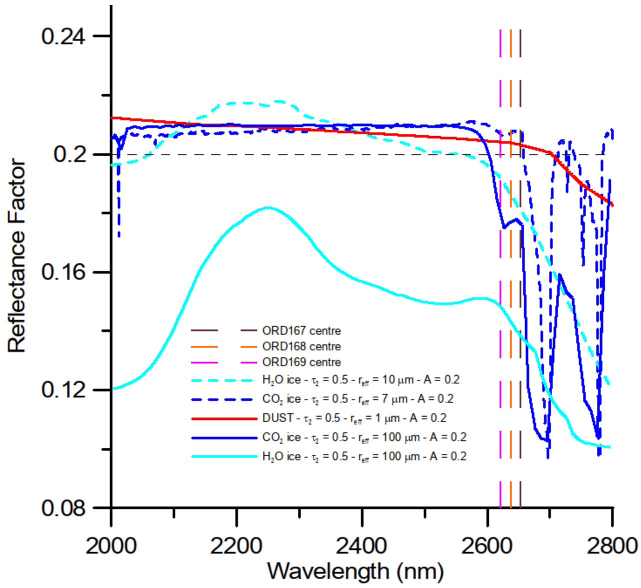

Figure 6.1: Simulated ice and dust spectra in the 2-2.8 μm range obtained by the MITRA tool (Adriani et al., 2015; Sindoni et al., 2017; Oliva et al., 2016, 2018). The simulations have been performed with the following characteristics: a surface albedo of 0.2 (A = 0.2), an incidence angle of 0° (i = 0°), and an optical depth at 2 μm of 0.5 ($\tau_2 = 0.5$). We describe all aerosol layers by adopting lognormal size distributions with an effective variance of 0.1 ($v_{eff} = 0.1$) and characteristic grain sizes (r_{eff}). Vertical dashed lines indicate the centres of orders. See the legend on the panel for the colour definition.

[4]See also Chapter 2.

Figure 6.1 presents simulated CO_2 ice, H_2O ice, and dust reflectance spectra using the Multiple scattering Inverse radiative TRansfer Atmospheric (MITRA) tool (Adriani et al., 2015; Sindoni et al., 2017; Oliva et al., 2016, 2018). MITRA code is based on the multi-solver LibRadtran radiative transfer package (Mayer and Kylling, 2005) and can be operated both as a forward model and as an inverse retrieval algorithm to study planetary atmospheres (Adriani et al., 2015; Sindoni et al., 2017; Oliva et al., 2016, 2018). In this study, we take advantage of the forward model in order to reproduce spectra in the LNO spectral range. Nevertheless, we do not attempt to derive aerosol microphysical information. Indeed, as we work in nadir mode, the signal is highly convoluted with the surface properties and therefore, abundance and grain size retrievals are characterised by non-negligible uncertainties when using only a few orders. Regarding the ice reflectance spectra, surface CO_2 ice and H_2O ice are simulated with effective radii of 100 μm ($r_{eff} = 100$ μm) (dark/light blue solid lines), while $r_{eff} = 7$ μm and 10 μm are respectively used for CO_2 ice and H_2O ice clouds (dark/light blue dashed lines). Conversely, the red solid line represents the dust spectrum with $r_{eff} = 1$ μm (Oliva et al., 2022). As highlighted by the vertical dashed green line, order 190 is located on the ice cloud continuum. The challenge of this work is to define a technique that exploits only orders 167, 168, 169 and that allows detection of H_2O ice clouds and frost separated from dust (see Section 6.3.2 and Section 6.4.2).

6.3.2 Frost and Clouds Index through the 2.7 μm Absorption Band

In the LNO spectral range, the surface reflectance is the main source of signal variability. Therefore, any effort to detect ice cloud's spectral signatures has to account for the surface contribution. Previous studies using MGS-TES (Christensen et al., 2001), MEX-OMEGA (Bibring et al., 2004b), and CRISM (Murchie et al., 2007) nadir observations have demonstrated albedo spatial variations over the whole Martian surface (Christensen et al., 2001; Viviano et al., 2014; Riu et al., 2019b). These albedo variations, coming from different surface mineralogy absorptions, also represent the main source of variability in LNO reflectance factors. By comparing LNO reflectance to a Martian albedo map it is possible to remove surface albedo contributions and to spotlight anomalous detections resulting from, for example, an ice cloud's spectral signature. To this extent, OMEGA data provide reflectance spectra in the NIR allowing the construction of albedo maps in the 0.97-2.7 μm spectral range (Riu et al., 2019b). Nevertheless, as cautioned by

Riu et al. (2019a), OMEGA albedo maps can be partially biased in low-albedo equatorial terrains, where plagioclase minerals predominate (Christensen et al., 2000; Poulet et al., 2009; Riu et al., 2019a). Indeed, in the NIR, this mineral phase presents a lack of spectral absorption features that may be altered by the presence of dust and could constitute a caveat for the construction of OMEGA albedo maps. On the contrary, TES is able to detect plagioclase features in the TIR range (Christensen et al., 2000), and therefore, takes into account the low-albedo equatorial terrains effect on the NOMAD spectra. Moreover, TES data are also filtered to partially minimise the effect of atmospheric dust and clouds. For these reasons, we will rely on the TES bolometric albedo (0.3 to 2.9 μm), instead of the NIR OMEGA albedo (0.97-2.7 μm), as a reference for evaluating anomalies in the LNO reflectance factors.

For each LNO observation, i, characterised by different longitudes and latitudes, we define for simplicity the LNO$_{Norm}$ ratio as

$$(LNO_{Norm})_i = \frac{R_i}{TES_i} \tag{6.2}$$

where R is the reflectance factor value taken at the centre of the selected order (i.e., at λ = 2622.3 nm, 2637.8 nm, and 2653.6 nm for orders 169, 168 and, 167 respectively), and TES is the bolometric Martian albedo value averaged in each considered LNO footprint. Such a ratio will be sensitive to anomalies pertaining to both ice and dust, and for this reason, we investigate how it behaves with the two components by performing simulations with the MITRA tool.

Figure 6.2 illustrates LNO$_{Norm}$ simulations of dust and H_2O ice, adopting average effective radii and optical depths, and considering order 169 as an example (dashed lines). The ice absorption makes the resulting curve depart significantly with respect to the dust curve. Conversely, the same behaviour is not observed in order 190, also shown in Figure 6.2 as reference, where the two curves are quite similar (solid lines). It is important to stress that changing the aerosol's microphysics in the simulations has an impact on the LNO$_{Norm}$ value, in principle making dust mimic ice anomalies especially on low-albedo terrains and hence, possibly yielding false positive detections.

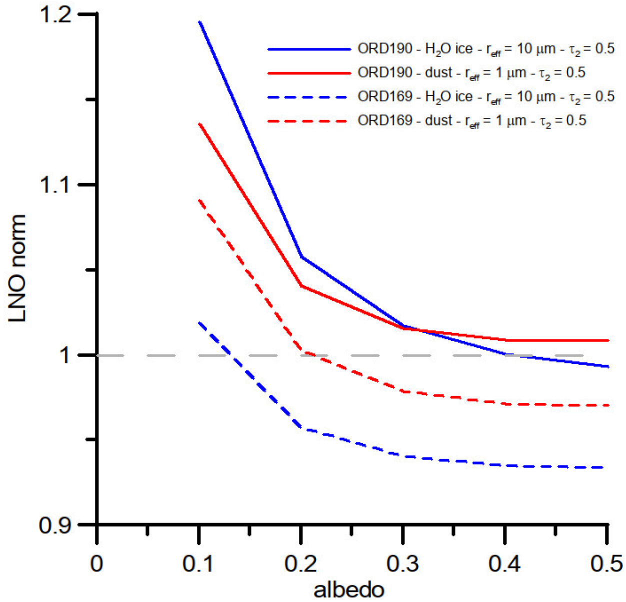

Figure 6.2: Simulated LNO$_{Norm}$ vs. arbitrary albedo obtained by the MITRA tool. The simulations have been performed for water ice and dust using orders 190 and 169. See the legend on the panel for the colour definition.

Given that LNO data moderate SNR, the LNO$_{Norm}$ parameter is affected by non-negligible fluctuations. In order to mitigate this effect, we combine LNO$_{Norm}$ of the three orders defining a Frost and Clouds Index as

$$FCI = \frac{1}{LNO_{Norm}167 \times LNO_{Norm}168 \times LNO_{Norm}169} \tag{6.3}$$

where $LNO_{Norm}167$, $LNO_{Norm}168$ and $LNO_{Norm}169$ are respectively the LNO$_{Norm}$ values defined in Section 6.3.2 for orders 167, 168, and 169.

Similarly to Figure 6.2, simulations have been performed for FCI in the presence of suspended dust and water ice particles (see Figure 6.3). Given the way FCI is defined, as expected, its simulated values are larger for water ice (blue line). While the LNO$_{Norm}$ ratio allows to spot anomalous detections in presence of water ice clouds, FCI allows to emphasise simultaneous detections happening in the three orders and helps to potentially derive a threshold value for ice detection as will be shown in Section 6.4.1. Nevertheless, it is important to mention that, despite the TES map being filtered to minimise the effect of atmospheric dust and clouds, it still contains surface ice (Christensen et al., 2001), increasing the uncertainty in transitional ice/no-ice regions. As in the case of the Ice Index (Oliva et al., 2022), the discussion coming from the FCI is semi-qualitative and the value that we derive later should not be considered as an actual threshold for ice detection, but rather an indication for abundant frost or dense water ice clouds.

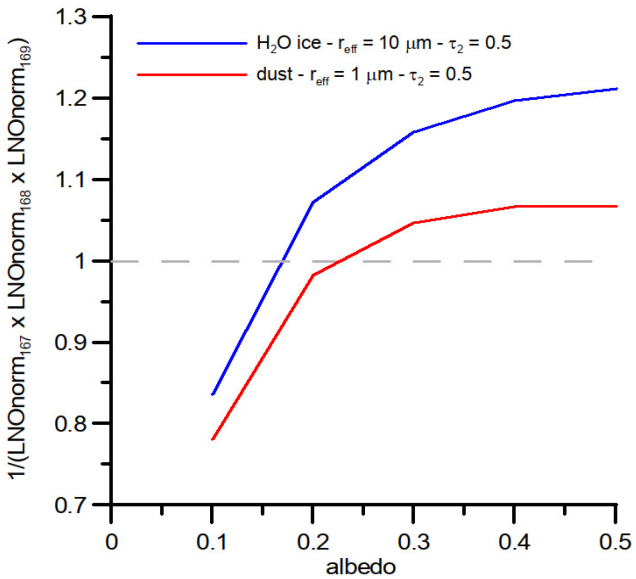

Figure 6.3: Simulated FCI vs. arbitrary albedo obtained by the MITRA tool. The simulations have been performed for water ice (in blue) and dust (in red) using orders 167, 168 and 169.

6.4 Data Analysis and Results

For this study, we analyse 1.5 Martian Years of NOMAD-LNO nadir infrared observations thanks to the three orders mentioned in Section 6.3.1. Table 6.1 presents the number of orbits acquired for each order. Even if order 168 has been deeply used in MY35, we globally note a fair distribution in the total number of observations between MY34 and 35.

	MY34: L_S = [150° - 360°]	**MY35: L_S = [0° - 360°]**	**Total**
Order 167	682	371	1053
Order 168	504	1144	1648
Order 169	694	403	1097
TOTAL	1880	1918	3798

Table 6.1: Number of LNO orbits through the 3 orders close to the 2.7 μm ice absorption band (i.e., 169, 168, and 167) in MY34 (starting at L_S = 150° which is the beginning of the NOMAD science phase) and MY35.

In order to focus the analysis on seasonal ice coverage, we construct a latitudinal-seasonal map of FCI (see Figure 6.4). Initially, all the LNO data are organised by latitude (from 90°N to 90°S) and time (MY34 and 35), expressed in terms of L_S, with a 2° × 2° binning. Each bin of latitude and L_S contains data averaged at all available longitudes. By computing the FCI map, we keep track of the observations falling into common bins for all the three orders. Then, we remove the worst-case scenarios with the lowest SNRs, i.e., below SNR ∼10. We hence select the LNO observations with a solar zenith angle lower than 60°, as larger illumination angles seriously affect the signal intensity measured by NOMAD. In order to keep a significant colour dynamic, in Figure 6.4 we saturate the colour bar for FCI values larger than 3. Important saturations can be observed at the highest latitudes in both hemispheres, i.e., when L_S = 180°-270° in MY34-35 in the Southern hemisphere and when L_S = 0°-45° in MY35 in the Northern hemisphere. These observations represent the sublimation phase of the polar cap (Piqueux et al., 2003; Langevin et al., 2007; Schmidt et al., 2009, 2010; Cull et al., 2010; Hansen et al., 2013; Oliva et al., 2022). Indeed, surface ice presents a strong absorption at 2.7 μm (see Figure 6.1) and directly impacts the FCI values. The polar regions are deeply discussed in Oliva et al. (2022), which investigates the LNO information content in order to obtain latitudinal-seasonal maps for CO_2 ice in both polar regions. Being outside the scope of this chapter, the polar caps observations are not discussed in detail here[5].

[5]See Chapters 3 and 4.

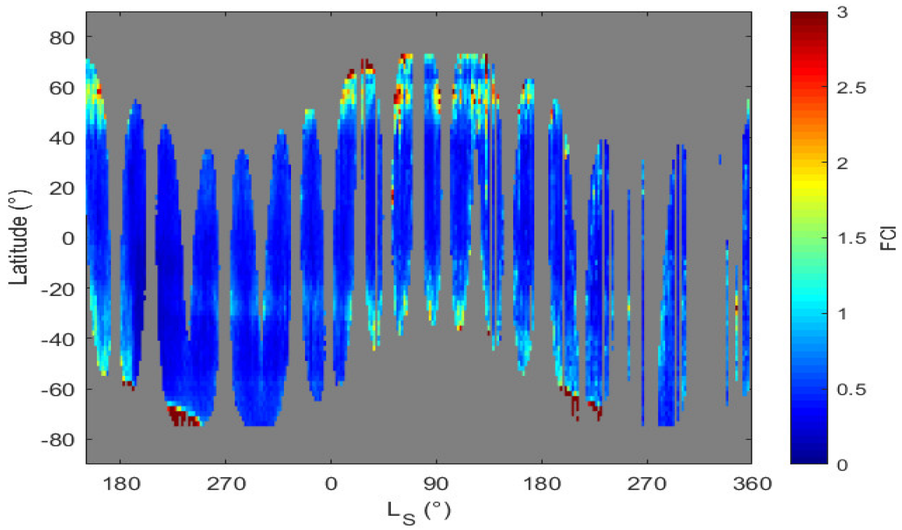

Figure 6.4: Latitudinal-seasonal map of FCI. Observations cover MY34, from L_S = 150° to 360°, and all MY35.

However, we observe bins with a high FCI value also in non-polar regions. In the Northern hemisphere, most of them can be found above latitude 40°N. Some high FCI values are also present around the equator for L_S = 45°-180° in MY35. In the South, from latitude 20°S to 40°S, FCI returns some saturated pixels for L_S = 150°-180° in MY34 and around L_S = 90° in MY35. The investigation of these non-polar high FCI pixels is discussed in the following section. First, we discuss the sensitivity of FCI to detect frost (see Section 6.4.1). Then, we attempt to derive a detection limit for water ice clouds (see Section 6.4.2).

On the other hand, as already mentioned in Section 6.3.2, different surface mineralogies are responsible for the global variations of surface albedo (Bandfield et al., 2000; Bandfield, 2002; Rogers and Christensen, 2003). This affects the measured reflectance, especially over regions of low surface albedo (Viviano et al., 2014; Szantai et al., 2021). It is worth noting that the high FCI values around latitude 60°N are over low surface albedo regions. This dark latitudinal band covers Acidalia and Utopia Planitia (Rogers et al., 2007). Szantai et al. (2021) studied the diurnal cloud life cycle over these large regions using OMEGA data. Similar to the NOMAD data analysis in this work, they defined a spectral ratio (Reversed Ice Cloud Index (ICIR) based on Madeleine et al. (2012a)) at the 3.1 μm water ice absorption band and used it as a proxy of the water ice column. The results are not always in agreement with the model predictions. They found the highest ICIR uncertainty (<20%) over Acidalia and Utopia Planitia, regions with low surface albedo. For that reason, we also investigate the possibility of having surface effect residues in the results (see Section 6.4.3).

6.4.1 Frost Detection

We discuss here the possibility to derive a threshold value for the detection of frost. In order to define a quantitatively and statistically robust threshold value, we compute the histogram of FCI values distribution in logarithmic X-scale. As shown in Figure 6.5, the bulk of the histogram follows a Gaussian distribution peaked at -0.35 ($\mu = -0.35$) with a standard deviation of 0.13 ($\sigma = 0.13$). Nevertheless, the distribution is not totally symmetrical around its mean value. We can observe a wing on the right-hand side of the distribution, corresponding to the high FCI pixels in Figure 6.4. Similarly to what has been done by Oliva et al. (2022), we are able to tune the threshold value so that the edge of polar caps is detectable. This happens for FCI values exceeding the average value of the distribution by 3.5σ. This threshold is indicated by the vertical dashed red line in Figure 6.5. As a comparison, we also estimate an average FCI value for polar deposits, represented by the vertical dashed blue line (Figure 6.5). Sensitive to surface ice deposits, the FCI value over the polar cap exceeds the average value of the distribution by 10σ.

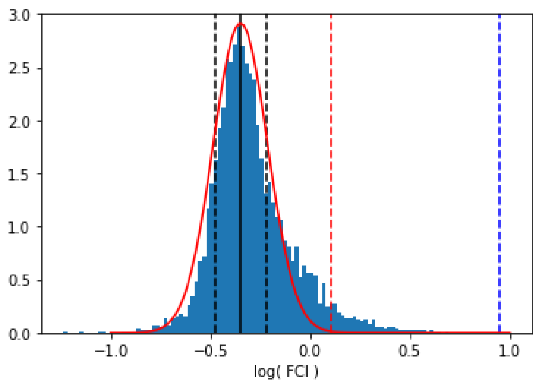

Figure 6.5: FCI values distribution in logarithmic X-scale for MY34-35. Solid black line: mean value of the distribution ($\mu = -0.35$). Dashed black line: standard deviation of the distribution ($\sigma = 0.13$). Dashed red line: mean value of FCI at the polar cap edge ($\mu+3.5\sigma$). Dashed blue line: mean value of FCI on the polar cap deposits ($\mu+10\sigma$).

We apply it on the FCI map of Figure 6.4 and present the results in Figure 6.6. As expected, detections in the polar regions (see regions 1, 2, and 3 in red) are in good agreement with the expected boundaries of the polar caps, but high values of FCI are also found at mid-latitudes. We now focus on these detections found at latitudes within the range of $\pm$ 30° (see regions from A to G in Figure 6.6). A possible explanation for these detections is the presence of ice surface deposits. In order to verify this hypothesis, we need to take into account two parameters: the surface temperature (T) and the Local Solar Time (LST). Indeed, even at mid-latitudes, temperatures may drop below the frost point, i.e., T $\sim$148K for CO_2 (Piqueux et al., 2016) and T $\sim$193K for H_2O (Carrozzo et al., 2009) at 610 Pa (average Martian pressure at 0 elevation). This can be achieved in the early morning just after the sunrise. Piqueux et al. (2016) observed surface temperatures consistent with CO_2 frost at all latitudes and predicted a survival time of less than 1 hour after sunrise. On the other hand, the Martian topography may play an important role, especially within ancient volcanoes, cracks, and craters. This complex geometry of terrain allows the existence of shadowed areas on a local surface, which can maintain low temperatures even during the day. Taking into account the LST (see Figure 6.6), we use the Mars Climate Database v5.3 (MCD) (Forget et al., 1999; Millour et al., 2018) in order to estimate the surface temperature for the mid-latitude detections in the end of MY34 (region A) and MY35 (from region B to G). For all these detections, the MCD predicted surface temperatures are listed in Table 6.2. It can be seen that MCD predicts surface temperatures that are always higher than the H_2O frost point (T >193K). We can hence exclude the presence of both CO_2 and H_2O frost even for 8:20 and 8:25 LST, where residual night frost can survive (see Table 6.2 for D1 and F1). Moreover, the MCD predictions for the regions A, E, F and, G seem consistent with Carrozzo et al. (2009) who observed H_2O frost only before L_S = 150°. In contrast, as mentioned above, frost can survive in shadowed regions along scarps and craters. However, this possibility is not easy to verify due to the large NOMAD nadir channel footprint (see Section 6.2).

Given the above discussion, we see that the interpretation of mid-latitude detections (regions A to G in Figure 6.6) as surface frost can be discarded. In contrast, the detections in the regions B, C and, D fall in the Aphelion season, i.e., L_S $\sim$60°-160°. During this season, the Aphelion Cloud Belt occurs every year at low latitudes. Therefore, these regions could be suitable for ACB detections. Moreover, in Figure 6.6, we can also see many detections present at high latitudes (above 40°N and below 30°S in MY34-35) which relate to another important atmospheric structure, the Polar Hood. We hence decide to verify the cloud hypothesis in the next section by selecting specific regions where clouds are expected to be present by general circulation models or have been observed by other instruments.

Region of Interest	**L$_S$ (°)**	**Latitude (°)**	**LST**	**T(K)**
A	301 (MY34)	−27	16:12	282
B	51	11 to 29	16:00	254
C	133	16 to 21	13:18	236
D1	117	−5	08:25	220
D2	129	−7	15:40	260
E1	225	17	15:55	251
E2	267	19	10:43	253
F1	205	−25	08:20	240
F2	218	−23	15:56	279
F3	255	−24 to −30	15:57	286
G	347	−23 to −36	15:38	265

Table 6.2: Solar longitudes (L$_S$), latitudes, local times (LST), and MCD predicted surface temperatures (T) of the regions of interest (A to F) identified in Figure 6.6. Numbers in the regions D, E, and F represent bins from left to right in each region.

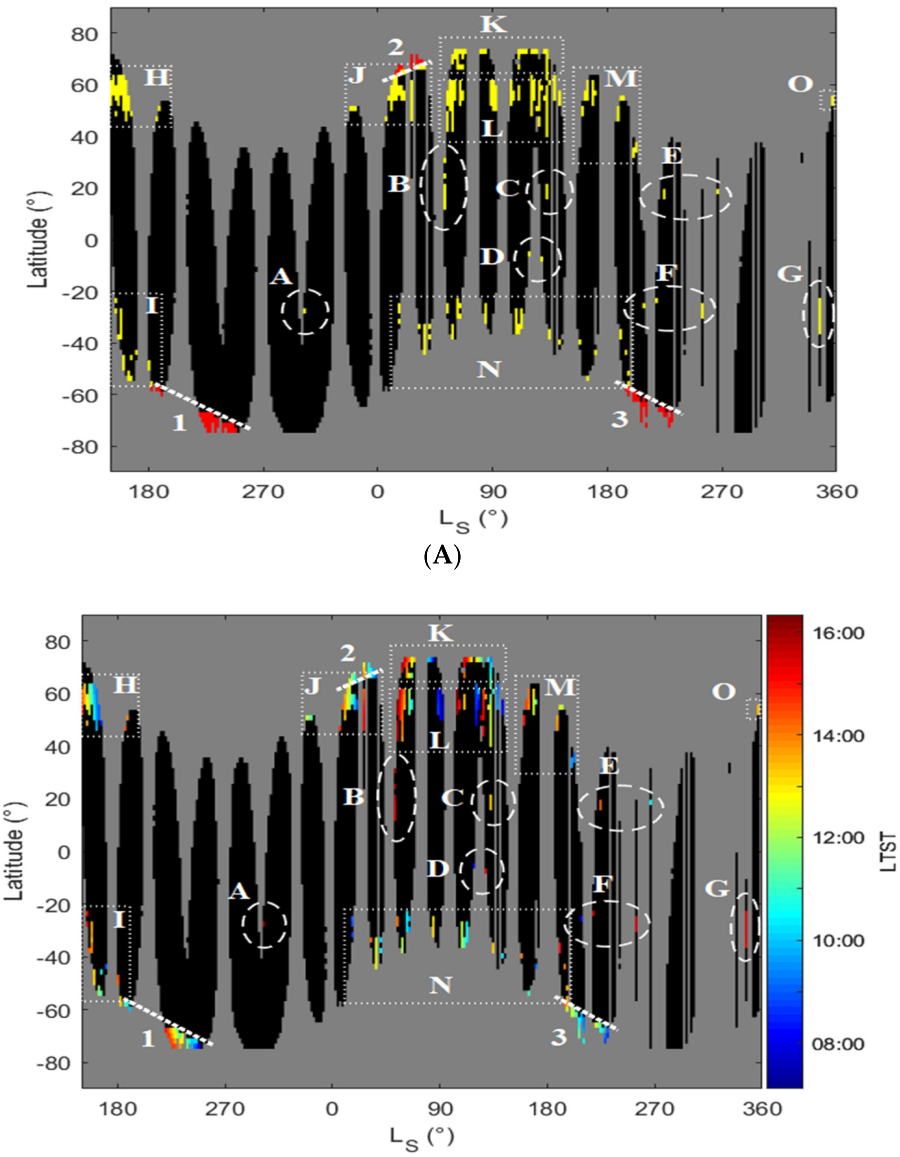

(A)

(B)

Figure 6.6: Latitudinal-seasonal maps of FCI. Observations cover MY34, from $L_S = 150°$ to $360°$, and all MY35. (A) Yellow and red points indicate a FCI value above 3.5σ. The regions 1, 2 and, 3 in red correspond to the expected boundaries of the polar caps. The letters define regions of interest for cloud detection in yellow. (B) Colour points indicate the corresponding LST.

6.4.2 Water Ice Cloud Detection

As already mentioned in the previous section, Figure 6.6 presents high FCI values even outside the red regions 1, 2 and, 3. In the Northern hemisphere, they are found above latitude 40°N. Moreover, we observe high values in the Southern hemisphere, mainly before L_S 180° (MY34) and around L_S 90° (MY35), in addition to the scattered detections at mid-latitudes (see Section 6.4.1). In this section, we verify the possibility to spot potential clouds using the FCI. To this extent, we highlight new regions of interest in which the detections are spotted (see the regions H to O in Figure 6.6). As we can observe, for the regions H to O in Figure 6.6, the LST mainly concentrates in a range of about 2 hours around noon. Nevertheless, early detections exist in region L (see at L_S 90° and 164° and latitudes around 50°N), with a 7:13 LST and 8:45 LST respectively. MCD simulations always predict surface temperatures higher than 197K and are, therefore, inconsistent with the presence of frost. For this reason, we suggest that the detections are related to atmospheric ice (see Section 6.3). However, it is important to keep in mind that this region may lead to surface effect residues present in the results (see Section 6.4 and Section 6.4.3 for more details).

Two main cloud structures can be observed on Mars: the Polar Hoods (PH) and the Aphelion Cloud Belt (ACB) (see Section 6.1) (Willame et al., 2017; Clancy et al., 2019; Wolff et al., 2019). The PH occurs above the high latitudes (∼40°N and ∼40°S) of the winter hemispheres. The Northern Polar Hood (NPH) is usually observed about three-quarters of the Martian Year, starting at L_S 150°, and covers all longitudes. Moreover, the NPH is always extended to the pole (Benson et al., 2011). Instead, the Southern Polar Hood (SPH) is an annular ring that is not extended to the pole due to less available water vapour in the South than in the North (Smith, 2008). The SPH is only present during two phases: between L_S = 10°-70° (phase 1) and between L_S = 100°-200° (phase 2) (Benson et al., 2010). During phase 1, the structure is extended over a large range of latitudes, namely from 30°S to 75°S. As shown in region N, FCI detections are present from latitude ∼25°S to 50°S. Given the period of observations (L_S = 0°-200°), the FCI results appear to be compatible with clouds in the SPH. Figure 6.7 presents a direct comparison with the MCD simulations. However, the limited coverage for the Southern hemisphere does not allow us to observe the whole cloud structure. Nevertheless, we are able to observe the evolution of the SPH at equatorward latitudes. Detections between L_S = 15°-83° appear compatible with phase 1. On the other hand, phase

2 seems to cover L_S 107° to 195°, following the recession of the polar cap. This phase is partially observed in region I (L_S = 153°-187°) due to the lack of observations in MY34. Moreover, it is worth noting that the specifics of the TGO orbit influence the spatial and temporal coverages of the NOMAD observations. Indeed, as shown in Figure 6.6, the LST changes over the latitudes and L_S. Nevertheless, important diurnal variations of water ice clouds occur in the Martian atmosphere. Such effects can hence affect the results, underestimating the presence of clouds compared to the MCD predictions (Wilson et al., 2007; Wu et al., 2022). For example, at L_S 20°, observations are acquired in the morning for the Southern hemisphere. At that time, MCD predicts a low water ice column at the probed latitudes (see Figure 6.7). On the other hand, at L_S ~100°, MCD simulations seem to be more in agreement with the FCI results by selecting a LST in the early afternoon (see Figure 6.7).

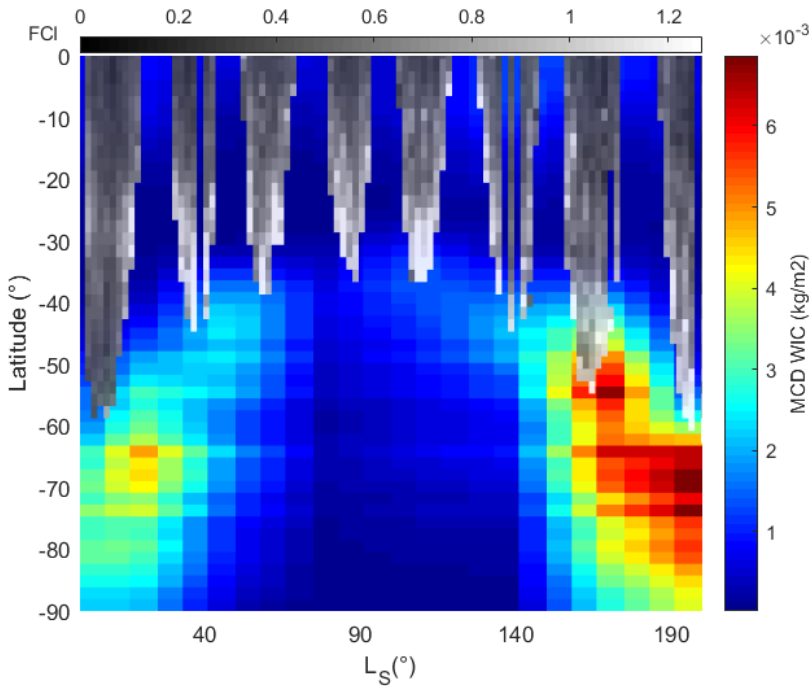

(A)

Continued on the next page.

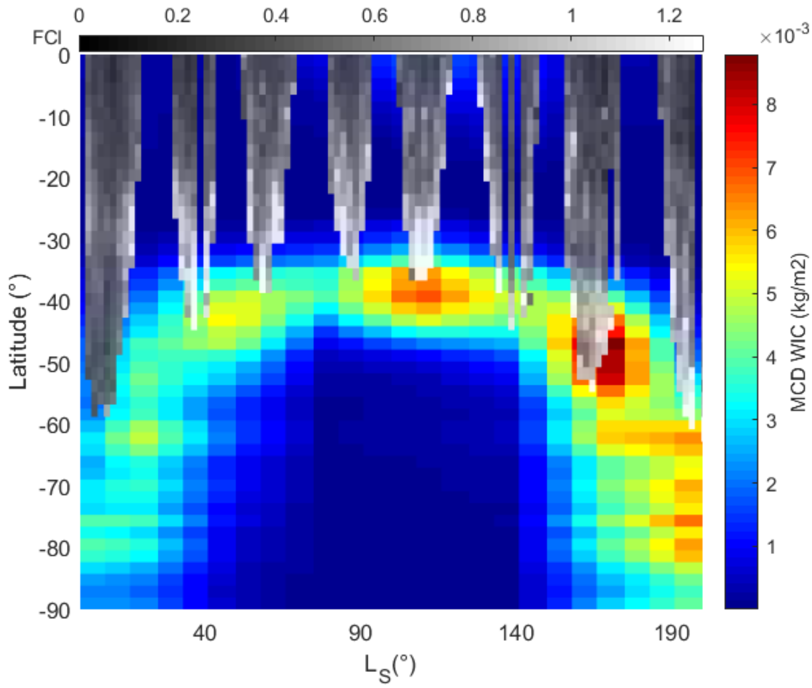

(B)

Figure 6.7: Comparison between the latitudinal-seasonal map of FCI (grey scale) with the one of MCD Water Ice Column (colour scale) for latitudes from 0° to 90°S and L_S 0° to 200°. Grey scale: FCI results in region N (see Figure 6.6). Saturated FCI values are in white (>3.5σ, see Section 6.4.1). Colour scale: MCD Water ice column at 9 LST (A), and 13 LST (B).

In the Northern hemisphere, we observe detections at the highest probed latitudes (see the regions J, K, M and, O) and around latitudes 50°N and 60°N (see the regions H and L). Detections in the regions H and M are compatible with the start of the NPH. Nevertheless, the limited coverage considerably reduces the number of observations during the Northern autumn and winter in MY34 and 35. On the other hand, the regions J and O appear in agreement with the end of the NPH. During spring (before L_S 40° in region J), the FCI indicates the presence of clouds up to latitude 50°N, suggesting an extended NPH. During the rest of spring and summer (L_S ~50°-150° in region K), detections are not consistent with previous studies (Benson et al., 2011; Willame et al., 2017; Wolff et al., 2019; Olsen et al., 2021). It is important to mention that the NOMAD instrument provides simultaneous observations of these clouds in the UV through the UVIS channel (see Section 6.2), that is sensitive to clouds and confirms their presence at latitude ~74°N (personal discussion with Y. Willame, ice clouds retrieval based on Willame et al. (2017)). Moreover, these results are also supported by the MCD predictions. Nevertheless, FCI detections in region L are uncommon, especially between L_S ~50° and 150°. At L_S ~50° and 150°, they cover latitudes up to 35°N. A possible explanation is that they are related to the Northern part of ACB, which seems to connect with the NPH. Although these detections are not predicted by MCD, they probably represent the so called 'cloud bridge' (Guha et al., 2021) detected during previous Martian Years (Liu et al., 2003; Smith, 2004; Mateshvili et al., 2007; Benson et al., 2010; Willame et al., 2017; Szantai et al., 2021). Given the disagreement between the model predictions and FCI detections, we decide to discuss the results for the region L in the next section.

Regarding the ACB, it is not visible in our results in Figure 6.6. The structure is known to appear at low latitudes (10°S to 30°N), with enhancements over volcanoes in the Tharsis region (Smith, 2009). Different types of clouds compose the cloud belt, ranging from formless morning thin haze to large-scale thick clouds. In terms of microphysical properties, two main groups have been observed for the thick clouds. The difference in particle size defines the core and the periphery of ACB. The first group corresponds to regions strongly controlled by local dynamics and topography. These clouds are observed over the Tharsis region with a 5 μm grain size. On the other hand, regional wind circulation forms the second group composed of large-scale clouds and is characterised by particle sizes of 2-3.5 μm (Wolff and Clancy, 2003; Madeleine et al., 2012a). In our results (Figure 6.6), only a couple of detections are present at equatorial regions during this season (see regions B, C and, D) and could be explained on the basis of the differences in morphology and microphysical properties described above. One of the reasons could be that the large LNOs footprint (Section 6.2) makes it difficult to detect optically thin hazes and clouds. On the other hand, large-scale cumulus clouds, from 5 to 10 km in size, could be detectable in the NOMAD nadir footprint. Nevertheless, they are relatively thin at the beginning of the Northern spring and only become thicker late in the ACB season. The thickest of these clouds have been observed during the early Northern summer, forming at the beginning of the afternoon (Benson et al., 2003; Madeleine et al., 2012a) consistently to the regions C and D. Moreover, the clouds' ice abundance could play an important role in their detection. Olsen et al. (2021) derived the water ice column (WIC) for MY26-32 using the nadir IR observations of OMEGA. They estimated two ranges of values, about 1.2-1.6 pr.μm over the ACB and 1.5-2.5 pr.μm over the PH. This distinction between the two cloud structures can explain the global results presented in Figure 6.6. While we register several detections over the PH, only a few isolated clouds are detected over the ACB. This behaviour suggests that the LNO nadir dataset is only sensitive to clouds with ice columns larger than 1.5 pr.μm.

As mentioned in Section 6.4.1, detections are also present at mid-latitudes during the perihelion season (L_S = 180°-360°, see regions A, E, F and, G in Figure 6.6). These results are difficult to confirm with the MCD predictions, although the simulations agree with the presence of clouds in region E for a 10:30-11 LST. Moreover, the results for the regions A, E and, F are not consistent with the OMEGA data analysis (Olsen et al., 2021). During the perihelion season, the solar flux increases and relatively warms the Martian atmosphere promoting dust activity. This hence limits water ice cloud column opacities (Smith, 2008). Nevertheless, previous works have demonstrated the presence of water ice clouds during this period. They mainly occur in the mesosphere (at altitudes above 50 km) (Clancy et al., 2019; Guzewich and Smith, 2019; Liuzzi et al., 2020). The results in the regions A, F, and G appear to be in agreement with the previous studies focused on MRO-CRISM (Murchie et al., 2007) and NOMAD-SO (SO channel, see Section 6.2) data analysis (Clancy et al., 2019; Liuzzi et al., 2020). They spotted water ice clouds around L_S 200°, 270°, 300°, and L_S 345°, which were also observed by SPICAM (Willame et al., 2017) for the regions A and G. Moreover, especially for the regions A and F, the detections correspond to the period of the perihelion cloud trails (PCT). This class of mesospheric clouds are formed between L_S 210° and 310° in the late morning to the mid-afternoon. Horizontally extended (200 to 1000 km), they are observed over specific regions between latitudes 5°S and 40°S, i.e., in the Arsia Mons, Syria, and Solis regions and along the Thaumasia Planitia, Valles Marineris margins, and the north east of Hellas Basin (Clancy et al., 2007, 2021). Given the above discussion, it is important to remind that the kind of threshold value that we use indicates abundant frost or dense water ice clouds instead of an absolute value for ice detection (see Section 6.3.2 and Section 6.4.1). Therefore, the FCI appears to be sensitive only to ice that is characterised by a particular microphysics. Nevertheless, some FCI detections (especially region L in Figure 6.6) are still difficult to justify with previous studies or the MCD predictions. For that reason, we discuss these results in the next section.

6.4.3 FCI sensitivity

It is worth noting that the detections in region L are over low surface albedo regions covering Acidalia and Utopia Planitia (Rogers et al., 2007). As already mentioned in Section 6.4, the dark latitudinal band around 60°N affects the measured reflectance (Viviano et al., 2014; Szantai et al., 2021). Therefore, we investigate in this section the possibility of having surface effects residues in the results of the region L (see Figure 6.6). We apply the FCI on observations between L_S 30° and 150° in MY35. In order to verify an eventual correlation between the FCI and the dark terrains, we can perform a direct comparison with the TES albedo map. The results are given in terms of latitude and longitude in Figure 6.8. As we can see, saturated values of the FCI ($>3.5\sigma$, see Section 6.4.1) are present over Acidalia Planitia and the North of that region (see red rectangle on the left panel). They can also be seen at the highest-probed latitudes in both hemispheres (see black circles on the left panel). These high index values should be related to the presence of water ice clouds (see Section 6.3.2 and Section 6.4.2). Nevertheless, by comparison with the right panel, we see that the high FCI values inside the red rectangle present a correlation with dark terrains. This can be explained by an overestimation of albedo values over dark regions at 2.7 μm with respect to LNO. Therefore, the high values in the red rectangle (see left panel) are likely linked to the presence of surface effect residues over Acidalia Planitia in the LNO data. This is hence in agreement with the OMEGA results in Szantai et al. (2021).

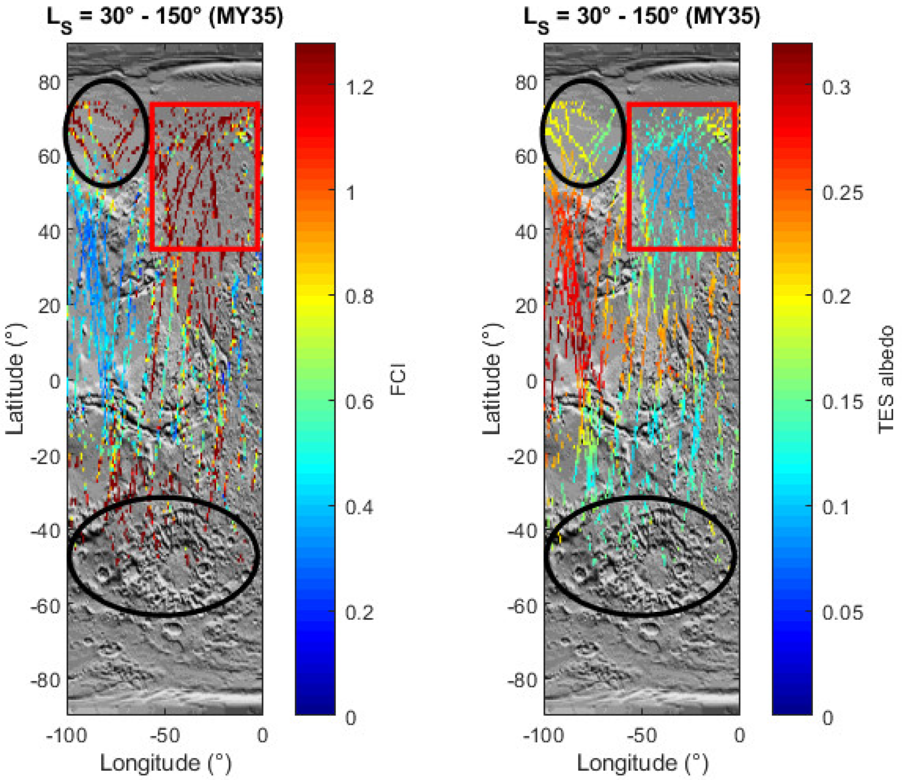

Figure 6.8: Left panel: LNO observations in MY35, from $L_S = 30°$ to 150°. Colour points indicate the FCI values saturated at 3.5σ (see Section 6.4.1). Right panel: TES albedo values falling in each bin of the LNO tracks in MY35, from $L_S = 30°$ to 150°. Red rectangle: correlation between high FCI values and region of low surface albedo. Black circle: example of high FCI values not correlated with regions of low surface albedo.

In Figure 6.8, the selected period corresponds to the aphelion season. The circles cover regions with an intermediate surface albedo. These regions are not comparable with dark regions in the Northern high latitudes (Rogers et al., 2007). Therefore, the saturated FCI values in both hemispheres are likely linked to the presence of clouds. As highlighted in Section 6.4.2, the low WIC of the ACB makes its detection difficult in the LNO spectral range (Olsen et al., 2021). The full ACB structure is not hence visible. For that reason, we attempt to derive the FCI sensitivity limit for cloud detection. From MCD simulations, we notice that the PH water ice column can take values of the same order as those of the surface water ice ($\sim 10^{-2}$ kg/m^2). They are then superior by a factor

10 to those of the ACB ($\sim 10^{-3}$ kg/m^2). However, the PH is not always fully detected (see region I in Figure 6.6). Moreover, some detections have been recorded around the equator during the Aphelion season (see the regions B-D in Figure 6.6). Local thick clouds in the ACB can hence be detected. In order to estimate the sensitivity limit of the FCI, we compare the FCI results in Figure 6.8 with the MCD predictions (see Figure 6.9). We can see that the WIC of the ACB takes values lower than 3×10^{-3} kg/m^2. In contrast, those in the centre of the SPH are generally higher than 5×10^{-3} kg/m^2, while the WIC of the NPH can reach 1.3×10^{-2} kg/m^2. From the saturated index values at the highest latitudes (white pixels), we can estimate the limit of the FCI sensitivity for cloud detection at $\sim 4\times10^{-3}$ kg/m^2. Some saturated pixels are found at mid latitudes, which may indicate the presence of thicker clouds compared to the rest of the ACB (see black circle). Nevertheless, as over Acidalia Planitia (see red rectangle), we suspect a surface effect in the detection inside the yellow rectangle. Indeed, this region covers a terrain with a low surface albedo (TES albedo lower than 0.1, see Figure 6.8).

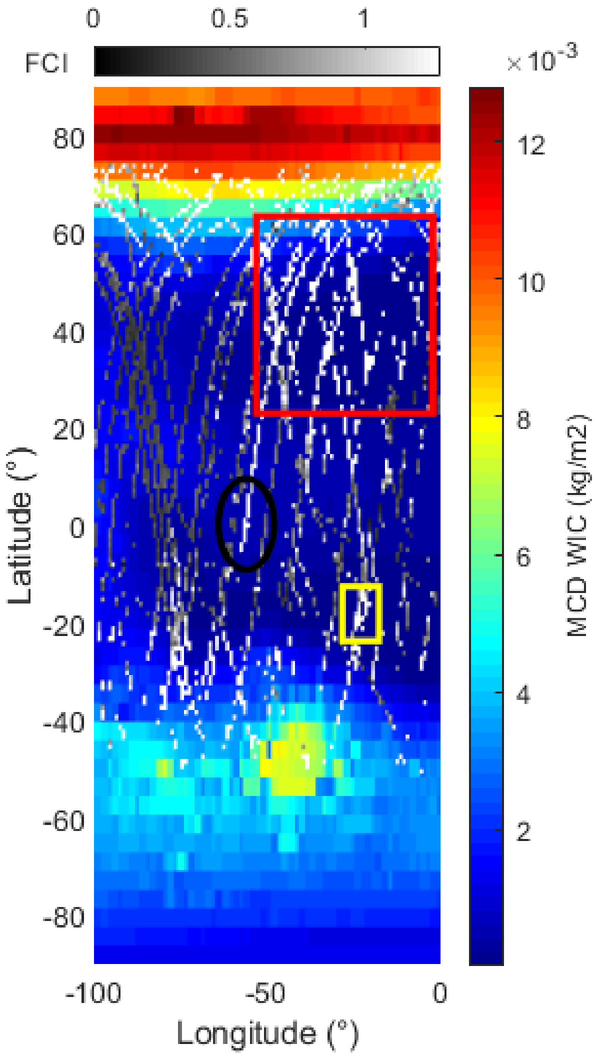

Figure 6.9: Comparison between the FCI results (grey scale) with the MCD Water Ice Column (colour scale) for all latitudes and longitude from 100° W to 0°. Grey scale: LNO observations in MY35, from L_S 30° to 150°. Saturated FCI values are in white (>3.5σ, see Section 6.4.1). Colour scale: MCD Water ice column simulation for L_S 150° and 15 LST.

6.5 Conclusions

NOMAD-LNO is a spectrometre mainly designed to investigate the presence of trace gases in the Martian atmosphere. The instrument uses preselected spectral orders to resolve the absorption lines of the single species. Due to this mode of operations and to its high resolving power, it cannot acquire a single spectrum over the full spectral range (see Section 6.2). Therefore, the spatial coverage linked to the full spectral range is also limited, since each spectral order observes a different footprint. Moreover, due to technical constraints imposed by the spacecraft, the SNR is not optimal. Finally, there is an intrinsic limitation linked to the spectral behaviour of ice clouds and dust. Depending on their microphysical properties, it can be really challenging to distinguish between them. Having all these constraints and limitations in mind, we have described a technique that takes advantage of three NOMAD-LNO diffraction orders (167, 168, and 169), covering the short wavelength shoulder of the 2.7 μm ice absorption band. The application of such a technique allows us to map surface ice and H_2O ice clouds into the Martian atmosphere. We applied the method on regions where ice clouds are either expected by general circulation models or have been observed by other instruments. The method is based on spectral ratios between LNO reflectance factor spectra and TES bolometric dust-cleaned albedo. We have defined a Frost and Cloud Index (FCI) as a useful proxy for ice mapping (see Section 6.3). We applied the method to the LNO dataset in Martian Years 34 and 35 (March 2018 to February 2021) excluding observations with SZA larger than 60° to avoid the lowest SNRs (see Section 6.4). As discussed in Section 6.4.2, the acquisition of data during MY34-35 allows us to construct seasonal maps for water ice clouds. The results appear in agreement with previous studies focused on Mars Express SPICAM/UV (Willame et al., 2017) and OMEGA data analysis (Olsen et al., 2021). FCI is sensitive to the Polar Hood clouds, although the full structure is not detected. Moreover, detections in the Aphelion Cloud Belt (ACB) are limited. This is consistent with previous OMEGA observations (Olsen et al., 2021) showing different physical properties between the two main Martian atmospheric structures and making the ACB less detectable in the infrared. We hence derived the LNO channel sensitivity limit for cloud detection (see Section 6.4.3).

Finally, the analysis presented in this chapter represents one of several studies dedicated to the exploitation of the LNO nadir dataset and opens the way for different perspectives. As a direct continuation to this work, further comparison with the NOMAD-UVIS channel about the cloud's detection is already planned. It will help to tune the FCI, hopefully to increase its sensitivity to ice clouds and to limit the number of false detections. In addition, an in-depth radiative transfer analysis of the 2.35 μm feature in CO_2 ice clouds spectra is currently being performed.

Chapter 7

General Conclusions

7.1 Summary

In this thesis, we studied surface ice (see **Chapters 3** and **4**) and ice clouds (see **Chapter 6**) on Mars (see also Table 7.1). We also investigated the effect of the 2018 global dust storm on the sublimation process of the Southern seasonal cap at global scale. To do this, we used nadir observations from the ExoMars-Trace Gas Orbiter NOMAD instrument. Although NOMAD is not primarily dedicated to surface analysis, it is the only high-resolution spectrometer currently operating around the Red Planet (see Section 1.3). We analysed data from March 2018 to December 2022, covering Martian Years 34 to 36. Considering instrumental characteristics and observation limitations (see **Chapter 2**), we defined spectral indices based on a selection of orders containing spectral ice absorption in the infrared wavelengths (see Table 7.1). This work extended the temporal coverage of seasonal processes in the polar caps and ice clouds.

Continuous observation of these seasonal processes is primordial to provide a better understanding of the interaction between the atmosphere and the surface. Indeed, the Martian climate is governed by the CO_2 and water cycle. These cycles are directly linked to the seasonal sublimation and condensation processes in the polar regions, which strongly influence the overall energy budget of the planet (Piqueux et al., 2015). In addition, the climate on Mars is also influenced by the dust load in the atmosphere (Smith, 2004; Newman et al., 2005). Extreme events, such as global dust storms, occur on Mars with large interannual variability (Smith, 2009). These events affect the CO_2 and water cycles (Piqueux et al., 2015).

In this chapter we return to the general questions raised in Section 1.4 to provide some answers based on the NOMAD-LNO results presented in this thesis.

1. In dust-free years, is there any variability in the caps?

We observed the Martian polar caps through latitudinal-seasonal maps in MY34-36 and identified at high spectral resolution CO_2 ice deposits in the polar regions, being the main component of the Southern seasonal cap (see **Chapters 3** and **4**). In addition, we analysed the sublimation of the Southern polar cap, which has the best spatial and temporal coverage compared to the North. The limited coverage of NOMAD observations in MY34-36 did not allow us to analyse the Northern seasonal processes of the cap. During dust-free years, i.e. in MY35-36, we observed a repeating seasonal pattern on a global scale (see **Chapter 4**). This is in good agreement with OMEGA observations from previous dust-free years (Langevin et al., 2007; Appéré et al., 2011) and MCD predictions (Millour et al., 2018). We confirmed that the retreat of the cap is repeatable throughout these Martian years and further refined our current knowledge of the Martian polar caps.

NOMAD's high spectral resolution offers the possibility to retrieve some microphysical ice properties. We performed a semi-qualitative equivalent grain size analysis using a radiative transfer model (Planetary Spectrum Generator model, Villanueva et al. (2018)) and found that the Southern CO_2 ice cap is characterised by ice slab in the centimetre range, in line with other studies (see **Chapter 4**). We also observed a decrease in the slab equivalent grain size with time as the polar cap sublimated. We reported no variability in slab equivalent grain size in MY35-36 compared to previous years.

2. What are the effects of the MY34 global dust storm on the dynamics of the Northern and Southern seasonal caps?

The global dust storm in MY34 provided an opportunity to study the effect of atmospheric dust on our ice detection method, i.e. spectral indices, and to analyse the sublimation of the Southern polar cap during such an extreme event. The large amount of dust released into the atmosphere during this period reduced the ice detection sensitivity of our spectral indices, with a decrease in efficiency of 40% (narrow band, e.g. 2.35 μm) and 85% (broad band, i.e. 2.7 μm), depending on the strength of the ice absorption band (see **Chapter 3**). Nevertheless, when compared to simulations that take into account dust activity in 2018 (Montabone et al., 2020), we found that our ice detection method was still effective. Using latitudinal-seasonal maps, we compared the sublimation of the Southern polar cap in MY34 with the seasonal retreat of the cap in MY35 and 36. At a global scale, we reported no interannual variations in the recession of the cap in MY34-36, highlighting the complexity of the effects of such an event on the polar ice cap (see **Chapter 4**). Future work could focus on the potential interannual variations in the recession of the cap at local scale (see Section 7.2).

3. Do ice clouds exhibit recurring seasonal behaviour, even in dusty years?

Our spectral approach proved that NOMAD is also able to detect atmospheric ice signatures. By analysing the 2.7 μm water ice band, we constructed seasonal maps for H_2O ice clouds, allowing to observe the Polar Hood clouds at high latitudes and their variability. We observed a few detections in the Aphelion Cloud Belt (ACB), but the whole structure was not visible. This is explained by the difference in ice abundance between the two main atmospheric structures on Mars, which makes the ACB less detectable in the infrared spectral region (see **Chapter 6**). The results obtained are consistent with previous studies (Willame et al., 2017; Clancy et al., 2019; Wolff et al., 2019; Szantai et al., 2021), highlighting the seasonal nature of the spatial distribution of clouds. It is difficult to know whether the MY34 global dust storm had any impact on cloud formation in MY35.

As explained in **Chapter 6**, we normalised the NOMAD data using TES bolometric albedo to minimise surface albedo effects, in order to detect signals coming from the presence of H_2O ice cloud. Nevertheless, we found that the low surface albedo regions around 60°N affected the results. Another option was to use OMEGA albedo map instead of TES albedo. Besides the low surface albedo effects around 60°N, we observed artefacts in the results over low surface albedo equatorial regions. One possibility would be to construct an albedo map from several instruments, taking into account their sensitivity to variations in surface albedo. OMEGA albedo could be used for high albedo regions such as Tharsis (see **Chapter 5**), and TES albedo for low surface albedo regions around the equator and medium surface albedo regions in general. Concerning the dark latitudinal band region around 60°N, it would be interesting to derive an albedo map for these regions from NOMAD observations.

We also detected mesospheric CO_2 ice clouds using the 2.35 μm CO_2 ice band. This is the first detection of such clouds using this band and highlights their seasonal distribution at equatorial latitudes in line with previous studies. Following a semi-qualitative grain size analysis, we found that these clouds are compatible with fine grains ranging from 1 nm to 10 nm (see **Chapter 3**). An in-depth analysis of CO_2 ice grain size using a dedicated radiative transfer model will provide additional information on their microphysical properties (see Section 7.2).

In addition, in the frame of a morning frost campaign, the Colour and Stereo Surface Imaging System (CaSSIS) and NOMAD-LNO acquired joint observations of the Martian volcanoes. Based on our spectral method, we detected extended morning frost on the Olympus Mons caldera. We reported no CO_2 ice signature, suggesting the presence of H_2O frost. Mars Global Climate Model simulations (Senel et al., 2021) predicted surface temperature above the CO_2 frost point, which confirmed the NOMAD-LNO results. Previous studies highlighted the presence of frost in equatorial regions (Schorghofer and Edgett, 2006; Carrozzo et al., 2009; Vincendon et al., 2010a). In these regions, low surface temperatures at night favour the condensation of CO_2 and/or H_2O. This frost can persist during the first hours after sunrise, or even during the day in places sheltered from direct sunlight. As for the summit of Olympus Mons, although the presence of frost is predicted by GCM simulations, this ongoing morning frost campaign of CaSSIS and NOMAD provided the first direct observation (see **Chapter 5**). More data are expected in the near future (see Section 7.2).

In summary, this study allowed to extend surface ice and ice clouds observations over 3 Martian Years by using NOMAD's nadir observations, which are different from those provided in the past by other spectrometers such as OMEGA and CRISM (see Section 2.4 in **Chapter 2**). **Chapters 3, 4, 6** come from publications in scientific journals of which I am the first author or co-author. Only **Chapter 5** is under consideration for publication. The main results reported in this thesis can be highlighted as follows:

1. Repeating seasonal pattern in the polar regions for MY34-36
2. No interannual variations in the recession of the Southern polar cap in MY34-36 due to the MY34 global dust storm
3. Recurring seasonal behaviour of H_2O ice clouds in MY34-35 (MY36 not analysed)
4. First detection of mesospheric CO_2 ice clouds through the 2.35 μm band
5. First direct detection of morning H_2O frost at the top of the Olympus Mons

Index	**167**	**168**	**169**	**189**	**190**	**193**	**Main interest**	**Comparison with**	**Information**
Ice Index			×		×		Polar caps	OMEGA dataset GCM simulations	Chapter 3
New Ice Index	×	×	×		×		Polar caps Sublimation analysis	GCM simulations	Chapter 4
SAM χ index				×			Surface CO_2 ice CO_2 ice clouds	GCM simulations Various datasets[a]	Chapter 3
BD2292						×	Surface CO_2 ice Sublimation analysis	GCM simulations	Chapter 4
Adapted Ice Index		×			×		Morning frost	CaSSIS dataset GCM simulations	Chapter 5
Frost and Cloud Index	×	×	×				H_2O ice clouds	Various datasets[b] GCM simulations	Chapter 6

Table 7.1: Spectral indices defined in this thesis for surface ice and ice clouds detection at high spectral resolution. Columns 2-7: orders used in each index. Order 167: 2.643-2.664 μm; order 168: 2.627-2.648 μm; order 169: 2.612-2.632 μm; order 189: 2.335-2.354 μm; order 190: 2.323-2.341 μm; order 193: 2.286-2.305 μm. Columns 8-10: Main interest of each index, comparison of their results with other datasets and the corresponding chapter for more details.

[a] Comparison with OMEGA dataset for surface CO_2 ice, and with NOMAD SO, OMEGA, CRISM and SPICAM for CO_2 ice clouds.
[b] Comparison with NOMAD UVIS, OMEGA, SPICAM and MARCI observations.

7.2 Areas for perspectives

As discussed in **Chapters 3** and **4**, the use of the 2.29 μm (order 193) and 2.35 μm (order 189) CO_2 ice bands is suitable for the analysis of Martian ice deposits. Using a dedicated radiative transfer model, the CO_2 ice deposits will be analysed in detail at high spectral resolution, providing insights into the microphysical properties of the small ice crystals. Continuous observations will increase the spatial coverage in the polar regions, allowing in-depth analysis of CO_2 ice grain size variation over time at a selected location. This will allow us to detect any seasonal or interannual changes in the condensation and sublimation processes at a local level, and to determine the amount of impurity (H_2O ice and/or dust) in the CO_2 ice layers over the seasons. Indeed, a global dust storm occurred in MY34, releasing significant amount of dust into the Martian atmosphere that could have been transported to the polar regions. Although no global interannual variations have been directly observed at the Southern polar cap during the 3 Martian Years of LNO observations, it may be different at a local level. It would be interesting to compare this with other datasets, such as observations from the CRISM spectrometer, or to analyse the surface temperature to determine the extent of the ice caps at a local level. Mars Climate Sounder (MCS) data would be useful for this further work. On the other hand, global observations of the extent of the polar ice caps can be useful in our understanding of variations in the planet's rotation. For example, it can help us to better interpret data from NASA's Rotation and Interior Structure Experiment (RISE) (Folkner et al., 2018), part of the Interior Exploration using Seismic Investigations, Geodesy and Heat Transport (InSight) mission (Banerdt et al., 2020), which showed a slow acceleration in the Martian rotation rate (Le Maistre et al., 2023).

In this work, we also discussed the ice cloud detection with NOMAD-LNO, which opened perspectives for the study of atmospheric ice. Spectral analysis at mid-latitudes is already planned for the mesospheric CO_2 ice clouds detection through the 2.29 μm (order 193) and 2.35 μm bands (order 189). Radiative transfer model will provide additional information on their distribution, seasonality and microphysical properties. Moreover, further comparison with the NOMAD UVIS channel is currently being performed for the Polar Hood clouds. This channel is more sensitive to ice clouds, but in contrast to NOMAD-LNO, it is not able to distinguish between H_2O ice and CO_2 ice. The following study consists of analysing the attenuation of the ozone absorption band present in UVIS data due to the presence of the Polar Hood clouds in order to estimate their altitude. Previously identified as H_2O ice with NOMAD-LNO, we will study their microphysical properties using a dedicated radiative transfer model. This will allow us to study their entire distribution and monitor their evolution over the seasons.

Considering the frost morning campaign (see **Chapter 5**), the joint observations with CaSSIS opened a new science for NOMAD under its detection limits. After the detection of extended H_2O frost on the Olympus Mons caldera, the acquisition of spectra has been adapted to reduce the field of view of the instrument in an attempt to detect diffuse frost. To achieve this, the spectral analysis will therefore be adjusted. Moreover, all efforts are now focused on the possible detection of CO_2 frost in the Tharsis region. Certain periods of the year maximise the chances of CO_2 frost detection (from L_S 90° to 120°), i.e. when the local surface temperature is as close as possible to the CO_2 frost point (~138K). Nevertheless, continuous data acquisition is crucial to better understand local meteorological phenomena in this particular region. It may allow us to observe a seasonal process of H_2O frost and/or CO_2 frost formation over the volcanoes.

Finally, the spectral method developed in this thesis can be applied to surface studies in general using spectrometers. For example, since 2021, NOMAD-LNO provides new nadir observations of Phobos, the largest Martian moon. Based on the same spectral approach, these observations allow to search for surface spectral features. We rely mainly on water ice, but also on carbonate and phyllosilicates, as there is no constraint from the presence of the atmosphere. In addition, the work will also prepare the next Japanese mission, the Martian Moons eXploration (MMX) mission (Kuramoto et al., 2022). With a launch scheduled for September 2024, the MMX probe will observe the two Martian moons (in particular using MIRS, a near-infrared spectrometer; Barucci et al. (2021)) and land on Phobos to collect surface samples in order to solve the mystery of its origin. Moreover, the spectral data analysis developed in this work will help us to better prepare for the calibration of the Thermal Infrared Imager (TIRI) observations (Okada et al., 2022) onboard ESA's Hera planetary defence mission during its fly-by of Mars (Michel et al., 2022). On the other hand, spectral data analysis on airless bodies will better prepare the ESA JUpiter ICy moon Explorer (JUICE) mission to Jupiter system and its icy moons (Grasset et al., 2013), in particular the scientific use of Moons And Jupiter Imaging Spectrometer (MAJIS) data (Guerri et al., 2018).

Appendix A

NOMAD-LNO characteristics and calibration

A.1 AOTF characteristics

As mentioned in Section 2.2.1, the AOTF is a passband filter crystal based on the Bragg diffraction, i.e. diffraction that occurs in a crystal when an acoustic wave is applied to an optical wave (Chang, 1974; Gottlieb et al., 1994). It can rapidly and precisely select different wavelengths of light, making them useful for applications such as spectral analysis, microscopy, and remote sensing.

The AOTF tuning curve, also called the AOTF tuning relation, expresses the relation between the radio frequency A needed to produce the Bragg diffraction and the AOTF passband, i.e. the selection of the desired diffraction orders (Chang, 1974, 1981; Mahieux et al., 2009). It is defined as

$$A = \frac{w\Delta n}{\lambda}(sin^4 i + sin^2 2i)^{1/2} \tag{A.1}$$

where i is the incident angle of the wave, w represents the acoustic velocity, Δn gives the birefringence of the crystal and λ is the central wavelength of a selected AOTF band. It is important to note that the AOTF tuning curve is temperature dependent. Temperature variations result in mechanical strain leading to a shift in the detected frequencies.

Reffered to an intrinsic problem, this issue was observed during the laboratory experiments (Neefs et al., 2015; Thomas et al., 2016; Liuzzi et al., 2019) (see Section 2.2.3).

As mentioned in Section 2.3.1, the AOTF itself, i.e. the AOTF transfer function, is theoretically defined as a strong peak surrounded on either side by second lobes, whose contribution is estimated to be less than 15 % of the main lobe. Therefore, the total observed flux can be affected by the contribution of adjacent orders due to the AOTF transfer function definition. For this reason, the AOTF calibration is a crucial step, particularly when interpreting LNO nadir data, where no reference measurements can be obtained due to no pointing towards the Sun (see Section 2.3.1 and Annexe A.3).

A.2 Echelle grating

A diffraction grating is an optical device that has a periodic structure capable of diffracting light into multiple beams that travel in different directions, each with a different angle of diffraction. This effect produces a form of structural colouration. The angles at which the beams are diffracted depend on several factors, including the angle at which the light waves strike the grating, the distance between the diffracting elements on the grating (i.e. the grooves), and the wavelength of the light. The diffraction grating can be placed on either a reflective (reflection grating) or transparent surface (transmission grating). Moreover, the gratings with wider groove spacings are called echelle gratings. They are mainly used for high angles in diffraction orders (Hutley, 1982; Palmer, 2020). Figure A.1 illustrates the incident light coming on a reflective grating and being diffracted into discrete directions. Each groove spaced at a distance of d can be viewed as a tiny and slit-shaped source of diffracted light. All angles are measured from the grating normal (dashed line perpendicular).

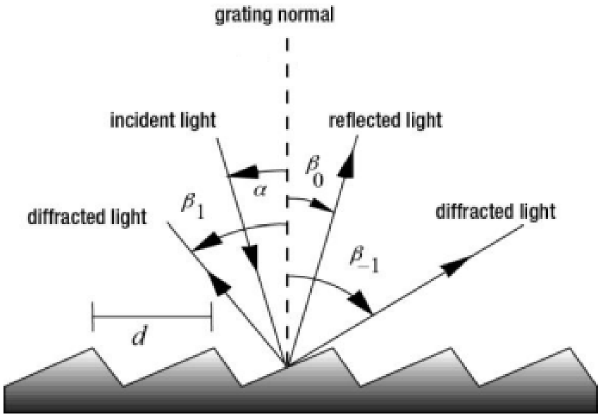

Figure A.1: Illustration of a reflective grating diffracting an incident beam. Each groove is spaced of a distance d. All angles are calculated from the grating normal, i.e. the vertical dashed line (Palmer, 2020).

Based on the wavelength of the light (λ), the incident (α) and emergent (β) angles and the groove spacing (d) of the diffraction grating, the grating equation describes the angular location at which constructive interference takes place, i.e. when diffracted lights have the same frequency and phase leading to an increase in the overall amplitude of the resulting wave (Hutley, 1982; Palmer, 2020). The integer m is the so-called diffraction order.

$$m\lambda = d(sin\alpha + sin\beta) \tag{A.2}$$

The Littrow configuration is a specific case where the incident α and diffraction β angles are the same, i.e. the light is diffracted toward its same incident direction. Additionally, the α and β angles are equal to the Blaze angle θ. This angle corresponds to the angle at which the grooves are inclined with respect to the grating surface. Therefore, the angle between the normal of the grooves and the normal of the grating surface is also the Blaze angle (Hutley, 1982; Palmer, 2020). In this configuration, the grating equation becomes

$$m\lambda = 2dsin\alpha = 2dsin\theta \tag{A.3}$$

Concerning the LNO channel, the echelle grating is used in near Littrow configuration. This means the incident and diffracted beams are separated. To do that, the grating is slighty tilted causing both beams to form a minor angle with the plane that is perpendicular to the grating surface and grooves. Moreover, there is a small deviation of the incident angle from the Blaze angle in the plane normal to the grooves and the surface (Neefs et al., 2015).

A.3 LNO spectral calibration

The analytical pixel number-wavelength relation mentioned in Section 2.3.1 is defined by a second-order polynomial,

$$\nu = (A \times p_t^2 + B \times p_t + C) \times m \tag{A.4}$$

where ν is the wavenumber of the pixel, m is the diffraction order and p_t is the temperature-corrected pixel number. To account for the effect of temperature on the pixel shift (see Section 2.2.3 and Annexe A.1), a linear relationship is defined as

$$p_t = p + D \times t \tag{A.5}$$

with p, the pixel number (from 0 to 320), t, the instrument temperature and the coefficient D given the pixel shift per degree Celsius due to the possible thermal background. The temperature-corrected pixel number relation is assumed to be constant for all orders.

Recent estimations have determined the value of D to be -0.85, which is in agreement with earlier approximations of -0.75 (Liuzzi et al., 2019; Cruz Mermy et al., 2022) and -0.83 (Thomas et al., 2022a). The different values can be explained by the number of full scans used, as these are continuously increasing. Regarding the coefficients in equation A.4, i.e. A, B and C, they are obtained through a quadratic fit of the relation between the center of solar lines (p_0) and the corresponding central wavenumber divided by the selected order, i.e. ν_0/m. Table A.1 reports the last results of the retrieved coefficients for the spectral calibration. The calibration error for the position of lines is always less than one single pixel.

A	**B**	**C**	**D**
$3.94e^{-9}$	$5.61e^{-4}$	22.47	−0.85

Table A.1: Retrieved coefficients for the LNO spectral calibration (personnal communication with Ian Thomas).

Thanks to the pixel number-wavelength relationship (see Equation A.4), it is possible to correlate the radio frequency A applied to the AOTF in terms of selected wavelengths, through the AOTF tuning relation (see Equation A.1) (Mahieux et al., 2008, 2009). By scanning the different orders, the depth of selected solar lines can be analysed through the AOTF frequency (see Section 2.3.1). This determines the frequency at which solar line intensity reaches maximum sensitivity. The variation of the AOTF frequency modifies the depth of a solar line. Analysing theses variations enables to determine the AOTF transfer function (TF), which can be fitted by a theoritical model. For the LNO channel, the model adopted for the AOTF transfer function is a combination of a sinc-squared function with a Gaussian function (Liuzzi et al., 2019; Cruz Mermy et al., 2022).

$$\begin{aligned} TF &= F_{sinc} + F_{Gauss} + F_{cont} \\ F_{sinc} &= I_0 w^2 \frac{\sin\left(\frac{\pi(\nu-\nu_0)}{w}\right)^2}{\pi^2(\nu-\nu_0)^2} \\ F_{Gauss} &= I_G \exp\left(\frac{-(\nu-\nu_0)^2}{\sigma_G^2}\right) \\ F_{cont} &= q + n(\nu-\nu_0) \end{aligned} \tag{A.6}$$

where,

- ν_0: AOTF transfer function center (cm^{-1})
- I_0: amplitude of the sinc-squared function
- w: location of the first zero-crossing of the sinc-squared function
- I_G: amplitude of the Gaussian function
- σ_G: standard deviation
- q and n: offset parameters of the continuum

Finally, the shape of the measured spectral continuum results from the incoming continuum from the Martian surface modulated by the shape of the AOTF transfer function (see Equation A.6) and the grating efficiency, which is defined by a sinc-squared function. This is called the Blaze function (Engman and Lindblom, 1982).

$$F_{Blaze} = w_p^2 \frac{\left(\sin \frac{\pi(p-p_0)}{w_p}\right)^2}{\pi^2 (p-p_0)^2} \tag{A.7}$$

Appendix B

The Snow, Ice, and Aerosol Radiative (SNICAR) model

Initially developed for H_2O snow on Earth (Flanner et al., 2007), the SNow Ice and Aerosol Radiation (SNICAR) tool has been extended to compute CO_2 and H_2O ice albedo under the Martian conditions (Singh and Flanner, 2016). It provides a framework to understand and quantify the effects of various factors, such as the observation conditions, i.e. the solar zenith angle, the grain size, the ice layer thickness, the type and concentration of impurity, on the surface ice albedo. The SNICAR model is continually evolving, with updated versions incorporating new parameterisations and improvements based on observational data and experimental studies. The tool is publicly available at: `https://github.com/mflanner/SNICARv3`.

In order to simulate surface ice albedo, the model is based on the two-stream approximation in the multiple scattering regime (Toon et al., 1989), with the delta-hemispheric mean approximation (Wiscombe, 1977). Moreover, the model takes advantage of the Mie theory, describing the scattering of light independently of the wavelengths by spherical particles, which are caracterised by their size (Bohren and Huffman, 1998; Liou, 2002). A fundamental physical property of particles is their refractive index, which determines their ability to absorb and/or scatter light. Defined as the ratio of the speed of light in vacuum to the speed of light in the material, the refractive index is composed of a real and imaginary part, representing the scattering and absorption respectively (He and Flanner, 2020). The SNICAR model uses the H_2O ice refractive indices from Warren and Brandt (2008) and the ones of CO_2 ice from Hansen (2005). Considering impurities such as Martian dust, the refractive indices come from Wolff et al. (2009, 2010).

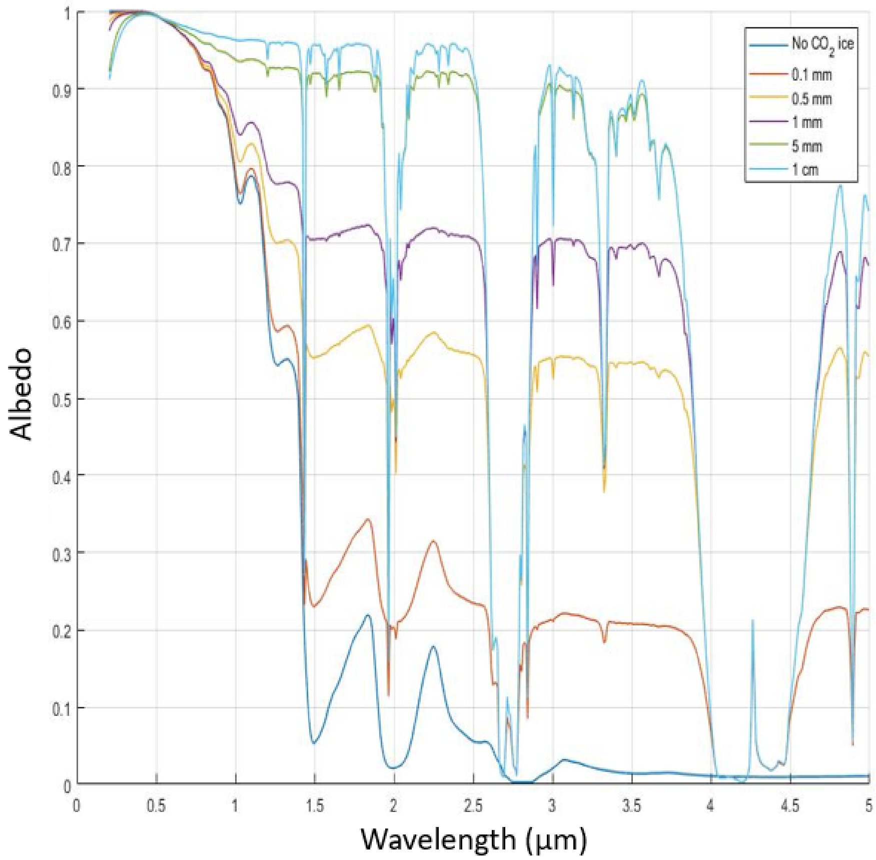

Figure B.1: Variation of the H_2O ice albedo spectrum due to the increase of the CO_2 ice layer on the top, under the following conditions: SZA = $0°$, H_2O ice layer thickness = 3 cm, H_2O ice density = 900 kg/m^3, CO_2 ice density = 1500 kg/m^3, grain size = 100 μm, surface albedo = 0.2.

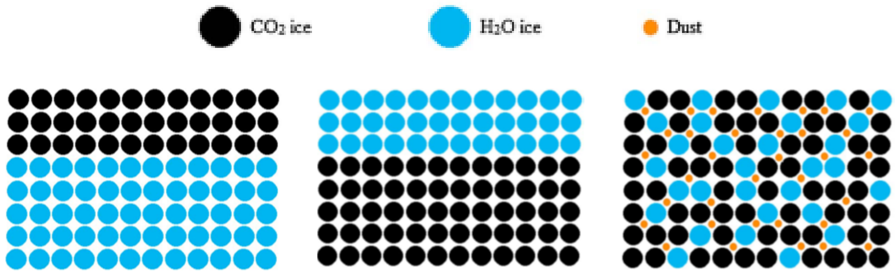

Figure B.2: Illustration of ice composition. Originally, the tool allows to define homogeneous layers superimposed with CO_2 ice on H_2O ice (left) and H_2O ice on CO_2 ice (middle). We added a third option: mixture composed of CO_2 ice and H_2O ice with dust impurities (right).

The tool contains 480 spectral bands, ranging from 0.2 to 5.0 μm, with a spectral resolution of 10 nm. As an example, Figure B.1 shows how the spectral albedo of a homogeneous H_2O ice layer can vary by adding CO_2 ice on the top. Nevertheless, the model is restricted to homogeneous layers. As these conditions are not always satisfied on Mars (see Section 4.4.2 and 4.5.2), we implemented heterogeneous layering in the code with the assistance of Deepak Singh and Mark Flanner, the authors of the SNICAR model. It is now possible to define layers composed of CO_2 ice and H_2O ice, and also incorporate impurities such as dust (see Figure B.2). This hence gives a global perspective and a better understanding of how albedo spectra can change in pure ice or in a mixture (see Figure B.3).

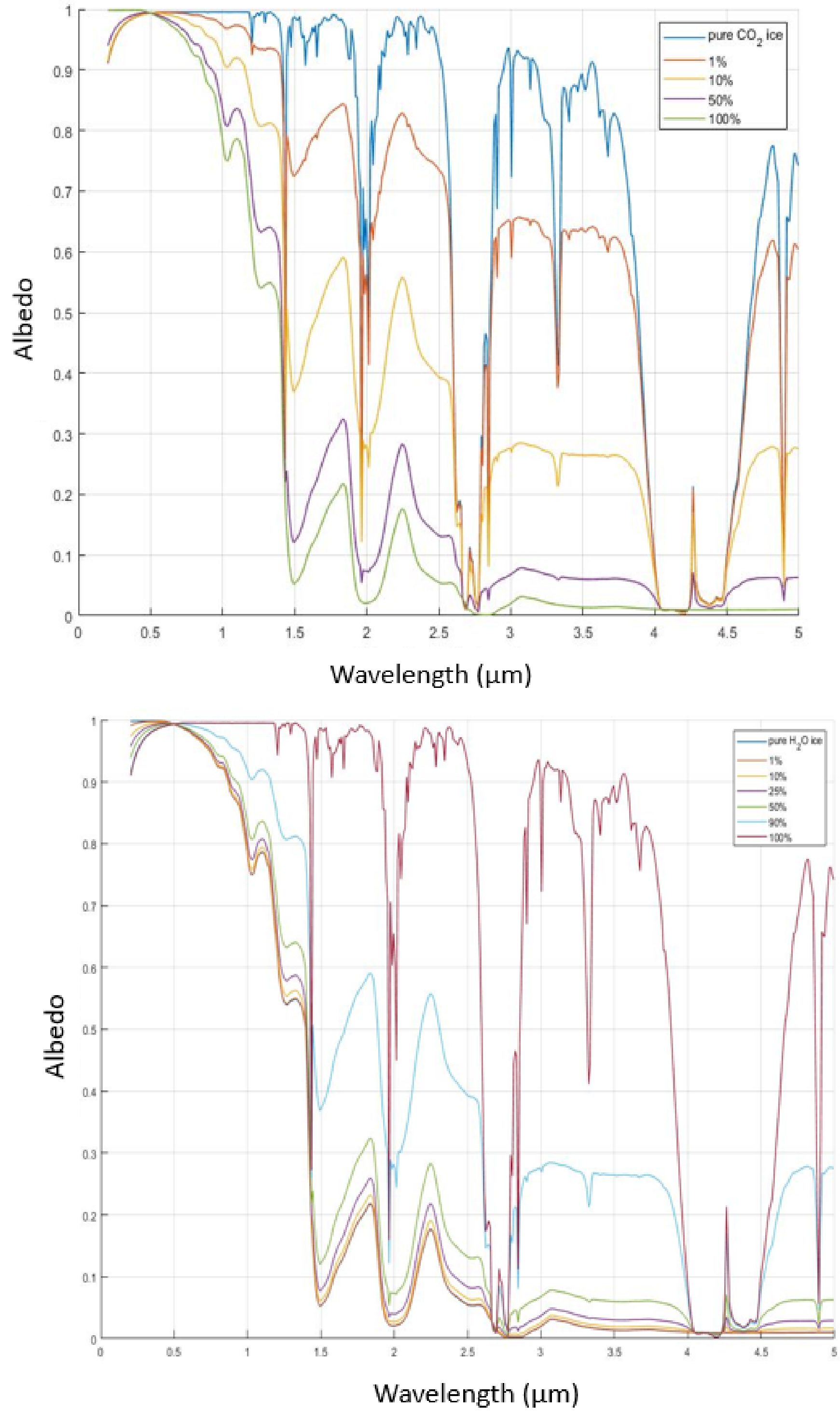

Figure B.3: Upper (bottom) panel shows the variation of the CO_2 ice (H_2O ice) albedo spectrum by adding H_2O ice (CO_2 ice) impurities. Same conditions as Figure B.1.

List of Publications

Articles

1. Dehant, V., Le Maistre, S., Baland, R.-M., Bergeot, N., Karatekin, Ö, Péters, M.-J., Rivoldini, A., **Ruiz Lozano, L.**, Temel, O., Van Hoolst, T., et al. (2020). The radioscience LaRa instrument onboard ExoMars 2020 to investigate the rotation and interior of Mars. *Planetary and Space Science* 180:104776.

2. Oliva, F., D'Aversa, E., Bellucci, G., Carrozzo, F. G., **Ruiz Lozano, L.**, Altieri, F., Thomas, I. R., Karatekin, Ö., Cruz Mermy, G., Schmidt, F., et al. (2022). Martian CO2 ice observation at high spectral resolution with ExoMars/TGO NOMAD. *Journal of Geophysical Research: Planets*, 127(6):e2021JE007083.

3. **Ruiz Lozano, L.**, Karatekin, Ö., Dehant, V., Bellucci, G., Oliva, F., D'Aversa, E., Carrozzo, F., Altieri, F., Thomas, I., Willame, Y., Robert, S., Vandaele, A., Daerden, F., Ristic, B., Patel, M., and López Moreno, J. (2022). Evaluation of the capability of ExoMars-TGO NOMAD infrared nadir channel for water ice clouds detection on Mars. *Remote Sens.*, 14(17):4143.

4. **Ruiz Lozano, L.**, Oliva, F., Karatekin, Ö., Bellucci, G., Dehant, V., D'Aversa, E., Carrozzo, F., Schmidt, F., Cruz Mermy, G., Thomas, I., Vandaele, A., Daerden, F., Ristic, B., Patel, M., and López-Moreno, J.-J. (2023). Observation of the Southern Polar cap during MY34-36 with ExoMars-TGO NOMAD-LNO. *Icarus*, `https://doi.org/10.1016/j.icarus.2023.115698`.

5. Valantinas, A., Thomas, N., Pommerol, A. , Hauber, E., **Ruiz Lozano, L.** , Bickel, V., Karatekin, Ö., Cem Senel, C., Temel, O., Tirsch, D., Munaretto, G., Pajola, M., Oliva, F., Schmidt, F., Thomas, I., McEwen, A., Almeida, M., Read, M., Ganesh Rangarajan, V., El-Maarry, M., Re, C., Carrozzo, F. G., D'Aversa,

E., Vandaele, A. C. and Cremonese, G. (2023). Water Frost on Martian volcanoes. *Under consideration.*

Conference presentations

1. **Ruiz Lozano, L.**, Karatekin, Ö., Caldiero, A., Temel, O., Dehant, V., Bellucci, G., Altieri, F., Thomas, I.R., Robert, S., and Vandaele, A.C., Use of LNO data for ices detection, *NOMAD Science Working Team 15*, Wroclaw, Poland, 2019.

2. **Ruiz Lozano, L.**, Karatekin, Ö., Caldiero, A., Temel, O., Thomas, I., Robet, S., Bellucci, G., Altieri, F., López Moreno, J. J., Vandaele, A. C., and Dehant, V.: Use of NOMAD Observations (Trace Gas Orbiter) for Mars surface depositions, *EPSC-DPS Joint Meeting 2019*, EPSC-DPS2019-1781-1, 2019.

3. **Ruiz Lozano, L.**, Karatekin, Ö., Dehant, V., Daerden, F., Thomas, I.R., Ristic, B., Patel, M.R., Bellucci, G., Lopez-Moreno, J.J. and Vandaele, A.C., Use of LNO data for ices detection (update), *Virtual NOMAD Science Working Team 17*, 2020.

4. **Ruiz Lozano, L.**, Karatekin, Ö., Caldiero, A., Imbreckx, A.-C., Temel, O., Dehant, V., Daerden, F., Thomas, I., Ristic, B., Patel, M., Bellucci, G., López Moreno, J. J., and Vandaele, A. C.: Use of TGO-NOMAD nadir observations for ices detection, *Europlanet Science Congress 2020*, online, 21 September-9 Oct 2020, EPSC2020-748, https://doi.org/10.5194/epsc2020-748, 2020.

5. **Ruiz Lozano L.**, Karatekin Ö., Dehant V., Bellucci G., Oliva F., Altieri F., D'Aversa E., Carrozzo F.G., Daerden F., Thomas I.R., Ristic B., Patel M.R., Lopez-Moreno J.J. and Vandaele A.C., Ice clouds with NOMAD-LNO, *Virtual NOMAD Science Working Team 18*, 2020.

6. **Ruiz Lozano, L.**, Karatekin, Ö., Dehant, V., Bellucci, G., Oliva, F., Altieri, F., Carrozzo, F. G., D'Aversa, E., Daerden, F., Thomas, I., Ristic, B., Willame, Y., Depiesse, C., Mason, J., Patel, M., López Moreno, J. J., and Vandaele, A. C.: Ice clouds detection with NOMAD-LNO onboard ExoMars Trace Gas Orbiter, *EGU General Assembly 2021*, online, 19-30 Apr 2021, EGU21-14775, https://doi.org/10.5194/egusphere-egu21-14775, 2021.

7. Oliva, F., D'Aversa, E., Bellucci, G., Carrozzo, F. G., Karatekin, Ö., **Ruiz Lozano, L.**, Altieri, F., Daerden, F., Thomas, I. R.,

Ristic, B., Mason, J., Willame, Y., Depiesse, C., Patel, M. R., Lopez-Moreno, J. J., Vandaele, A. C., and Amoroso, M.: Mars dust microphysical properties retrieval through TGO/NOMAD UVIS and LNO channels combined nadir datasets analysis, *European Planetary Science Congress 2021*, online, 13-24 Sep 2021, EPSC2021-501, https://doi.org/10.5194/epsc2021-501, 2021.

8. **Ruiz Lozano, L.**, Karatekin, Ö., Dehant, V., Bellucci, G., Oliva, F., D'Aversa, E., Altieri, F., Carrozzo, F., Willame, Y., Thomas, I. & Vandaele, A. Water ice clouds detection with NOMAD-LNO nadir channel on board ExoMars TGO, *CHIANTI TOPICS 5th International Focus Workshop*, Florence, Italy, 2022.

9. Oliva, F., D'Aversa, E., Bellucci, G., Carrozzo, F. G., **Ruiz Lozano, L.**, Altieri, F., Thomas, I. R., Karatekin, Ö., Cruz Mermy, G., Schmidt, F., et al, Martian CO2 ice characterization through ExoMars/TGO NOMAD-LNO channel nadir high resolution data, *CHIANTI TOPICS 5th International Focus Workshop*, Florence, Italy, 2022.

10. Montabone, L., Heavens, N.G., Pankine, A., Wolff, M., Cardesin-Moinelo, A., Geiger, B., Forget, F., Millour, E., Spiga, A., Guzewich, S. D., Karatekin, O., Ritter, B., **Ruiz Lozano, L.**, Senel, C. B., Temel, O., Lillis, R. J., Olsen, K. S., Read, P. L., Vandaele, A.C., Aoki, S., Daerden, F., Neary, L., Battalio, J.M., et al. The case and approach for continuous, simultaneous, global mars weather monitoring from orbit, *7th Mars Atmosphere Modelling and Observations workshop (MAMO)*, Paris, 2022.

11. Montabone, L., Heavens, N.G., Cardesin-Moinelo, A., Forget, F., Guzewich, S. D., Karatekin, O., Lillis, R., Olsen, K., Vandaele, A. C., Wolff, M., Aoki, S., Battalio, J.M., Bertrand, T., Daerden, F., Gebhardt, C., Geiger, B., Giuranna, M., Greybush, S. J., Hernández-Bernal, J., Kleinboehl, A., Lewis, S. R., Machado, P., Millour, E., Mischna, M. A., Montmessin, F., Nakagawa, H., Neary, L., Ogohara, K., Oliva, F., Pankine, A., Read, P. L., Ritter, B., Robert, S., **Ruiz Lozano, L.**, Sánchez-Lavega, A., Senel, C. B., Spiga, A., Tamppari, L. K., Temel, O., Titov, D., Vincendon, M., Wang, H., Wolkenberg, P. & Young, R. M. B. The case and approach for continuous, simultaneous, quasi-global weather monitoring on Mars, *44th COSPAR Scientific Assembly*, Athens, Space Studies of the Earth-Moon System, Planets, and Small Bodies of the Solar System (B) Forward Planning for the Exploration of Mars, 2022.

12. **Ruiz Lozano, L.**, Karatekin, Ö., Dehant, V., Bellucci, G., Oliva, F., D'Aversa, E., Altieri, F., Carrozzo, F. G., Willame, Y., Thomas, I., Daerden, F., Ristic, B., Patel, M., López Moreno, J. J., and Vandaele, A. C.: Evaluation of the capability of ExoMars-TGO NOMAD infrared nadir channel for water ice clouds detection on Mars, *Europlanet Science Congress 2022*, Granada, Spain, 18-23 Sep 2022, EPSC2022-946, https://doi.org/10.5194/epsc2022-946, 2022.

13. Oliva, F., D'Aversa, E., Bellucci, G., Carrozzo, F. G., **Ruiz Lozano, L.**, Karatekin, O., Daerden, F., Thomas, I., Ristic, B., Patel, M., Lopez-Moreno, J.-J., Vandaele, A. C., and Sindoni, G.: Minimum Noise Fraction analysis of ExoMars/TGO NOMAD-LNO channel nadir data: SNR enhancement and application, *Europlanet Science Congress 2022*, Granada, Spain, 18-23 Sep 2022, EPSC2022-561, https://doi.org/10.5194/epsc2022-561, 2022.

14. Oliva, F., D'Aversa, E., Bellucci, G., Carrozzo, F. G., **Ruiz Lozano, L.** and Karatekin, Ö., Update on LNO nadir data Minimum Noise Fraction (MNF) analysis, *NOMAD Science Working Team 22*, Brussels, 2022.

15. Oliva, F., D'Aversa, E., Bellucci, G., Carrozzo, F. G., **Ruiz Lozano, L.**, Karatekin, Ö., Thomas, I. R., Daerden, F., Ristic, B., Patel, M.R., Lopez-Moreno, J.-J., Vandaele, A. C., Sindoni, G., Application of the Minimum Noise Fraction technique to ExoMars/TGO NOMAD-LNO channel nadir data: SNR enhancement evaluation, *XVII Congresso di Scienze Planetarie*, Perugia, Italy, 2023.

16. Oliva, F., D'Aversa, E., Bellucci, G., Carrozzo, F. G., **Ruiz Lozano, L.**, Karatekin, Ö., Thomas, I. R., Daerden, F., Ristic, B., Patel, M.R., Lopez-Moreno, J.-J., Vandaele, A. C., Sindoni, G., LNO nadir data MNF analysis update, *NOMAD Science Working Team 23*, Matsushima, Japon, 2023.

17. **Ruiz Lozano, L.**, Karatekin, Ö., Thomas, I. R., Phobos observations with LNO: short update, *NOMAD Science Working Team 24*, Potenza, Italy, 2023.

White paper

1. Smith, I. B., et al., Solar-System-Wide Significance of Mars Polar Science, A White Paper submitted to the Planetary Sciences Decadal Survey 2023-2032, https://www.lpi.usra.edu/decadal_whitepaper_proposals/

Bibliography

Abetti, A. and Abetti, G. (1910). Giovanni Virginio Schiaparelli. *Astrophysical Journal*, 32:313–319.

Adriani, A., Moriconi, M., D'Aversa, E., Oliva, F., and Filacchione, G. (2015). Faint luminescent ring over Saturn's polar hexagon. *The Astrophysical Journal Letters*, 808:L16.

Almeida, M., Read, M., Thomas, N., Cremonese, G., Becerra, P., Borrini, G., and et al. (2023). Targeting and image acquisition of martian surface features with tgo/cassis. *Planetary and Space Science*, 231:105697.

Andrieu, F., Schmidt, F., Douté, S., and Chassefière, E. (2018). Ice state evolution during spring in Richardson crater, Mars. *Icarus*, 315:158–173.

Aoki, S., Sato, T. M., Giuranna, M., Wolkenberg, P., Sato, Y., Nakagawa, H., and Kasaba, Y. (2018). Mesospheric CO2 ice clouds on Mars observed by Planetary Fourier Spectrometer onboard Mars Express. *Icarus*, 302:175–190.

Aoki, S., Vandaele, A., Daerden, F., Villanueva, G., Liuzzi, G., Thomas, I., Erwin, J., Trompet, L., Robert, S., Neary, L., et al. (2019). Water vapor vertical profiles on Mars in dust storms observed by TGO/NOMAD. *J. Geophys. Res. Planets*, 124(11):3482–3497.

Aoki, S., Vandaele, A. C., Daerden, F., Villanueva, G. L., Liuzzi, G., Clancy, R. T., Lopez-Valverde, M. A., Brines, A., Thomas, I. R., Trompet, L., Erwin, J. T., Neary, L., Robert, S., Piccialli, A., Holmes, J. A., Patel, M. R., Yoshida, N., Whiteway, J., Smith, M. D., Ristic, B., Bellucci, G., Lopez-Moreno, J. J., and Fedorova, A. A. (2022). Global Vertical Distribution of Water Vapor on Mars: Results From 3.5 Years of ExoMars-TGO/NOMAD Science Operations. *Journal of Geophysical Research: Planets*, 127(9):e2022JE007231.

Appéré, T., Schmitt, B., Langevin, Y., Douté, S., Pommerol, A., Forget, F., and et al. (2011). Winter and spring evolution of northern seasonal deposits on Mars from OMEGA on Mars Express. *Journal of Geophysical Research*, 116:E05001.

Arvidson, R. E., Ashley, J. W., Bell III, J. F., Chojnacki, M., Cohen, J., Economou, T. E., Farrand, W. H., Fergason, R., Fleischer, I., Geissler, P., Gellert, R., Golombek, M. P., Grotzinger, J. P., Guinness, E. A., Haberle, R. M., Herkenhoff, K. E., Herman, J. A., Iagnemma, K. D., Jolliff, B. L., Johnson, J. R., Klingelhöfer, G., Knoll, A. H., Knudson, A. T., Li, R., McLennan, S. M., Mittlefehldt, D. W., Morris, R. V., Parker, T. J., Rice, M. S., Schröder, C., Soderblom, L. A., Squyres, S. W., Sullivan, R. J., and Wolff, M. J. (2011). Opportunity Mars Rover mission: Overview and selected results from Purgatory ripple to traverses to Endeavour crater. *Journal of Geophysical Research: Planets*, 116(E7).

Arvidson, R. E., Bell III, J. F., Bellutta, P., Cabrol, N. A., Catalano, J. G., Cohen, J., Crumpler, L. S., Des Marais, D. J., Estlin, T. A., Farrand, W. H., Gellert, R., Grant, J. A., Greenberger, R. N., Guinness, E. A., Herkenhoff, K. E., Herman, J. A., Iagnemma, K. D., Johnson, J. R., Klingelhöfer, G., Li, R., Lichtenberg, K. A., Maxwell, S. A., Ming, D. W., Morris, R. V., Rice, M. S., Ruff, S. W., Shaw, A., Siebach, K. L., de Souza, P. A., Stroupe, A. W., Squyres, S. W., Sullivan, R. J., Talley, K. P., Townsend, J. A., Wang, A., Wright, J. R., and Yen, A. S. (2010). Spirit Mars Rover Mission: Overview and selected results from the northern Home Plate Winter Haven to the side of Scamander crater. *Journal of Geophysical Research: Planets*, 115(E7).

Bandfield, J. (2002). Global mineral distributions on Mars. *J. Geophys. Res.*, 107.

Bandfield, J., Christensen, P., and Smith, M. (2000). Spectral data set factor analysis and end-member recovery: Application to Martian atmospheric particulates. *J. Geophys. Res.*, 105:9573–9588.

Banerdt, W. B., Smrekar, S. E., Banfield, D., Giardini, D., Golombek, M., Johnson, C. L., Lognonné, P., Spiga, A., Spohn, T., Perrin, C., Stähler, S. C., Antonangeli, D., Asmar, S., Beghein, C., Bowles, N., Bozdag, E., Chi, P., Christensen, U., Clinton, J., Collins, G. S., Daubar, I., Dehant, V., Drilleau, M., Fillingim, M., Folkner, W., Garcia, R. F., Garvin, J., Grant, J., Grott, M., Grygorczuk, J., Hudson, T., Irving, J. C. E., Kargl, G., Kawamura, T., Kedar, S., King, S., Knapmeyer-Endrun, B., Knapmeyer, M., Lemmon, M., Lorenz, R., Maki, J. N., Margerin, L., McLennan, S. M., Michaut, C., Mimoun, D., Mittelholz, A., Mocquet, A., Morgan, P., Mueller, N. T., Murdoch, N., Nagihara, S., Newman, C., Nimmo, F., Panning, M., Pike, W. T., Plesa, A.-C., Rodriguez, S., Rodriguez-Manfredi, J. A., Russell, C. T., Schmerr, N., Siegler, M., Stanley, S., Stutzmann, E., Teanby, N., Tromp, J., van Driel, M., Warner, N., Weber, R., and Wieczorek, M. (2020). Initial results from the InSight mission on Mars. *Nature Geoscience*, 13(3):183–189.

Banfield, D., Spiga, A., Newman, C., Forget, F., Lemmon, M., Lorenz, R., Murdoch, N., Viudez-Moreiras, D., Pla-Garcia, J., Garcia, R. F., Lognonné, P., Karatekin, O., Perrin, C., Martire, L., Teanby, N., Hove, B. V., Maki, J. N., Kenda, B., Mueller, N. T., Rodriguez, S., Kawamura, T., McClean, J. B., Stott, A. E., Charalambous, C., Millour, E., Johnson, C. L., Mittelholz, A., Määttänen, A., Lewis, S. R., Clinton, J., Stähler, S. C., Ceylan, S., Giardini, D., Warren, T., Pike, W. T., Daubar, I., Golombek, M., Rolland, L., Widmer-Schnidrig, R., Mimoun, D., Beucler, E., Jacob, A., Lucas, A., Baker, M., Ansan, V., Hurst, K., Mora-Sotomayor, L., Navarro, S., Torres, J., Lepinette, A., Molina, A., Marin-Jimenez, M., Gomez-Elvira, J., Peinado, V., Rodriguez-Manfredi, J.-A., Carcich, B. T., Sackett, S., Russell, C. T., Spohn, T., Smrekar, S. E., and Banerdt, W. B. (2020). The atmosphere of Mars as observed by InSight. *Nature Geoscience*, 13(3):190–198.

Barucci, M. A., Reess, J.-M., Bernardi, P., Doressoundiram, A., Fornasier, S., Le Du, M., Iwata, T., Nakagawa, H., Nakamura, T., André, Y., Aoki, S., Arai, T., Baldit, E., Beck, P., Buey, J.-T., Canalias, E., Castelnau, M., Charnoz, S., Chaussidon, M., Chapron, F., Ciarletti, V., Delbo, M., Dubois, B., Gauffre, S., Gautier, T., Genda, H., Hassen-Khodja, R., Hervet, G., Hyodo, R., Imbert, C., Imamura, T., Jorda, L., Kameda, S., Kouach, D., Kouyama, T., Kuroda, T., Kurokawa, H., Lapaw, L., Lasue, J., Le Deit, L., Ledot, A., Leyrat, C., Le Ruyet, B., Matsuoka, M., Merlin, F., Miyamoto, H., Moynier, F., Nguyen Tuong, N., Ogohara, K., Osawa, T., Parisot, J., Pistre, L., Quertier, B., Raymond, S. N., Rocard, F., Sakanoi, T., Sato, T. M., Sawyer, E., Tache, F., Trémolières, S., Tsuchiya, F., Vernazza, P., and Zeganadin, D. (2021). MIRS: an imaging spectrometer for the MMX mission. *Earth, Planets and Space*, 73(1):211.

Basalla, G. (2006). Percival Lowell: Champion of Canals. In *Civilized*

Life in the Universe: Scientists on Intelligent Extraterrestrials. Oxford University Press.

Becerra, P., Smith, I. B., Hibbard, S., Andres, C., Bapst, J., Bramson, A. M., Buhler, P. B., Coronato, A., Diniega, S., Emmett, J., Galofre, A. G., Herny, C., Kahre, M., Knightly, J. P., Nerozzi, S., Pascuzzo, A., Portyankina, G., Rabassa, J., Tamppari, L. K., Titus, T. N., Whitten, J., and Yoldi, Z. (2021). Past, Present, and Future of Mars Polar Science: Outcomes and Outlook from the 7th International Conference on Mars Polar Science and Exploration. *The Planetary Science Journal*, 2(5).

Bei, L., Dennis, G. I., Miller, H. M., Spaine, T. W., and Carnahan, J. W. (2004). Acousto-optic tunable filters: fundamentals and applications as applied to chemical analysis techniques. *Progress in Quantum Electronics*, 28(2):67–87.

Bell, J., Wolff, M., and Morris, R. (2001). NASA and The Hubble Heritage Team (STScI/AURA). HubbleSite News Release:https://hubblesite.org/contents/news-releases/2001/news-2001-31.html.

Bell, J. F., McSween Jr., H. Y., Crisp, J. A., Morris, R. V., Murchie, S. L., Bridges, N. T., Johnson, J. R., Britt, D. T., Golombek, M. P., Moore, H. J., Ghosh, A., Bishop, J. L., Anderson, R. C., Brückner, J., Economou, T., Greenwood, J. P., Gunnlaugsson, H. P., Hargraves, R. M., Hviid, S., Knudsen, J. M., Madsen, M. B., Reid, R., Rieder, R., and Soderblom, L. (2000). Mineralogic and compositional properties of Martian soil and dust: Results from Mars Pathfinder. *Journal of Geophysical Research: Planets*, 105(E1):1721–1755.

Bell, J. F., Wolff, M. J., Malin, M. C., Calvin, W. M., Cantor, B. A., Caplinger, M. A., Clancy, R. T., Edgett, K. S., Edwards, L. J., Fahle, J., Ghaemi, F., Haberle, R. M., Hale, A., James, P. B., Lee, S. W., McConnochie, T., Noe Dobrea, E., Ravine, M. A., Schaeffer, D., Supulver, K. D., and Thomas, P. C. (2009). Mars Reconnaissance Orbiter Mars Color Imager (MARCI): instrument description, calibration, and performance. *J. Geophys. Res. Planets*, 114(8).

Benson, J., Boney, B., James, P., Shan, K., Cantor, B., and Caplinger, M. (2003). The seasonal behavior of water ice clouds in the Tharsis and Valles Marineris regions of Mars: Mars orbiter camera observations. *Icarus*, 165:34–52.

Benson, J. and James, P. (2005). Yearly comparisons of the martian polar caps: 1999–2003 Mars Orbiter Camera observations. *Icarus*, 174(2):513–523.

Benson, J., James, P., Cantor, B., and Remigio, R. (2006). Interannual variability of water ice clouds over major Martian volcanoes observed by MOC. *Icarus*, 184:365–371.

Benson, J., Kass, D., and Kleinböhl, A. (2011). Mars' north polar hood as observed by the Mars Climate Sounder. *J. Geophys. Res. Planets*, 116.

Benson, J. L., Kass, D. M., Kleinböhl, A., McCleese, D. J., Schofield, J. T., and Taylor, F. W. (2010). Mars' south polar hood as observed by the Mars Climate Sounder. *Journal of Geophysical Research: Planets*, 115.

Bernard-Michel, C., Douté, S., Fauvel, M., Gardes, L., and Girard, S. (2009). Retrieval of Mars surface physical properties from OMEGA hyperspectral images using regularized sliced inverse regression. *Journal of Geophysical Research: Planets*, 114(E6).

Bibring, J.-P., Combes, M., Langevin, Y., Soufflot, A., Cara, C., Drossart, P., and et al. (1989). Results from the ISM experiment. *Nature*, 341(6243):591–593.

Bibring, J.-P., Langevin, Y., Gendrin, A., Gondet, B., Poulet, F., Berthe, M., and the OMEGA team (2005). Mars surface diversity as revealed by the OMEGA/Mars Express observations. *Science*, 307(5715):1576–1581.

Bibring, J.-P., Langevin, Y., Poulet, F., Gendrin, A., Gondet, B., Berthé, M., Soufflot, A., Drossart, P., Combes, M., Bellucci, G., Moroz, V., Mangold, N., Schmitt, B., and OMEGA team, the (2004a). Perennial water ice identified in the south polar cap of Mars. *Nature*, 428(6983):627–630.

Bibring, J.-P., Soufflot, A., Berthé, M., Langevin, Y., Gondet, B., Drossart, P., Buoyé, M., Combes, M., Puget, P., Semery, A., et al. (2004b). OMEGA: Observatoire pour la Minéralogie, l'Eau, les Glaces et l'Activité. In *Mars Express: The Scientific Payload*, volume 1240, pages 37–49. ESA, ESA Publications Division.

Bierson, C. J., Phillips, R. J., Smith, I. B., Wood, S. E., Putzig, N. E., Nunes, D., and Byrne, S. (2016). Stratigraphy and evolution of the buried CO2 deposit in the Martian south polar cap. *Geophysical Research Letters*, 43(8):4172–4179.

Bills, B. G. and Nerem, R. S. (2001). Mars topography: Lessons learned from spatial and spectral domain comparisons of Mars Orbiter Laser Altimeter and U.S. Geological Survey data. *Journal of Geophysical Research: Planets*, 106(E12):32915–32925.

Boardman, J. W. (1992). *SIPS User's Guide Spectral Image Processing System, Version 1.2.* Center for the Study of Earth from Space.

Boardman, J. W. and Kruse, F. A. (1994). Automated spectral analysis: A geological example using AVIRIS data, north Grapevine Mountains, Nevada. In *Proceedings of the 10th Thematic Conference on Geologic Remote Sensing*, pages I–407–I–418. Environmental Research Institute of Michigan.

Bohren, C. F. and Huffman, D. R. (1998). *Absorption and Scattering of Light by Small Particles.* WILEY-VCH Verlag GmbH & Co. KGaA.

Bonev, P. B., James, P. B., Bjorkman, J. E., and Wolff, M. J. (2002). Regression of the mountains of mitchel polar ice after the onset of a global dust storm on mars. *Geophysical Research Letters*, 29:2017.

Braude, A. S., Montmessin, F., Olsen, K. S., Trokhimovskiy, A., Korablev, O. I., Lefèvre, F., and et al. (2022). No detection of SO2, H2S, or OCS in the atmosphere of Mars from the first two Martian years of observations from TGO/ACS. *A&A*, 658.

Broquet, A. and Andrews-Hanna, J. C. (2023). Geophysical evidence for an active mantle plume underneath elysium planitia on mars. *Nature Astronomy*, 7(2):160–169.

Brown, A., Calvin, W., McGuire, P., and Murchie, S. L. (2010). Compact Reconnaissance Imaging Spectrometer for Mars (CRISM) south polar springtime recession mapping: First Mars year of observations. *Journal of Geophysical Research*, 115:E00D13.

Brown, A. J., Calvin, W. M., and Murchie, S. L. (2012). Compact Reconnaissance Imaging Spectrometer for Mars (CRISM) north polar springtime recession mapping: First 3 Mars years of observations. *Journal of Geophysical Research*, 117(E12):E00J20.

Brown, A. J., Piqueux, S., and Titus, T. N. (2014). Interannual observations and quantification of summertime H2O ice deposition on the Martian CO2 ice south polar cap. *Earth and Planetary Science Letters*, 406:102–109.

Byrne, S. and Ingersoll, A. (2003). A sublimation model for martian south polar ice features. *Science*, 299:1051–1053.

Calvin, W., Cantor, B., and James, P. (2017). Interannual and seasonal changes in the south seasonal polar cap of Mars: Observations from MY 28-31 using MARCI. *Icarus*, 292:144–153.

Calvin, W., James, P., Cantor, B., and Dixon, E. (2015). Interannual and seasonal changes in the north polar ice deposits of mars: Observations from my 29-31 using marci. *Icarus*, 251:181–190. Dynamic Mars.

Calvin, W. M. and Martin, T. Z. (1994). Spatial variability in the seasonal south polar cap of mars. *Journal of Geophysical Research*, 99(E10):21143–21152.

Carr, M. H. (1974). Tectonism and volcanism of the Tharsis Region of Mars. *Journal of Geophysical Research (1896-1977)*, 79(26):3943–3949.

Carr, M. H. (1996). Water erosion on Mars and its biologic implications. *Endeavour*, 20(2):56–60.

Carrozzo, F. G., Bellucci, G., Altieri, F., D'aversa, E., and Bibring, J.-P. (2009). Mapping of water frost and ice at low latitudes on Mars. *Icarus*, 203(2):406–420.

Cataldo, G., Childs, B., Corliss, J., Feehan, B., Gage, P., Lin, J., Mukherjee, S., Neuman, M., Pellerano, F., Sarli, B., Szalai, C., Teeney, L., Kam, J. V., White, T., Yew, C., and Zumwalt, C. (2022). Mars Sample Return - An Overview of the Capture, Containment and Return System. In *73rd International Astronautical Congress (IAC)*, Paris, France. International Astronautical Congress (IAC). IAC-22-A3.3A.10.

Cazenave, A. and Balmino, G. (1981). Meteorological effects on the seasonal variations on the rotation of Mars. *Geophysical Research Letters*, 8(3):245–248.

Chang, I. C. (1974). Noncollinear acousto-optic filter with large angular aperture. *Applied Physics Letters*, 25(7):370–372.

Chang, I. C. (1981). Acousto-optic tunable filters. *Optical Engineering*, 20:824–829.

Chapman, C. (2004). Space weathering of asteroid surfaces. *Annual Review of Earth and Planetary Sciences*, 32:539–567.

Chicarro, A., Martin, P., and Trautner, R. (2004). The Mars Express mission: an overview. *Mars Express: the scientific payload*, 1240:3–13.

Chiodini, G., Avino, R., Brombach, T., Caliro, S., Cardellini, C., De Vita, S., and et al. (2004). Fumarolic and diffuse soil degassing west of Mount Epomeo, Ischia, Italy. *Journal of Volcanology and Geothermal Research*, 133(1):291–309.

Christensen, P., Bandfield, J. L., Hamilton, V. E., Howard, A. D., Lane, M. D., Piatek, J. L., Ruff, S., and Stefanov, W. L. (2000). A thermal emission spectral library of rock-forming minerals. *J. Geophys. Res. Planets*, 105:9735–9739.

Christensen, P., Jakosky, B., Kieffer, H., Malin, M., McSween, H., Nealson, K., Mehall, G., Silverman, S., Ferry, S., Caplinger, M., and Ravine, M. (2004). The thermal emission imaging system (themis) for the mars 2001 odyssey mission. *Space Science Reviews*, 110(1-2):85–130.

Christensen, P. R., Bandfield, J. L., Bell III, J. F., Gorelick, N., Hamilton, V. E., Ivanov, A., and et al. (2003). Morphology and Composition of the Surface of Mars: Mars Odyssey THEMIS Results. *Science*, 300(5628):2056–2061.

Christensen, P. R., Bandfield, J. L., Hamilton, V. E., Ruff, S. W., Kieffer, H. H., Titus, T. N., Malin, M. C., Morris, R. V., Lane, M. D., Clark, R. L., et al. (2001). Mars Global Surveyor Thermal Emission Spectrometer experiment: Investigation description and surface science results. *Journal of Geophysical Research: Planets*, 106:23823–23872.

Clancy, R., Grossman, A., Wolff, M., James, P., Rudy, D., Billawala, Y., Sandor, B., Lee, S., and Muhleman, D. (1996). Water vapor saturation at low altitudes around Mars aphelion: A key to mars climate? *Icarus*, 122:36–62.

Clancy, R., Montmessin, F., Benson, J., Daerden, F., Colaprete, A., and Wolff, M. (2017a). Mars Clouds. In Haberle, R. and Clancy, R. and Forget, F. and Smith, M. and Zurek, R., editor, *The Atmosphere* *and Climate of Mars*, Cambridge Planetary Science, pages 76–105. Cambridge University Press, Cambridge.

Clancy, R., Sandor, B., Wolff, M., Christensen, P., Smith, M., Pearl, J., Conrath, B., and Wilson, R. (2000). An intercomparison of ground-based millimeter, MGS TES, and Viking atmospheric temperature measurements: Seasonal and interannual variability of temperatures and dust loading in the global Mars atmosphere. *Journal of Geophysical Research*, 105.

Clancy, R. T. and Sandor, B. J. (1998). CO_2 ice clouds in the upper atmosphere of Mars. *Geophysical Research Letters*, 25(4):489–492.

Clancy, R. T., Smith, M. D., Lefèvre, F., McConnochie, T. H., Sandor, B. J., Wolff, M. J., et al. (2017b). Vertical profiles of Mars 1.27 μm O2 dayglow from MRO CRISM limb spectra: Seasonal/global behaviors, comparisons to LMD GCM simulations, and a global definition for Mars water vapor profiles. *Icarus*, 293:132–156.

Clancy, R. T., Wolff, M. J., and Christensen, P. R. (2003). Mars aerosol studies with the MGS TES emission phase function observations: Optical depths, particle sizes, and ice cloud types versus latitude and solar longitude. *J. Geophys. Res. Planets*, 108.

Clancy, R. T., Wolff, M. J., Smith, M. D., Kleinböhl, A., Cantor, B. A., Murchie, S. L., Toigo, A. D., Seelos, F. P., Lefèvre, F., Montmessin, F., et al. (2019). The distribution, composition, and particle properties of Mars mesospheric aerosols: An analysis of CRISM visible/near-IR limb spectra with context from near-coincident MCS and MARCI observations. *Icarus*, 328:246–273.

Clancy, R. T., Wolff, M. J., Whitney, B. A., Cantor, B. A., and Smith, M. D. (2007). Mars equatorial mesospheric clouds: Global occurrence and physical properties from Mars Global Surveyor Thermal Emission Spectrometer and Mars Orbiter Camera limb observations. *Journal of Geophysical Research: Planets*, 112(E4):E04004.

Clancy, T., Wolff, M., Heavens, N., James, P., Lee, S., Sandor, B., Cantor, B., Malin, M., Tyler, D., and Spiga, A. (2021). Mars perihelion cloud trails as revealed by MARCI: Mesoscale topographically focused updrafts and gravity wave forcing of high altitude clouds. *Icarus*, 362:114411.

Clark, R. N. and Roush, T. L. (1984). Reflectance spectroscopy: Quantitative analysis techniques for remote sensing applications. *Journal of Geophysical Research: Solid Earth*, 89(B7):6329–6340.

Colaprete, A. and Toon, O. B. (2003). Carbon dioxide clouds in an early dense Martian atmosphere. *Journal of Geophysical Research*, 108(E4):5025.

Cruz Mermy, G., Schmidt, F., Thomas, I., Daerden, F., Ristic, B., Patel, M., Lopez-Moreno, J.-J., Bellucci, G., and Vandaele, A. (2022). Calibration of NOMAD on ExoMars Trace Gas Orbiter: Part 3 - LNO validation and instrument stability. *Planetary and Space Science*, 218:105399.

Cull, S., Arvidson, R. E., Mellon, M., Wiseman, S., Clark, R., Titus, T., Morris, R. V., and McGuire, P. (2010). Seasonal H2O and CO2 ice cycles at the Mars Phoenix landing site: 1. Prelanding CRISM and HiRISE observations. *Journal of Geophysical Research: Planets*, 115(E00D16).

Curran, R. J., Conrath, B. J., Hanel, R. A., Kunde, V. G., and Pearl, J. C. (1973). Mars: Mariner 9 Spectroscopic Evidence for H2O Ice Clouds. *Science*, 182(4110):381–383.

Cushing, G. E. and Titus, T. N. (2008). MGS-TES thermal inertia study of the Arsia Mons Caldera. *Journal of Geophysical Research*, 113.

Daerden, F., Neary, L., Villanueva, G., Liuzzi, G., Aoki, S., Clancy, R. T., et al. (2022). Explaining NOMAD D/H observations by cloud-induced fractionation of water vapor on Mars. *Journal of Geophysical Research: Planets*, 127(2):e2021JE007079.

Daerden, F., Neary, L., Viscardy, S., Garcia, M. A., Clancy, R. T., Smith, M., Encrenaz, T., and Fedorova, A. (2019). Mars atmospheric chemistry simulations with the GEM-Mars general circulation model. *Icarus*, 326:197–224.

Daerden, F., Whiteway, J. A., Davy, R., Verhoeven, C., Komguem, L., Dickinson, C., Taylor, P. A., and Larsen, N. (2010). Simulating observed boundary layer clouds on Mars. *Geophysical Research Letters*, 37.

Daubar, I. J., Dundas, C. M., Byrne, S., Geissler, P., Bart, G. D., McEwen, A. S., and et al. (2016). Changes in blast zone albedo patterns around new martian impact craters. *Icarus*, 267:86–105.

D'Aversa, E., Oliva, F., Altieri, F., Sindoni, G., Carrozzo, F. G., Bellucci, G., and et al. (2022). Vertical distribution of dust in the Martian atmosphere: OMEGA/MEx limb observations. *Icarus*, 371:114702.

Defraigne, P., de Viron, O., Dehant, V., Van Hoolst, T., and Hourdin, F. (2000). Mars rotation variations induced by atmospheric CO2 and winds. *Journal of Geophysical Research (Planets)*, 105(E10):24563–24570.

Dehant, V., Le Maistre, S., Baland, R.-M., Bergeot, N., Karatekin, Ö., Péters, M.-J., Rivoldini, A., Ruiz Lozano, L., Temel, O., Van Hoolst, T., Yseboodt, M., Mitrovic, M., Kosov, A. S., Valenta, V., Thomassen, L., Karki, S., Al Khalifeh, K., Craeye, C., Gurvits, L. I., Marty, J.-C., Asmar, S. W., and Folkner, W. M. (2020). The radioscience LaRa instrument onboard ExoMars 2020 to investigate the rotation and interior of Mars. *Planetary and Space Science*, 180:104776.

Dickson, J., Kerber, L., Fassett, C., and Ehlmann, B. (2018). A Global, Blended CTX Mosaic of Mars with Vectorized Seam Mapping: A New Mosaicking Pipeline Using Principles of Non-Destructive Image Editing. In *49th Annual Lunar and Planetary Science Conference*, Lunar and Planetary Science Conference, page 2480.

Dollfus, A. (1973). New optical measurements of planetary diameters IV. Size of the north polar cap of Mars. *Icarus*, 18(1):142–155.

Dundas, C. M., Becerra, P., Byrne, S., Chojnacki, M., Daubar, I. J., Diniega, S., and et al. (2021). Active Mars: A Dynamic World. *Journal of Geophysical Research: Planets*, 126(8):e2021JE006876.

Efron, B. and Tibshirani, R. (1994). *An Introduction to the Bootstrap*. Chapman and Hall/CRC, 1st edition.

Elachi, C. and van Zyl, J., editors (2021). *Introduction to the Physics and Techniques of Remote Sensing*, pages i–xvii. John Wiley & Sons, Ltd.

Engman, S. A.-C. and Lindblom, P. R. (1982). Blaze characteristics of echelle gratings. *Applied optics*, 21 23:4356–62.

Evans, J. E. and Maunder, E. W. (1903). Experiments as to the Actuality of the "Canals" observed on Mars. *Monthly Notices of the Royal Astronomical Society*, 63(8):488–499.

Farley, K. A., Williford, K. H., Stack, K. M., Bhartia, R., Chen, A., de la Torre, M., Hand, K., Goreva, Y., Herd, C. D., Hueso, R., et al. (2020). Mars 2020 mission overview. *Space Science Reviews*, 216:1–41.

Fedorova, A., Bertaux, J.-L., Betsis, D., Montmessin, F., Korablev, O., Maltagliati, L., and Clarke, J. (2018). Water vapor in the middle atmosphere of mars during the 2007 global dust storm. *Icarus*, 300:440–457.

Fedorova, A., Korablev, O., Bertaux, J.-L., Rodin, A., Kiselev, A., and Perrier, S. (2006). Mars water vapor abundance from SPICAM IR spectrometer: Seasonal and geographic distributions. *Journal of Geophysical Research*, 111(E9):E09S08.

Fernando, A. M., Wolff, M. J., and Forget, F. (2023). Seasonal variations of orographic clouds on Mars with MRO/MARCI observations and the Mars Planetary Climate Model. *Icarus*, 400:115559.

Fischbacher, G., Martin, L., and Baum, W. (1969). Martian polar cap boundaries. Final report, part A Contract 951547, Jet Propulsion Laboratory, Pasadena, CA.

Flanner, M., Zender, C., Randerson, J., and Rasch, P. J. (2007). Present-day climate forcing and response from black carbon in snow. *Journal of Geophysical Research: Atmospheres*, 112(D11):D11202.

Fleming, G. R., Longworth, J., and Krueger, B. P. (2018). Photochemical reaction. *Encyclopedia Britannica*.

Folkner, W. M., Dehant, V., Le Maistre, S., Yseboodt, M., Rivoldini, A., Van Hoolst, T., Asmar, S. W., and Golombek, M. P. (2018). The Rotation and Interior Structure Experiment on the InSight Mission to Mars. *Space Science Reviews*, 214(5):100.

Forget, F., Hansen, G. B., and Pollack, J. B. (1995). Low brightness temperatures of Martian polar caps: CO2 clouds or low surface emissivity? *Journal of Geophysical Research*, 100(E10):21219–21234.

Forget, F., Hourdin, F., Fournier, R., Hourdin, C., Talagrand, O., and Collins, M. (1999). Improved general circulation models of the Martian atmosphere from the surface to above 80 km. *J. Geophys. Res.*, 104(E10):24155–24175.

Forget, F., Hourdin, F., and Talagrand, O. (1998). CO2 snowfall on Mars: Simulation with a general circulation model. *Icarus*, 131(2):302–316.

Forget, F. and Pierrehumbert, R. (1997). Warming early Mars with carbon dioxide clouds that scatter infrared radiation. *Science*, 278(5341):1273–1276.

Forget, F., Wordsworth, R., Millour, E., et al. (2013). 3D modelling of the early Martian climate under a denser CO2 atmosphere: temperatures and CO2 ice clouds. *Icarus*, 222:81–99.

Formisano, V., Angrilli, F., Arnold, G., Atreya, S., Bianchini, G., Biondi, D., Blanco, A., Blecka, M., Coradini, A., Colangeli, L., Ekonomov, A., Esposito, F., Fonti, S., Giuranna, M., Grassi, D., Gnedykh, V., Grigoriev, A., Hansen, G., Hirsh, H., Khatuntsev, I., Kiselev, A., Ignatiev, N., Jurewicz, A., Lellouch, E., Lopez Moreno, J., Marten, A., Mattana, A., Maturilli, A., Mencarelli, E., Michalska, M., Moroz, V., Moshkin, B., Nespoli, F., Nikolsky, Y., Orfei, R., Orleanski, P., Orofino, V., Palomba, E., Patsaev, D., Piccioni, G., Rataj, M., Rodrigo, R., Rodriguez, J., Rossi, M., Saggin, B., Titov, D., and Zasova, L. (2005). The planetary fourier spectrometer (pfs) onboard the european mars express mission. *Planetary and Space Science*, 53(10):963–974. First Results of the Planetary Fourier Spectrometer aboard the the Mars Express Mission.

Formisano, V., Atreya, S., Encrenaz, T., Ignatiev, N., and Giuranna, M. (2004). Detection of Methane in the Atmosphere of Mars. *Science*, 306(5702):1758–1761.

Formisano, V., Maturilli, A., Giuranna, M., D'Aversa, E., and Lopez-Valverde, M. A. (2006). Observations of non-LTE emission at 4 5 microns with the planetary Fourier spectrometer abord the Mars Express mission. *Icarus*, 182(1):51–67.

Fraeman, A., Murchie, S., Arvidson, R., Clark, R., Morris, R., Rivkin, A., and Vilas, F. (2014). Spectral absorptions on Phobos and Deimos in the visible/near infrared wavelengths and their compositional constraints. *Icarus*, 229:196–205.

Geminale, A., Formisano, V., and Giuranna, M. (2008). Methane in Martian atmosphere: Average spatial, diurnal, and seasonal behaviour. *Planetary and Space Science*, 56(9):1194–1203.

Gendrin, A., Mangold, N., Bibring, J.-P., Langevin, Y., Gondet, B., Poulet, F., Bonello, G., Quantin, C., Mustard, J., Arvidson, R., and LeMouélic, S. (2005). Sulfates in Martian Layered Terrains: The OMEGA/Mars Express View. *Science*, 307(5715):1587–1591.

Gerakines, P. A. and Hudson, R. L. (2020). A Modified Algorithm and Open-source Computational Package for the Determination of Infrared Optical Constants Relevant to Astrophysics. *The Astrophysical Journal*, 901.

Gérard, J.-C., Aoki, S., Willame, Y., Gkouvelis, L., Depiesse, C., Thomas, I., and et al. (2020). Detection of green line emission in the dayside atmosphere of Mars from NOMAD-TGO observations. *Nature Astronomy*, 4(11):1049–1052.

Giardini, D., Lognonné, P., Banerdt, W. B., Pike, W. T., Christensen, U., Ceylan, S., and et al. (2020). The seismicity of Mars. *Nature Geoscience*, 13(3):205–212.

Gillespie, H. E., Greybush, S. J., and Wilson, R. J. (2020). An Investigation of the Encirclement of Mars by Dust in the 2018 Global Dust Storm Using EMARS. *Journal of Geophysical Research: Planets*, 125(7):e2019JE006106.

Giuranna, M., Hansen, G., Formisano, V., Zasova, L., Maturilli, A., Grassi, D., and Ignatiev, N. (2007). Spatial variability, composition and thickness of the seasonal north polar cap of Mars in mid-spring. *Planetary and Space Science*, 55(10):1328–1345.

Giuranna, M., Wolkenberg, P., Grassi, D., Aronica, A., Aoki, S., Scaccabarozzi, D., Saggin, B., and Formisano, V. (2019). The current weather and climate of Mars: 12 years of atmospheric monitoring by the Planetary Fourier Spectrometer on Mars Express. *Icarus*, 353:113406. From Mars Express to Exomars.

Glandorf, D. L., Colaprete, A., Tolbert, M. A., and Toon, O. B. (2002). CO2 snow on Mars and Early Earth: Experimental constraints. *Icarus*, 160:66–72.

Glotch, T. D., Edwards, C. S., Yesiltas, M., Shirley, K. A., McDougall, D. S., Kling, A. M., Bandfield, J. L., and Herd, C. D. K. (2018). MGS-TES Spectra Suggest a Basaltic Component in the Regolith of Phobos. *Journal of Geophysical Research: Planets*, 123(10):2467–2484.

Gottlieb, M. S., Gotzoulis, A. P., Pape, D. R., and Kulakov, S. V. (1994). *Acousto-optic tunable filters*, pages 197–283.

Government Publishing Office (2019). *Astronomical Almanac for the Year 2020*. U.S. Government Printing Office.

Graham, D. J. and Midgley, N. G. (2000). Graphical representation of particle shape using triangular diagrams: an Excel spreadsheet method. *Earth Surface Processes and Landforms*, 25(13):1473–1477.

Grasset, O., Dougherty, M., Coustenis, A., Bunce, E., Erd, C., Titov, D., Blanc, M., Coates, A., Drossart, P., Fletcher, L., Hussmann, H., Jaumann, R., Krupp, N., Lebreton, J.-P., Prieto-Ballesteros, O., Tortora, P., Tosi, F., and Van Hoolst, T. (2013). JUpiter ICy moons Explorer (JUICE): An ESA mission to orbit Ganymede and to characterise the Jupiter system. *Planetary and Space Science*, 78:1–21.

Green, A. A., Berman, M., Switzer, P., and Craig, M. (1988). A transformation for ordering multispectral data in terms of image quality with implications for noise removal. *IEEE Transactions on Geoscience and Remote Sensing*, 26(1):65–74.

Greybush, S. J., Gillespie, H. E., and Wilson, R. J. (2019). Transient eddies in the TES/MCS Ensemble Mars Atmosphere Reanalysis System (EMARS). *Icarus*, 317:158–181.

Guerri, I., Fabbri, A., Tommasi, L., Amoroso, M., Mugnuolo, R., Filacchione, G., Fonti, S., Piccioni, G., Saggin, B., Tosi, F., Zambelli, M., and Taiti, A. (2018). The optical design of the majis instrument on board of the juice mission. page 49.

Guha, B. K., Jagabandhu, P., and Zhaopeng, W. (2021). Observation of aphelion cloud belt over Martian tropics, its evolution, and associated dust distribution from MCS data. *Advances in Space Research*, 67(5):1392–1411.

Guzewich, S. D. and Smith, M. D. (2019). Seasonal Variation in Martian Water Ice Cloud Particle Size. *Journal of Geophysical Research: Planets*, 124(2):636–643.

Gómez-Elvira, J., Armiens, C., Carrasco, I., Genzer, M., Gómez, F., Haberle, R., Hamilton, V. E., Harri, A.-M., Kahanpää, H., Kemppinen, O., Lepinette, A., Martín Soler, J., Martín-Torres, J., Martínez-Frías, J., Mischna, M., Mora, L., Navarro, S., Newman, C., de Pablo, M. A., Peinado, V., Polkko, J., Rafkin, S. C. R., Ramos, M., Rennó, N. O., Richardson, M., Rodríguez-Manfredi, J. A., Romeral Planelló, J. J., Sebastián, E., de la Torre Juárez, M., Torres, J., Urquí, R., Vasavada, A. R., Verdasca, J., and Zorzano, M.-P. (2014). Curiosity's rover environmental monitoring station: Overview of the first 100 sols. *Journal of Geophysical Research: Planets*, 119(7):1680–1688.

Haberle, R. M. (1997). Mars: Atmosphere. In *Encyclopedia of Planetary Science.*, pages 432–441. Springer Netherlands, Dordrecht.

Haberle, R. M. (2015). Solar system/sun, atmospheres, evolution of atmospheres — planetary atmospheres. In *Encyclopedia of Atmospheric Sciences*, pages 168–177.

Haberle, R. M., Clancy, R. T., Forget, F., Smith, M. D., and Zurek, R. W. (2017). *The atmosphere and climate of Mars.* Cambridge University Press.

Hales, T. C. and Roering, J. J. (2007). Climatic controls on frost cracking and implications for the evolution of bedrock landscapes. *Journal of Geophysical Research: Earth Surface*, 112(F2).

Hanel, R., Schlachman, B., Breihan, E., Bywaters, R., Chapman, F., Rhodes, M., and et al. (1972). Mariner 9 michelson interferometer. *Applied Optics*, 11(11):2625.

Hansen, C., Byrne, S., Portyankina, G., Bourke, M., Dundas, C., McEwen, A., Mellon, M., Pommerol, A., and Thomas, N. (2013). Observations of the northern seasonal polar cap on Mars: I. Spring sublimation activity and processes. *Icarus*, 225:881–897.

Hansen, G. B. (2005). Ultraviolet to near-infrared absorption spectrum of carbon dioxide ice from 0.174 to 1.8 μm. *Journal of Geophysical Research*, 110(E11003).

Hapke, B. (1981). Bidirectional reflectance spectroscopy: 1. theory. *Journal of Geophysical Research: Solid Earth*, 86(B4):3039–3054.

Hapke, B. (2012). *Theory of Reflectance and Emittance Spectroscopy.* Cambridge University Press, 2nd edition.

Harris, S. and Rowan-Robinson, M. (1977). The brightest sources in the AFCRL Survey. *Astronomy and Astrophysics*, 60:405–412.

Hart, H. M. and Jakosky, B. M. (1986). Composition and stability of the condensate observed at the Viking lander 2 site on Mars. *Icarus*, 66(1):134–142.

He, C. and Flanner, M. (2020). *Snow Albedo and Radiative Transfer: Theory, Modeling, and Parameterization*, pages 67–133. Springer International Publishing, Cham.

Hernández, P., Pérez, N., Salazar, J., Sato, M., Notsu, K., and Wakita, H. (2000). Soil gas CO2, CH4, and H2 distribution in and around Las Cañadas caldera, Tenerife, Canary Islands, Spain. *Journal of Volcanology and Geothermal Research*, 103(1):425–438.

Hernández-Bernal, J., Sánchez-Lavega, A., del Río-Gaztelu Urrutia, T., Ravanis, E., Cardesín-Moinelo, A., Connour, K., Tirsch, D., Ordóñez-Etxeberria, I., Gondet, B., Wood, S., et al. (2021). An extremely elongated cloud over Arsia mons volcano on Mars: I. Life cycle. *J. Geophys. Res. Planets*, 126(7):e2020JE006517.

Herr, K. and Pimental, G. (1969). Infrared absorptions near three microns recorded over the polar cap of Mars. *Science*, 166(3907):496–499.

Hess, S. L., Henry, R. M., and Tillman, J. E. (1979). The seasonal variation of atmospheric pressure on Mars as affected by the south polar cap. *Journal of Geophysical Research*, 84:2923–2927.

Hess, S. L., Ryan, J. A., Tillman, J. E., Henry, R. M., and Leovy, C. B. (1980). The annual cycle of pressure on Mars measured by Viking landers 1 and 2. *Geophysical Research Letters*, 7:197–200.

Hutley, M. C. (1982). Diffraction gratings. *Techniques of Physics*, 6:76.

International Astronomical Union (2013). Proceedings of the International Astronomical Union. volume 10.

Iwasaki, K., Saito, Y., and Akabane, T. (1986). Martian south polar cap 1973. *Publications of the Astronomical Society of Japan*, 38(2):267–275.

James, P., Malolepszy, K., and Martin, L. (1987). Interannual variability of Mars' south polar cap. *Icarus*, 71(2):298–305.

James, P., Martin, L., Henson, J., and Birch, P. (1990). Seasonal recession of Mars' south polar cap in 1986. *Journal of Geophysical Research*, 95(B2):1337–1341.

James, P. B., Briggs, G. A., Barnes, J. R., and Spruck, A. (1979). Seasonal recession of mars' south polar cap as seen by viking. *Journal of Geophysical Research*, 84:2889–2922.

Jiang, C., Jiang, Y., Li, H., and Du, S. (2023). Initial results of the meteorological data from the first 325 sols of the Tianwen-1 mission. *Scientific Reports*, 13(1):3325.

Jones, K. L., Arvidson, R. E., Guinness, E. A., Bragg, S. L., Wall, S. D., Carlston, C. E., and Pidek, D. G. (1979). One Mars Year: Viking Lander Imaging Observations. *Science*, 204(4395):799–806.

Jordan, R., Picardi, G., Plaut, J., Wheeler, K., Kirchner, D., Safaeinili, A., Johnson, W., Seu, R., Calabrese, D., Zampolini, E., Cicchetti, A., Huff, R., Gurnett, D., Ivanov, A., Kofman, W., Orosei, R., Thompson, T., Edenhofer, P., and Bombaci, O. (2009). The Mars express MARSIS sounder instrument. *Planetary and Space Science*, 57(14):1975–1986.

Kahn, R. (1984). The spatial and seasonal distribution of Martian clouds and some meteorological implications. *Journal of Geophysical Research: Space Physics*, 89(A8):6671–6688.

Kahre, M. A., Hollingsworth, J. L., Haberle, R. M., and Wilson, R. J. (2015). Coupling the Mars dust and water cycles: the importance of radiative-dynamic feedbacks during northern hemisphere summer. *Icarus*, 260:477–480.

Karatekin, Ö., de Viron, O., Lambert, S., Dehant, V., Rosenblatt, P., Van Hoolst, T., and Le Maistre, S. (2011). Atmospheric angular momentum variations of Earth, Mars and Venus at seasonal time scales planet. *Planetary and Space Science*, 59:923–933.

Karatekin, Ö., Dehant, V., and Van Hoolst, T. (2006). Martian global-scale CO_2 exchange from time-variable gravity measurements. *Journal of Geophysical Research: Planets*, 111(E6):E06003.

Karatekin, Ö., Duron, J., Rosenblatt, P., Van Hoolst, T., Dehant, V., and Barriot, J. (2005). Mars' time-variable gravity and its determination: simulated geodesy experiments. *Journal of Geophysical Research: Planets*, 110(E6):E06001.

Kass, D. M., Schofield, J. T., Kleinböhl, A., McCleese, D. J., Heavens, N. G., Shirley, J. H., and Steele, L. J. (2019). Mars climate sounder observation of Mars' 2018 global dust storm. *Geophysical Research Letters*, 46(23).

Kass, D. M., Schofield, J. T., Kleinböhl, A., McCleese, D. J., Heavens, N. G., Shirley, J. H., and Steele, L. J. (2020). Mars Climate Sounder Observation of Mars' 2018 Global Dust Storm. *Geophysical Research Letters*, 47(23):e2019GL083931.

Khuller, A. R., Christensen, P. R., Harrison, T. N., and Diniega, S. (2021). The distribution of frosts on Mars: Links to present-day gully activity. *Journal of Geophysical Research: Planets*, 126(3):e2020JE006577.

Kieffer, H. (1970). Spectral reflectance of CO2-H2O Frosts. *Journal of Geophysical Research (1896-1977)*, 75(3):501–509.

Kieffer, H., Christensen, P., and Titus, T. (2006). CO2 jets formed by sublimation beneath translucent slab ice in Mars' seasonal south polar cap. *Nature*, 442:793–796.

Kieffer, H. and Titus, T. (2001). TES mapping of Mars' north seasonal cap. *Icarus*, 154(1):162–180.

Kieffer, H. G., Neugebauer, G., Munch, G., Chase, S., and Miner, E. (1972). Infrared thermal mapping experiment: The viking mars orbiter. *Icarus*, 16(1):47–56.

Kieffer, H. H. (1979). Mars south polar spring and summer temperatures: A residual CO2 frost. *Journal of Geophysical Research: Solid Earth*, 84(B14):8263–8288.

Kieffer, H. H., Titus, T. N., Mullins, K. F., and Christensen, P. R. (2000). Mars south polar spring and summer behaviour observed by TES: Seasonal cap evolution controlled by frost grain size. *Journal of Geophysical Research*, 105(E4):9653–9699.

Kleinböhl, A., Spiga, A., Kass, D. M., Shirley, J. H., Millour, E., Montabone, L., and Forget, F. (2020). Diurnal Variations of Dust During the 2018 Global Dust Storm Observed by the Mars Climate Sounder. *Journal of Geophysical Research: Planets*, 125(1):e2019JE006115.

Knutsen, E. W., Villanueva, G. L., Liuzzi, G., Crismani, M. M., Mumma, M. J., Smith, M. D., Vandaele, A. C., Aoki, S., Thomas, I. R., Daerden, F., Viscardy, S., Erwin, J. T., Trompet, L., Neary, L., Ristic, B., Lopez-Valverde, M. A., Lopez-Moreno, J. J., Patel, M. R., Karatekin, O., and Bellucci, G. (2021). Comprehensive investigation of Mars methane and organics with ExoMars/NOMAD. *Icarus*, 357:114266.

Konopliv, A. S., Asmar, S. W., Folkner, W. M., Özgür Karatekin, Nunes, D. C., Smrekar, S. E., Yoder, C. F., and Zuber, M. T. (2011). Mars high resolution gravity fields from MRO, Mars seasonal gravity, and other dynamical parameters. *Icarus*, 211(1):401–428.

Korablev, O., Olsen, K. S., Trokhimovskiy, A., Lefèvre, F., Montmessin, F., Fedorova, A. A., Toplis, M. J., Alday, J., Belyaev, D. A., Patrakeev, A., Ignatiev, N. I., Shakun, A. V., Grigoriev, A. V., Baggio, L., Abdenour, I., Lacombe, G., Ivanov, Y. S., Aoki, S., Thomas, I. R., Daerden, F., Ristic, B., Erwin, J. T., Patel, M., Bellucci, G., Lopez-Moreno, J.-J., and Vandaele, A. C. (2021). Transient HCl in the atmosphere of Mars. *Science Advances*, 7(7).

Korablev, O., Vandaele, A., Montmessin, F., and et al. (2019). No detection of methane on Mars from early ExoMars Trace Gas Orbiter observations. *Nature*, 568(7752):517–520.

Kruse, F. A., Lefkoff, A., and Dietz, J. (1993). Expert system-based mineral mapping in northern Death Valley, California/Nevada, using the airborne visible/infrared imaging spectrometer (AVIRIS). *Remote Sensing of Environment*, 44(2):309–336.

Kuramoto, K., Kawakatsu, Y., Fujimoto, M., Araya, A., Barucci, M. A., Genda, H., Hirata, N., Ikeda, H., Imamura, T., Helbert, J., Kameda, S., Kobayashi, M., Kusano, H., Lawrence, D. J., Matsumoto, K., Michel, P., Miyamoto, H., Morota, T., Nakagawa, H., Nakamura, T., Ogawa, K., Otake, H., Ozaki, M., Russell, S., Sasaki, S., Sawada, H., Senshu, H., Tachibana, S., Terada, N., Ulamec, S., Usui, T., Wada, K., Watanabe, S.-i., and Yokota, S. (2022). Martian moons exploration MMX: sample return mission to Phobos elucidating formation processes of habitable planets. *Earth, Planets and Space*, 74(1):12.

Lange, L., Forget, F., Banfield, D., Wolff, M., Spiga, A., Millour, E., and et al. (2022). Insight pressure data recalibration, and its application to the study of long-term pressure changes on Mars. *Journal of Geophysical Research: Planets*, 127:e2022JE007190.

Langevin, Y., Bibring, J. P., Montmessin, F., Forget, F., Vincendon, M., Douté, S., Poulet, F., and Gondet, B. (2007). Observations of the South Seasonal Cap of Mars During Recession in 2004-2006 by the OMEGA Visible/Near-Infrared Imaging Spectrometer on Board Mars Express. *J. Geophys. Res.*, 112:E08S12.

Langevin, Y., Douté, S., Vincendon, M., Forget, F., Lebonnois, S., and Forget, G. (2006). No signature of clear CO2 ice from the 'cryptic' regions in Mars' south seasonal polar cap. *Nature*, 442(7104):790–792.

Langevin, Y., Poulet, F., Bibring, J.-P., and Gondet, B. (2005a). Sulfates in the North Polar Region of Mars Detected by OMEGA/Mars Express. *Science*, 307(5715):1584–1586.

Langevin, Y., Poulet, F., Bibring, J.-P., Schmitt, B., Douté, S., and Gondet, B. (2005b). Summer Evolution of the North Polar Cap of Mars as Observed by OMEGA/Mars Express. *Science*, 307(5715):1581–1584.

Larson, H. P. and Fink, U. (1972). Identification of carbon dioxide frost on the Martian polar caps. *The Astrophysical Journal*, 171:L91–L95.

Le Maistre, S., Rivoldini, A., Caldiero, A., Yseboodt, M., Baland, R.-M., Beuthe, M., Van Hoolst, T., Dehant, V., Folkner, W. M., Buccino, D., Kahan, D., Marty, J.-C., Antonangeli, D., Badro, J., Drilleau, M., Konopliv, A., Péters, M.-J., Plesa, A.-C., Samuel, H., Tosi, N., Wieczorek, M., Lognonné, P., Panning, M., Smrekar, S., and Banerdt, W. B. (2023). Spin state and deep interior structure of Mars from InSight radio tracking. *Nature*.

Le Maistre, S., Rivoldini, A., and Rosenblatt, P. (2019). Signature of Phobos' interior structure in its gravity field and libration. *Icarus*, 321:272–290.

Lee, J. B., Woodyatt, A. S., and Berman, M. (1990). Enhancement of high spectral resolution remote-sensing data by a noise-adjusted principal components transform. *IEEE Transactions on Geoscience and Remote Sensing*, 28(3):295–304.

Lefèvre, F. and Forget, F. (2009). Observed variations of methane on Mars unexplained by known atmospheric chemistry and physics. *Nature*, 460(7256):720–723.

Leighton, R. B. and Murray, B. C. (1966). Behavior of carbon dioxide and other volatiles on Mars. *Science*, 153(3732):136–144.

Leighton, R. B., Murray, B. C., Sharp, R. P., Allen, J. D., and Sloan, R. K. (1965). Mariner IV photography of Mars: Initial results. *Science*, 149(3684):627–630.

Liou, K. (2002). Chapter 5 - Light Scattering by Atmospheric Particulates. In *An Introduction to Atmospheric Radiation*, volume 84 of *International Geophysics*, pages 169–256. Academic Press.

Liu, J., Richardson, M. I., and Wilson, R. J. (2003). An assessment of the global, seasonal, and interannual spacecraft record of Martian climate in the thermal infrared. *Journal of Geophysical Research*, 108:5089.

Liuzzi, G., Villanueva, G. L., Crismani, M. M., Smith, M. D., Mumma, M. J., Daerden, F., Aoki, S., Vandaele, A. C., Clancy, R. T., Erwin, J., et al. (2020). Strong variability of Martian water ice clouds during dust storms revealed from ExoMars Trace Gas Orbiter/NOMAD. *Journal of Geophysical Research: Planets*, 125(1):e2019JE006250.

Liuzzi, G., Villanueva, G. L., Mumma, M. J., Smith, M. D., Daerden, F., Ristic, B., Thomas, I., Vandaele, A. C., Patel, M. R., Lopez-Moreno, J.-J., and Bellucci, G. (2019). Methane on Mars: New insights into the sensitivity of CH4 with the NOMAD/ExoMars spectrometer through its first in-flight calibration. *Icarus*, 321:671–690.

Liuzzi, G., Villanueva, G. L., Trompet, L., Crismani, M. M. J., Piccialli, A., Aoki, S., and et al. (2021). First detection and thermal characterization of terminator CO2 ice clouds with ExoMars/NOMAD. *Geophysical Research Letters*, 48:e2021GL095895.

López-Valverde, M. A., Funke, B., Brines, A., Stolzenbach, A., Modak, A., Hill, B., González-Galindo, F., Thomas, I., Trompet, L., Aoki, S., Villanueva, G., Liuzzi, G., Erwin, J., Grabowski, U., Forget, F., López-Moreno, J. J., Rodriguez-Gómez, J., Ristic, B., Daerden, F., Bellucci, G., Patel, M., Vandaele, A.-C., and the NOMAD team (2023). Martian Atmospheric Temperature and Density Profiles During the First Year of NOMAD/TGO Solar Occultation Measurements. *Journal of Geophysical Research: Planets*, 128(2):e2022JE007278.

López-Valverde, M. A., Gerard, J., González-Galindo, F., Vandaele, A. C., Thomas, I., Korablev, O., and et al. (2018). Investigations of the Mars upper atmosphere with ExoMars Trace Gas Orbiter. *Space Science Reviews*, 214(1):29.

Madeleine, J., Forget, F., Spiga, A., Wolff, M., Montmessin, F., Vincendon, M., Jouglet, D., Gondet, B., Bibring, J., Langevin, Y., et al. (2012a). Aphelion water-ice cloud mapping and property retrieval using the OMEGA imaging spectrometer onboard Mars Express. *J. Geophys. Res.*, 117.

Madeleine, J.-B., Forget, F., Millour, E., Montabone, L., and Wolff, M. J. (2011). Revisiting the radiative impact of dust on Mars using the LMD Global Climate Model. *Journal of Geophysical Research: Planets*, 116(E11).

Madeleine, J.-B., Forget, F., Millour, E., Navarro, T., and Spiga, A. (2012b). The influence of radiatively active water ice clouds on the Martian climate. *Geophysical Research Letters*, 39(23).

Mahieux, A., Berkenbosch, S., Clairquin, R., Fussen, D., Mateshvili, N., Neefs, E., Nevejans, D., Ristic, B., Vandaele, A. C., Wilquet, V., Belyaev, D., Fedorova, A., Korablev, O., Villard, E., Montmessin, F., and Bertaux, J.-L. (2008). In-flight performance and calibration of SPICAV SOIR onboard Venus Express. *Applied optics*, 47(13):2252—2265.

Mahieux, A., Vandaele, A. C., Robert, S., Wilquet, V., Drummond, R., Montmessin, F., and Bertaux, J. L. (2012). Densities and temperatures in the Venus mesosphere and lower thermosphere retrieved from SOIR on board Venus Express: carbon dioxide measurements at the Venus terminator. *J. Geophys. Res.*, 117:E07001.

Mahieux, A., Wilquet, V., Drummond, R., Belyaev, D., Federova, A., and Vandaele, A. (2009). A new method for determining the transfer function of an Acousto optical tunable filter. *Opt. Express*, 17(3):2005–2014.

Malin, M. C., Bell III, J. F., Cantor, B. A., Caplinger, M. A., Calvin, W. M., Clancy, R. T., and et al. (2007). Context Camera Investigation on board the Mars Reconnaissance Orbiter. *Journal of Geophysical Research: Planets*, 112(E5).

Malin, M. C., Calvin, W., Clancy, R. T., Haberle, R. M., James, P. B., Lee, S. W., Thomas, P. C., and Caplinger, M. A. (2001). The Mars Color Imager (MARCI) on the Mars Climate Orbiter. *J. Geophys. Res. Planets*, 106:17651–17672.

Malin, M. C. and Cantor, B. A. (2021). MRO MARCI Weather Report for the week of 29 November 2021 - 5 December 2021. Malin Space Science Systems Captioned Image Release. MSSS-599.

Maltagliati, L., Titov, D. V., Encrenaz, T., Melchiorri, R., Forget, F., Garcia-Comas, M., Keller, H. U., Langevin, Y., and Bibring, J.-P. (2008). Observations of atmospheric water vapor above the Tharsis volcanoes on Mars with the OMEGA/MEx imaging spectrometer. *Icarus*, 194(1):53–64.

Martínez, G. M., Newman, C. N., De Vicente-Retortillo, A., Fischer, E., Renno, N. O., Richardson, M. I., Fairén, A. G., Genzer, M., Guzewich, S. D., Haberle, R. M., Harri, A.-M., Kemppinen, O., Lemmon, M. T., Smith, M. D., de la Torre-Juárez, M., and Vasavada, A. R. (2017). The Modern Near-Surface Martian Climate: A Review of In-situ Meteorological Data from Viking to Curiosity. *Space Science Reviews*, 212(1):295–338.

Marzo, G. A., Roush, T. L., Blanco, A., Fonti, S., and Orofino, V. (2006). Cluster analysis of planetary remote sensing spectral data. *Journal of Geophysical Research: Planets*, 111(E3).

Mateshvili, N., Fussen, D., Vanhellemont, F., Bingen, C., Dodion, J., Montmessin, F., Perrier, S., Dimarellis, E., and Bertaux, J.-L. (2007). Martian ice cloud distribution obtained from SPICAM nadir UV measurements. *Journal of Geophysical Research*, 112:E07004.

Mayer, B. and Kylling, A. (2005). Technical note: The libRadtran software package for radiative transfer calculations-Description and examples of use. *Atmospheric Chemistry and Physics Discussions*, 5:1319–1381.

McConnochie, T. H., Bell, J. F., Savransky, D., Wolff, M. J., Toigo, A. D., Wang, H., Richardson, M. I., and Christensen, P. R. (2010). Themis-Vis observations of clouds in the Martian mesophere: Altitudes, wind speeds, and decameter-scale morphology. *Icarus*, 210:545–565.

McEwen, A., Eliason, E., Bergstrom, J., Bridges, N., Hansen, C., Delamere, W., Grant, J., Gulick, V., Herkenhoff, K., Keszthelyi, L., Kirk, R., Mellon, M., Squyres, S., Thomas, N., and Weitz, C. (2007). Mars Reconnaissance Orbiter's High-Resolution Imaging Science Experiment (HiRISE). *Journal of Geophysical Research: Planets*, 112:S02.

McGuire, P. C., Bishop, J. L., Brown, A. J., Fraeman, A. A., Marzo, G. A., Frank Morgan, M., Murchie, S. L., Mustard, J. F., Parente, M., Pelkey, S. M., Roush, T. L., Seelos, F. P., Smith, M. D., Wendt, L., and Wolff, M. J. (2009). An improvement to the volcano-scan algorithm for atmospheric correction of CRISM and OMEGA spectral data. *Planetary and Space Science*, 57(7):809–815.

Michel, P., Küppers, M., Campo Bagatin, A., Carry, B., Charnoz, S., De León, J., Fitzsimmons, A., Gordo, P., Green, S., Herique, A., Juzi, M., Karatekin, Ö., Kohout, T., Lazzarin, M., Murdoch, N., Okada, T., Palomba, E., Pravec, P., Snodgrass, C., and Carnelli, I. (2022). The ESA Hera Mission: Detailed Characterization of the DART Impact Outcome and of the Binary Asteroid (65803) Didymos. *The Planetary Science Journal*, 3:160.

Millour, E., Forget, F., and Spiga, A. (2018). The Mars Climate Database, Version 5.3. `https://doi.org/10.5281/zenodo.1465554`.

Mischna, M. A., Lee, C., and Richardson, M. (2012). Development of a fast, accurate radiative transfer model for the Martian atmosphere, past and present. *Journal of Geophysical Research: Planets*, 117(E10).

Montabone, L., Forget, F., Millour, E., Wilson, R., Lewis, S., Cantor, B., Kass, D., Kleinböhl, A., Lemmon, M., Smith, M., and Wolff, M. (2015). Eight-year climatology of dust optical depth on Mars. *Icarus*, 251:65–95. Dynamic Mars.

Montabone, L., Spiga, A., Kass, D. M., Kleinböhl, A., Forget, F., and Millour, E. (2020). Martian Year 34 Column Dust Climatology from Mars Climate Sounder Observations: Reconstructed Maps and Model Simulations. *Journal of Geophysical Research: Planets*, 125(8):e2019JE006111.

Montmessin, F., Bertaux, J.-L., Quémerais, E., Korablev, O., Rannou, P., Forget, F., Perrier, S., Fussen, D., Lebonnois, S., Rébérac, A., and Dimarellis, E. (2006). Subvisible CO_2 ice clouds detected in the mesosphere of Mars. *Icarus*, 183(2):403–410.

Montmessin, F., Forget, F., Rannou, P., Cabane, M., and Haberle, R. M. (2004). Origin and role of water ice clouds in the Martian water cycle as inferred from a general circulation model. *Journal of Geophysical Research: Planets*, 109.

Montmessin, F., Gondet, B., Bibring, J., Langevin, Y., Drossart, P., Forget, F., and Fouchet, T. (2007). Hyperspectral imaging of convective CO_2 ice clouds in the equatorial mesosphere of Mars. *J. Geophys. Res. Planets*, 112:E11S90.

Moores, J. E., King, P. L., Smith, C. L., Martinez, G. M., Newman, C. E., Guzewich, S. D., Meslin, P.-Y., Webster, C. R., Mahaffy, P. R., Atreya, S. K., and Schuerger, A. C. (2019). The Methane Diurnal Variation and Microseepage flux at Gale Crater, Mars as Constrained by the ExoMars Trace Gas Orbiter and Curiosity Observations. *Geophysical Research Letters*, 46(16):9430–9438.

Mumma, M. J., Villanueva, G. L., Novak, R. E., Hewagama, T., Bonev, B. P., DiSanti, M. A., Mandell, A. M., and Smith, M. D. (2009). Strong Release of Methane on Mars in Northern Summer 2003. *Science*, 323(5917):1041–1045.

Munaretto, G., Pajola, M., Cremonese, G., Re, C., Lucchetti, A., Simioni, E., and et al. (2020). Implications for the origin and evolution of Martian Recurring Slope Lineae at Hale crater from CaSSIS observations. *Planetary and Space Science*, 187:104947.

Munaretto, G., Pajola, M., Lucchetti, A., Cremonese, G., Simioni, E., Re, C., and et al. (2022). Multiband photometry of Martian Recurring Slope Lineae (RSL) and dust-removed features at Horowitz crater, Mars from TGO/CaSSIS color observations. *Planetary and Space Science*, 214:105443.

Munaretto, G., Pajola, M., Lucchetti, A., Re, C., Cremonese, G., Simioni, E., and et al. (2021). Topographic correction of HiRISE and CaSSIS images: Validation and application to color observations of Martian albedo features. *Planetary and Space Science*, 200:105198.

Munguira, A., Hueso, R., Sánchez-Lavega, A., Torre-Juarez, M., Martinez, G. M., Newman, C., Sebastian, E., Lepinette, A., Vicente-Retortillo, A., Chide, B., Lemmon, M., Bertrand, T., Lorenz, R., Banfield, D., Gomez-Elvira, J., Martin-Soler, J., Navarro Lopez, S., Pla-García, J., Rodriguez-Manfredi, J., and Torres, J. (2023). Near Surface Atmospheric Temperatures at Jezero From Mars 2020 MEDA Measurements. *Journal of Geophysical Research: Planets*, 128.

Murchie, S., Arvidson, R., Bedini, P., Beisser, K., Bibring, J.-P., Bishop, J., Boldt, J., Cavender, P., Choo, T., Clancy, R. T., et al. (2007). Compact Reconnaissance Imaging Spectrometer for Mars (CRISM) on Mars Reconnaissance Orbiter (MRO). *J. Geophys. Res. Planets*, 112.

Murchie, S. L., Kirkland, L. E., Erard, S., Mustard, J. F., and Robinson, M. S. (2000). Near-Infrared Spectral Variations of Martian Surface Materials from ISM Imaging Spectrometer Data. *Icarus*, 147:444–471.

Määttänen, A., Montmessin, F., Gondet, B., Scholten, F., Hoffmann, H., González-Galindo, F., Spiga, A., Forget, F., Hauber, E., Neukum, G., Bibring, J.-P., and Bertaux, J.-L. (2010). Mapping the mesospheric CO2 clouds on Mars: MEx/OMEGA and MEx/HRSC observations and challenges for atmospheric models. *Icarus*, 209(2):452–469.

Navarro, T., Madeleine, J.-B., Forget, F., Spiga, A., Millour, E., Montmessin, F., and Määttänen, A. (2014). Global Climate Modeling of the Martian water cycle with improved microphysics and radiatively active water ice clouds. *Journal of Geophysical Research: Planets*, 119(7):1479–1495.

Neary, L., Daerden, F., Aoki, S., Whiteway, J., Clancy, R. T., Smith, M., et al. (2020). Explanation for the increase in high altitude water on Mars observed by NOMAD during the 2018 global dust storm. *Geophysical Research Letters*, 47(7):e2019GL084354.

Neefs, E., Vandaele, A. C., Drummond, R., Thomas, I. R., Berkenbosch, S., Clairquin, R., Delanoye, S., Ristic, B., Maes, J., Bonnewijn, S., Pieck, G., Equeter, E., Depiesse, C., Daerden, F., Ransbeeck, E. V., Nevejans, D., Rodriguez-Gómez, J., López-Moreno, J.-J., Sanz, R., Morales, R., Candini, G. P., Pastor-Morales, M. C., del Moral, B. A., Jeronimo-Zafra, J.-M., Gómez-López, J. M., Alonso-Rodrigo, G., Pérez-Grande, I., Cubas, J., Gomez-Sanjuan, A. M., Navarro-Medina, F., Thibert, T., Patel, M. R., Bellucci, G., Vos, L. D., Lesschaeve, S., Vooren, N. V., Moelans, W., Aballea, L., Glorieux, S., Baeke, A., Kendall, D., Neef, J. D., Soenen, A., Puech, P.-Y., Ward, J., Jamoye, J.-F., Diez, D., Vicario-Arroyo, A., and Jankowski, M. (2015). NOMAD spectrometer on the ExoMars trace gas orbiter mission: part 1—design, manufacturing and testing of the infrared channels. *Appl. Opt.*, 54(28):8494–8520.

Neukum, G., Jaumann, R., and the HRSC Co-Investigator Team (2004). Hrsc: The high resolution stereo camera of mars express. In *ESA SP-1240*, page 19.

Nevejans, D., Neefs, E., Van Ransbeeck, E., Berkenbosch, S., Clairquin, R., De Vos, L., Moelans, W., Glorieux, S., Baeke, A., Korablev, O., Vinogradov, I., Kalinnikov, Y., Bach, B., Dubois, J.-P., and Villard, E. (2006). Compact high-resolution spaceborne echelle grating spectrometer with acousto-optical tunable filter based order sorting for the infrared domain from 2.2 to 4.3 μm. *Applied Optics*, 45(22):5191–5206.

Newman, C. E., Lewis, S. R., and Read, P. L. (2005). The atmospheric circulation and dust activity in different orbital epochs on Mars. *Icarus*, 174:135–160.

Okada, T., Tanaka, S., Sakatani, N., Shimaki, Y., Arai, T., Senshu, H., Demura, H., Sekiguchi, T., Ishizaki, T., Kouyama, Blommaert, J., and Karatekin, O. (2022). DEVELOPMENT OF THERMAL INFRARED MULTIBAND IMAGER TIRI FOR HERA MISSION.

Oliva, F., Adriani, A., Moriconi, M., Liberti, G. L., D'Aversa, E., and Filacchione, G. (2016). Clouds and hazes vertical structure of a Saturn's giant vortex from Cassini/VIMS-V data analysis. *Icarus*, 278:215–237.

Oliva, F., D'Aversa, E., Bellucci, G., Carrozzo, F. G., Ruiz Lozano, L., Altieri, F., Thomas, I. R., Karatekin, Ö., Cruz Mermy, G., Schmidt, F., et al. (2022). Martian CO_2 ice observation at high spectral resolution with ExoMars/TGO NOMAD. *Journal of Geophysical Research: Planets*, 127(6):e2021JE007083.

Oliva, F., Geminale, A., D'Aversa, E., Altieri, F., Bellucci, G., Carrozzo, F., Sindoni, G., and Grassi, D. (2018). Properties of a Martian local dust storm in Atlantis chaos from OMEGA/MEX data. *Icarus*, 300:1–11.

Olsen, K. S., Forget, F., Madeleine, J.-B., Szantai, A., Audouard, J., Geminale, A., Altieri, F., Bellucci, G., Oliva, F., Montabone, L., et al. (2021). Retrieval of the water ice column and physical properties of water-ice clouds in the Martian atmosphere using the OMEGA imaging spectrometer. *Icarus*, 353:113229.

Owen, T. (1992). The composition and early history of the atmosphere of Mars. In *Mars*, pages 818–835. University of Arizona Press, Tucson, AZ.

Owen, T., Biemann, K., Rushneck, D. R., Biller, J. E., Howarth, D. W., and Lafleur, A. L. (1977). The composition of the atmosphere at the surface of Mars. *Journal of Geophysical Research*, 82(28):4635–4639.

Oyama, V. I. and Berdahl, B. J. (1977). The Viking Gas Exchange experiment results from Chryse and Utopia surface samples. *Journal of Geophysical Research*, 82(28):4669–4676.

Pajola, M., Lucchetti, A., Semenzato, A., Poggiali, G., Munaretto, G., Galluzzi, V., and et al. (2021). Lermontov crater on Mercury: Geology, morphology and spectral properties of the coexisting hollows and pyroclastic deposits. *Planetary and Space Science*, 195:105136.

Palmer, C. (2020). *DIFFRACTION GRATING HANDBOOK, eighth edition*.

Patel, M. R., Antoine, P., Mason, J.-P., Leese, M. R., Hathi, B., Stevens, A. H., Dawson, D., Gow, J. P., Ringrose, T. J., Holmes, J. A., et al. (2017). NOMAD spectrometer on the ExoMars Trace Gas Orbiter mission: Part 2—Design, manufacturing, and testing of the ultraviolet and visible channel. *Applied optics*, 56(10):2771–2782.

Pelkey, S. M., Mustard, J. F., Murchie, S., Clancy, R. T., Wolff, M., Smith, M., Milliken, R., Bibring, J.-P., Gendrin, A., Poulet, F., Langevin, Y., and Gondet, B. (2007). Crism multispectral summary products: Parameterizing mineral diversity on mars from reflectance. *Journal of Geophysical Research: Planets*, 112(E8).

Pieters, C., Murchie, S., Thomas, N., and Britt, D. (2014). Composition of surface materials on the Moons of Mars. *Planetary and Space Science*, 102:144–151.

Piqueux, S., Byrne, S., and Richardson, M. (2003). Sublimation of Mars's southern seasonal CO_2 ice cap and the formation of spiders. *J. Geophys. Res.*, 108:5084.

Piqueux, S., Kleinböhl, A., Hayne, P. O., Heavens, N. G., Kass, D. M., McCleese, D. J., Schofield, J. T., and Shirley, J. H. (2016). Discovery of a widespread low-latitude diurnal CO_2 frost cycle on Mars. *Journal of Geophysical Research: Planets*, 121(7):1174–1189.

Piqueux, S., Kleinböhl, A., Hayne, P. O., Kass, D. M., Schofield, J. T., and McCleese, D. J. (2015). Variability of the martian seasonal CO_2 cap extent over eight Mars Years. *Icarus*, 251:164–180. Dynamic Mars.

Plescia, J. B. (2004). Morphometric properties of Martian volcanoes. *Journal of Geophysical Research: Planets*, 109(E3).

Pommerol, A. and et al. (2011). Evolution of south seasonal cap during martian spring: Insights from high-resolution observations by hirise and crism on mars reconnaissance orbiter. *Journal of Geophysical Research: Planets*, 116:E08007.

Pommerol, A., Thomas, N., Almeida, M., Read, M., Becerra, P., Cesar, C., and et al. (2022). In flight radiometric calibration of the ExoMars TGO Colour and Stereo Surface Imaging System. *Planetary and Space Science*, page 105580.

Poulet, F., Mangold, N., Platevoet, B., Bardintzeff, J., Sautter, V., Mustard, J., Bibring, J., Pinet, P., Langevin, Y., Gondet, B., et al. (2009). Quantitative compositional analysis of Martian mafic regions using the MEx/OMEGA reflectance data: 2. Petrological implications. *Icarus*, 201:84–101.

Presley, M. and Christensen, P. (2010). Thermal conductivity measurements of particulate materials: 4. Effect of bulk density for granular particles. *Journal of Geophysical Research*, 115.

Ramsley, K. R. and Head, J. W. (2021). The Origins and Geological Histories of Deimos and Phobos: Hypotheses and Open Questions. *Space Science Reviews*, 217:1–24.

Re, C., Fennema, A., Simioni, E., Sutton, S., Mège, D., Gwinner, K., and et al. (2022). CaSSIS based stereo products for Mars after three years in orbit. *Planetary and Space Science*, 219:105515.

Richardson, M. I., Toigo, A. D., and Newman, C. E. (2007). PlanetWRF: A general purpose, local to global numerical model for planetary atmospheric and climate dynamics. *Journal of Geophysical Research: Planets*, 112(E9).

Richardson, M. I., Wilson, R. J., and Rodin, A. V. (2002). Water ice clouds in the Martian atmosphere: General circulation model experiments with a simple cloud scheme. *Journal of Geophysical Research: Planets*, 107.

Riu, L., Poulet, F., Bibring, J.-P., and Gondet, B. (2019a). The M3 project: 2—Global distributions of mafic mineral abundances on Mars. *Icarus*, 322:31–53.

Riu, L., Poulet, F., Carter, J., Bibring, J.-P., Gondet, B., and Vincendon, M. (2019b). The M3 project: 1—A global hyperspectral imagecube of the Martian surface. *Icarus*, 319:281–292.

Rodgers, C. D. (2000). *Inverse Methods for Atmospheric Sounding*. Number 2 in Series on Atmospheric, Oceanic and Planetary Physics. World Scientific, Singapore.

Rogers, A., Bandfield, J., and Christensen, P. (2007). Global spectral classification of Martian low-albedo regions with Mars Global Surveyor Thermal Emission Spectrometer (MGS-TES) data. *J. Geophys. Res.*, 112(E2).

Rogers, D. and Christensen, P. (2003). Age relationship of basaltic and andesitic surface compositions on Mars: Analysis of high-resolution TES observations of the northern hemisphere. *J. Geophys. Res.*, 108(E5).

Rosenblatt, P. (2011). The origin of the Martian moons revisited. *Astronomy and Astrophysics Review*, 19(44):1–26.

Rosenblatt, P., Charnoz, S., Dunseath, K., Terao-Dunseath, M., Trinh, A., Hyodo, R., Genda, H., and Toupin, S. (2016). Accretion of Phobos and Deimos in an extended debris disc stirred by transient moons. *Nature Geoscience*, 9(8):581–583.

Ruiz Lozano, L., Karatekin, Ö., Dehant, V., Bellucci, G., Oliva, F., D'Aversa, E., Carrozzo, F., Altieri, F., Thomas, I., Willame, Y., Robert, S., Vandaele, A., Daerden, F., Ristic, B., Patel, M., and López Moreno, J. (2022). Evaluation of the Capability of ExoMars-TGO NOMAD Infrared Nadir Channel for Water Ice Clouds Detection on Mars. *Remote Sens.*, 14(17):4143.

Ruiz Lozano, L., Oliva, F., Karatekin, O., Bellucci, G., Dehant, V., D'Aversa, E., Carrozzo, F., Schmidt, F., Cruz Mermy, G., Thomas, I., Vandaele, A., Daerden, F., Ristic, B., Patel, M., and López-Moreno, J.-J. (2023). Observation of the Southern Polar cap during MY34-36 with ExoMars-TGO NOMAD LNO. *Icarus*, page 115698.

Saunders, R., Arvidson, R., Badhwar, G., Boynton, W., Christensen, P., Cucinotta, F., Feldman, W., Gibbs, R., Kloss, C., Landano, M., Mase, R., McSmith, G., Meyer, M., Mitrofanov, I., Pace, G., Plaut, J., Sidney, W., Spencer, D., Thompson, T., and Zeitlin, C. (2004). 2001 mars odyssey mission summary. *Space Science Reviews*, 110(1):1–36.

Schaefer, E. I., McEwen, A. S., and Sutton, S. S. (2019). A case study of recurring slope lineae (RSL) at Tivat crater: Implications for RSL origins. *Icarus*, 317:621–648.

Schmidt, F., Douté, S., Schmitt, B., Vincendon, M., Bibring, J.-P., Langevin, Y., and Team, O. (2009). Albedo control of Seasonal South Polar Cap recession on Mars. *Icarus*, 200:374–394.

Schmidt, F., Schmitt, B., Douté, S., Forget, F., Jian, J., Martin, P., Langevin, Y., Bibring, J., and Team, O. (2010). Sublimation of the Martian CO_2 Seasonal South Polar Cap. *Planet. Space Sci.*, 58:1129–1138.

Schmitt, B., Quirico, E., Trotta, F., and Grundy, W. M. (1998). Optical properties of ices from UV to infrared. In Schmitt, B., De Bergh, C., and Festou, M., editors, *Solar System Ices*, volume 227 of *Astrophysics and Space Science Library*, pages 143–166. Springer.

Schofield, J. T., Barnes, J. R., Crisp, D., Haberle, R. M., Larsen, S., Magalhães, J. A., and et al. (1997). The Mars Pathfinder atmospheric structure investigation/meteorology (ASI/MET) experiment. *Science*, 278(5344):1752–1758.

Schorghofer, N. and Edgett, K. S. (2006). Seasonal surface frost at low latitudes on mars. *Icarus*, 180(2):321–334.

Seelos, F. P., Seelos, K. D., Murchie, S. L., Novak, M. A. M., Hash, C. D., Morgan, M. F., Arvidson, R. E., Aiello, J., Bibring, J.-P., Bishop, J. L., Boldt, J. D., Boyd, A. R., Buczkowski, D. L., Chen, P. Y., Clancy, R. T., Ehlmann, B. L., Frizzell, K., Hancock, K. M., Hayes, J. R., Heffernan, K. J., Humm, D. C., Itoh, Y., Ju, M., Kochte, M. C., Malaret, E., McGovern, J. A., McGuire, P., Mehta, N. L., Moreland, E. L., Mustard, J. F., Nair, A. H., Núñez, J. I., O'Sullivan,

J. A., Packer, L. L., Poffenbarger, R. T., Poulet, F., Romeo, G., Santo, A. G., Smith, M. D., Stephens, D. C., Toigo, A. D., Viviano, C. E., and Wolff, M. J. (2023). The CRISM investigation in Mars orbit: Overview, history, and delivered data products. *Icarus*, page 115612.

Seidelmann, P., Archinal, B., A'Hearn, M., Conrad, A., Consolmagno, G., Hestroffer, D., Hilton, J., Krasinsky, G., Neumann, G., Oberst, J., Stooke, P., Tedesco, E., Tholen, D., Thomas, P., and Williams, I. (2007). Report of the IAU/IAG Working Group on cartographic coordinates and rotational elements: 2006. *Celestial Mechanics and Dynamical Astronomy*, 98(3):155–180.

Senel, C. B., Temel, O., Lee, C., Newman, C. E., Mischna, M. A., Muñoz-Esparza, D., and et al. (2021). Interannual, Seasonal and Regional Variations in the Martian Convective Boundary Layer Derived From GCM Simulations With a Semi-Interactive Dust Transport Model. *Journal of Geophysical Research: Planets*, 126(10):e2021JE006965.

Seu, R., Phillips, R. J., Biccari, D., Orosei, R., Masdea, A., Picardi, G., Safaeinili, A., Campbell, B. A., Plaut, J. J., Marinangeli, L., Smrekar, S. E., and Nunes, D. C. (2007). Sharad sounding radar on the mars reconnaissance orbiter. *Journal of Geophysical Research: Planets*, 112(E5).

Simioni, E., Re, C., Mudric, T., Cremonese, G., Tulyakov, S., Petrella, A., and et al. (2021). 3DPD: A photogrammetric pipeline for a PUSH frame stereo cameras. *Planetary and Space Science*, 198:105165.

Sindoni, G., Grassi, D., Adriani, A., Mura, A., Moriconi, M. L., Dinelli, B. M., Filacchione, G., Tosi, F., Piccioni, G., Migliorini, A., et al. (2017). Characterization of the white ovals on Jupiter's southern hemisphere using the first data by the JUNO/JIRAM instrument: Jupiter ovals as seen by JIRAM/JUNO. *Geophysical Research Letters*, 44(9):4660–4668.

Singh, D. and Flanner, M. G. (2016). An improved carbon dioxide snow spectral albedo model: Application to Martian conditions. *Journal of Geophysical Research: Planets*, 121(10):2037–2054.

Smith, D. E., Zuber, M. T., Frey, H. V., Garvin, J. B., Head, J. W., Muhleman, D. O., and et al. (2001). Mars Orbiter Laser Altimeter: Experiment summary after the first year of global mapping of Mars. *Journal of Geophysical Research: Planets*, 106(E10):23689–23722.

Smith, D. E., Zuber, M. T., Solomon, S. C., Phillips, R. J., Head, J. W., Garvin, J. B., Banerdt, W. B., Muhleman, D. O., Pettengill, G. H., Neumann, G. A., Lemoine, F. G., Abshire, J. B., Aharonson, O., David, C., null, Hauck, S. A., Ivanov, A. B., McGovern, P. J., Zwally, H. J., and Duxbury, T. C. (1999). The Global Topography of Mars and Implications for Surface Evolution. *Science*, 284(5419):1495–1503.

Smith, M., Daerden, F., Neary, L., Khayat, A., Holmes, J., Patel, M., Villanueva, G., Liuzzi, G., Thomas, I., Ristic, B., et al. (2021). The climatology of carbon monoxide on Mars as observed by NOMAD nadir-geometry observations. *Icarus*, 362:114404.

Smith, M. D. (2004). Interannual variability in TES atmospheric observations of Mars during 1999-2003. *Icarus*, 167:148–165.

Smith, M. D. (2008). Spacecraft observations of the Martian atmosphere. *Annual Review of Earth and Planetary Sciences*, 36:191–219.

Smith, M. D. (2009). THEMIS observations of Mars aerosol optical depth from 2002-2008. *Icarus*, 202:444–452.

Smith, M. D. and Guzewich, S. D. (2019). The Mars global dust storm of 2018. In *49th International Conference on Environmental Systems*, pages 1–18, Boston, Massachusetts.

Smith, M. D., Wolff, M. J., Clancy, R. T., Kleinböhl, A., and Murchie, S. L. (2013). Vertical distribution of dust and water ice aerosols from CRISM limb-geometry observations. *J. Geophys. Res. Planets*, 118:321–334.

Smith, M. D., Wolff, M. J., Clancy, R. T., and Murchie, S. L. (2009). Compact Reconnaissance Imaging Spectrometer observations of water vapor and carbon monoxide. *Journal of Geophysical Research*, 114:E00D03.

Sneed, E. D. and Folk, R. L. (1958). Pebbles in the Lower Colorado River, Texas: A Study in Particle Morphogenesis. *The Journal of Geology*, 66(2):114–150.

Spiga, A., Forget, F., Madeleine, J.-B., Montabone, L., Lewis, S. R., and Millour, E. (2011). The impact of martian mesoscale winds on surface temperature and on the determination of thermal inertia. *Icarus*, 212(2):504–519.

Stamnes, K., Thomas, G. E., and Stamnes, J. J. (2017). *Radiative Transfer in the Atmosphere and Ocean*. Cambridge University Press, Cambridge.

Stcherbinine, A., Edwards, C. S., Smith, M. D., Wolff, M. J., Haberle, C., Al Tunaiji, E., Smith, N. M., Saboi, K., Anwar, S., Lange, L., and Christensen, P. R. (2023). Diurnal and seasonal mapping of martian ices with emirs. *Geophysical Research Letters*, 50(12):e2023GL103629.

Steele, L. J., Lewis, S. R., and Patel, M. R. (2014). The radiative impact of water ice clouds from a reanalysis of Mars Climate Sounder data. *Geophysical Research Letters*, 41(13):4471–4478.

Streeter, P. M., Lewis, S. R., Patel, M. R., Holmes, J. A., and Kass, D. M. (2020). Surface warming during the 2018/mars year 34 global dust storm. *Geophysical Research Letters*, 47(9):e2019GL083936.

Stähler, S. C., Mittelholz, A., Perrin, C., Kawamura, T., Kim, D., Knapmeyer, M., and et al. (2022). Tectonics of Cerberus Fossae unveiled by marsquakes. *Nature Astronomy*, 6(12):1376–1386.

Svedhem, H., Titov, D., Taylor, F., and Witasse, O. (2009). Venus Express mission. *Journal of Geophysical Research: Planets*, 114(E5).

Svitek, T. and Murray, B. (1990). Winter frost at Viking Lander 2 site. *Journal of Geophysical Research: Solid Earth*, 95(B2):1495–1510.

Symonds, R. B., Rose, W. I., Bluth, G. J. S., and Gerlach, T. M. (1994). Chapter 1. VOLCANIC-GAS STUDIES: METHODS, RESULTS, AND APPLICATIONS. In Carroll, M. R. and Holloway, J. R., editors, *Volatiles in Magmas*, pages 1–66. De Gruyter.

Szantai, A., Audouard, J., Forget, F., Olsen, K., Gondet, B., Millour, E., Madeleine, J., Pottier, A., Langevin, Y., and Bibring, J. (2021). Martian cloud climatology and life cycle extracted from Mars Express OMEGA spectral images. *Icarus*, 353:114101.

Temel, O., Senel, C. B., Porchetta, S., Muñoz-Esparza, D., Mischna, M. A., Van Hoolst, T., van Beeck, J., and Özgür Karatekin (2021). Large eddy simulations of the Martian convective boundary layer: Towards developing a new planetary boundary layer scheme. *Atmospheric Research*, 250:105381.

Thomas, I. R., Aoki, S., Trompet, L., Robert, S., Depiesse, C., Willame, Y., Cruz-Mermy, G., Schmidt, F., Erwin, J. T., Vandaele, A. C., Daerden, F., Mahieux, A., Neefs, E., Ristic, B., Hetey, L., Berkenbosch, S., Clairquin, R., Beeckman, B., Patel, M. R., Lopez-Moreno, J. J., and Bellucci, G. (2022a). Calibration of NOMAD on ESA's ExoMars Trace Gas Orbiter: Part 2 - The Limb, Nadir and Occultation (LNO) channel. *Planetary and Space Science*, 218:105410.

Thomas, I. R., Vandaele, A., Robert, S., Neefs, E., Drummond, R., Daerden, F., Delanoye, S., Ristic, B., Berkenbosch, S., Clairquin, R., Maes, J., Bonnewijn, S., Depiesse, C., Mahieux, A., Trompet, L., Neary, L., Willame, Y., Wilquet, V., Nevejans, D., Aballea, L., Moelans, W., Vos, L. D., Lesschaeve, S., Vooren, N. V., Lopez-Moreno, J.-J., Patel, M. R., Bellucci, G., and the NOMAD Team (2016). Optical and radiometric models of the NOMAD instrument part II: the infrared channels - SO and LNO. *Opt. Express*, 24(4):3790–3805.

Thomas, N., Cremonese, G., Ziethe, R., and et al. (2017). The Colour and Stereo Surface Imaging System (CaSSIS) for the ExoMars Trace Gas Orbiter. *Space Sci Rev*, 212:1897–1944.

Thomas, N., Pommerol, A., Almeida, M., Read, M., Cremonese, G., Simioni, E., and et al. (2022b). Absolute calibration of the Colour and Stereo Surface Imaging System (CaSSIS). *Planetary and Space Science*, 211:105394.

Thomas, N., Stelter, R., Ivanov, A., Bridges, N., Herkenhoff, K., and McEwen, A. (2011). Spectral heterogeneity on Phobos and Deimos: HiRISE observations and comparisons to Mars Pathfinder results. *Planetary and Space Science*, 59(13):1281–1292. Exploring Phobos.

Tillman, J. E., Johnson, N. C., Guttorp, P., and Percival, D. B. (1993). The Martian annual atmospheric pressure cycle: Years without great dust storms. *Journal of Geophysical Research*, 98(E6):10963–10971.

Titov, D. V., Moroz, V. I., Grigoriev, A. V., Rosenqvist, J., Combes, M., Bibring, J.-P., and Arnold, G. (1994). Observations of water vapour anomaly above Tharsis volcanoes on Mars in the ISM (Phobos-2) experiment. *Planetary and Space Science*, 42(11):1001–1010.

Titus, T. and Kieffer, H. (2002). A Comparison of the Mars South Polar Recession Rates Between 1999 and 2001.

Titus, T., Kieffer, H., and Christensen, P. (2003). Exposed water ice discovered near the south pole of Mars. *Science*, 299:1048–1051.

Titus, T. N., Calvin, W. M., Kieffer, H. H., Langevin, Y., and Prettyman, T. H. (2008). Martian Polar Processes. In Bell, J. F., editor, *The*

Martian Surface: Composition, Mineralogy, and Physical Properties, pages 578–598. Cambridge University Press.

Titus, T. N., Kieffer, H. H., Mullins, K. F., and Christensen, P. R. (2001). TES premapping data: Slab ice and snow flurries in the Martian north polar night. *Journal of Geophysical Research: Planets*, 106(E10):23181–23196.

Toon, O. B., McKay, C. P., Ackerman, T. P., and Santhanam, K. (1989). Rapid calculation of radiative heating rates and photodissociation rates in inhomogeneous multiple scattering atmospheres. *Journal of Geophysical Research*, 94:16,287–16,301.

Vago, J., Witasse, O., Svedhem, H., Baglioni, P., Haldemann, A., Gianfiglio, G., Blancquaert, T., McCoy, D., and De Groot, R. (2015). ESA ExoMars program: the next step in exploring Mars. *Solar System Research*, 49:518–528.

Valantinas, A., Becerra, P., Pommerol, A., Tornabene, L. L., Affolter, L., Cremonese, G., and et al. (2021). CaSSIS Color and multi-angular observations of martian slope streaks. *Planetary and Space Science*, 209:105373.

Van De Hulst, H. C. (1981). *Light Scattering by Small Particles*. Dover Publications, Inc.

Van den Acker, E., Van Hoolst, T., de Viron, O., Defraigne, P., Dehant, V., Forget, F., and Hourdin, F. (2002). Influence of the winds and of the CO2 mass exchange between the atmosphere and the polar ice caps on Mars' orientation parameters. *Journal of Geophysical Research (Planets)*, 107(E7):9–1, CiteID 5055.

Vandaele, A., Korablev, O., Daerden, F., Aoki, S., Thomas, I., Altieri, F., López-Valverde, M., Villanueva, G., Liuzzi, G., Smith, M., et al. (2019). Martian dust storm impact on atmospheric H_2O and D/H observed by ExoMars Trace Gas Orbiter. *Nature*, 568(7753):521–525.

Vandaele, A., Mahieux, A., Robert, S., Drummond, R., Wilquet, V., and Bertaux, J. (2015a). Carbon monoxide short term variability observed on Venus with SOIR/VEX. *Planetary and Space Science*, 113-114:237–255. SI:Exploration of Venus.

Vandaele, A., Neefs, E., Drummond, R., Thomas, I., Daerden, F., Lopez-Moreno, J.-J., Rodriguez, J., Patel, M., Bellucci, G., Allen, M., Altieri, F., Bolsée, D., Clancy, T., Delanoye, S., Depiesse, C., Cloutis, E., Fedorova, A., Formisano, V., Funke, B., Fussen, D., Geminale, A., Gérard, J.-C., Giuranna, M., Ignatiev, N., Kaminski, J., Karatekin, O., Lefèvre, F., López-Puertas, M., López-Valverde, M., Mahieux, A., McConnell, J., Mumma, M., Neary, L., Renotte, E., Ristic, B., Robert, S., Smith, M., Trokhimovsky, S., Auwera, J. V., Villanueva, G., Whiteway, J., Wilquet, V., and Wolff, M. (2015b). Science objectives and performances of NOMAD, a spectrometer suite for the ExoMars TGO mission. *Planetary and Space Science*, 119:233–249.

Vandaele, A. C., Lopez-Moreno, J.-J., Patel, M. R., Bellucci, G., Daerden, F., Ristic, B., Robert, S., Thomas, I. R., Wilquet, V., Allen, M., Alonso-Rodrigo, G., Altieri, F., Aoki, S., Bolsée, D., Clancy, T., Cloutis, E., Depiesse, C., Drummond, R., Fedorova, A., Formisano, V., Funke, B., González-Galindo, F., Geminale, A., Gérard, J.-C., Giuranna, M., Hetey, L., Ignatiev, N., Kaminski, J., Karatekin, O., Kasaba, Y., Leese, M., Lefèvre, F., Lewis, S. R., López-Puertas, M., López-Valverde, M., Mahieux, A., Mason, J., McConnell, J., Mumma, M., Neary, L., Neefs, E., Renotte, E., Rodriguez-Gomez, J., Sindoni, G., Smith, M., Stiepen, A., Trokhimovsky, A., Vander Auwera, J., Villanueva, G., Viscardy, S., Whiteway, J., Willame, Y., Wolff, M., and the NOMAD Team (2018). NOMAD, an Integrated Suite of Three Spectrometers for the ExoMars Trace Gas Mission: Technical Description, Science Objectives and Expected Performance. *Space Science Reviews*, 214(5):80.

Vandaele, A. C., Willame, Y., Depiesse, C., Thomas, I. R., Robert, S., Bolsée, D., Patel, M. R., Mason, J. P., Leese, M., Lesschaeve, S., Antoine, P., Daerden, F., Delanoye, S., Drummond, R., Neefs, E., Ristic, B., Lopez-Moreno, J.-J., Bellucci, G., and the NOMAD Team (2015c). Optical and radiometric models of the NOMAD instrument part I: the UVIS channel. *Opt. Express*, 23(23):30028–30042.

Vasavada, A. R. (2022). Mission overview and scientific contributions from the Mars Science Laboratory Curiosity rover after eight years of surface operations. *Space Science Reviews*, 218(3):14.

Villanueva, G. L., Smith, M. D., Protopapa, S., Faggi, S., and Mandell, A. M. (2018). Planetary Spectrum Generator: An accurate online radiative transfer suite for atmospheres, comets, small bodies and exoplanets. *Journal of Quantitative Spectroscopy and Radiative Transfer*, 217:86–104.

Vincendon, M. (2015). Identification of Mars gully activity types associated with ice composition. *Journal of Geophysical Research: Planets*, 120(11):1859–1879.

Vincendon, M., Forget, F., and Mustard, J. (2010a). Water ice at low to midlatitudes on Mars. *Journal of Geophysical Research: Planets*, 115(E10).

Vincendon, M., Langevin, Y., Poulet, F., Bibring, J.-P., Gondet, B., and Jouglet, D. (2008). Dust aerosols above the south polar cap of Mars as seen by OMEGA. *Icarus*, 196(2):488–505. Mars Polar Science IV.

Vincendon, M., Mustard, J., Forget, F., Kreslavsky, M., Spiga, A., Murchie, S., and Bibring, J.-P. (2010b). Near-tropical sub surface ice deposits on Mars. *Geophysical Research Letters*, 37(1):L01202.

Vincendon, M., Pilorget, C., Gondet, B., Murchie, S., and Bibring, J.-P. (2011). New near-IR observations of mesospheric CO_2 and H_2O clouds on Mars. *Journal of Geophysical Research: Planets*, 116(E11).

Viviano, C. E., Seelos, F. P., Murchie, S. L., Kahn, E. G., Seelos, K. D., Taylor, H. W., Taylor, K., Ehlmann, B. L., Wiseman, S. M., Mustard, J. F., et al. (2014). Revised CRISM spectral parameters and summary products based on the currently detected mineral diversity on Mars. *J. Geophys. Res. Planets*, 119:1403–1431.

Viúdez-Moreiras, D., Newman, C. E., Torre, M., Martinez, G., Guzewich, S., Lemmon, M., and et al. (2019). Effects of the MY34/2018 global dust storm as measured by MSL REMS in Gale crater. *Journal of Geophysical Research: Planets*, 124(7):1899–1912.

Warren, S. G. and Brandt, R. E. (2008). Optical constants of ice from the ultraviolet to the microwave: A revised compilation. *Journal of Geophysical Research*, 113(D14220).

Webster, C. R. and Mahaffy, P. R. (2011). Determining the local abundance of Martian methane and its' 13C/12C and D/H isotopic ratios for comparison with related gas and soil analysis on the 2011 Mars Science Laboratory (MSL) mission. *Planetary and Space Science*, 59(2):271–283. Methane on Mars: Current Observations, Interpretation and Future Plans.

Webster, C. R., Mahaffy, P. R., Atreya, S. K., Moores, J. E., Flesch, G. J., Malespin, C., McKay, C. P., Martinez, G., Smith, C. L., Martin-Torres, J., Gomez-Elvira, J., Zorzano, M.-P., Wong, M. H., Trainer, M. G., Steele, A., Archer, D., Sutter, B., Coll, P. J., Freissinet, C., Meslin, P.-Y., Gough, R. V., House, C. H., Pavlov, A., Eigenbrode, J. L., Glavin, D. P., Pearson, J. C., Keymeulen, D., Christensen, L. E., Schwenzer, S. P., Navarro-Gonzalez, R., Pla-García, J., Rafkin, S. C. R., Álvaro Vicente-Retortillo, Kahanpää, H., Viudez-Moreiras, D., Smith, M. D., Harri, A.-M., Genzer, M., Hassler, D. M., Lemmon, M., Crisp, J., Sander, S. P., Zurek, R. W., and Vasavada, A. R. (2018). Background levels of methane in Mars' atmosphere show strong seasonal variations. *Science*, 360(6393):1093–1096.

Willame, Y., Vandaele, A., Depiesse, C., Lefèvre, F., Letocart, V., Gillotay, D., and Montmessin, F. (2017). Retrieving cloud, dust and ozone abundances in the martian atmosphere using SPICAM/UV nadir spectra. *Planet. Space Sci.*, 142:9–25.

Wilquet, V., Drummond, R., Mahieux, A., Robert, S., Vandaele, A. C., and Bertaux, J. L. (2012). Optical extinction due to aerosols in the upper haze of Venus: four years of SOIR/VEX observations from 2006 to 2010. *Icarus*, 217:875–881.

Wilson, R. J. and Guzewich, S. D. (2014). Influence of water ice clouds on nighttime tropical temperature structure as seen by the Mars Climate Sounder. *Geophysical Research Letters*, 41(10):3375–3381.

Wilson, R. J., Neumann, G. A., and Smith, M. D. (2007). Diurnal variation and radiative influence of Martian water ice clouds. *Geophysical Research Letters*, 34(2).

Wiscombe, W. J. (1977). The delta-Eddington approximation for a vertically inhomogeneous atmosphere. Technical Note TN-121 + STR, National Center for Atmospheric Research, Boulder, Colorado.

Wiscombe, W. J. (1980). Improved Mie scattering algorithms. *Applied Optics*, 19(9):1505–1509.

Withers, P. (2012). Empirical Estimates of Martian Surface Pressure in Support of the Landing of Mars Science Laboratory. *Space Sci Rev*, 170:837–860.

Wolff, M. J. and Clancy, R. T. (2003). Constraints on the size of Martian aerosols from Thermal Emission Spectrometer observations. *J. Geophys. Res. Planets*, 108.

Wolff, M. J., Clancy, R. T., Kahre, M. A., Haberle, R. M., Forget, F., Cantor, B. A., and Malin, M. C. (2019). Mapping water ice clouds on Mars with MRO/MARCI. *Icarus*, 332:24–49.

Wolff, M. J., Smith, M. D., Clancy, R. T., Arvidson, R., Kahre, M., Seelos IV, F., Murchie, S., and Savijärvi, H. (2009). Wavelength dependence of dust aerosol single scattering albedo as observed by the Compact Reconnaissance Imaging Spectrometer. *Journal of Geophysical Research*, 114(E00D04).

Wolff, M. J., Todd Clancy, R., Goguen, J. D., Malin, M. C., and Cantor, B. A. (2010). Ultraviolet dust aerosol properties as observed by MARCI. *Icarus*, 208(1):143–155.

Wolkenberg, P., Giuranna, M., Grassi, D., Aronica, A., Aoki, S., Scaccabarozzi, D., and Saggin, B. (2018). Characterization of dust activity on Mars from MY27 to MY32 by PFS-MEX observations. *Icarus*, 310:32–47.

Wolkenberg, P., Giuranna, M., Smith, M. D., Grassi, D., and Amoroso, M. (2020). Similarities and Differences of Global Dust Storms in MY 25, 28, and 34. *Journal of Geophysical Research: Planets*, 125(3):e2019JE006104. e2019JE006104 2019JE006104.

Wu, Z., Li, T., Heavens, N., Newman, C., Richardson, M., Yang, C., Li, J., and Cui, J. (2022). Earth-like thermal and dynamical coupling processes in the Martian climate system. *Earth-Sci. Rev.*, 229:104023.

Zurek, R. W. and Smrekar, S. E. (2007). An overview of the Mars Reconnaissance Orbiter (MRO) science mission. *Journal of Geophysical Research: Planets*, 112(E5).